Sub-cellular metabolomics investigation of mitochondrial CI deficiency in cytosol & mitochondria of Ndufs4 mice

G van der Walt



orcid.org/0000-0001-5383-439X

Dissertation accepted in partial fulfilment of the requirements for the degree *Master of Science in Biochemistry* at the North-West University

Supervisor: Prof R Louw

Graduation May 2022

260168771

ACKNOWLEDGEMENTS

I thank my supervisor, **Prof Roan Louw**, for his guidance, patience and enthusiastic support. I have yet to meet a better mentor for an atypical student such as myself. Furthermore, I would like to acknowledge the following individuals that collectively enabled the success of this study:

- **Dr Shayne Mason** and **Prof Zander Lindeque,** for their assistance in performing NMR spectroscopy, LC-MS/MS, data processing, and their role in the publications stemming from this study.
- **Peet Jansen van Rensburg** and **Tiaan van Zyl,** for their guidance and assistance regarding the LC-MS/MS and NMR spectroscopy analyses.
- **Prof Francois van der Westhuizen** and **Dr Marianne Pretorius,** for helping with sampling during the heavily access-restricted first phases of the COVID-19 pandemic.
- **Dr Hayley Miller,** for her lead and guidance in performing Seahorse respirometry.
- **Luciano Willemse,** for his assistance in method establishment, experimental work, and being a constant source of friendship, inspiration and support throughout our 7-year journey at the NWU.
- **Charl du Plessis,** for his assistance in method establishment, experimental work and being a dependable colleague and friend.
- **Daneel Nel,** for her assistance in sample collection, genotyping and data processing.
- **Kobus Venter, Antoinette Fick** and **Jaco Vermeulen** of the PCDDP (NWU) for their roles in animal breeding, colony maintenance and test animal euthanasia.
- **Dr Mari van Reenen,** of the CHM (NWU) for her statistical consultation.
- **Valerie Viljoen,** for the language editing of this dissertation.
- **Anandi, Laurene, Kirsten** and **Zinandré,** for the mutual venting sessions, group psychology and coffee breaks outside the Biochemistry building every day.
- **Michelle, Maryke, Belinda** and all the other members of the **Mitochondria Research Laboratory** for their constant emotional support, laughs and fellowship.

Finally, I thank my family and dearest friends. Without the rock-solid emotional support, love and financial inputs of my mother and father, **Sonja** and **Sarel**, none of this would have been possible. To me chosen family, **Armagh, Dewald, Chante, Jani, Danitza** and the entire **Potch Tribe**- thank you for giving me a home away from home and shaping the person I have become. Above all, I thank the **Divine Wisdom** that pervades the beautiful logic of nature and imbued me with the ability to study its majesty in both scientific rigor and childlike wonder.

ABSTRACT

Mitochondrial Complex I (CI) is regarded as the foremost entry point for electrons that fuel oxidative phosphorylation. CI deficiency (CID) is the most common mitochondrial disease (MD) in humans and Leigh syndrome (LS), an MD characterized by progressive neuromuscular degeneration, is a debilitating result thereof. The complex clinical and biochemical LS manifestations lead to difficult diagnosis and a lack of effective treatment strategies, thus model systems such as whole-body *Ndufs4* knockout (KO) mice have greatly contributed to our understanding of the underlying pathogenesis. Through tissue-level metabolic characterization of the neural and muscular involvement at the forefront of the *Ndufs4* KO phenotype, several critical metabolic pathways were shown to contribute to the observed MD. Although organelle-specific regulation of the involved enzymes and metabolites is well supported by literature, no compartment-specific metabolic studies have been conducted in this model to date.

The aim of this study was to adapt existing cell fractioning procedures for subsequent mitochondrial and cytosolic metabolomics in *Ndufs4* KO whole brain and skeletal muscle to address this research gap. Hypothesis-generating metabolomics methods utilizing proton nuclear magnetic resonance spectroscopy (^{1}H-NMR), gas chromatography time-of-flight mass spectrometry (GC-TOF-MS) and liquid chromatography tandem mass spectrometry (LC-MS/MS) were applied at various stages.

We firstly present a novel methodology for mitochondrial and cytosolic purification isolation via magnetically activated cell sorting (MACS) and a novel filtration method. Complementary enzymatic, proteomic and respirometric assays proved the superior mitochondrial yield and purity of MACS over a standard centrifugal method, while mitochondrial integrity was not affected. The cytosolic fraction was accordingly shown to be sufficiently organelle free for metabolic comparison. Concentration curves of metabolite standards showed that the buffer environment does not critically detriment measurement precision, linearity or accuracy. Finally, a pilot application of this methodology to wildtype (WT) mouse brain fractions delivered 60–70 viable metabolites with sufficient accuracy and identity confidence for further *in vivo* metabolomics study.

In application of the developed workflow to a statistically viable cohort of *Ndufs4* KO and WT mice (n = 8 each), LS-related metabolic compartmentalization was shown. Untargeted ^{1}H-NMR and targeted LC-MS/MS amino acid and acylcarnitine profiling delivered 40–45 viable metabolites with excellent measurement precision and confident identification. The significantly altered brain metabolites showed increases in key bioenergetic intermediates- with greater

effect at the mitochondrial level. These features corroborated previous studies, implicating the role of neural redox (NADH, $FADH_2$) dysregulation and anabolic perturbations underlying mitochondrially-initiated integrated stress responses. Compartmentalized decreases in muscle bioenergetic intermediates emphasized the role of mitochondrial lactate and creatine metabolism, while providing evidence for disturbed proteostasis due to prolonged energy deficit. Additionally, a first report of sub-cellular calcium (Ca^{2+}) and magnesium (Mg^{2+}) measurement via ^{1}H-NMR also revealed Ca^{2+} accumulation specific to the neural mitochondria, contrasted by bicompartmental Mg^{2+} depletion in the muscle fractions.

In summary, this study provides a simple, cost-effective pipeline for sub-cellular metabolomics in mammalian disease models. In application, this methodology provides proof of mitochondrial/cytosolic compartmentalization in known pathological *Ndufs4* KO metabolic pathways. These results should pave the way for better understanding of mitochondrial metabolism in MD, towards improved diagnostic and therapeutic strategies.

Keywords: Sub-cellular metabolomics, compartmentalization, multi-platform metabolomics, MACS, mitochondria, cytosol, mitochondrial disease, *Ndufs4* knockout mice.

TABLE OF CONTENTS

ACKNOWLEDGEMENTS ..... **I**
ABSTRACT ..... **II**
LIST OF TABLES ..... **IX**
LIST OF FIGURES ..... **X**
LIST OF REACTIONS ..... **XII**
LIST OF SYMBOLS, UNITS, ABBREVIATIONS & LATIN TERMS ..... **XIII**

CHAPTER 1: INTRODUCTION **1**
1.1 Background, rationale and problem statement **2**
1.1 Aim and objectives **3**
1.2 Dissertation structure **4**
1.3 Study outcomes: Specific research outputs **5**
1.3.1 Published peer-reviewed article I (Chapter 4, Annexure C) 5
1.3.2 Published peer-reviewed article II (Chapter 5, Annexure D) 6
1.4 Ethical considerations and financial support **6**
1.5 Author contributions **6**

CHAPTER 2: LITERATURE STUDY **8**
2.1 Introduction **9**
2.2 Mitochondrial structure and organization **9**
2.2.1 Mitochondrial genome 9
2.2.2 Mitochondrial diversity and dynamic sub-population distribution 10
2.2.3 Overview of mitochondrial contributions to cellular homeostasis 10
2.3 Oxidative phosphorylation and the electron transport chain **11**
2.3.1 Structure and Organization 11
2.3.2 Functional mechanisms of the OXPHOS system 12
2.3.3 Contributing electron shuttles 14
2.4 Mitochondrial Complex I: frontline workhorse of the ETC **14**
2.4.1 CI structure 14
2.4.2 CI function 14
2.4.3 Biogenesis and CI assembly 16
2.4.4 The Ndufs4 subunit of CI 16
2.5 Mitochondrial disease **17**
2.5.1 Defining primary mitochondrial disease 18
2.5.2 Prevalence, genetics and clinical phenotype 18
2.5.3 Perturbed metabolic and signalling pathways 19
2.5.4 Proposed metabolic adaptations to MD 21
2.6 Complex I dysfunction and Leigh syndrome **21**
2.6.1 Complex I dysfunction and NDUFS4 in the context of MD 21
2.6.2 Leigh syndrome: Specific prevalence and pathology 22
2.7 *Ndufs4* knockout mice as adequate human Leigh Syndrome models **22**
2.7.1 Clinical Phenotype 24
2.7.2 Biochemical and metabolic characteristics 24

2.8 *Ndufs4* KO mouse metabolomics: Current insights and limitations 25
2.8.1 Metabolomics: introduction and value in MD research.....25
2.8.2 Tissue-specific metabolic profiles: the brain as primary LS target 26
2.8.3 Quadriceps metabolomics: special glycolytic fibre perturbations 26
2.9 Principles of metabolic compartmentalization.....27
2.10 Mitochondria as unique metabolic spaces.....28
2.10.1 Mitochondrial metabolite transport 29
2.11 Assaying mitochondrial metabolic compartmentalization 30
2.11.1 Metabolic flux analysis and mitochondrial isolation.....30
2.11.2 Mitochondrial isolation strategies for metabolome profiling.....30
2.11.3 Limitations inhibiting large-scale application 31
2.12 Current mitochondria-specific MD metabolomics knowledge 33
2.12.1 Sub-cellular metabolomics of ETC dysfunction.....33
2.13 Experimental design.....34

CHAPTER 3: METHODS & MATERIALS 37
3.1 Introduction 38
3.2 Animals and sampling.....38
3.2.1 Origin information and husbandry 38
3.2.2 Sample groups and sizes 39
3.2.3 Euthanasia according to ethical endpoints.....39
3.2.4 Tissue collection and sampling 40
3.3 Confirmation of genotype 40
3.3.1 Chemical and Primer information 40
3.3.2 Instrumentation and Software 41
3.3.3 Genotyping protocol 41
3.3.3.1 DNA isolation and quantification.....41
3.3.3.2 PCR amplification 42
3.3.3.3 Electrophoresis and imaging.....43
3.4 Standard compound preparations for buffer testing.....44
3.5 Established DC mitochondrial isolation 44
3.5.1 Instrumentation.....45
3.5.2 Established and standardized DC methodology 45
3.6 Fractioned magnetic isolation: MACS kit 46
3.6.1 Instrumentation.....47
3.6.2 Established and standardized MACS methodology 47
3.7 Comparison of analytical efficiency.....49
3.7.1 BCA Protein quantification 49
3.7.1.1 Instrumentation and software.....49
3.7.1.2 Methodology 49
3.7.2 Yield interrogation via CS recovery 50
3.7.2.1 Instrumentation and Software.....51
3.7.2.2 Methodology 51
3.7.2.3 Data analysis and processing.....51
3.7.3 Confirmation of MACS purity via Western blot 52
3.7.3.1 Instrumentation and software.....52
3.7.3.2 Fraction-specific sample preparation 53

3.7.3.3 SDS-PAGE separation....53
3.7.3.4 Blotting and imaging....54
3.7.4 Probing mitochondrial integrity by respiratory coupling via Seahorse respirometry....55
3.7.4.1 Instrumentation and software....56
3.7.4.2 Protocol....57
3.7.4.3 Data analysis....57
3.8 *Ndufs4* KO Metabolomics workflow overview....58
3.8.1 Internal standard preparation and addition prior to all analyses....60
3.9 GC-TOF-MS analyses....61
3.9.1 Instrumentation and Software....61
3.9.2 Sample preparation....61
3.9.2.1 Quality control samples....62
3.9.2.2 Derivatization....62
3.9.3 Analysis parameters....63
3.10 ^{1}H-NMR analyses....63
3.10.1 Instrumentation and Software....63
3.10.2 TSP chemical shift standard and sample preparation....64
3.10.3 Quality control samples, batch structure and run details....65
3.10.4 Analysis parameters....65
3.10.5 Sample recollection....66
3.11 LC-MS/MS Analyses....66
3.11.1 Instrumentation and Software....66
3.11.2 Isotope-labelled reference standard and Sample preparation....66
3.11.2.1 Derivatization....67
3.11.3 QC samples, batch structure and run details....68
3.11.4 Analysis parameters....68
3.12 Metabolomics data extraction, processing and statistical analyses....71
3.12.1 Biological samples: Data extraction and quality inspection....71
3.12.2 Data pre-processing....72
3.12.3 Data pre-treatment....73
3.12.4 Univariate and multi-variate statistics....74
3.13 GC-TOF-MS and ^{1}H-NMR method variations for standard compound mixture analyses....75

CHAPTER 4: NOVEL MITOCHONDRIAL & CYTOSOLIC PURIFICATION PIPELINE FOR COMPARTMENT-SPECIFIC METABOLOMICS IN MAMMALIAN DISEASE MODEL TISSUES....77
4.1 Background....78
4.2 Methods and Materials....80
4.2.1 Spiked standard compounds....80
4.2.2 Animals and Sampling....80
4.2.3 Mitochondrial isolation via differential centrifugation (DC)....81
4.2.4 Fractioned magnetic mitochondrial separation (FMMS)....81
4.2.5 Citrate synthase enzyme activity....82
4.2.6 Western Blotting....82

4.2.7 Measurement of oxygen consumption and respiratory control ratio (RCR) 83
4.2.8 Complimentary GC-TOF-MS and ^{1}H-NMR Metabolic profiling 83
4.2.8.1 Extract preparation and derivatization 84
4.2.8.2 Instrumentation and analysis parameters 85
4.2.8.3 Data extraction and processing 85
4.3 Results and Discussion 86
4.3.1 Establishment of MACS-based fractioning workflow for application in mouse tissues 86
4.3.1.1 Protocol variations produce mitochondrial isolates of sufficient yield 86
4.3.1.2 Novel filtering approach depletes residual organelles to produce cytosolic fractions 88
4.3.1.3 Mitochondrial purity and integrity unaffected by selected protocol adaptations 89
4.3.2 Effect of MACS buffers on GC-TOF-MS and NMR metabolomics 90
4.3.2.1 GC-TOF-MS analysis of standard compounds in MACS environment 90
4.3.2.1.1 Analytical precision 91
4.3.2.1.2 Linearity 92
4.3.2.2 ^{1}H-NMR analysis of standard compounds in MACS buffer vs SOP aqueous environment 92
4.3.2.2.1 Analytical precision 93
4.3.2.2.2 Relative accuracy 94
4.3.2.2.3 Quantitative linearity 95
4.3.3 Applicability of selected methodology to mouse model tissues 95
4.3.3.1 Pilot GC-TOF-MS analysis of mitochondria and cytosol 96
4.3.3.2 Probing the applicability of a limited-volume ^{1}H-NMR protocol 97
4.4 Conclusion 98
4.5 Supplementary Results 100
4.5.1 Detailed CS yield and protein results 100
4.5.2 Additional GC-TOF-MS and ^{1}H-NMR results 102

CHAPTER 5: SUB-CELLULAR METABOLOMICS CONTRIBUTES MITOCHONDRIA-SPECIFIC METABOLIC INSIGHTS TO A MOUSE MODEL OF LEIGH SYNDROME 106
5.1 Introduction 107
5.2 Results 110
5.2.1 Experimental rationale and data quality 110
5.2.2 Metabolome coverage and data clean-up 112
5.2.3 Compartment-specific, significant *Ndufs4* KO metabolite alterations 114
5.2.4 Amino acids accumulate in whole-brain CI-deficient mitochondria to a greater extent than cytosolic or region-specific metabolomics can fully elucidate 116
5.2.5 Differential depletion of quadriceps mitochondrial and cytosolic metabolites related to CID muscle metabolic reprogramming 117

5.2.6 First report of tissue and compartment-specific bivalent cation measurement in *Ndufs4* KO mice highlights role of metal homeostasis in integrated stress responses 120
5.3 Discussion 121
5.3.1 Contribution towards *in vivo Ndufs4* KO Model and *in vitro* CID knowledge base 121
5.3.2 Limitations and future directions 123
5.4 Materials and methods 124
5.4.1 Animals and sampling 124
5.4.2 Mitochondrial isolation and cytosol preparation 125
5.4.3 Metabolomics group structure and preparation for multiplatform studies 125
5.4.4 Internal standards and quality control samples 126
5.4.5 Untargeted ^{1}H-NMR spectroscopy 126
5.4.6 LC-MS/MS amino acid and acylcarnitine profiling 127
5.4.7 Data processing 128
5.4.8 Statistical analyses 129
5.5 Supplementary results 130

CHAPTER 6: SUMMARY, CONCLUSIONS & RECOMMENDATIONS 135
6.1 Introduction 136
6.2 Summary and conclusions 136
6.2.1 Sample collection phase 136
6.2.2 Phase A: Establishing a suitable MACS methodology for mitochondrial and cytosolic fraction preparation from *Ndufs4* KO mice 137
6.2.3 Phase B: Probing the viability of metabolomics in the MACS buffer environment and the produced tissue fractions 138
6.2.4 Phase C: First application of sub-cellular metabolomics towards the elucidation of *Ndufs4* KO mitochondrial metabolic alterations 139
6.3 Strengths and limitations of the present study 140
6.3.1 *Ndufs4* KO and WT mouse breeding and sampling 140
6.3.2 MACS mitochondrial isolation and cytosol filtration 141
6.3.3 Cell fraction quality control 142
6.3.4 Multi-platform metabolomics of mitochondrial and cytosolic isolates 143
6.4 Recommendations and prospects for future research 144
6.4.1 MACS-based metabolomic applications to mitochondria-related disease 144
6.4.2 Sub-cellular resolution of Leigh syndrome and Complex I disfunction 145
ANNEXURE A: CHEMICAL & REAGENT INFORMATION 146
ANNEXURE B: SAMPLED ANIMAL DETAILS 152
ANNEXURE C: PUBLISHED PEER-REVIEWED PAPER I 154
ANNEXURE D: PUBLISHED PEER-REVIEWED PAPER II 170
REFERENCES 193

LIST OF TABLES

Table 3-1: Primers used during *Ndufs4* genotyping 41

Table 3-2 : IS details and analyzed amounts across all samples and platforms 60

Table 3-3: MRM Parameters for metabolites and internal standards monitored 69

Table 4-1: Precision and quantitative linearity of selected standards in MACS buffer environment, analyzed by GC-TOF-MS. 91

Table 4-2: Comparison of precision (%CV) and relative recovery of standard compounds analyzed via ^{1}H-NMR in either MACS buffer environment or pure water (SOP).....94

Table 4-3: List of filtered and annotated compounds detected by GC-TOF-MS as common features in both brain mitochondrial and cytosolic extracts. 104

Table 4-4: List of filtered and annotated compounds detected by GC-TOF-MS as features unique to brain mitochondrial and cytosolic extracts, respectively.....105

Table 5-1: VIP compounds identified by univariate statistical and practical significance testing. 114

Table 5-2: Positively detected features by LC-MS/MS and ^{1}H-NMR.....131

LIST OF FIGURES

Figure 2-1: Mitochondrial structure and OXPHOS system organization/function. 12

Figure 2-2: Graphic representation of Q-cycle and G3P shuttle functionality in relation to ETC activity.....13

Figure 2-3: Complex I structure, organization and functional mechanistics.....15

Figure 2-4: Common mitochondrial disease manifestations in various organ systems. 19

Figure 2-5: Creation, biochemical and clinical phenotype of *Ndufs4* KO mice. 23

Figure 2-6: Different forms of metabolic compartmentalization in biological systems. 28

Figure 2-7: Methodological hurdles limiting sub-cellular metabolomic applications.....32

Figure 2-8: Schematic summary of experimental strategy.....35

Figure 3-1: Example genotyping results 43

Figure 3-2: Summarised DC mitochondrial and cytosolic isolation protocol. 45

Figure 3-3: Established MACS workflow for mitochondrial & cytosolic purification. 47

Figure 3-4: Typical OCR vs time graph obtained from XFe96 coupling assay 56

Figure 3-5: Final multi-platform metabolomic workflow for mitochondrial isolates and cytosolic filtrates 59

Figure 3-6: Currently accepted metabolite identification confidence levels 75

Figure 4-1: Comparison of mitochondrial enrichment from brain tissue for DC and MACS methods (n=3). 87

Figure 4-2: Comparison of fraction purity of DC and MACS methods by immunoblotting against compartment-specific proteins.....89

Figure 4-3: Comparison of features detected in the mitochondrial (n = 1; 3 replicates) and cytosolic (n = 1; 3 replicates) fractions of *Ndufs4* WT mouse brain.....97

Figure 4-4: Selection of antibody dilution and mitochondrial elution parameters for quadricep muscle tissues (150 mg). 100

Figure 4-5: Comparison of CS distribution during various steps of the fractioning workflow for whole-brain and quadricep tissues. 100

Figure 4-6: Unprocessed Western Blot results 101

Figure 4-7: Linearity graphs for the selected nine standards in MACS buffer, analyzed via GC-TOF-MS (A – I) 102

Figure 4-8: Fig. S5 Visualization of other selected NMR internal standards A) TSP and B) 3-PBA, at 750 uM true concentration, and their unreliability in the high-ionic MACS environment. 103

Figure 4-9: Comparison of linearity for the ^{1}H-NMR measured compounds in MACS environment and water. 103

Figure 4-10: Compounds detected via ^{1}H-NMR in mitochondrial and cytosolic fractions of mouse quadricep muscle. 104

Figure 5-1: Graphical abstract summarizing experimental rationale and core results of the *Ndufs4* KO *versus* WT sub-cellular metabolomics study. 110

Figure 5-2: Summarized workflow for the study. 111

Figure 5-3: Technical variance and data quality for each ^{1}H-NMR and LC-MS/MS batch. 112

Figure 5-4: Comparison of viable metabolite presence and gross abundance across sample matrices. 113

Figure 5-5: Compartment−specific metabolite alterations in *Ndufs4* KO whole brain, identified by ^{1}H−NMR and LC−MS/MS. 116

Figure 5-6: Compartment-specific metabolite alterations in *Ndufs4* KO quadriceps muscle, identified by ^{1}H-NMR and LC-MS/MS. 119

Figure 5-7: Compartment-specific magnesium and calcium levels, detected as EDTA chelates by ^{1}H-NMR. 121

Figure 5-8: Scatterplots of raw and TUS normalized total feature sum vs run order per NMR batch, indicating applicability of the applied normalization strategy. 130

Figure 5-9: Scatterplots of raw and TUS normalized total feature sum vs run order per LC-MS/MS batch, indicating applicability of the applied normalization strategy. 131

Figure 5-10: PLS-DA projections of the univariately selected VIP features for each tissue or cell-compartment sample matrix. 133

Figure 5-11: Additional compartment-specific metabolite alterations in *Ndufs4* KO whole-brain, identified by ^{1}H-NMR and LC-MS/MS. 134

Figure 5-12: Additional compartment-specific metabolite alterations in *Ndufs4* KO quadricep muscle, identified by ^{1}H-NMR and LC-MS/MS. 134

.

LIST OF EQUATIONS

Equation 3-1: Determining protein concentration from BCA output. 50

Equation 3-2: Calculating normalized CS activity.....52

Equation 3-3: Calculating CS enrichment (yield).....52

Equation 3-4: Generalized logarithm transformation. 74

Equation 3-5: Pareto scaling of metabolomics data. 74

LIST OF REACTIONS

Reaction 3-1: CoA formation by CS catalysis. 50

Reaction 3-2: TNB formation from CoA-SH and DTNB.....50

Reaction 3-3: Oximation of ketone groups by methoxamine-HCl 62

Reaction 3-4: Silylation of active hydrogen groups by BSTFA.....62

Reaction 3-5: Butylation of active hydrogen groups by butanolic-HCl 67

LIST OF SYMBOLS, UNITS, ABBREVIATIONS & LATIN TERMS

Symbols	
&	And
-/-	Homozygous knockout genotype; both alleles of interest are absent from the specific gene locus
~	Approximately
+/-	Heterozygous knockout genotype; one allele of interest is absent from the specific gene locus, while the other is present
+/+	Homozygous knockout genotype; both alleles of interest are present at the specific gene locus
<	Less than
>	Larger than
±	Plus-minus; approximately
x	Times
↑	Increase
↓	Decrease
©	Copyright
®	Registered
™	Trademark
♂	Male
♀	Female
I	One (Roman numeral)
II	Two (Roman numeral)
III	Three (Roman numeral)
IV	Four (Roman numeral)
V	Five (Roman numeral)
Ø	Diameter
α	Alpha
β	Beta
Δ	Delta (signifying change)
ε	Molar extinction coefficient
λ	Wavelength
v	Reaction velocity
ΔpH_m	Mitochondrial pH gradient
Δpmf	Proton motive force
$\Delta\psi_m$	Mitochondrial membrane potential
Units of measurement	
%	Percentage
x*g*	Relative centrifugal force; as a factor of gravitational acceleration
°	Degrees
°C	Degrees Celsius
Abs	Absorbance
amu	Atomic mass units
cm	Centimetres
eV	Electron volt
g	Grams
Hz	Hertz; unit of frequency
kb	Kilobase; one thousand nucleotide base pairs
kDa	Kilodaltons
L	Litres
M	Molarity; moles solute per litre solvent

m/z	Mass-to-charge ratio
mAbs	Milliabsorbance; one thousandth of an absorbance unit
mg	Milligram
MHz	Megahertz
mL	Millilitre
mm	Millimetre
mM	Millimolar
mol	Mole
mV	Millivolt
N	Normality; molar concentration divided by an equivalence factor
ng	Nanogram
nm	Nanometre
nmol	Nanomole
pH	Potential of hydrogen; negative natural logarithm of the molar H^+ concentration
ppm	Parts per million
psi	Pound-force per square inch; unit of pressure
V	Volt
v/v	Volume of solute per volume of solvent
w/v	Weight of solute per volume of solvent
µg	Microgram
µL	Microlitre
µM	Micromolar

Abbreviations

1C	One-carbon; metabolism relating methyl group transfer
^{1}H-NMR	Proton nuclear magnetic resonance spectroscopy
3’	3-prime hydroxyl group of a polynucleotide chain
3-HB	3-Hydroxybutyric acid
3-PBA	3-Phenylbutyric acid
5’	5-prime phosphate group of a polynucleotide chain
5’ to 3’	Conventional polynucleotide directionality; from 5-prime to 3-prime end
ADP	Adenosine diphosphate
Ala	L-alanine
AM	*Ante meridiem* (Latin): before noon
AMP	Adenosine monophosphate
ARE	United Arab Emirates (ISO 3166 alpha-3 code)
Arg	L-arginine
Asn	L-asparagine
Asp	L-aspartate
ATF	Activating transcription factors
ATP	Adenosine triphosphates
ATPase	Adenosine triphosphatase
AVMA	American Veterinary Medical Association
BAIBA	β-aminoisobutyric acid
BCA	Bicinchoninic acid
BCAA	Branched-chain amino acid
bp	Base pairs
BrCy	Cytosol fraction of whole-brain samples
BrMi	Mitochondrial fraction of whole-brain samples
BSA	Bovine serum albumin
BSTFA	*N,O*-bis(trimethylsilyl)trifluoro acetamide
C0-carnitine	Carnitine
C12-carnitine	Dodecanoyl carnitine
C14-carnitine	Myristoyl carnitine
C16-carnitine	Palmitoyl carnitine

C18-carnitine	Stearoyl carnitine
C2-carnitine	Acetylcarnitine
C3-carnitine	Propionyl carnitine
C4-carnitine	Butanoyl carnitine
C5-carnitine	Isovaleryl carnitine
C6-carnitine	Hexanoyl carnitine
C8-carnitine	Octanoyl carnitine
CI	Complex I; NADH:ubiquinone oxidoreductase; EC 1.6.5.3 or confidence interval (depending on context)
CII	Complex II; succinate:ubiquinone oxidoreductase; EC 1.3.5.1
CIII	Complex III; ubiquinol:ferricytochrome oxidoreductase; EC 1.10.2.2
Citru	Citrulline
CIV	Complex IV; ferricytochrome-c:oxygen oxidoreductase; EC 1.9.3.1
CV	Complex V; ATP synthase; EC 3.6.1.3 or coefficient of variation (depending on context)
Ca^{2+}	Calcium(II) ion
cAMP	Cyclic adenosine monophosphate
Cat. #	Catalogue number
CHE	Sweden (ISO 3166 alpha-3 code)
Chol	Choline
(m/c) CK	Creatine kinase (mitochondrial or cytosolic isoform)
CO_2	Carbon dioxide
CoA	Coenzyme A
CS	Citrate synthase
Cu^{+}	Copper(I) ion
Cu^{2+}	Copper(II) ion
$CuSO_4$	Cupper(II) sulphate
COSY	Correlation spectroscopy
%CV	Percentage coefficient of variation
Cyt c	Cytochrome c (oxidized form)
D_2O	Deuterium oxide / deuterated water
DC	Differential centrifugation
DEU	Germany (ISO 3166 alpha-3 code)
DHAP	Dihydroxyacetone phosphate
DMPA	*N,N*-dimethyl-L-phenylalanine
DMSO	Dimethyl sulfoxide
DNA	Deoxyribonucleic acid
DTNB	2,2'-Dinitro-5,5'-dithiobenzoic acid
D-value	Effect size value of practical significance
e^{-}	Electron
e.g.	*Exempli gratia* (Latin): for example
EC number	Enzyme commission number
EDTA	Ethylenediaminetetraacetic acid
EGTA	Ethylene glycol-bis(β-aminoethyl ether)-*N,N,N',N'*-tetraacetic acid
EI	Electron impact
ESI	Electrospray ionization
ETC	Electron transport chain
etc.	*Etcetera* (Latin): indicates similar items are applicable but not mentioned
ETF	Electron transfer flavoprotein
ETFDH	Electron transfer flavoprotein:ubiquinone dehydrogenase
ETF-QO	Formal nomenclature for ETFDH
FAD^{+}	Flavin adenine dinucleotide (oxidized form)
$FADH_2$	Flavin adenine dinucleotide (reduced form)
FDA	Food and Drug Administration (USA)
FDR	False discovery rate correction

Fe^{2+}	Iron(II) ion
Fe^{3+}	Iron(III) ion
Fe-S	Iron-sulphur
FGF-21	Fibroblast growth factor 21
FMMS	Fractioned magnetic mitochondrial separation
FMN	Flavin mononucleotide (oxidized form)
FRA	France (ISO 3166 alpha-3 code)
GBR	United Kingdom (ISO 3166 alpha-3 code)
GC-TOF-MS	Gas chromatography time-of-flight mass spectrometry
GDF-15	Growth differentiation factor 15
Gln	L-glutamine
Glu	L-glutamate
Gly	Glycine
G3P	Glycerol-3-phosphate
(m/c)GPDH	Glycerol-3-phosphate dehydrogenase (Mitochondrial/cytosolic isoform)
GSH	Glutathione (reduced)
GSSG	Glutathione (oxidized)
H^+	Hydrogen ion; proton
H_2O	Water
H_2O_2	Hydrogen peroxide
HCl	Hydrochloric acid
HEPES	2-[4-(2-hydoxyethyl)piperazin-1-yl] ethanesulfonic acid
HET	Heterozygous; carrying one mutated and one wildtype allele.
HPLC	High-performance liquid chromatography
HPro	4-Hydroxyproline
HSP-60	Heat shock protein 60
ID	Identification number
IMM	Inner mitochondrial membrane
IMS	Intermembrane space
IS	Internal standard
ISR	Integrated stress response
ITA	Italy (ISO 3166 alpha-3 code)
JRES	J-Resolved two-dimensional nuclear magnetic resonance spectroscopy
K^+	Potassium ion
KCl	Potassium chloride
KH_2PO_4	Potassium phosphate monobasic
KOH	Potassium hydroxide
KSS	Kearns-Sayre syndrome
Lac	L-lactate
LAMP-2	Lysosome associated membrane protein
LC-MS/MS	Liquid chromatography tandem mass spectrometry
(m)LDH	Lactate dehydrogenase (Mitochondrial isoform)
LDS	Lithium dodecyl sulphate
LLOD	lower limit of detection
LOHN	Leber’s hereditary optic neuropathy
loxP	Locus of X(cross)-over P1
LS	Leigh syndrome
LS-M	MACS-kit LS column for lysate separation
Lys	L-lysine
MACS	Magnetically activated cell sorting
MAS	Mitochondrial assay solution for Seahorse respirometry
MD	Mitochondrial disease
MELAS	Mitochondrial encephalopathy, lactic acidosis and stroke-like episodes
MERFF	Mitochondrial encephalopathy with ragged red fibres
MFA	Metabolic flux analysis

MI	Mitochondrial isolation
MILS	Maternally inherited Leigh syndrome
MRM	Multiple reaction monitoring
MSTUS	Mass spectral total useful signal
mtDNA	Mitochondrial DNA
mTORC1	Mammalian/mechanistic target of rapamycin complex 1
n	Number of; amount
N-module	NADH binding module of Complex I
N/A	Not applicable
Na^+	Sodium ion
NaCl	Sodium chloride
NAD^+	Nicotinamide adenine dinucleotide (oxidized)
NADH	Nicotinamide adenine dinucleotide (reduced)
$NADP^+$	Nicotinamide adenine dinucleotide phosphate (oxidized)
NADPH	Nicotinamide adenine dinucleotide phosphate (reduced)
NaN_3	Sodium azide
nDNA	Nuclear DNA
NDUFS4	NADH:ubiquinone oxidoreductase iron-sulphur protein 4
Ndufs4	NADH:ubiquinone oxidoreductase iron-sulphur protein 4 encoding gene
Ndufs4$^{-/-}$	Ndufs4 knockout mouse
NIST	National Institute of Standards and Technology
NLD	Netherlands (ISO 3166 alpha-3 code)
NMR	Nuclear magnetic resonance spectroscopy
NOESY	Nuclear overhauser effect spectroscopy
NRF	National Research Foundation of South Africa
NWU	North-West University
O_2	Molecular oxygen
$O_{2\text{-}}$	Superoxide anion
OMIM	Online Mendelian Inheritance in Man
OMM	Outer mitochondrial membrane
Orn	Ornithine
OXPHOS	Oxidative phosphorylation
P	Postnatal age (in days)
P module	Proton pumping module of Complex I
PCA	Principal component analysis
PCDDP	Preclinical Drug Development Platform
PCR	Polymerase chain reaction
P_D module	Distal proton pumping module of Complex I
Phe	L-phenylalanine
P_i	Inorganic phosphate
P_P module	Proximal proton pumping module of Complex I
Pro	L-proline
ProDH	Proline dehydrogenase
PSST	NADH:ubiquinone oxidoreductase core subunit S7; NDUFS7
p-value	Probability value; the probability of a type I statistical error
Q	Ubiquinone; coenzyme Q (oxidized)
Q module	Ubiquinone binding module of Complex I
QC	Quality control or quality control sample
QH_2	Ubiquinone; coenzyme Q (reduced)
QuCy	*Quadriceps femoris* muscle cytosolic fraction
QuMi	*Quadriceps femoris* muscle mitochondrial fraction
R^2	Coefficient of determination; indication of data linearity
RC	Respiratory chain
Redox	Reduction-oxidation
RNA	Ribonucleic acid

(mt)ROS	(Mitochondria-derived) Reactive oxygen species
rpm	Revolutions per minute
rRNA	Ribosomal ribonucleic acid
R.T.	Retention time
S/N	Centrifugal supernatant or signal-to-noise ratio; depending on context
SAVC	South African Veterinary Council
SB	Separation buffer provided in commercial MACS kit
SC	Supercomplex
SD	Standard deviation
Ser	L-serine
SDS-PAGE	Sodium dodecyl sulphate polyacrylamide gel electrophoresis
SLC	Solute carrier proteins
SOP	Standard operating procedure
SPF	Specific pathogen-free area
Src	Sarcosine
Thr	L-threonine
TIA	Technology Innovation Agency of South Africa
T_m	Melting temperature
TMCS	Trimethylchlorosilane
TMS	Trimethylsilyl
TNB	2-Nitro-5-thiobenzoic acid
tRNA	Transfer ribonucleic acid
$Trx(SH)_2$	Reduced thioredoxin
Trx(SS)	Oxidized thioredoxin
Tyr	L-tyrosine
TSP	Trimethylsilyl propionic acid
TXI	Triple-resonance inverse
USA	United States of America (ISO 3166 alpha-3 code)
UC	Ultracentrifugation
UCS	Units of citrate synthase activity measured
UV	Ultraviolet
v	Version; related to software
Val	L-valine
VIP	Variable important in projection
VDAC	Voltage-dependant anion channel
vs	*Versus* (Latin): against, compared or contrast between terms.
VUmc	Vrije Universiteit (VU) university medical centre
WT	Wildtype; genetically unaltered sample
ZAF	Republic of South Africa (ISO 3166 alpha-3 code)
β-Ala	Beta-alanine
Δatp4	Yeast model of mitochondrial complex IV ATP4 protein knockout
Δsdh2	Yeast model of mitochondrial complex II SDH2 protein knockout

Latin terms

Ad libitum	According to pleasure; without restriction
De novo	Anew; from the beginning
Homo sapiens	A species of primates to which modern humans belong
In vitro	In the glass; a process outside of a living organism
In vivo	In life; a process within a living organism
Mus musculus	Rodent species commonly known as a house mouse
Post-mortem	After death

CHAPTER 1

Introduction

1.1 Background, rationale and problem statement

Mitochondrial disease (MD) defines an umbrella term of pathologies that represent the most prevalent group of inborn metabolic errors amongst patients, with 1 in 4000-5000 new-borns affected. Despite knowing the underlying pathogenic mutations, MD patients still present vast clinical and biochemical heterogeneity- thus many cases are still undiagnosed, treatment options are limited, and no cures currently exist (Russell *et al.*, 2020). Dysfunction of the mitochondrial oxidative phosphorylation (OXPHOS) system's Complex I (CI) is the most common form of MD that often leads to a severe childhood-onset neuromuscular disease known as Leigh syndrome (LS) (Lake *et al.*, 2015; Quintana *et al.*, 2010). Due to the rarity and severity of clinical cases, animal models contribute vastly to our understanding of the mechanisms underlying MD- with the whole-body *Ndufs4* knockout (KO) mouse model being one of the most reliable for CI deficiency, as these animals presents with a progressive LS-like phenotype.

Current research on *Ndufs4* KO mice suggests the LS phenotype is neurologically driven- with only a few sub-cortical brain regions being responsible for most of the pathology (Johnson *et al.*, 2020; Quintana *et al.*, 2010). Recent evidence, however, shows a greater involvement of muscle perturbation in the overall syndrome than previously expected- as the neuromuscular systems are highly integrated, muscle contributes to whole-body energy availability, and these two tissues are frequently affected in various MDs (Foriel *et al.*, 2018; Terburgh *et al.*, 2019). Assessing the metabolite content of *Ndufs4* KO brain and skeletal muscle tissues has convincingly shown characteristic perturbations in core energy metabolism, oxidative state and biosynthetic pathways, with tissue-, cell type-, and age-specific patterns (Terburgh *et al.*, 2019; Terburgh *et al.*, 2021). Despite the metabolome being the closest phenotypic indicator, it is unknown to which extent the mitochondrial dysfunction affects mitochondrial metabolism alone in comparison to the whole-cell repercussions thereof.

In that regard, recent methodologies focusing on studying mitochondrial metabolism separate from that of the cytosol promise to give compartment-specific clarity on the interdependent yet separately regulated metabolism of these organelles in response to energy deficiency. As the field of sub-cellular metabolomics is still in its infancy, no adequate methodologies exist for studying the mitochondria and cytosol-specific metabolism of mammalian MD models without further genetic manipulation- and concurrently no previous studies have investigated metabolic compartmentalization in the brain and muscle of *Ndufs4* KO mice.

1.1 Aim and objectives

The aim of this study is to establish and implement a mitochondrial isolation, cytosolic purification and sub-cellular metabolomics approach for investigating metabolic compartmentalization in *Ndufs4* KO brain and skeletal muscle. This study is divided into three sections based on this aim, which will be met by accomplishing the objectives detailed below.

1. **Breeding, genotyping and sample collection**, performed before and during the main study phases
   1.1. Interbreeding and euthanasia of the required mice as part of the larger study. Initial genotyping at weening age was also performed outside the scope of this study.
   1.2. Collect whole brain and quadricep muscle tissue for immediate mitochondrial and cytosolic isolation, as well as tailsnips for genotype confirmation.
   1.3. *Post-mortem* confirmation of sample animal genotypes by polymerase chain reaction.

2. **Phase A:** Standardization and assessment of the sub-cellular fractionation protocol
   2.1. Tissue homogenization and standardization of the cell fractioning procedure:
      2.1.1. Mitochondrial isolation via kit-based magnetically activated cell sorting (MACS).
      2.1.2. Filtering of the post-mitochondrial supernatant to produce a cytosolic fraction.
      2.1.3. Preparing differential centrifugation (DC) derived mitochondria and cytosol as analytical control for the above-mentioned fractions.
   2.2. Compare the yield of all produced fractions and intermediate samples as citrate synthase activity enrichment.
   2.3. Compare fraction purities through SDS-PAGE and Western blotting.
   2.4. Show mitochondrial inner membrane integrity via Seahorse respirometry.

3. **Phase B:** Establishment of multi-platform metabolomics in the MACS buffer environment.
   3.1. Adapt an in-house gas chromatography time-of-flight mass spectrometry (GC-TOF-MS) method for the untargeted analysis of MACS-derived fractions in the kit-supplied isolation buffer, using a mixture of pure metabolite reference standards.
   3.2. Adapt an in-house miniaturized nuclear magnetic resonance spectroscopy (^{1}H-NMR) method for the untargeted analysis of MACS-derived fractions in the specified kit-supplied isolation buffer, using a mixture of pure metabolite reference standards.

3.3. Determine biological applicability and repeatability of the entire fractioning and metabolomics workflow in *Ndufs4* wildtype (WT)[1] brain mitochondria and cytosol.

4. **Phase C:** Sub-cellular metabolomics investigation of *Ndufs4* KO and WT mice.
   4.1. Adapt an in-house LC-MS/MS profiling method to obtain precise measurement of amino acid and acylcarnitine ratios in post-NMR, MACS-derived fractions.
   4.2. Sub-cellular metabolic profiling of *Ndufs4* KO and WT skeletal muscle and brain via ^{1}H-NMR and LC-MS/MS.
      4.2.1. Confirm metabolite identities by 2D-NMR and LC-MS/MS profiling of pure reference standards for each targeted amino acid and acylcarnitine
   4.3. Data pre-processing and pre-treatment.
   4.4. Statistical analysis and discriminatory metabolite discovery.
   4.5. Pathway analysis and biological interpretation.

1.2 Dissertation structure

This dissertation is presented in chapter format as required by the North-West University (NWU), comprising six total chapters. Two peer-reviewed academic journal publications, presented as published with minor alterations[2] to fit the format of the dissertation, comprise the results section of this study (Chapter 4 and 5).

Chapter 1 describes the rationale, problem statement, aim and objectives of the entire study. The dissertation structure, research outcomes, financial and ethical considerations are also detailed here. As required by copyright law, the express permission of all co-authors to present the peer-reviewed papers for examination here is provided at the end of this chapter.

Chapter 2 provides a comprehensive literature review of the OXPHOS system, CI, the NDUFS4 CI subunit and mitochondrial diseases- with focus on CID, Leigh syndrome and the *Ndufs4* KO mouse model. Finally, the novel field of sub-cellular metabolomics, its applications, limitations and value in mitochondrial disease research conclude this chapter.

---

[1] Throughout this dissertation *Ndufs4* KO, WT and heterozygous (HET) denote the *Ndufs4*$^{-/-}$, *Ndufs4*$^{+/+}$ and *Ndufs4*$^{+/-}$ genotypes, respectively. The superscript annotation is only used when referring to creation and genotypic characterisation of the mouse model.

[2] This includes text formatting, reconciling section and figure numbers as well as referencing styles and adding supplementary information after the main text of each published chapter. Abstracts, keywords and author declarations, as shown in the annexed publications, are also not presented in the chapters

Chapter 3 details the materials and methods utilized to meet the study objectives. Instrumentation, protocols and quality control measures are provided- while the reagents and consumables used are tabulated in Annexure A for convenient reference.

Chapter 4 presents the first peer-reviewed paper published in *Metabolomics* (Van der Walt & Louw, 2020), which describes the viability of our designed MACS workflow for sub-cellular metabolomics. The outcomes of MACS method optimizations, proof of its superiority to DC isolation and evidence of minimal kit buffer interference in NMR and GC-MS analyses are shown. Finally, biological applicability of the methodology is shown in brain-derived mitochondrial and cytosolic fractions from *Ndufs4* WT mice.

Chapter 5 provides the aim-defining, peer-reviewed *Metabolites* publication (Van der Walt *et al.*, 2021), showing the designed methodology's ability to elucidate compartment-specific metabolic alterations in *Ndufs4* KO mice, *versus* WT. The paper provides evidence of biologically important compartmentalization of mitochondrial and cytosolic metabolic reactions, previously shown to contribute to the *Ndufs4* KO brain and muscle metabolic profiles.

Chapter 6 offers a summary of the entire study's results together with concluding remarks. The strengths and limitations of each phase, as well as future research directions, are detailed.

Annexures to the study entail the following: **A)** Alphabetised table of all reagents and consumables used, **B)** details on the animals used in this study, **C-D)** the two published papers in their journal format.

1.3 Study outcomes: Specific research outputs

This study contributes to the field of natural science (metabolomics methodology and mitochondrial disease research) through two peer-reviewed journal publications in internationally accredited journals.

1.3.1 Published peer-reviewed article I (Chapter 4, Annexure C)

Van der Walt, G. & Louw, R. 2020. Novel mitochondrial and cytosolic purification pipeline for compartment-specific metabolomics in mammalian disease model tissues. *Metabolomics*, 16(7):78.

The article (https://doi.org/10.1007/s11306-020-01697-9) was published in the Springer journal, *Metabolomics* (https://www.springer.com/journal/11306), with an impact factor of **4.290** (2020). This journal publishes a broad scope of research regarding metabolomics technology,

methodology and application to natural science research. Author guidelines are available at the following web link:

https://www.springer.com/journal/11306/submission-guidelines#Instructions%20for%20Authors

1.3.2 Published peer-reviewed article II (Chapter 5, Annexure D)

Van der Walt, G., Lindeque, J.Z., Mason, S. & Louw, R. 2021. Sub-Cellular Metabolomics Contributes Mitochondria-Specific Metabolic Insights to a Mouse Model of Leigh Syndrome. *Metabolites*, 11(10):658.

This article (https://doi.org/10.3390/metabo11100658) was published in the MDPI open-access journal, Metabolites (https://www.mdpi.com/journal/metabolites), with impact factor **4.932** (2020). The journal publishes a range of papers pertaining to metabolite discovery, metabolomics methods and applications in metabolic biochemistry, systems biology and biotechnology research. Author instructions and guidelines are available at:

https://www.mdpi.com/journal/metabolites/instructions.

1.4 Ethical considerations and financial support

This research forms part of a larger research project, ethically approved by the AnimCare animal research ethics committee of the NWU in 2016 (NWU-00001-15-A5), with the work in this dissertation approved as a sub-study under the main project (NWU-000568-19-S5). Minimal risk category 0 as stipulated by AnimCareREC applies in this instance, as the tissues were obtained fresh from mice already being euthanized for the purposes of the main study, with no additional interventions or animals required. All animals were maintained, and procedures performed in line with research, training and drug development ethics codes of South Africa – complying with national legislation.

This study was financially enabled and supported by the Department of Science and Technology, and National Research Foundation (DTS-NRF, Grant numbers 92736 and 117424), as well as South Africa's Technological Innovation Agency (TIA, Grant Metabol.01) and the NWU's postgraduate funding mechanisms. Opinions and conclusions expressed are those of the authors alone and are not necessarily attributed to the NRF, TIA or NWU.

1.5 Author contributions

Paper I (Chapter 4): The methodology was acquired and designed by both Gunter van der Walt and Roan Louw, after van der Walt mediated the ethic application process. Analytical work and

data processing were mostly performed by Gunter van der Walt, with support from Roan Louw. Gunter van der Walt wrote the manuscript, under the supervision of Roan Louw, while the latter oversaw the review and editing process.

Paper II (Chapter 5): Gunter van der Walt was predominantly involved in method design, sample collection, experimental work, data analysis, graphic design of manuscript images and manuscript writing. Shayne Mason participated in NMR method design, troubleshooting and manuscript review, while solely being responsible for ^{1}H-NMR analyses and data extraction. Zander Lindeque was actively involved in method design, LC-MS/MS analytical setup, data processing and manuscript review. Roan Louw, as the principal investigator, was key to acquiring scientific, ethical and financial support for the study, while also being actively involved in metabolomics analyses, data interpretation, manuscript writing and supervision.

All authors signed the declaration on this page:

I hereby give express consent that the above-mentioned articles may be used in the dissertation of Mr Gunter van der Walt, towards examination for the degree M.Sc. Biochemistry. I declare that my role in the study as co-author, as defined in Section 1.5 of page 6 and 7, is an accurate representation of my contributions.

Prof. R. Louw: ----------

Dr S.W. Mason: ----------

Prof. J.Z. Lindeque: ----------

Mr G van der Walt: ----------

CHAPTER 2

Literature Study

- Mitochondrial biology
- Mitochondrial disease and metabolism
- Sub-cellular metabolomics

2.1 Introduction

This chapter constitutes a thorough literature background for the present study, providing the reader with the necessary context and concepts for interpreting the outcomes thereof. Firstly, mitochondrial biology, the OXPHOS system and Complex I are detailed. Part II describes current knowledge on the specific disease state (Leigh Syndrome) and animal model (*Ndufs4* KO mice) employed within the context of mitochondrial disease research, as well as introducing metabolomics and its contribution to understanding the complex tissue-specific perturbations in this model. Part III thoroughly reviews the current state of sub-cellular, mitochondria targeted metabolomics research, exposing the gap that exists in the availability and application of said techniques to *in vivo* models of MD. Finally, the chapter ends with the experimental strategy utilized towards addressing this problem.

2.2 Mitochondrial structure and organization

Mitochondria are eukaryotic cell compartments, or organelles, with variable morphology. An outer mitochondrial membrane (OMM) partitions the mitochondria from the rest of the intracellular content, while the inner membrane (IMM) maintains an innermost matrix volume and a functional intermembrane space (IMS). IMM segments protrude into the matrix through a series of invaginations (cristae), mainly to increase the surface area for incorporation of several transmembrane proteins, including the components of the oxidative phosphorylation (OXPHOS) system (Mannella, 2006; Nunnari & Suomalainen, 2012). The matrix houses several compartment-specific catabolic and anabolic enzymes as well as the mitochondria's own unique genome.

2.2.1 Mitochondrial genome

A mitochondrial genome underlies one of the most important features of mitochondrial biology: dual regulation by nuclear (nDNA) as well as mitochondrial DNA (mtDNA) (Calvo *et al.*, 2016; Karlberg *et al.*, 2000). The mitochondrial genome closely resembles bacterial nucleic acid populations, presenting as thousands of circular copies in a single mitochondrion, clustered in nucleoids along the IMM, with no introns and a single non-coding region (D-loop) providing the binding site for transcriptional and translational machinery (Chinnery & Hudson, 2013; Legros *et al.*, 2004). An almost fully maternal inheritance pattern as well as significantly higher mutation rates *versus* nDNA, leads to great heterogeneity in and between organisms/cells (Carling *et al.*, 2011; Pagnamenta *et al.*, 2021). Regarding the content of mtDNA, this ~16,5 kilobase nucleic acid contains 37 genes. Thirteen of these genes encode various subunits of the OXPHOS system, while the majority encode transfer RNA and ribosomal RNA components necessary for

mtDNA-derived protein synthesis (Chinnery & Hudson, 2013; Gustafsson *et al.*, 2016; Legros *et al.*, 2004). Notably, all other components supporting mitochondrial genetic regulation, expression and biological function are synthesized from nDNA with attached mitochondrial targeting sequences and must be actively imported via OMM/IMM transporter proteins (Calvo *et al.*, 2016; Kulawiak *et al.*, 2013).

2.2.2 Mitochondrial diversity and dynamic sub-population distribution

Great heterogeneity exists in the size, morphology, sub-cellular localization and abundance of mitochondria within cells, where most eukaryotic cells contain hundreds to thousands of these organelles. As a result, different cell types and even different intracellular locales, can present vastly different mitochondrial sub-populations (Nunnari & Suomalainen, 2012; Schiaffino & Reggiani, 2011). At the core of this dynamism, mitochondria can fuse and segment (through the processes of fusion and fission) as well as actively migrate along the cytoskeleton (Aouacheria *et al.*, 2017; Chen & Chan, 2009). Additionally, several mechanisms regulate the mitochondrial volume in correlation to the specific cell's energetic needs, thus tissues with high energy demand (such as the brain, skeletal muscles, heart, liver and kidneys) typically contain considerably more mitochondria than other tissues, and concomitantly higher mtDNA copy numbers (Esterhuizen *et al.*, 2017; Kaasik *et al.*, 2007).

2.2.3 Overview of mitochondrial contributions to cellular homeostasis

This energy-dependant, tissue-specific mitochondrial distribution emphasizes the organelle's main role in energy homeostasis, as the primary source of adenosine triphosphate (ATP) via the OXPHOS system (Nunnari & Suomalainen, 2012; Schiff *et al.*, 2011). Mitochondria, therefore, represent a crucial part of a cell's adaptation to any condition that stresses energy metabolism, as they also underlie several mechanisms for monitoring and reporting cellular energetic states and distress (Frezza, 2017; Quirós *et al.*, 2016). Multiple, bidirectional signalling cascades thus exist between the mitochondria and nucleus of cells for executing these adaptations (mito-nuclear crosstalk)[3], underlined by mitochondrial redox state ($NADH/NAD^+$ and $FADH_2/FAD^+$)[4] and reactive oxygen species (ROS) regulation, calcium signalling, apoptosis initiation and activation of innate immune responses. Alongside these regulatory mechanisms, mitochondria also contribute greatly to catabolic and anabolic cell metabolism, being central to the regulation

[3] Mito-nuclear crosstalk primarily involves anterograde (nucleus to mitochondria) and retrograde (mitochondria to nucleus) signalling pathways.

[4] Main cellular electron shuttles towards the ETC: reduced/oxidated nicotinamide adenine dinucleotide ($NADH/NAD^+$) and flavin-adenine dinucleotide ($FADH_2/FAD^+$)

of glucose, amino acid, nucleotide, lipid, sulphur and metal metabolism (Esterhuizen *et al.*, 2017; Picard *et al.*, 2016).

2.3 Oxidative phosphorylation and the electron transport chain

2.3.1 Structure and Organization

As previously described (Section 2.2), and shown in Figure 2-1, the IMM contains the five OXPHOS enzyme complexes (CI – CV)[5], which underlie several of the critical mitochondrial functions outlined in this chapter. CI -IV, alongside their free-moving, intercomplex, membrane soluble electron carriers, ubiquinone (Q) and cytochrome c (cyt c), form the electron transport chain (ETC). Each of these polypeptide enzymes has their own well-studied functions; however they are known to merge in various combinations, known as respiratory supercomplexes (SCs) (Genova & Lenaz, 2014; Milenkovic *et al.*, 2017).

Whether ETC enzymes exist solely in these complexes (solid state model) or variably as SCs or individual enzymes (plasticity model) is still a matter of much scientific debate, although these assemblies present several advantages over freestanding ETC complexes and a large portion of the individual enzyme pools (30% of CIV to 90% of CI) are found in the two most abundant SCs ($CI/CIII_2/CIV_{1-4}$ and $CI/CIII_2$) in mammalian cells (Acin-Perez & Enriquez, 2014; Barrientos & Ugalde, 2013). Reportedly, SCs help stabilize individual ETC assemblies, enhance electron flux by substrate channelling or shuttling and the modulation of RC-related ROS production. For instance, the largest eukaryotic SC known as the respirasome ($CI/CIII_2/CIV_{1-4}$), contains all the necessary components for transporting electrons from NADH to oxygen, and reportedly serves an important role in the assembly and stability of CI subunits (Genova & Lenaz, 2014; Lenaz *et al.*, 2016; Wu *et al.*, 2016).

[5] Complex I: NADH:ubiquinone oxidoreductase (EC 1.6.5.3), Complex II: succinate:ubiquinone oxidoreductase (EC 1.3.5.1), Complex III: ubiquinol:ferrocytochrome c oxidoreductase (EC 1.10.2.2), Complex IV: ferrocytochrome c oxidoreductase (EC 1.9.3.1) and Complex V: ATP phosphohydrolase/ ATPase (EC 3.6.1.3).

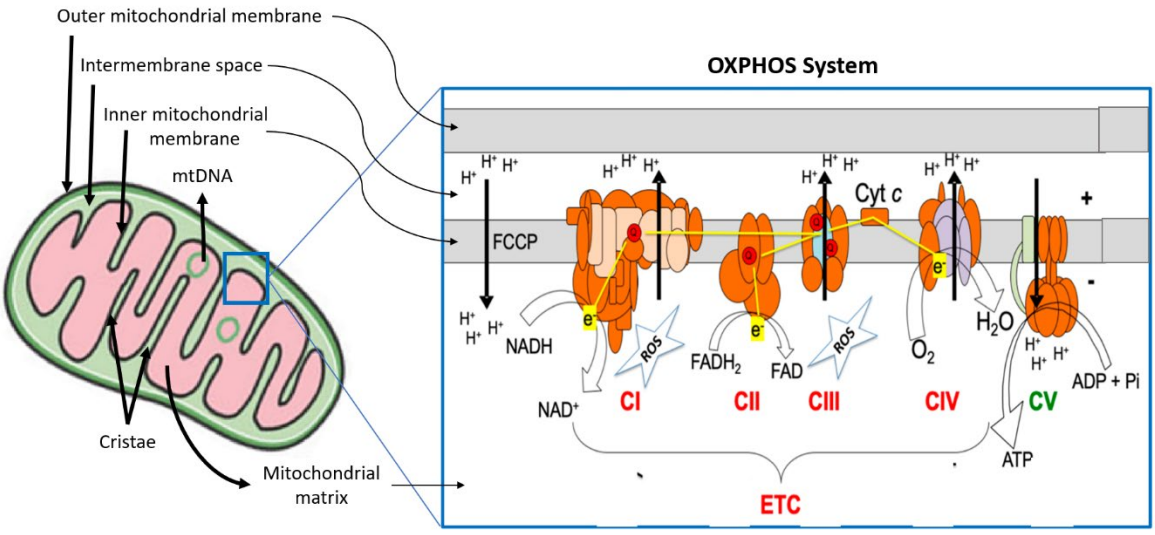


Figure 2-1: Mitochondrial structure and OXPHOS system organization/function. The double-membraned mitochondrial structure is depicted, showing the mitochondrial genome (mtDNA) in the matrix and oxidative phosphorylation (OXPHOS) system embedded in the inner membrane, as well as the characteristic IMM folds called cristae. Complex I to V (CI, CII, CIII, CIV, CV) is shown, with schematics of its electron (e^-) transport and proton (H^+) pumping functionalities towards adenosine triphosphate (ATP) synthesis form adenosine diphosphate (ADP) and inorganic phosphate (P_i). The electrons are obtained from NADH or $FADH_2$ oxidation (CI or CII, respectively) and finally transferred to oxygen to produce water or reactive oxygen species (ROS). *Adapted and reprinted from Riley et al. (2018) and Garrido-Perez et al. (2020), as permitted by the Creative Commons Attribution Licence (CC BY 4.0).*

2.3.2 Functional mechanisms of the OXPHOS system

When describing the functions of the ETC and OXPHOS system, however, it still serves to follow the logic of the individual enzymes' contributions towards ATP generation. Most electrons liberated from carbohydrate, lipid and protein catabolism are presented to the ETC at CI (via oxidation of NADH back to NAD^+), reducing Q to QH_2. CII serves as electron acceptor from $FADH_2$-producing reactions, again generating QH_2 (Canto *et al.*, 2015; Schiff *et al.*, 2011). Regardless of the origin, QH_2 is ultimately oxidized at CIII, producing 2 reduced cyt c molecules for each Q molecule regenerated. This Q-cycle (Figure 2-2), as well as the alternative QH_2-producing catabolic pathways (Section 2.3.3), have recently been shown to play a prominent role in ETC fuelling when NADH oxidation is impaired (McDonald *et al.*, 2018; Terburgh *et al.*, 2019). All the liberated electrons, converging at cyt c, are finally transferred to O_2 in a final CIV-mediated oxidoreductase reaction with water as the by-product.

A vital consequence of this electron transport is the generation of a proton circuit across the IMM, via the proton pumping action of CI, CIII and CIV. Electron transport leads to electrical and/or conformational changes within each complex, which is coupled to translocation of H^+ from the mitochondrial matrix to the IMS. As the IMS now contains a relatively higher H^+ concentration, it represents a more acidic and positively charged space relative to the matrix.

This induced pH difference (ΔpH_m = ~ 0.8 / 50 mV) and membrane potential ($\Delta\psi_m$ = ~ 120-180 mV; due to cation concentration differential) constitute the two-fold electrochemical potential difference across the IMM, which provides the proton-motive force[6] (Δpmf in mV) for ATP synthesis (Berry *et al.*, 2018; Logan *et al.*, 2016). The Δpmf supports H^+ flux back to the matrix and electrochemical equilibrium; when these protons flow through the CV pump module, this force is converted into the required energy for phosphorylating ADP (with Pi substrate) to ATP. Electrons may also leak from the mitochondria through various mechanisms, a process which importantly regulates the Δpmf, especially in the absence of ATP synthesis (Berry *et al.*, 2018). Notably, the NADH and $FADH_2$ electron donors lead to different proton translocation stoichiometries, as NADH dehydrogenases lead to a total of ten protons translocated for each electron pair finally transferred to O_2, whereas Q-linked dehydrogenases deliver only six protons per pair (Brand & Nicholls, 2011).

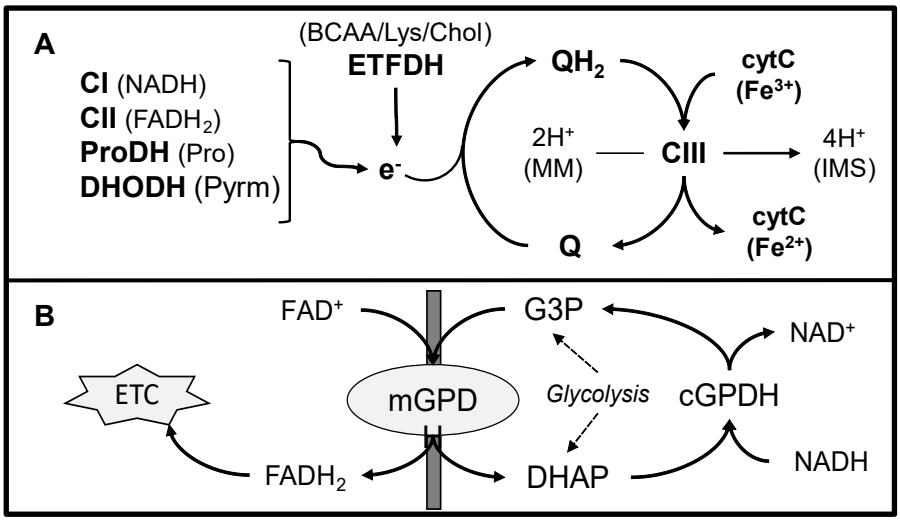


Figure 2-2: Graphic representation of Q-cycle and G3P shuttle functionality in relation to ETC activity. The Q-cycle (A), as reduced (Q) and oxidized ubiquinone (QH_2) intermediates, is shown with all the contributing electron donors. NADH and $FADH_2$, as well as the proline (Pro)- and pyrimidine catabolic (Pyrm) enzymes, dihydrooroate dehydrogenases (ProDH and DHODH) donate electrons directly to Q. Electron transfer flavoprotein dehydrogenases (ETFDH) transfer electrons from branched chain amino acid (BCAA), lysine (Lys) and choline (Chol) metabolism to the Q-cycle. Electron transfer between QH_2 and CIII reduces the iron moiety of cytochrome C [cytC(Fe^{3+})], leading to H^+ translocation from the mitochondrial matrix (MM) to the IMS. The G3P shuttle (B) involves mitochondrial and cytosolic forms of glycerol-3-phosphate (G3P) dehydrogenases (mGPDH/cGPDH). cGPDH converts dihydroxyacetone phosphate (DHAP) to G3P while regenerating NAD^+ from NADH, whereas mGPDH (bound to the IMM) recycles G3P to produce intramitochondrial $FADH_2$ that directly feeds the ETC.

[6] Proton-motive force is formally defined as the transmembrane potential divided by Faraday's constant [$\Delta pmf = \Delta\psi_m - 59\ \Delta pH_m$;Logan *et al.* (2016)].

2.3.3 Contributing electron shuttles

A substantial portion of the matrix NADH and $FADH_2$ pools is provided by the set of redox reactions that integrate major carbohydrate, lipid and amino acid catabolic pathways, known as the tricarboxylic acid cycle (TCA, a.k.a. Krebs cycle) (Martinez-Reyes & Chandel, 2020). As the IMM is impermeable to either of these redox substrates, several metabolite shuttle mechanisms serve to indirectly transfer reducing equivalents from the cytosol to the ETC (Mráček *et al.*, 2013; Yang & Sauve, 2016). A notable example is the glycerol-3-phosphate (G3P) shuttle (Figure 2-2); wherein an IMM-bound G3P dehydrogenase (mGPDH, EC 1.1.5.3) generates mitochondrial $FADH_2$ concomitant to its cytosolic oxidation of G3P to dihydroxyacetone phosphate (DHAP). As mentioned in the previous section, many other enzymes across both compartments donate electrons to the Q pool, either directly or through the electron transfer flavoprotein (ETF) system (McDonald *et al.*, 2018; Terburgh *et al.*, 2019). In ETF-mediated reactions, flavin-dependant dehydrogenases of the fatty acid, branched-chain amino acid (BCAA) and choline metabolic pathways donate electrons to ETF, and subsequently to the Q pool. Exemplary ETF-independent Q cycle fuelling enzymes include proline dehydrogenase and dihydro-orotate dehydrogenase from mitochondrial proline and pyrimidine metabolism, respectively.

2.4 Mitochondrial Complex I: frontline workhorse of the ETC

2.4.1 CI structure

The first complex of the ETC (NADH:ubiquinone oxidoreductase) is also the largest and most complex of the four enzymes. CI is an L-shaped, ~980 kDa multimeric enzyme, with 14 catalytically active core subunits and 31 accessory subunits (Figure 2-3), each with distinct structure and function (Hirst & Roessler, 2016; Sazanov, 2015; Wirth *et al.*, 2016). In studies of CI, these subunits are often grouped based on their position in the holo-CI enzyme, or their respective functions. Morphologically, CI consists of a hydrophilic matrix-penetrating arm and a lipophilic, IMM-integrated membrane arm. The matrix arm contains seven core nDNA-encoded subunits that facilitate the electron transfer functionalities of CI-, namely NADH oxidation and (N) and ubiquinol reducing (Q) modules. The membrane arm constitutes the proton pumping module (P) of CI, with seven core mtDNA-encoded subunits sub-categorized as proximal (P_P) and distal (P_D) proton pump modules, respectively (D'Imprima *et al.*, 2016; Wirth *et al.*, 2016).

2.4.2 CI function

As the first entry point of electrons to the ETC via NADH, CI is responsible for up to 40% of the total Δpmf required for ATP synthesis (Hirst & Roessler, 2016; Hoefs *et al.*, 2012). The matrix

arm facilitates the transfer of said electrons from NADH, through a series of iron-sulphur (Fe-S) clusters and finally to Q-, while the membrane arm utilizes energy liberated from these successive redox reactions toward active proton translocation from the matrix to the IMS (Figure 2-3). This sequence of events is initiated by NADH binding to the NDUFV1 subunit in the N-module, and subsequent electron transfer to the flavin mononucleotide moiety (FMN) (Vinogradov & Grivennikova, 2016). Reduced FMN again transfers these electrons through a series of seven successive Fe-S clusters in the matrix arm, to 4Fe-4S moieties contained in Q-module PSST subunits, where Q is finally reduced to QH2. The electron flow from these reactions then finally energizes the core P-module subunits responsible for proton translocation. Although still unclear, current hypotheses suggest Q reduction, and subsequent removal from the PSST site leads to conformational changes in these sites. This presumably facilitates contact of charged ubiquinone sites between the matrix and membrane arms, resulting in charge transmission therethrough (Vinogradov & Grivennikova, 2016; Zickermann *et al.*, 2015).

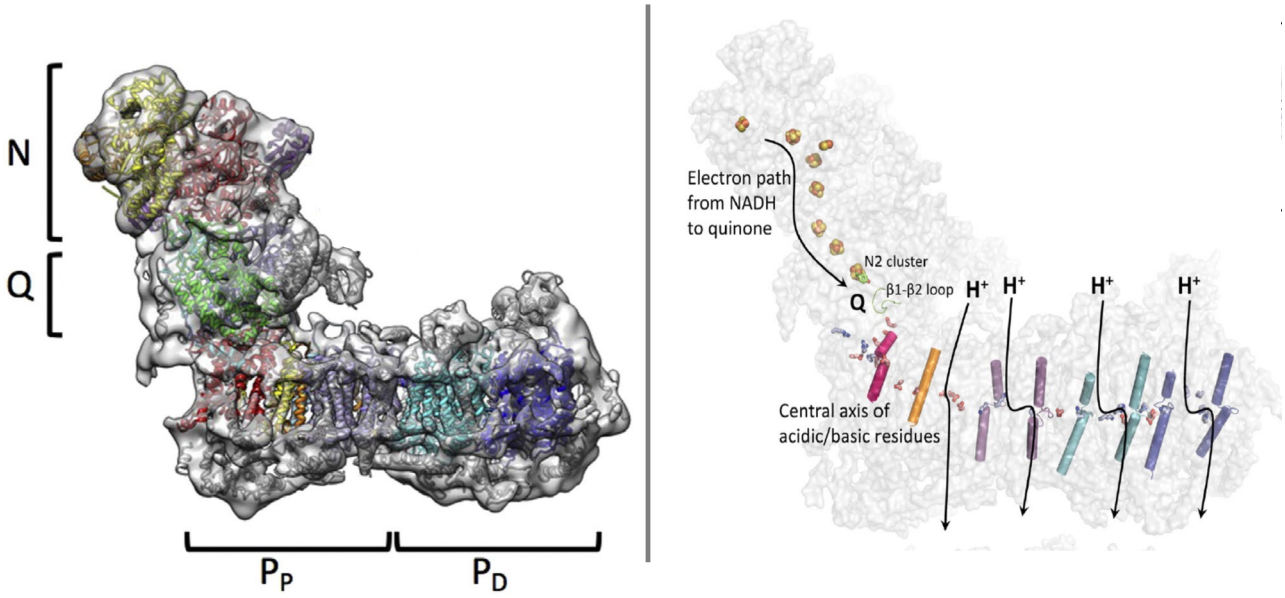


Figure 2-3: Complex I structure, organization and functional mechanistics. The left image shows CI's structure as determined by cryo-electron microscopy and X-ray crystallography, outlining the NADH oxidation (N), ubiquinone reduction (Q), proximal and distal proton pumping modules (P_P and P_D), respectively. On the right, the iron-sulphur clusters and proton-pumping modules responsible for CI functionality are shown in relation to the total structure, as well as the summarized mechanism of electron transport and proton translocation following NADH oxidation. *Adapted and reprinted from D'Imprima et al. (2016); Wirth et al. (2016), Copyright (2016), with permission from Elsevier.*

Regarding the role of CI subunits, much is also still unclear, although it is known that CI function depends on correct assembly of all subunits, as well as regular clearance and replacement of old/damaged subunits (Guerrero-Castillo *et al.*, 2017; Kahlhofer *et al.*, 2017). Mounting evidence supports CI subunits' role in adequate holoenzyme assembly and structural stability, as well as providing contact points for SC assembly (Lenaz *et al.*, 2016; Papa *et al.*, 2010; Wirth

et al., 2016). In addition to said structural roles, certain subunits have also been found to attenuate ROS production by CI, as well as aiding in protection of the enzyme against its damaging oxidative effects (Emmerzaal *et al.*, 2020; Stroud *et al.*, 2016; Vinogradov & Grivennikova, 2016).

2.4.3 Biogenesis and CI assembly

The assembly of CI remains a complex process, which still requires much study towards full elucidation. Regardless, compartment-specific transcription and translation of the required nDNA and mtDNA subunits initiate this process. Most of these premature subunits are of cytosolic origin and must thus be imported by the collective action of specific mitochondrial transport proteins, such as the OMM translocase family (TOM) and their IMM equivalents (TIM), to ensure their correct localization within mitochondrial sub-compartments (Kulawiak *et al.*, 2013; Matic *et al.*, 2018). Current evidence supports a highly coordinated, sequential assembly mechanism involving the action of at least 14 different assembly factors that do not present in the final CI structure (Guerrero-Castillo *et al.*, 2017). A current modular assembly model suggests an initial formation of five precursor polypeptides (N, Q/P_P-a, P_P-b, P_D-a, P_D-b), before these intermediates associate to produce the mature CI. Presumably, the central membrane regions P_P-b and P_D-a form the first association, before the addition of Q/P_P-a and P_D-b, while the pre-assembled N-module appears to be the last to join the assembly (Kahlhofer *et al.*, 2017; Stroud *et al.*, 2016). In line with the prevalence of CI in the biologically important respirasome SC and the notion that SC formation stabilizes CI structure (Section 2.3.1), recent evidence supports a model wherein CIII and CIV also first associate with the premature P_P-b/P_D-a CI-scaffold before the process of CI assembly is completed (Fang *et al.*, 2021; Guerrero-Castillo *et al.*, 2017; Wu *et al.*, 2016). This cooperative assembly model would then presumably take preference over the alternate model wherein individual, fully mature complexes are assimilated into SCs.

2.4.4 The Ndufs4 subunit of CI

In line with the objectives of this study, the CI subunit NADH dehydrogenase (ubiquinone) Fe-S protein 4 (NDUFS4) is known to contribute widely to CI assembly, stability and function (Kruse *et al.*, 2008; Quintana *et al.*, 2010). This 175 amino acid (18 kDa) peptide is derived from the nDNA *Ndufs4* gene (Human gene ID 4724, chromosome five or murine gene ID 17993, chromosome 13), transcribed and translated in the cytosol (Kahlhofer *et al.*, 2017; Papa, 2002). Two key sequences within the NDUFS4 peptide regulate its subsequent import into the mitochondria for CI assembly: an amino terminal (N-terminal) mitochondrial targeting sequence, recognized by the facilitating TOM22 transporter and a canonical RVSTK (arginine-valine-

serine-threonine-lysine) carboxyl terminal (C-terminal) sequence (Ingraham *et al.*, 2009; Papa, 2002).

While the former sequence directly determines this subunit's localization, the latter is a critical site for post-translational modifications (phosphorylation) required for mitochondrial NDUFS4 import. This cyclic adenosine monophosphate (cAMP) mediated phosphorylation has been shown to not only regulate NDUFS4 import, but also its maturation and incorporation in CI, while the level of phosphorylation is also directly correlated to CI activity levels (Papa *et al.*, 2010; Scacco *et al.*, 2003). Regardless, a complete NDUFS4 subunit (as an N-module constituent) is incorporated in each CI during the latter stages of assembly, contacting the central N-module 75 kDa subunit as well as three central Q-module subunits (Zhu *et al.*, 2016). These associations presumably contribute to NDUFS4's stabilizing function, as knockout thereof in a model yeast CI led to diminished CI activity and concomitant increases in CI-derived ROS (Kahlhofer *et al.*, 2017). Despite the remaining questions regarding its absolute contribution, the importance of NDUFS4 in healthy CI function is evident.

2.5 Mitochondrial disease

Given the prevalent role of mitochondria in several critical cell biological functions, it is no surprise that dysfunction of their intrinsic and related components may be causal to, or resulting from the pathogenesis of several complex disorders (Craven *et al.*, 2017; Nunnari & Suomalainen, 2012). Several cancer types rely on metabolic programming, including at the mitochondrial level, to sustain their hypermetabolic phenotype, while diabetes mellitus patients present with perturbed mitochondrial function and morphology in their pancreatic β-cells (Fex *et al.*, 2018; Neagu *et al.*, 2019). Myocardial mitochondria are involved in multiple adaptive responses due to common cardiovascular disorders (Karamanlidis *et al.*, 2013), while innate immune functions during infection depend largely on oxidative-to-reductive shifts in mitochondrial metabolism (Tiku *et al.*, 2020). Notably, neurodegenerative conditions from Alzheimer's to Parkinson's disease and multiple sclerosis also famously involve metabolic perturbation and adaptation at the mitochondrial level in conjunction with their characteristic neurodegenerative hallmarks (Li *et al.*, 2021).

2.5.1 Defining primary mitochondrial disease

In contrast to the aforementioned (secondary) mitochondrial disorders, primary mitochondrial disease (PMD) is distinguished as being directly caused by deleterious mutations in genes encoding OXPHOS subunits, assembly factors or systems directly related to OXPHOS protein homeostasis. PMDs are the most prevalent form of inborn metabolic disorders, however, their pathogenic mechanisms remain to be fully elucidated. Being more of an umbrella-term for related genetic disorders, multiple mutations may lead to PMD, resulting in an array of heterogeneous biochemical and clinical phenotypes (Craven *et al.*, 2017; Thompson *et al.*, 2020). Given our limited current understanding of all the interrelated effects of MD, no cure currently exists for any of these conditions, with current treatments focusing on symptomatic and quality of life improving interventions (Picard *et al.*, 2016; Russell *et al.*, 2020).

2.5.2 Prevalence, genetics and clinical phenotype

PMDs have a relatively high incidence in their overall classification as rare diseases, presenting in 1 of 4000 to 5000 human births (Craven *et al.*, 2017; Gorman *et al.*, 2016). As both nDNA and mtDNA contribute to mitochondrial biology, mutations in more than 350 genes (with various inheritance patterns) from both genetic systems can lead to PMD. The greatest proportion, however, result from the predominant nDNA-derived sequences (~75%); most of which are inherited via autosomal recessive patterns, followed by cases of autosomal dominant and X-linked dominant mutations (Gorman *et al.*, 2015; Thompson *et al.*, 2020). Resultantly, a wide variety of clinical symptoms are prevalent in MD patients, implicating multiple organ systems, differential onset periods (neonatal to adult-onset) and orders of severity (mild to severe and fatal). Nuclear DNA mutations underlie three quarters of all childhood-onset PMDs, which are generally the most severe clinical forms (Alston *et al.*, 2017).

Regarding the affected body systems, almost any ATP-dependant cell may reverberate the effects of diminished OXPHOS function, while post-mitotic tissues with the highest energy demand (e.g., central nervous system or CNS, heart, skeletal muscle, liver and kidneys) are most commonly affected in a multi-systemic fashion (Figure 2-4). Given the overlapping heterogeneity amongst these disorders, patients can often not be distinctly classified based on their clinical presentation, but their symptoms may be organized into systematic syndrome classifications[7]. Notwithstanding, common clinical features of MD range from hypotonia,

[7] Notable examples include Leigh Syndrome, Pearson's syndrome, LHON, MELAS, MERFF, KSS & MILS (Craven *et al.*, 2017; Ylikallio & Suomalainen, 2012)

vomiting and fatigue to generalized weakness, seizures and encephalopathy (disorder of brain structure/function) (Alston *et al.*, 2017; Craven *et al.*, 2017; Ylikallio & Suomalainen, 2012).

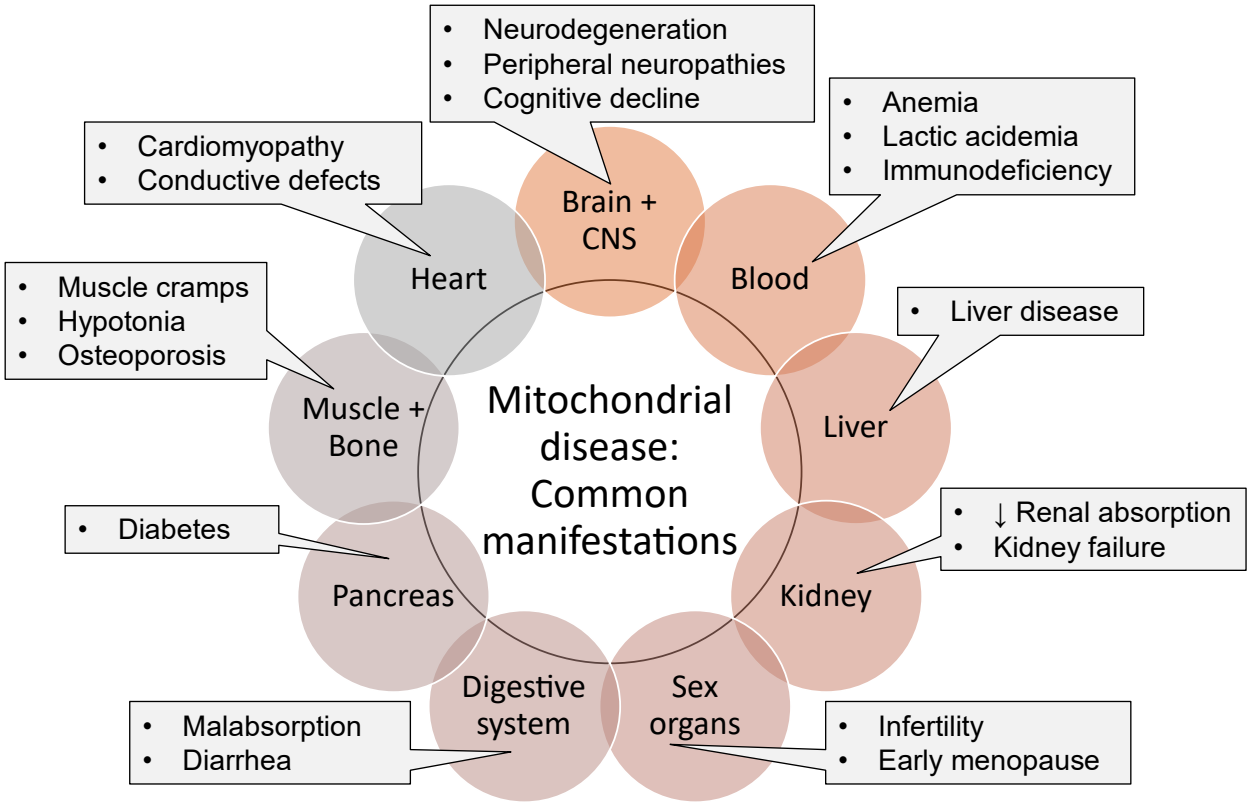


Figure 2-4: Common mitochondrial disease manifestations in various organ systems. Mitochondrial diseases can manifest in most organ systems, with varied symptomatic presentation affected by an individual's unique genetic background, exogenous factors (e.g., diet) and the nature of the underlying pathogenic mutation. The most common symptoms per organ system (central nervous system, blood, heart, liver, musculoskeletal, pancreas, digestive system, kidney and sex organs) are shown here.

2.5.3 Perturbed metabolic and signalling pathways

Despite the majority of MD causing mutations directly affecting OXPHOS components, decreased ATP/ADP ratios alone cannot account for the resulting complex pathophysiology. A substantial number of recent studies rather support the notion that mitochondrial stress responses, triggered by the molecular defect, majorly drive the observed pathology (Khan *et al.*, 2017; Quirós *et al.*, 2016). During these responses, molecules that form part of the cell's bioenergetic sensing/signalling pathways engage in mito-nuclear crosstalk (described in Section 2.2.3), attempting to up-regulate the production of nuclear-encoded mitochondrial components necessary for reprogramming mitochondrial and whole-cell metabolism towards adaptation against the defect. The effectivity of these adaptive responses during MD ultimately determines whether homeostasis can be restored; concurrently, the availability of metabolites and co-factors necessary for these adaptations stands as a viable contributor to many observed MD phenotypes (Emmerzaal *et al.*, 2020; Samluk *et al.*, 2018).

Several components of mito-nuclear crosstalk, which serve to integrate multiple core mitochondrial functions towards cellular homeostasis, are altered during MD. The redox substrate pools for ETC electron transport, NADH/NAD^+ and $FADH_2$/FAD^+, are primarily altered when ETC complexes are perturbed (Sharma *et al.*, 2021; Yang & Sauve, 2016). Accumulation or depletion of these compounds typically alters the flux in many metabolic pathways wherein they act either as products or substrates, which may drive further metabolic changes. The cellular redox status depends upon these substrates to sustain oxidative metabolism, reductive biosynthesis and antioxidant production, alongside the NADPH/$^+$, glutathione (GSH/GSSG) and thioredoxin [Trx(SH)/Trx(S_2)] redox buffer systems involved in ROS homeostasis (Go & Jones, 2013; Schieber & Chandel, 2014). Increased mitochondria-derived ROS (mtROS)[8] and concurrent signalling pathways are also deemed a key driver in MD pathology (Schieber & Chandel, 2014; Stepien *et al.*, 2017). Exemplary mtROS sources include CI, CII, CIII, mitochondrial GPDH, and several dehydrogenases (proline, pyruvate, ETF-QO, α-ketoglutarate, etc.). Contrary to the popular belief that ROS involvement in pathology stems majorly from oxidative damage to cellular components, recent research rather emphasizes their role in critical signalling pathways. At physiological concentrations, mtROS is vital to signalling pathways underlying gene expression and redox homeostasis, as well as the initiation of several mito-nuclear crosstalk mechanisms (Sies & Jones, 2020).

ETC disturbance also expectedly lowers the $\Delta\psi_m$, although perturbed OXPHOS activity alone, does not seem to fully account for this loss in transmembrane potential (Hüttemann *et al.*, 2008; Pfeffer & Chinnery, 2013; Zorova *et al.*, 2018). As expounded in Section 2.3.2, the $\Delta\psi_m$ is a main contributor to the Δpmf that drives ATP synthesis, and thus serves as a sensitive reporter of the cellular energetic state. Moreover, the resulting transmembrane potential regulates the assembly and activity of IMM/OMM transporters responsible for mitochondrial protein and metabolite import, as well as those facilitating ion exchange (e.g., Ca^{2+}, Mg^{2+}, Na^+, & K^+). Concurrently, metal homeostasis, especially Ca^{2+} balance and signalling, can also be perturbed during MD (Aouacheria *et al.*, 2017; Craven *et al.*, 2017; Koshenov *et al.*, 2021). Ca^{2+} homeostasis is a multi-organelle task, with the functional mitochondria-endoplasmic reticulum coupling contributing largely to calcium's role in bioenergetic enzyme (e.g., ATPase) up-regulation, contractile protein function, stress responses and cell death event initiation (Eysert *et al.*, 2020; Walter & Hajnóczky, 2005).

[8] ROS stem from the monoelectronic reduction of O_2 to O_2^-; while this is the primary source of mtROS, it can only cross the IMM as H_2O_2. Mitochondria are, however, not the only source of cellular ROS

2.5.4 Proposed metabolic adaptations to MD

Various “omics” technologies have been utilized towards elucidating the complex plethora of adaptive responses to MD, revealing multiple putative biomarkers with varying levels of sensitivity and disease specificity. Transcriptomics implicate two cytokines, fibroblast growth factor (FGF-21; fasting response related) and growth differentiation factor (GDF-15; related to cell growth signalling) as the most specific MD biomarkers, although their elevation is not exclusive to MD (Lehtonen *et al.*, 2021; Tyynismaa *et al.*, 2010). Similar energy state signalling mechanisms underlie accumulation of these factors and perturbed fatty- and amino acid metabolism in MD, linking their perturbation with attempted metabolic adaptation (Esterhuizen *et al.*, 2017). Anabolic pathways, mostly regulated via mammalian target of rapamycin complex (mTORC1), are equivalently involved in the adaptive process, concurrently, implicating up-stream activating transcription factors (ATF) that mediate nutrient availability and biosynthetic mechanisms (Johnson *et al.*, 2014; Khan *et al.*, 2017). Proteomics has contributed to the understanding of this metabolic shift, revealing increases in glycolytic and protein acetylation enzyme amounts during MD, with variable alterations in levels of dehydrogenases and ribosomal proteins reported across studies (Gucek & Sack, 2021; Sahebekhtiari *et al.*, 2016).

Metabolomics, as the study of small-molecule intermediates of metabolism, have also identified several metabolite biomarkers (pyruvate, lactate, alanine, creatine, thymidine, etc.) related to MD (Esterhuizen *et al.*, 2017; Gucek & Sack, 2021). Although large-scale metabolomic datasets for MD patients are scarce, the study of animal models has led to the comprehensive resolution of many metabolic adaptations to MD (Iommarini *et al.*, 2015; Torraco *et al.*, 2015). Despite the limited transferability of cross-species data, as illustrated by Esterhuizen *et al.* (2017), many pathways show apparently consistent alteration across the different studied systems. Several of these implicate the effects of altered redox couples ($NADH/NAD^+$ and $FADH_2/FAD^+$), increased reliance on glycolysis-derived ATP, variably increased anabolic pathways and those that provide the metabolites and co-factors for select biosynthetic reactions. Common metabolic adaptations include an increased glycolytic flux to pyruvate, lactate and alanine, ketone body (acetoacetate, hydroxybutyrate) accumulation, perturbed TCA, β-oxidation, carnitine, lysine and BCAA metabolism (Esterhuizen *et al.*, 2017; Li *et al.*, 2021; Roede *et al.*, 2012).

2.6 Complex I dysfunction and Leigh syndrome

2.6.1 Complex I dysfunction and NDUFS4 in the context of MD

Given the complex organization and central role of ETC complex I in mitochondrial function, it is no surprise that isolated CI deficiency (CID; OMIM 252010) is the single largest cause of

primary MD, accounting for ~30% of all cases (Emmerzaal *et al.*, 2020; Hoefs *et al.*, 2012; Rodenburg, 2016). With an incidence of 1 in 10 000 live births, pathology becomes apparent within one year of age, progresses rapidly and often fatally. CID patients present with various clinical manifestations, in line with the heterogenous genetic origins from both contributing genomes, although nDNA mutations underlie the most cases (70 – 80%). To date, pathogenic mutations in 20 of the 38 nDNA-encoded CI subunits and nine specific assembly factors have been identified, while such deleterious mutations can afflict all seven mtDNA-encoded subunits.

With 13 currently attributed pathogenic mutations, *Ndufs4* is considered a mutational hotspot in CI (Fiedorczuk & Sazanov, 2018; Papa, 2002; Scacco *et al.*, 2003). These mutations mainly lead to loss of functional NDUFS4 subunits, with missense-, nonsense-, frameshift, splicing and point mutations, as well as multi-exon deletions being variably involved. In main justification of the model investigated here, *Ndufs4* mutations lead to Leigh- and Leigh-like[9] syndrome (LS), which represents ~80% of all CID patients (Finsterer, 2008; Quintana *et al.*, 2010).

2.6.2 Leigh syndrome: Specific prevalence and pathology

LS, also known as subacute necrotizing encephalopathy (OMIM 256000), represents one of the most common neurometabolic diseases, as well as the most heterogenous and frequently diagnosed paediatric MD phenotype, affecting ~1 in 40 000 new-borns (Alves *et al.*, 2020; Lake *et al.*, 2015; Rahman *et al.*, 2017). Importantly, of the ~100 identified LS-causing genes, *Ndufs4* mutations account for some of the more severe autosomal-inherited clinical cases. The majority of cases present LS in early infancy (although adult-onset cases are rarely observed), with a neurodegenerative phenotype correlating with mitochondrial dysfunction and bilateral necrotic lesions in specific brain regions (Adjobo-Hermans *et al.*, 2020; Ortigoza-Escobar *et al.*, 2016). A wide array of symptoms may thus result from *Ndufs4* mutation; however, clinical hallmarks include early-onset failure to thrive, developmental delay, respiratory anomalies and feeding difficulties, as well as progressive psychomotor deterioration, muscle hypotonia, retarded reflexes, cardiomyopathy and seizures, eventually leading to death in infancy or early childhood (Finsterer, 2008; Lake *et al.*, 2015; Rahman *et al.*, 2017).

2.7 *Ndufs4* knockout mice as adequate human Leigh Syndrome models

Animal models have been proven essential in elucidating the neural involvement of LS, given the scarcity, diagnosis difficulties and brief lifespan in LS patients. Laboratory-bred mouse models, especially, present *in vivo* mammalian systems with controlled environmental and

[9] Clinical manifestations that strongly resemble LS, but do not fulfil key diagnostic criteria (i.e., serum lactate increase, typical neuroimaging and pathology), are termed Leigh-like syndromes.

genetic contributions to study the pathogenic nuances in this disease. Central to this study, one of the best characterized models closest to the LS patient phenotype is the whole-body *Ndufs4* knockout (*Ndufs4*$^{-/-}$; KO). These animals develop similar clinical manifestations to CID and LS patients around post-natal age (P) 35, presenting progressive encephalomyopathy that leads to early death around P50-60.

The mice used here were obtained from Jackson Laboratories, graciously donated by Richard Palmiter; they represent a mixed genetic background of laboratory mouse strains, carrying an induced heterozygous *Ndufs4* mutation (*Ndufs4*$^{+/-}$; HET). The mutant allele was created by deletion of exon two through a classic Cre-loxP recombination strategy (Figure 2-5). Briefly, this process constitutes the introduction of loxP sites at the flanks of *Ndufs4* exon two in the germline of one strain and crossing of these mice with another strain containing the Cre recombinase; during this crossing, the Cre and loxP sites interact, leading to excision of exon two. This importantly precludes the synthesis and incorporation of mature NDUFS4, as exon two encodes the N-domain mitochondrial targeting sequence and the first 17 amino acids of the mature protein. HET mice are interbred to produce homozygous, whole-body *Ndufs4* knockout mice, as well as homozygous wildtype mice (*Ndufs4*$^{+/+}$; WT).

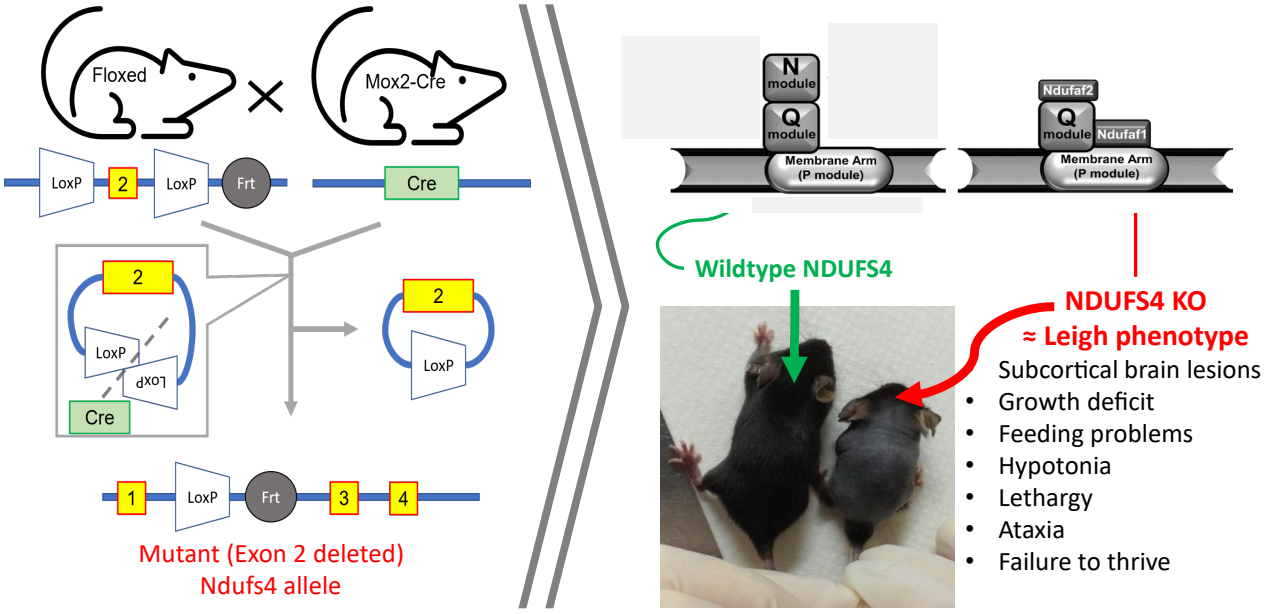


Figure 2-5: Creation, biochemical and clinical phenotype of *Ndufs4* KO mice. Floxed mice (with recombinantly inserted loxP sites flanking the allele for *Ndufs4* exon 2 and an frt site) are crossed with mice expressing the Mox2-Cre recombinase enzyme, leading to excision of exon 2 via DNA recombination during fertilization. This produces the mutant *Ndufs4*$^{-/-}$ allele (with one remaining loxP and frt site in exon 2's place), which subsequently precludes synthesis of the mature NDUFS4 subunit and incorporation of the CI N-module (top right grey image), which leads to a loss of active CI. The resulting KO mice possess a Leigh-like phenotype, presenting with alopecia, smaller size than the WTs containing fully mature CI and other characteristic LS symptoms. *Adapted and reprinted from Leong et al. (2012) as permitted by the Creative Commons Attribution Licence (CC BY 4.0).*

2.7.1 Clinical Phenotype

The first significant difference between KO pups and their WT/HET littermates is observed around P12, where KO mice present markedly smaller (Ingraham *et al.*, 2009; Kruse *et al.*, 2008). Between P16 and P24, alopecia (hair loss) affects the KO mice, presumably as a manifestation of the systemic inflammation due to whole-body *Ndufs4* KO. At this age, an increase in bone mass (due to reduced osteoclastogenesis) and blindness with cataracts also become apparent due to energetic restriction in the osteolytic and optic neural systems, respectively. Lethargy and halt of weight gain set in at ~P30, while the onset of encephalomyopathy follows shortly thereafter (~P35), characterized by ataxia, motor neuron dysfunction and hearing loss (Jin *et al.*, 2014; Quintana *et al.*, 2010).

Between P30 and P35, *Ndufs4* KO mice apparently display normal food and oxygen consumption at different phases of their circadian cycle (Kruse *et al.*, 2008), however, recent literature emphasizes the possibility that feeding difficulties that were not captured in the short three-day span of the aforementioned study (Foriel *et al.*, 2018). Regardless, at this time rapid decreases in body fat and seizures become prevalent amongst the KO pups, weight loss and ataxia further worsen from P35 to P50. Within 10 days after this point (P50 – 60), these animals die from a fatal necrotizing encephalomyopathy, closely emulating late-stage LS patients (Johnson *et al.*, 2013; Ortigoza-Escobar *et al.*, 2016; Quintana *et al.*, 2010).

2.7.2 Biochemical and metabolic characteristics

As NDUFS4 is known to be essential for CI assembly and stability (Section 2.4.4), its deletion in this model directly affects ETC enzyme abundances and activity. Absence of NDUFS4 disrupts the final stages of CI assembly (i.e., N-module incorporation), leading to two partially assembled CI complexes and a concurrent loss of mature, functional CI (Adjobo-Hermans *et al.*, 2020; Scacco *et al.*, 2003). This leads to markedly reduced CI activity, as observed in both patient fibroblasts and *Ndufs4* KO mice, while various levels of residual activity can still be measured across different biological systems. Between 20% and 30% residual CI activity has been measured in the brain of these animals, with similar amounts reported in skeletal muscles (Alam *et al.*, 2015; Calvaruso *et al.*, 2012; Terburgh *et al.*, 2019; Terburgh *et al.*, 2021). Decreased CI activity was also reported in the heart, kidney, liver, pancreas and lung tissues, at 44%, 25%, 19%, 17% and 9% of WT levels, respectively. Residual CI activity is ascribed to the role of SCs (Section 2.3.1.), as the association of immature CI with other ETC complexes may support limited CI-coupled respiration (Calvaruso *et al.*, 2012; Fang *et al.*, 2021). The severity of bioenergetic perturbation in a particular tissue is inversely proportional to the residual CI activity therein. Considering the interrelated nature of ETC complexes, concurrent alterations in CII to

CIV levels have also been reported in response to CID; however, differences in experimental design have delivered widely differing CII-CIV expression levels in *Ndufs4* KO mice (Alam *et al.*, 2015; Calvaruso *et al.*, 2012; Kruse *et al.*, 2008; Terburgh *et al.*, 2019; Ugalde *et al.*, 2004).

While OXPHOS deficiencies such as CID would presumably alter the ATP/ADP ratios and O_2 consumption, contrasting results have been reported for different NDUFS4 KO systems. Subsequent decrease in O_2 consumption by a dysfunctional RC, despite a thoroughly oxygenated environment, paradoxically implicates a hypoxia response (Jain *et al.*, 2019; Lee & Wolfgang, 2012). In contrast, normal adenylate turnover (ATPase activity, catalytic rate, phosphorylation capacity) was found in both immortalised patient fibroblasts and KO mouse skeletal muscle, as well as mitochondria isolated from these muscles (Alam *et al.*, 2015; Kruse *et al.*, 2008; Valsecchi *et al.*, 2012). Minimal to no decreases in O_2 consumption were concurrently reported in these studies, while decreases in arterial CO_2 and subsequent respiratory alkalosis has rather been hypothesized to be the major pathogenic aberration to oxygen metabolism and signalling in these cellular contexts (Kruse *et al.*, 2008; Pronicka, 2017). These varying, tissue-specific alterations in core bioenergetic parameters expectedly result in various, heterogenous protein-level and metabolic changes.

2.8 *Ndufs4* KO mouse metabolomics: Current insights and limitations

2.8.1 Metabolomics: introduction and value in MD research

As metabolite profiles constitute the endpoint of metabolic reactions and closest description of the phenotype, metabolomic studies have contributed largely to the current understanding of MD-related changes in cellular biology (Esterhuizen *et al.*, 2017; Newgard, 2017). Given the multi-systemic and tissue-specific nature of LS pathology, the level of metabolic specificity observed is directly related to the choice of sample studied. Urine and serum metabolite profiles represent the sum of all tissue secretions/excretions, thus overall energy deficiency biomarkers such as elevated serum/urine lactate and alanine underlie most MDs; however, the contributions of differentially affected tissues, such as the brain, skeletal muscle, liver and kidneys, cannot be deconvoluted at this level. Concordantly, *Ndufs4* KO mice present with normal serum lactate and glucose levels, yet increases in glycolytic and oxidative stress markers of *Ndufs4* KO whole brain samples have often been detected, while these changes in levels of related metabolites and enzymes were not reported in various studies of the skeletal muscles from this model (Johnson *et al.*, 2013; Kruse *et al.*, 2008; Terburgh *et al.*, 2019; Valsecchi *et al.*, 2012).

2.8.2 Tissue-specific metabolic profiles: the brain as primary LS target

Patterns of central nervous system (CNS) dysfunction are not only characteristic of LS, but neural disturbance has been convincingly shown to be the main driver of the phenotype in *Ndufs4* KO mice (Johnson *et al.*, 2020; Quintana *et al.*, 2010). Several nuances of neural physiology render it more sensitive to energy deprivation than other high ATP-consuming tissues, including very high moment-to-moment energy needs, limited nutrient storage capacity and metabolic flexibility towards utilizing alternative ETC fuels, greater susceptibility to oxidative stress and the sustenance of neurotransmitter metabolism in addition to its general metabolic requirements (Breuer *et al.*, 2013; Cobley *et al.*, 2018; Harris *et al.*, 2012). Studies on whole *Ndufs4* KO brains have reported metabolite profiles indicative of the summative effect of the KO on brain energy metabolism (Johnson *et al.*, 2013; Takahashi *et al.*, 2019).

Shuttling of lactate and fatty acids between microglia (neural immune cells) and neurons presumably underlie the characteristic gliosis[10] and neuroinflammation in LS; however, substantial current evidence especially implicates the involvement of neuronal subpopulations that rely on neurotransmitters derived from glutamate metabolism (Harris *et al.*, 2012; Yudkoff, 2017). Accordingly, the most pronounced metabolic defect in *Ndufs4* KO brains relates to a cluster of glutamate-related metabolites[11], detected as significantly decreased at both a pre-lesion and advanced LS age (P30, P45). BCAA's, especially leucine, also show marked increases in *Ndufs4* KO brains (Yudkoff, 2017). Importantly, leucine, lysine and proline accumulation also serve to activate mTORC1 anabolic signalling (Johnson *et al.*, 2020; Oka *et al.*, 2013; Son *et al.*, 2020). Accumulated proline levels indicate the up-regulation of cyclical proline synthesis and catabolism (via an $FADH_2$-generating dehydrogenase) to supplement the ETC and vent redox stress by regenerating $NAD(P)^+$ (McDonald *et al.*, 2018; Schwörer *et al.*, 2020). These results, although informative, cannot elucidate the contribution of specific cell types, metabolite shuttles and mitochondrial sub-populations to LS pathology.

2.8.3 Quadriceps metabolomics: special glycolytic fibre perturbations

While previously disregarded as secondary effects of the phenotype, disturbed skeletal muscle metabolism has recently been shown to contribute greatly to the breathing and locomotor difficulties in *Ndufs4* KO models (Foriel *et al.*, 2018; Pronicka, 2017), while muscular deficiencies are implicated in most MDs overall (Thompson *et al.*, 2020). Type IIB muscle fibres are known as glycolytic fibres, as they rely more on glycolysis to meet their energetic needs and

[10] Proliferation and infiltration of non-neuronal cells in the normally tightly organized neuronal networks.
[11] Glutamine, glutamate, pyroglutamate, GABA and α-ketoglutarate

accordingly present two to three times less mitochondria than Type I (oxidative, mitochondria rich) fibres (Schiaffino & Reggiani, 2011; Zhang *et al.*, 2017). Although CI activity was reduced by ~80% in both the quadriceps femoris- and soleus muscles (representative glycolytic and oxidative muscle models, respectively) of *Ndufs4* KO mice, the lower total mitochondrial population of quadriceps resulted in threefold lower residual ETC activity and more perturbed metabolism than in the soleus[12] (Terburgh *et al.*, 2019). TCA cycle-related aberrations were more significant in the quadriceps, presenting greater lactate depletion and accumulation of the acetyl-CoA derivatives (Terburgh *et al.*, 2019). Depletion of various metabolites related to the ETF-QO system and G3P shuttle, as well as proline depletion and lysine accumulation, indicate adaptive responses aiming to restore OXPHOS function (McDonald *et al.*, 2018; Terburgh *et al.*, 2019). Overall, the glycolytic quadriceps presented more severe depletion of intermediates, higher amounts of structural protein degradation markers and concurrently greater atrophy.

Quadriceps muscles were thus selected for this study, alongside the contrasting, highly oxidative milieu of the disease-driving *Ndufs4* KO brain to uncover the nuances of mitochondrial contribution to similar, yet differentially perturbed pathways in this model.

2.9 Principles of metabolic compartmentalization

Eukaryotes have evolved efficient ways of separating the thousands of heterogenous chemical reactions that mediate cellular homeostasis (Figure 2-6), without which, unwanted or futile reactions and toxic by-products would abound (Goodman *et al.*, 2018; Sivanand *et al.*, 2018). Chemical compartmentalization is achieved via different chemical/enzymatic co-factors that orchestrate pathways with similar intermediates but different intended outcomes. Spatial compartmentalization is mediated by the physical segregation of related enzymes (mostly via membranes) to maintain separate chemical milieus in the same cell (Berry *et al.*, 2018; Brand & Nicholls, 2011). Finally, temporal compartmentalization is mediated via time-based regulation of enzyme expression and activity in response to external signals. These categorizations are not distinctive; metabolite shuttling, for example, represents a combined chemical/spatial mechanism, usually obtained via physical association of the involved enzymes (Acin-Perez & Enriquez, 2014).

[12] Indicative of a biochemical threshold effect: adaptive mechanisms can only compensate up to a certain percentage of lost activity, whereafter overall dishomeostasis and pathology become apparent.

Importantly, metabolic compartmentalization between the mitochondrial and cytosolic[13] space is a key feature in many of the pathways involved in the *Ndufs4* KO phenotype described thus far, and compartment-specific contributions to the observed metabolic reprogramming could not be efficiently discerned by the whole-cell metabolomic studies performed to date (Johnson *et al.*, 2020; Terburgh *et al.*, 2019; Terburgh *et al.*, 2021). In that regard, spatial and chemical mechanisms are of prime importance in this study.

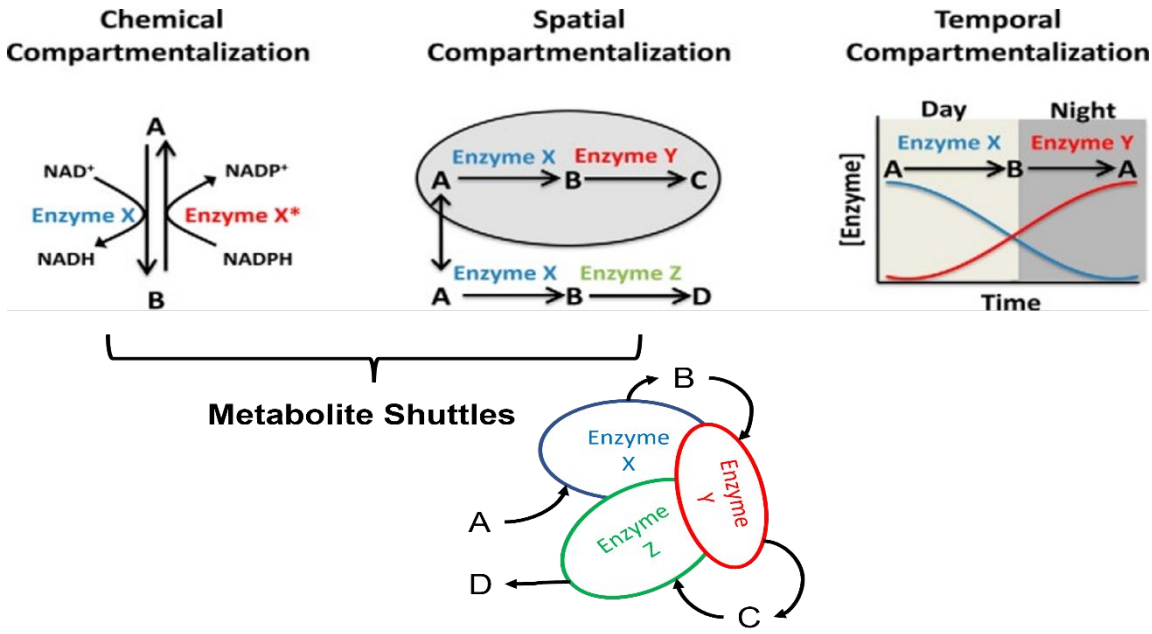


Figure 2-6: Different forms of metabolic compartmentalization in biological systems. Chemical compartmentalization is mediated by different enzymes mediating different reactions between similar intermediates; spatial compartmentalization involves different enzymatic pathways for the same compounds in physically separate compartments and temporal compartmentalization relates to differential enzyme expression/activation in response to environmental cues. Metabolite shuttles represent a hybrid chemical/physical mechanism, wherein a series of reactions is favoured through physical association of the involved enzymes. *Adapted and reprinted from Goodman et al. (2018) as permitted by the Creative Commons Attribution Licence (CC BY 4.0).*

2.10 Mitochondria as unique metabolic spaces

Due to the amount of critical biochemical pathways that intersect at the mitochondrial level, these organelles are regarded as metabolic and signalling hubs in eukaryotic cells, orchestrating all these functions towards homeostasis in response to stressors (McDonald *et al.*, 2018; Nunnari & Suomalainen, 2012; Stepien *et al.*, 2017). Metabolic pathways can, therefore, be either fully compartment specific or regulated across multiple organelles. Together, all these compartmentalizing mechanisms lead to a unique mitochondrial metabolome, with close cytosolic correlation (Chen *et al.*, 2016; Liu & Xu, 2018). Considering critical pathways that are

[13] Cytoplasm refers to the entirety of the extra-nuclear content in cells, where cytosol defines only the cellular volume that is not included in any organelle.

specific to the mitochondria, the central TCA cycle reactions and OXPHOS system are the most defining. Furthermore, it has been shown in hepatocytes and skeletal muscle that separate pools of the critical bioenergetic co-factors NAD^+/NADH, FAD^+/$FADH_2$ and ATP/ADP are kept in the mitochondrial and cytosolic compartments (Goodman *et al.*, 2018; Matuszczyk *et al.*, 2015). Exemplary pathways involving bicompartmental regulation include those related to amphibolic amino acid substrates (Broër & Palacin, 2011; Hewton *et al.*, 2021), such as proline, lysine and glutamate. There are also certain pathways that are fully expressed in both compartments but separately regulated, a notable example from that described thus far, being the 1C/folate metabolism (Ducker & Rabinowitz, 2017; Ducker *et al.*, 2016). Regardless of how individual pathways are split across the mitochondria and cytosol, IMM and OMM transporters represent a fulcrum for their regulation, supplying substrates, removing by-products and regulating fluxes in compartment-specific pathways (Becker & Wagner, 2018; Palmieri, 2013; Yoshida, 2021).

2.10.1 Mitochondrial metabolite transport

Both the IMM and OMM contain transmembrane proteins dedicated towards import and export of metabolic substrates. The OMM is relatively porous and thus more permeable to metabolite exchanges than the IMM (Section 2.2). A traditional view of OMM transport holds that a voltage-dependant anion channel (VDAC1) mainly regulates flow of mitochondrial metabolites, as it allows the free diffusion of anionic molecules <5 kDA in and out of the IMS (Colombini, 2004). This channel notably exchanges mitochondrial ATP for cytosolic ADP and is often found as part of membrane complexes (with mitochondrial creatine kinases or mCK, hexokinases, IMM adenylate carriers, etc.), thus it has been proven to fulfil a critical role in bicompartmental bioenergetic sensing and regulation (Bonilla *et al.*, 2021; Pastorino & Hoek, 2008).

The main contributors to metabolic compartmentalization between the mitochondria and cytosol, however, are the various distinct transporter proteins permeating the IMM (Palmieri, 2013; Palmieri & Pierri, 2010; Palmieri & Monne, 2016). The SLC25 (solute carrier) members are the largest contributing protein class in that regard, as they collectively serve amino acid, carboxylate, nucleotide and co-factor transport. Notably, the crucial import of pyruvate and lactate to mitochondria is mediated by entirely different solute carriers, namely monocarboxylate transporters (MCT1-4) from the SLC16 family, while long-awaited identification of the serine transporter mediating 1-C metabolism unexpectedly came from the sideroflexin protein family (SFXN1/3) (Hewton *et al.*, 2021; Kory *et al.*, 2018; Yoshida, 2021). The driving force of both VDAC and SLC proteins' translocating function is a combination of a substrate concentration gradient, as well as the $\Delta\psi_m$ maintained by ETC activity (Becker & Wagner, 2018; Palmieri & Pierri, 2010). Therefore, changes in bioenergetic parameters due to MD is hypothesized to strongly affect the metabolic gating functions mediated by these transporters.

2.11 Assaying mitochondrial metabolic compartmentalization

Given the compartment-specific regulation of mitochondria and cytosolic pathways critical to cellular homeostasis, much effort has recently been directed towards deconvoluting the mitochondrial contribution from the rest of the cell in diseased states (Chen *et al.*, 2016; Lewis *et al.*, 2014; Liu & Xu, 2018; Van Vranken & Rutter, 2016; Walzel *et al.*, 2002). This is further complicated by the volumetric ratios between these compartments, as mitochondrial content varies significantly between cell types and does not typically exceed 20-30% of the total volume in even the most oxidative cells (Kaasik *et al.*, 2007). Thus, compounds derived from both cell compartments cannot be accurately attributed to disturbance in either one, while alterations in mitochondria-specific metabolites may be diluted beyond significance or even detection in the far more voluminous total cellular extract. While still a niche field, sub-cellular metabolic flux measurement and metabolome profiling have become imperative to elucidating the phenotypic mosaicism attributed to MD at the mitochondrial level.

2.11.1 Metabolic flux analysis and mitochondrial isolation

Regarding the directionality and magnitude of energy flow through metabolic pathways, metabolic flux analysis (MFA) serves to follow isotope-labelled compounds through metabolic reactions and compartments, thus giving insight on spatiotemporal compartmentalization (Gravel *et al.*, 2014; Wiechert, 2001). While this methodology can give great direct measurement of metabolic fluxes and how they are disturbed by disease, MFA is inherently limited by the *a priori* defined target molecules/pathways, only interrogating a small fraction of the total metabolome. In contrast to MFA, most sub-cellular metabolomic studies to date rely on first isolating mitochondria from the rest of the cell, measuring the metabolome therein, and comparing these results to that of the post-mitochondrial isolate (representative of the cytoplasm) or total cellular metabolite profile. The crux of these methods is a rapid, simple mitochondrial isolation (MI) strategy that delivers isolates of high purity and yield, without compromising the integrity of the IMM that would lead to organelle rupture and unrepresentative fraction metabolite profiles. MI for metabolomics is typically achieved via i) differential centrifugation (DC), ii) ultracentrifugation (UC), or iii) immunocapture methodologies, following collection and homogenization of the cell/tissue samples (Franko *et al.*, 2013; Kappler & Lehmann, 2019; Pan *et al.*, 2018).

2.11.2 Mitochondrial isolation strategies for metabolome profiling

Most current sub-cellular metabolomics studies utilize DC isolation, as this common laboratory technique can be performed easily with little technical expertise (Go *et al.*, 2014a; Pan *et al.*,

2018). Despite its rapid and widely applicable workflow, DC isolates are usually of lower yield and purity[14] than the other mentioned strategies; as smaller than typical mitochondria may not precipitate, larger or cytoskeleton-anchored mitochondria can precipitate with the nuclei in the initial steps, and organelles (such as lysosomes and endosomes) of roughly the same size and volume as mitochondria may co-precipitate with the mitochondrial fraction. UC utilizes a sucrose or percoll density gradient and high-speed centrifugation to force separation of cell constituents by virtue of their density (Khattar *et al.*, 2016; Kiebish *et al.*, 2008b). While UC delivers mitochondria of significantly higher purity and yield than DC, it is more expensive, complex (requiring precise preparation of the sucrose gradient beforehand) and timeous.

However, the focus of this chapter lies with MI, based on immunopurification principles. Miltenyi *et al.* (1990) first described a novel method utilizing monoclonal antibodies, engineered as superparamagnetic bead conjugates, with specificity for a ubiquitous OMM protein, TOM22[15] (Hornig-Do *et al.*, 2009). Kit-based magnetically activated cell-sorting (MACS) utilizing this principle have seen widespread application, being successfully used to isolate neural, synaptosomal and liver mitochondria, amongst others (Hubbard *et al.*, 2019; Lee *et al.*, 2019). MACS has consistently been shown to outperform other methods on basis of mitochondrial purity, while matching or exceeding DC/UC yield and minimizing IMM rupture due to mechanical (centrifugal) force (Afanasyeva *et al.*, 2018; Chen *et al.*, 2016). A critical drawback to this system, however, is the timeous incubation and slow column-based separation steps that inevitably lead to unwanted metabolic turnover[16] and some mitochondrial uncoupling and matrix content loss. In the context of the established *Ndufs4* KO mouse strains available, and without further genetic manipulation or crossbreeding, the kit-based MACS method was selected for this study due to the application flexibility, ease of use and superior performance in comparison to UC/DC techniques.

2.11.3 Limitations inhibiting large-scale application

While the MI step is regarded as the most critical towards accurate sub-cellular metabolomic results, it is imperative to point out that every part of the process introduces analytical hurdles that must be considered in experimental design. A recent review groups the critical points as shown in Figure 2-7: i) Sample handling, ii) isolation buffer selection, iii) tissue homogenization iv) mitochondrial isolation and v) metabolomic methodology (Liu & Xu, 2018).

---

[14] Mitochondrial yield is majorly assessed by compartment-specific protein or enzyme enrichment assays, while IMM integrity is usually expressed as RC respiratory coupling measurement.
[15] Translocase of the outer membrane 22, a core transporter of the mitochondrial protein import system.
[16] Post-mortem changes in metabolome due to residual enzyme activity & spontaneous reactions.

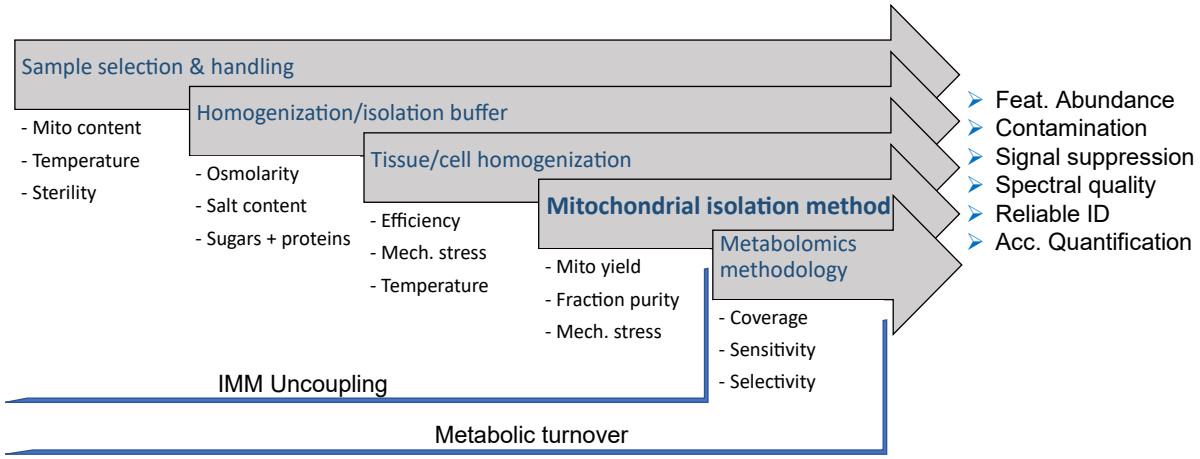


Figure 2-7: Methodological hurdles limiting sub-cellular metabolomic applications. Each phase of the isolated mitochondrial metabolomic workflow is shown as grey arrows, with the critical factors to control listed for each. Every step, from sampling to mitochondrial isolation, may incur IMM rupture and mitochondrial metabolite leakage, while metabolic turnover is a detrimental factor throughout. All these factors affect the technical quality and biological accuracy of the observed metabolite profiles (blue arrowheads). Acc: accurate, feat: feature, ID: identification, mech: mechanical, Mito: Mitochondria.

Firstly, the nuances of mitochondrial populations in different samples must be considered. Brain tissue contains more mitochondria than skeletal muscles, thus a large difference in mitochondrial yield between these tissues can be expected (Schiaffino & Reggiani, 2011; Zhou *et al.*, 2018). As isolated mitochondria are known to gradually lose IMM coupling with time (Corcelli *et al.*, 2010; Schmitt *et al.*, 2013), great focus is placed on performing the MI step as rapidly as possible, at near-freezing temperatures and in a sterile environment. The homogenization method applied is seen as the most critical step towards maximizing intact mitochondrial yield (Gross *et al.*, 2011; Shibata *et al.*, 2015). Researchers strive towards a homogenization method that can efficiently break all the cells but minimize mechanical/thermal stress in each sample matrix studied. The selection of homogenization and MI buffers is also critical (Liu & Xu, 2018). The addition of salts (sodium/potassium phosphates) and sugars (mannitol/sucrose) in classic MI buffers towards pH and osmotic buffering was shown by Corcelli *et al.* (2010) to severely influence the produced NMR or MS spectra. Regardless of the MI technique applied, a balance should be found between sufficient mitochondrial yield and purity, time efficiency, robustness and application flexibility, and this “sweet spot” is entirely dependent on the context of each tissue/cell milieu studied (Kappler & Lehmann, 2019; Liu & Xu, 2018). While popular approaches use either whole-cell or centrifugal supernatant samples as comparison, these are not sufficient to directly assess compartmentalization between mitochondria and cytosol, as other organelles are still present. Few present studies have focused on producing a purified cytosolic fraction as well (Matuszczyk *et al.*, 2015).

All these factors eventually affect the metabolite abundance and metabolomics spectral data quality that directly influence the selection of metabolomic platforms for analyses. Metabolite identification is an ongoing problem, as only ~11% of the putative mitochondrial metabolome, as well as only half of the shared mitochondrial/cytosolic composition is known (Liu & Xu, 2018; Roede *et al.*, 2012). Despite these issues, mitochondria-specific metabolomics has been proven to identify significant changes in various mitochondria-related disease models that went unseen at the appropriate whole-cell level, proving its value towards elucidating more target-specific pathological metabolic alterations (Go *et al.*, 2014a; Kiebish *et al.*, 2008a; Kiebish *et al.*, 2013; Roede *et al.*, 2012).

2.12 Current mitochondria-specific MD metabolomics knowledge

Many characteristics of mitochondria-specific metabolism have come to light through sub-cellular omics studies. It was confirmed through metabolite and enzyme assays that lactate is imported and metabolised inside the mitochondria by a mitochondrial isoform of lactate dehydrogenase, implicating new roles for lactate metabolism in matrix redox balance (Passarella *et al.*, 2008; Young *et al.*, 2020). Similarly, creatine and ATP levels in the mitochondria have been proven to be regulated separately from the cytosolic pools, with the prime function of the IMS-located mCK complex being maintenance of a favourable kinetic environment for ATP synthesis (i.e., ↑ADP/ATP) (Bonilla *et al.*, 2021; Schlattner *et al.*, 2006). Through sub-cellular strategies, it was shown that matrix-derived aspartate is crucial for cell proliferation, while the total matrix amino acid pool is also seemingly regulated separately from the cytosolic equivalent, correlating closely with proteolytic products and translational substrate requirements of mitochondrially synthesized proteins (Birsoy *et al.*, 2015; Ross-Inta *et al.*, 2008; Van Vranken & Rutter, 2015). While interrogation of mitochondria-specific metabolism has revealed valuable information on metabolic compartmentalization in health and complex disease (Lee *et al.*, 2019; Wang *et al.*, 2016), its application to models of direct ETC insult is lacking, with few comparable studies performed to date (Chen *et al.*, 2016; Gravel *et al.*, 2014; Pan *et al.*, 2018; Villa-Cuesta & Rand, 2015).

2.12.1 Sub-cellular metabolomics of ETC dysfunction

Gravel *et al.* (2014) utilized principles of MFA and DC-enriched mitochondria to clarify TCA cycle perturbations in mouse skeletal muscle due to pharmacological ETC inhibition. During rotenone-mediated CI inhibition, NADH accumulation and aberrant TCA cycling was prominently shown. Importantly, the decreased succinate, citrate and oxaloacetate levels detected in this study correlated well with results obtained in the CI-deficient quadriceps of *Ndufs4* KO mice (Section 2.8.3) (Alam *et al.*, 2015; Terburgh *et al.*, 2019). Utilizing HeLa cells, mitochondria

isolated therefrom and the CI inhibitor piercidin (alongside antimycin and oligomycin simulating CIII/CV inhibition, respectively), Chen *et al.* (2016) described several mitochondria-specific metabolic effects. The measured whole-cell and mitochondrial metabolomes were significantly different, and the matrix content showed greatest perturbation in response to CI inhibition. Their results again showed that the most prominent metabolic changes relate to disturbed $NADH/NAD^+$ ratios, while proving a ~30-fold greater perturbation of the matrix ratio in comparison to whole cells. Significant accumulation of acetyl-CoA and acetyl carnitine in the matrix was shown to be distinguishing of CI inhibition, correlating with *Ndufs4* KO studies done to date (Johnson *et al.*, 2020; Terburgh *et al.*, 2019; Terburgh *et al.*, 2021; Valsecchi *et al.*, 2012).

Pan *et al.* (2018) were the only group thus far to study genetic ETC dysfunction at sub-cellular level, utilizing Δ*sdh2* and Δ*atp4* yeast models of CII and CV inhibition, respectively. Their results showed greater metabolic change at the mitochondria-specific metabolome in response to genetic ETC injury, compared to the cytoplasmic fraction. Glutamate and aspartate were again implicated, as well as serine, glycine, proline and ornithine, all in line with *Ndufs4* KO mouse studies performed thus far (Johnson *et al.*, 2020; Terburgh *et al.*, 2019; Terburgh *et al.*, 2021). Despite the overlap of sub-cellular metabolomic applications for mouse models and the promising outcomes of studies in other models of ETC dysfunction, and considering the primarily mitochondrial repercussions of PMD, the paucity of mitochondria-specific MD studies is resounding. To the best of our knowledge, there is no current literature describing mitochondrial and cytosolic purification from the tissues of existing MD models for subsequent multi-platform metabolomics, and no mitochondrially resolved metabolic studies of LS or *Ndufs4* KO in general (Kappler & Lehmann, 2019; Liu & Xu, 2018).

2.13 Experimental design

The experimental design applied in this manuscript towards addressing the aforementioned problem, was executed in three phases (Figure 2-8), resulting in two separate peer-reviewed research outputs. Throughout the duration of phases, A and B, HET mice were bred to produce the WT and *Ndufs4* KO males for this study. Samples were collected from these animals (n = 8 KO, n = 8 WT) intermittently as they came of age (P45-50), following their euthanasia by cervical dislocation. Collected tissues were either frozen at -80 °C for later analysis (tailsnips) or immediately processed via sub-cellular fractioning (quadriceps and brain). The resulting mitochondrial and cytosolic samples were immediately frozen at -80 °C. All genotypes were confirmed using PCR of the *Ndufs4* gene within the DNA isolates from the tailsnips.

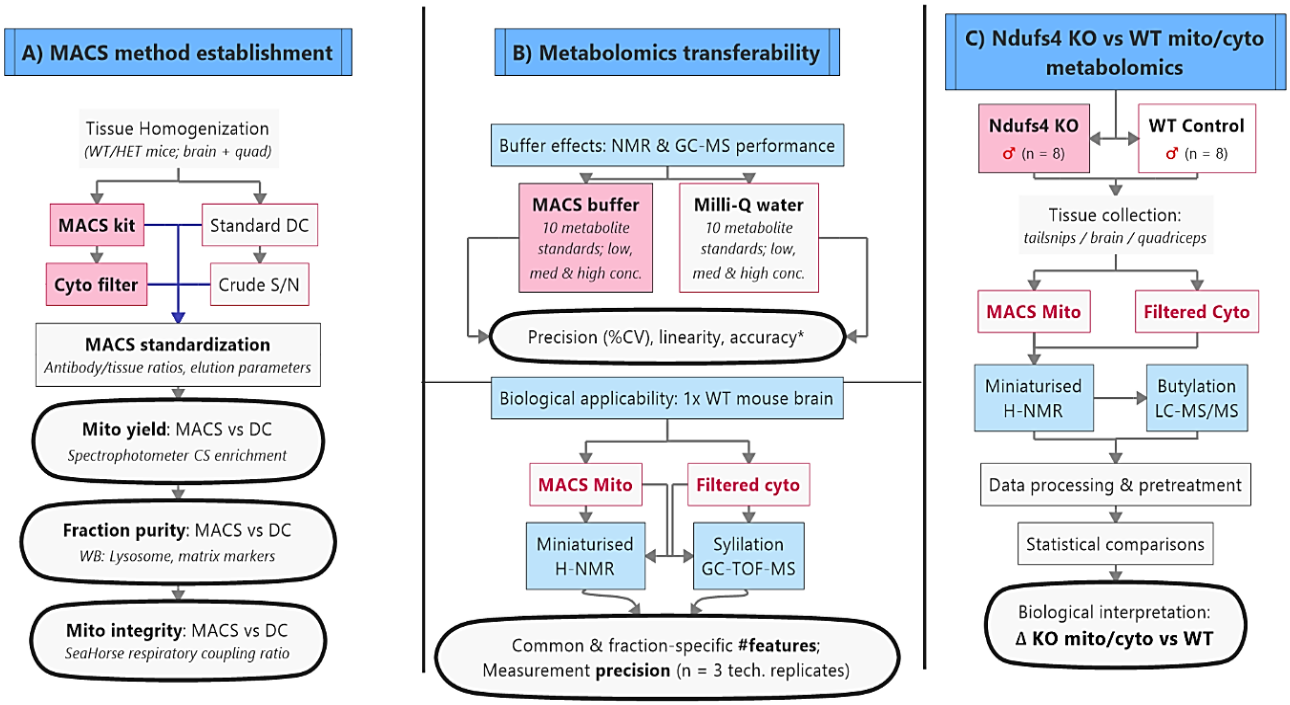


Figure 2-8: Schematic summary of experimental strategy. Flowchart of the different experimental phases, excluding sample collection, which was performed throughout. Phase A involved standardization of the MACS method and proof of improved yield, purity and integrity of the isolated mitochondria, compared to a standard DC method. Phase B evaluated the applicability of metabolite measurement in the MACS buffers as well as a trial of the workflow in *Ndufs4* WT brain fractions to show biological applicability. Phase C finally entailed application of the entire workflow to equal groups of WT and KO mice to elucidate significant compartment-specific metabolic alterations in brain and muscle mitochondria/cytosol due to *Ndufs4* KO. Conc: concentration, CS: citrate synthase, %CV: coefficient of variation, Cyto: cytosol, GC-TOF-MS: gas chromatography time-of-flight mass spectrometry, H-NMR, proton nuclear magnetic resonance LC-MS/MS: liquid chromatography tandem mass spectrometry, Mito: mitochondria, S/N: centrifugal supernatant, tech: technical, WB: Western blot.

Phase A and B entailed establishment of the central MACS mitochondrial isolation and cytosolic purification methods for the brain and muscle, all these experiments were performed using WT (n = 8) and HET (n = 6) not utilized by this or any other study. In phase A, the standard MACS protocol was adapted to optimize yield from the brain and skeletal muscle, according to defined parameters (Hornig-Do *et al.*, 2009; Hubbard *et al.*, 2019), alongside establishment of the reverse-flow centrifugal filtration method for cytosol purification. Thereafter, the yield, purity and IMM integrity of the obtained mitochondria were compared to that of mitochondria isolated by our standard, in-house DC method. Yield was measured as the percentage enrichment of mitochondria-localized citrate synthase (CS) activity in the isolates *versus* the preceding homogenates. Purity was assessed via Western blot against typical fraction contamination markers (Lysosome co-precipitation in mitochondria, mitochondrial matrix marker in cytosol). IMM integrity was measured by respirometry and expressed as the respiratory coupling between oxygen consumption and proton translocation.

Phase B concerned probing the effects of the MACS methodology (specifically the provided mitochondrial isolation buffers) on down-stream gas chromatography time-of-fight mass spectrometry (GC-TOF-MS) and proton NMR (^{1}H-NMR) metabolomics. In that regard, a mixture of ten pure chemical standards of common intracellular metabolites were analyzed within the MACS buffer environment (n = 10 technical repeats) and in pure water as control (n = 10) at a low, medium and high concentration level. Linearity and precision were calculated for each individual compound on either platform, while relative accuracy was calculated for the ^{1}H-NMR results as well. Method establishment concluded with a pilot ^{1}H-NMR and GC-TOF-MS analysis of *Ndufs4* WT-derived brain mitochondria and cytosol (n = 3 technical replicates), from which the noise and %CV-filtered compounds detected as unique to each fraction and present in both were listed with feature identification confidence and measurement stability values. The results of Phase A and B, published as Van der Walt and Louw (2020) (Annexure C), are described in chapter 4.

Phase C involved the titular mitochondrial and cytosolic metabolomic comparison of *Ndufs4* KO males to age and sex-matched controls. Internal standards were added to the cytosolic and mitochondrial extracts to achieve equivalent final internal standard (IS) concentrations. Half of each sample was aliquoted separately and stored for GC-TOF-MS analyses, which unfortunately could not be performed to date due to fatal equipment errors at the time of analyses. The other half of each extract was prepared for ^{1}H-NMR analyses in two separate batches (WT, KO brain and quad mitochondria in batch one, and the corresponding cytosol in the other), utilizing a non-destructive, ultrafiltration approach applicable for minimum-volume biological samples. After NMR analyses, the samples were recollected, a small portion dedicated for 2D-NMR metabolite identity confirmation, and the rest extracted for LC-MS/MS analyses by cold acetonitrile. Stable isotopes of seven amino acids and acylcarnitines were added to each sample, before targeted profiling of these chemical classes proceeded in two separate batches equivalent to the grouping used for NMR analysis. After data extraction, clean-up and pre-treatment (signal sum normalization and outlier correction), univariate statistical comparison of KO and WT mitochondrial metabolite abundances followed alongside equivalent comparison of WT and KO cytosol to indicate compartment-specific alterations due to *Ndufs4* KO. These results, achieving the titular objective of this study, were recently published as Van der Walt *et al.* (2021) (Annexure D) and are detailed in chapter 5.

CHAPTER 3

Methods and Materials

- Animals and Sampling
- Phase A: MACS method establishment
- Phase B and C: Metabolomic Methods

3.1 Introduction

Herein is described the materials, instrumentation and methodology applied to meet the overall objectives of the study (a full alphabetised list of reagents and chemicals is attached as Annex A). This chapter is divided into four parts, firstly detailing the animal model, sampling and preparation of standard compounds for the metabolomics method development phase; thereafter, the developed and applied standard methods are described in sequence of their designation in the experimental strategy outlined (Fig 2-8) at the end of Chapter 2.

The differential centrifugation (DC) and MACS mitochondrial isolation and cytosolic filtering methods established in phase A are firstly described. Protocols for spectrophotometrically determining protein concentration by bicinchoninic acid (BCA) assay and CS enrichment as a measure of mitochondrial yield, are listed. Western blot methods for quantifying compartment-specific proteins LAMP-2 (Lysosome) and Hsp-60 (mitochondrial matrix) follows, before the applicable procedures for determining the respiratory coupling ratio (RCR) of isolated mitochondria by Seahorse XFe96 respirometry. GC-TOF-MS, ^{1}H-NMR and LC-MS/MS methods utilized in phase B and C are globally detailed, with specific alterations thereof; for i) the pilot probe of WT mouse brain and muscle isolates published in peer-reviewed paper 1 and ii) Comparative sub-cellular metabolomics of *Ndufs4* WT and KO mice, as published in peer-reviewed paper 2 (Chapter 5).

3.2 Animals and sampling

3.2.1 Origin information and husbandry

The original heterozygous *Ndufs4*$^{+/-}$ (B6.129S4-*Ndufs4*$^{tm1.1Rpa}$/J) breeding trios (consisting of one male and two female mice) were obtained from Jackson Laboratory (#027058, JAX, USA). The animals were bred, housed and monitored by a research animal technician in the specific pathogen-free unit of the Vivarium (SAVC reg. #FR15/13458) of the Pre-Clinical Drug Development Platform (PCDDP; NWU, ZAF). They were housed in polysulphone type II long, individually ventilated cages (396 x 215 x 172 mm) held under temperature- (22 ± 1 °C), humidity- (55 ± 10 %) and light-controlled (12:12 hour light/dark cycle) conditions with standard laboratory chow (Rodent Breeder, Cat. #RM1845, LabChef, ZAF) and water provided *ad libitum*.

Male KO (*Ndufs4*$^{-/-}$) mice along with age- and sex-matched controls (*Ndufs4*$^{+/+}$; WT) were exclusively used in this study to avoid known differences in hormone cycles, tissue-specific metabolism and, consequently, metabolic profiles between sexes (Ruoppolo *et al.*, 2018; Wells *et al.*, 2016). Heterozygous mice, along with excess WT males and KO females born during the

breeding process were also employed for initial method development experiments as to save on breeding time and costs. The genotypes were confirmed by PCR on tailsnip-derived DNA.

3.2.2 Sample groups and sizes

Metabolomics is most informative with adequately large sample groups for increased statistical power. However, timeous and expensive breeding programs necessitate a midway between statistically adequate and practically feasible sample group sizes. Power calculations for this study thus factored in that these mice are bred and kept in homogenous environmental condition, while they also represent genetic replicates of a single model (Kruse *et al.*, 2008; Valsecchi *et al.*, 2012). The minimum required animal numbers were determined, in collaboration with Statistical Consultation Services (Faculty of Natural and Agricultural Sciences, NWU, RSA) as such that the largest metabolic effects of practical significance (D > 1,0) can be inferred with 80% power; an adequate figure for such a pilot study of novel methodology[17].

The required number of animals per group (WT and KO) were determined to be n = 8 for metabolomic analyses, and the applicability of these group sizes were confirmed using standard software (G*-Power 3 R-package) for power calculations in metabolomic studies (Faul *et al.*, 2007). Fourteen mice of various genotypes, surplus to those required for all other research or breeding purposes, have also been used throughout the preliminary method standardizing phases A and B as they became available, bringing the total to 30 mice used. Batch, specimen and sampling details are fully expounded in Annexure B.

3.2.3 Euthanasia according to ethical endpoints

The mice used in this study were euthanized between postnatal day (P) 45-50 to correlate with pre-determined relevant ethical endpoints in *Ndufs4* KO studies, as significant central nervous system symptoms are only apparent at this age (Kayser *et al.*, 2016). Humane endpoint score sheets were used throughout (SOP_Viv_Anim 27: Determining pain and distress in lab rodents) to establish whether any mice needed to be considered for euthanasia (score of 10 to 14) or be euthanized immediately (score of 15 to 20). This was the function of the PCDDP research animal technician in charge of the colony. Euthanasia was also performed by the appropriate technician via cervical dislocation, as described by the AVMA (Leary *et al.*, 2013) – in order to avoid adverse effects of anaesthesia on cellular and mitochondrial metabolism (Quintana *et al.*, 2012). The animals were euthanized after a 12 hour fasting period at the same time of day

[17] Previous similar metabolomics studies are mostly used as basis for power calculations. With no such study available in this pilot- a purely statistical approach to power and significance levels was followed.

(11:00 AM to 12:00 PM) in order to reduce inter-animal physiological variation (Deprez *et al.*, 2002).

3.2.4 Tissue collection and sampling

Immediately following euthanasia, various tissues including the tail-snips, brain and skeletal muscle (quadriceps femoris) were rapidly excised. Whole brains were removed first, before being divided hemispherically, as such that equal halves of the brain could be allocated to two concurrent studies from the Mitochondrial Research Laboratory. The left half of the brain was consistently taken for this study, while the right half was dedicated to another, pertaining to the encompassing topic of biochemical investigation in *Ndufs4* KO mice. Thereafter, both quadricep muscle groups, positioned on the anterior portion of the proximal femur, were removed. Tail-snips were taken to confirm the *Ndufs4* genotype as described in Section 3.3.

As mice of the correct genotype became available, their tissues were collected and immediately placed on ice before being brought back to the lab for sampling. The acquired tissues were finely cut using sterile scalpel blades and a sterilized dissection table placed on ice. 100 milligrams (mg) brain tissue and/or 150 mg quadriceps was weighed off for mitochondrial isolation, as described in Sections 3.5 and 3.6. Due to the comparatively rapid turnover of metabolites (Deprez *et al.*, 2002; Erban *et al.*, 2007), every precaution was taken to avoid alterations in metabolite concentrations; the whole procedure was performed at 0-4 °C from tissue isolation, with mitochondrial isolation being performed immediately thereafter and as rapidly as possible. All samples were clearly marked and either immediately used or stored at -80 °C for later use. Record of animal details (ID number, litter number, genotype, sex, tissue type and date of collection) were kept as the samples were obtained (Annexure B).

3.3 Confirmation of genotype

PCR Genotyping was performed to distinguish the *Ndufs4* genotypes of all breeding pairs and litters at ~P21, according to the standard technique described by Valsecchi *et al.* (2012), this was done as part of the breeding and selection programme for the overall study. This section, however, pertains to the confirmation of the determined genotypes, utilizing the same protocol, but applied to the post-mortem collected tail-snips of mice selected for this study.

3.3.1 Chemical and Primer information

For the isolation of genomic DNA from tailsnips, the Quick DNA™ MiniPrep plus Kit (Thermo Fisher Scientific, USA), utilizing Zymo-Spin™ IIC columns and collection tubes, was used (See Annex A for details on all chemicals and reagents). Wherever de-ionized water was applicable,

Milli-Q water (purified by the Milli-Q® system, Merck Millipore™, USA) was used. For the PCR amplification of *Ndufs4* DNA, the Phire™ Tissue Direct PCR Master Mix Kit (Thermo Fisher Scientific, USA) was used together with specific forward and reverse (*Ndufs4* 1060 and *Ndufs4* Rev, Inqaba Biotec™, ZAF) primers designed for the *Ndufs4* gene by Valsecchi *et al.* (2012).

Table 3-1: Primers used during *Ndufs4* genotyping

Primer	5' – 3' Sequence	Melting Temperature (°C)	Bases
***Ndufs4* 1060**	AGCCTGTTCTCATACCTCGG	62.45	20
***Ndufs4* Rev**	TTGTGCTTACAGGTTCAAAGTGA	59.2	23

3.3.2 Instrumentation and Software

Instrumentation used during DNA isolation and quantification includes: the 5418 Benchtop Centrifuge (Eppendorf, DEU), vortex mixer (VELP® Scientifica, ITA), ABH 2 dry block heater (Labotec, ZAF), NanoDrop® ND1000 spectrophotometer (Thermo Fisher Scientific, USA) and Operating Software (v 3.8.1). For PCR amplification and electrophoretic characterization of DNA, the T100™ Thermal Cycler, Sub-Cell® GT Cell Horizontal electrophoresis apparatus and ChemiDoc™ MP system with Image Lab (v 5.2.1) software were used, all purchased form Bio-Rad, ZAF.

3.3.3 Genotyping protocol

3.3.3.1 DNA isolation and quantification

Genomic DNA was isolated from tailsnips according to the standard protocol for solid tissue prescribed for the Quick DNA™ MiniPrep plus Kit. Utilizing flame-sterilized scalpels and sterile petri dishes, each sample was cut to 3-5 millimeters (mm) in length and placed into a collection tube. Tissue lysis was achieved by incubating the samples at 55 °C (2 hours) in a mixture of solid tissue lysis buffer (95 microliters; µL), nuclease-free H_2O (95 µL), and proteinase K (10 µL of 20 mg/mL stock), being vortex mixed for 30 seconds every 30 minutes. During this process, connective tissues and the membranes of cells and nuclei are chemically lysed to release nuclear DNA. Before the centrifugal removal of insoluble debris (12,000 ×*g*, 1 minute), 400 µL genomic binding buffer was added and the contents mixed by vortex for 30 seconds. Supernatants were then transferred to spin column-collection tube assemblies and centrifuged (12,000 ×*g*, 1 minute) to bind DNA to the silica column while separating it from the flow-through. DNA binding is enabled by the large amounts of chaotropic salts and alcohol in the binding

buffer, which disrupt hydrogen bonds between nucleic acids and surrounding water, thus promoting hydrophobic interactions between the DNA and silica column.

Bound DNA was subjected to three separate wash steps for removing contaminants (i.e., excess salts, RNA and protein). Firstly, gDNA pre-wash buffer (400 µL) was added on to the column, followed by centrifugation (10,000 ×*g*, 1 minute). This step was repeated twice more, but using rather gDNA wash buffer (700 and 200 µL , respectively). Finally, spin columns were transferred to sterile microcentrifuge tubes and DNA was eluted by incubating the column-bound DNA at room temperature (2-5 minutes) in 25 µL pre-heated (65 °C) DNA elution buffer, followed by centrifugation (12,000 ×*g*, 1 minute). This process was repeated to obtain a 50 µL dilution of isolated DNA for each sample, to be stored at −20 ºC for further use.

The isolated DNA was quantified as described by Meissner-Roloff (2009). Practical experience has shown that DNA concentration measurements fluctuate after successive freeze-thaw cycles; therefore, this procedure was only performed immediately before PCR amplification and electrophoresis. DNA samples were completely thawed and resuspended by gently vortexing, after which the NanoDrop® ND1000 spectrophotometer was used to determine the concentration of the DNA at a wavelength of 260 nm. In addition, DNA purity was assessed by determining the ratio of DNA absorbance (Abs) to a measurement of protein absorbance at 280 nm (A260/A280), with an A260/A280 ratio of ~ 1.8, indicating acceptable DNA purification.

3.3.3.2 PCR amplification

Conventional PCR amplification was used to differentiate between the three possible genotypes; homozygous wild-types (*Ndufs4*$^{+/+}$), homozygous knockouts (*Ndufs4*$^{-/-}$) and heterozygous carrier mice (*Ndufs4*$^{+/-}$), based on the length of a section spanning the site of excision in the mutant *Ndufs4* alleles. Therefore, the primers were designed corresponding to the introns flanking *Ndufs4* exon two (Valsecchi *et al.*, 2012), as shown in Table 3.1. In addition to the isolated genomic DNA samples, three control samples representing each of the three genotypes in question, were also amplified.

Samples were first diluted to 25 nanograms(ng)/µL in nuclease-free water according to their measured DNA concentrations. All PCR amplifications were done in a final reaction volume of 10 µL , containing: 2× Phire™ Tissue Direct PCR Master Mix, 0.5 micromolar (µM) *Ndufs4* forward and reverse primers, nuclease-free H_2O and 25 ng (1 µL) DNA. The Phire master mix contains a Phire Hotstart™ II DNA polymerase, which, due to its high replicative fidelity, ensures higher specificity compared to benchmark polymerases commonly used in PCR, and thus greater confidence in the obtained results. The DNA samples were amplified according to the

following PCR cycle conditions: i) initial incubation at 98 °C (5 minutes) to ensure total DNA denaturation as all internucleotide hydrogen bonds are broken and Phire polymerase activation; ii) cyclical incubations at: 98 °C (5 seconds), 57.3 °C (5 seconds) for primer annealing, and 72 °C (20 seconds) for optimal polymerase activity and DNA extension; and iii) 34 repeats of the above-mentioned cyclical process, amplifying the amount of target sequence-carrying amplicons multiple times; iv) final incubation at 72 °C (1 minute) to ensure amplicon completion.

3.3.3.3 Electrophoresis and imaging

To separate and identify the amplified PCR fragments in each sample, electrophoresis was performed using a 1 % (weight/volume; w/v) agarose gel containing Ethidium bromide (0.5 µg/mL) as a nucleic acid stain in 1× Bionic™ Buffer. To each gel, 10 µL of diluted (30 %, v/v) PCR products and 100 basepair (bp) DNA Ladder (containing a 2:1:3 ratio of DNA ladder, 6x DNA loading dye and nuclease-free H_2O) were loaded, respectively. The sample DNA does not require addition of a loading dye to be visualised under UV light, as the Phire™ mastermix already contains a suitable dye. Thereafter, the gel was run at 40 V (15 minutes), followed by 70 V (~ 1.5 hours) to separate amplicons. The principal of separation is that DNA of different lengths incur different migration tempos through the porous gel matrix, inversely proportionate to their size. Therefore, the smaller mutated amplicons will travel faster and appear lower down on the electrophoretogram than the full-length *Ndufs4* exon 2.

Next, the gel was photographed under ultraviolet (UV) light, thereby visualizing the amplicons and their sizes. The genotypes were then identified based upon fragment length as the amplicons of *Ndufs4*$^{+/+}$ (WT), *Ndufs4*$^{-/-}$ (KO) and *Ndufs4*$^{+/-}$ (Het) DNA, respectively. Bands are displayed corresponding to two intact *Ndufs4* allele segments (1229 bp), two shortened allele segments without the second *Ndufs4* exon (429 bp), as well as one allele with (1229 bp) and without (429 bp) the second *Ndufs4* exon. This is visually represented in Figure 3-1.

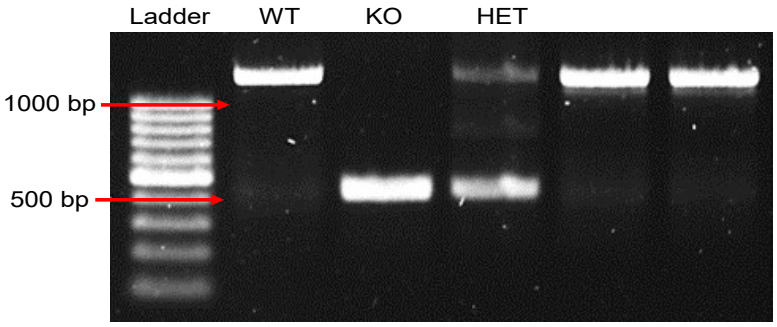


Figure 3-1: Example genotyping results The photo depicts a 100-1000 bp DNA ladder (lane 1) and *Ndufs4* amplicons of control (lane 1-4) and test samples (lane 5, 6). DNA from wildtype (WT, lane 2) animals present with the intact *Ndufs4* amplicon (1229 bp), while homozygous KO (lane 3) DNA contains the same amplicon, truncated by 800 bp via exon 2 deletion (429 bp). Heterozygous (HET, lane 4) DNA displays both bands for the intact and truncated *Ndufs4* amplicon.

3.4 Standard compound preparations for buffer testing

Dilutions of nine commercially available metabolites, commonly found in the affected tissues during the pathogenic course of CI-deficiency (Esterhuizen *et al.*, 2017; Terburgh *et al.*, 2019), were prepared as analytical standards for investigating the effect of the selected mitochondrial isolation buffer constituents on chemical analyses (Section 3.8 and 3.9). Sodium pyruvate (Pyr), sodium L-lactate, L-alanine, L-valine, potassium L-glutamate monohydrate, L-aspartic acid, glycine, 3-hydroxybutyric acid and 2-hydroxybutyrate were respectively dissolved in de-ionized water (Merck Millipore®, USA) to produce 50 mM stock solutions (2 mL) for each compound. These mixtures were vortexed for full dissolution, while the addition of 50 µL hydrochloric acid was required to acidify phenylalanine to achieve full dissolution in water.

A combined stock concentration containing 5 mM of each metabolite was prepared by adding together 200 µL of each compound stock and 200 µL de-ionized water (or water containing the ^{1}H-NMR internal standards; section 3.8.1) to achieve a 2 mL volume. This stock was diluted 10x, 20x and 100x to produce 500, 250 or 50 µM stocks – resulting in 4 mL being available for each corresponding concentration range. The dilutions were performed twice for each concentration range; once in Milli-Q water as a reference standard, and once in MACS Separation buffer (#130-096-946) at 1x final dilution (1x SB), containing 10% lysis buffer (Miltenyi Biotec, GER). This 90:10 mixture of the kit-provided separation buffer and lysis buffer, mimics the ratio applied for the used MACS protocol (See section 3.6.2.) and thus represents an adequate simulation of the buffer environment to be used for producing the sub-cellular fractions analyzed in this study.

3.5 Established DC mitochondrial isolation

DC methods are the cheapest, simplest and most widely used preparative strategies for sub-cellular metabolomics (Section 2.11.2). As such, a DC method originally published by (Pan *et al.*, 2018) for yeast sub-cellular studies was adapted in our laboratory for application to MD mouse models (Van der Walt, 2018). This established methodology, summarised in Figure. 3-2, was used as a comparative mitochondrial isolation method to the MACS fractioning strategy which stands as the main focus of the study.

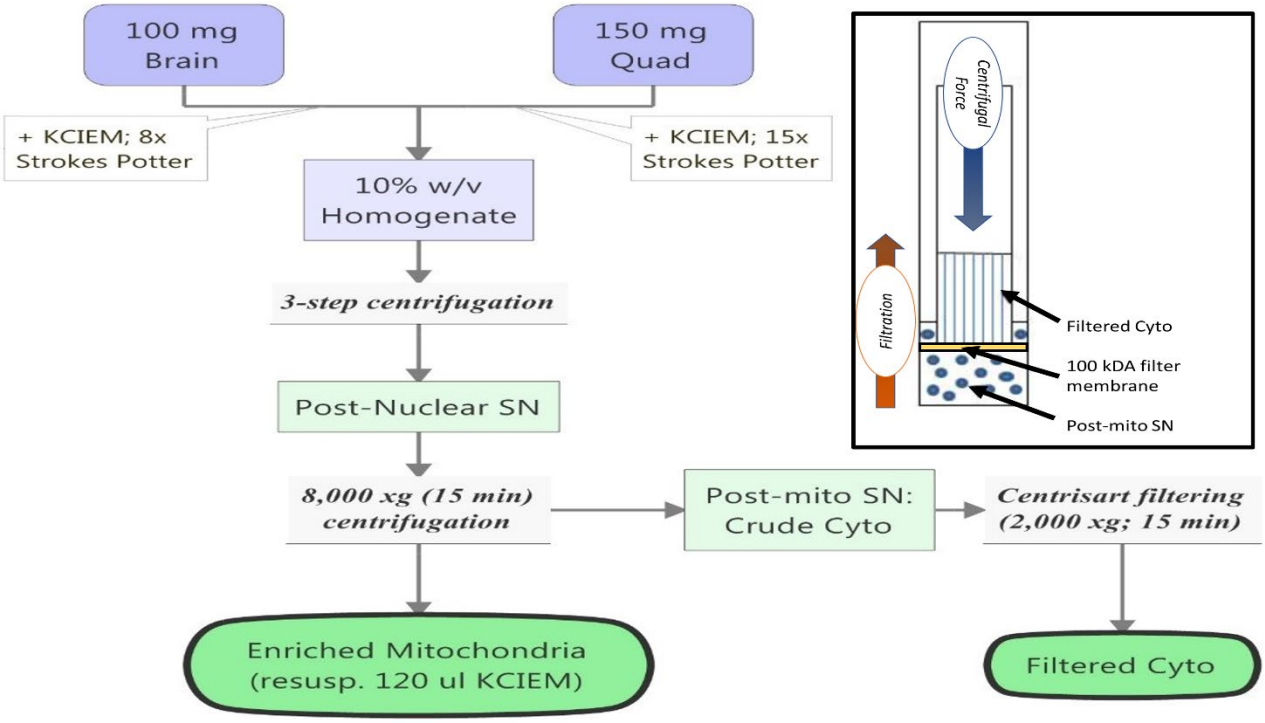


Figure 3-2: Summarised DC mitochondrial and cytosolic isolation protocol. This flow diagram illustrates the homogenization process for whole brain or quadricep muscle tissue in the KCIEM (KCl, EDTA, MOPS) isolation buffer, as well as the centrifugal speeds (x*g*) utilized for producing enriched mitochondria and filtered cytosol. The graphic insert (top right) illustrates the principle of Centrisart filtration, wherein the direction of filtrate flow is opposite to that of the applied centrifugal force. Cyto: cytosol fraction, kDa: kilodalton, SN: centrifugal supernatant, x*g*: centrifugal force as g-force factor.

3.5.1 Instrumentation

The instrumentation used for homogenization and DC cellular fractioning, included a Potter-Elvehjem homogenizer (#P7859-1EA, Sigma Aldrich, USA) and Heraeus™ Multifuge™ X3R Centrifuge (#75004516, Thermo Scientific, USA).

3.5.2 Established and standardized DC methodology

Mitochondria were isolated in optimized mass spectrometry (MS) compatible KClEM isolation buffer [180 mM KCl, 1 mM EDTA and 5 mM MOPS-KOH[18] (pH 7.2)], as first described by Corcelli *et al.* (2010). The salts in the buffer present the mitochondria with an isotonic environment to prevent mitochondrial swelling and rupture, while avoiding the sucrose and mannitol associated with other isolation buffers that can interfere with GC-MS and NMR analysis. Once the brain and/or quadricep muscle was obtained, cut finely using sterile scalpel blades while kept on ice and sampled for whole-cell metabolomics (Section 3.2.4), the required

[18] Ethylenediaminetetraacetic acid and 3-(N-morpholino) proanesulphonic acid - potassium hydroxide

mass for mitochondrial isolation was weighed off. From the 100 mg brain isolates (or 150 mg quadriceps muscle), a 10% w/v tissue lysate was prepared in ice-cold KCIEM buffer via eight strokes of the Potter-Elvehjem homogenizer. Using a fixed-angle rotor pre-cooled to 4˚C, the nuclei and cellular debris were pelleted and discarded after subsequent rounds of centrifugation at 250 x*g* (2 minutes), 1,000 x*g* (4 minutes) and 1,900 x*g* (4 minutes). The post-nuclear supernatant was subjected to 8,000 x*g* centrifugation for 15 minutes to pellet mitochondria. Enriched mitochondria were frozen at -80 °C and resuspended in KCIEM to 120 µL final volume immediately preceding each subsequent analysis.

Post-mitochondrial supernatants, which represent a crude cytosolic (cytoplasmic) fraction, were collected and filtered using Centrisart® 100 kilodalton (kDa) centrifugal cut-off filters (#13269E, Sigma Aldrich, USA). This represents a simple and cost-effective way to remove large membrane rests, whole mitochondria or any other organelles. Before use, these filters were prepared by three rounds of centrifugation (2,000 x*g*; 5 minutes) using Milli-Q water to clear any excess glycerol from the membrane. The post-mitochondrial supernatant was transferred to the filter tube and a cylinder containing the pre-wet filter membrane, placed over the liquid. The setup was accelerated to 2,000 x*g* for 15 minutes in a swinging-bucket rotor at 4 °C. The membrane cylinder is forced downward, while sample devoid of molecules exceeding 100 kDa molecular weight flows through the membrane to be extracted and stored as the cytosolic fraction (700 -1000 µL). This design minimizes the chance of organelle rupture and fractional cross-contamination associated with traditional centrifugal filters, where sample is placed on top of the membrane and centrifugally forced against it.

During Phase A, a 2 mL total homogenate was prepared using double the indicated tissue mass to be split evenly for DC or MACS isolation, thus eliminating biological variation as a limitation to the comparison. The resulting fraction in-between every successive step was sampled as to track mitochondrial enrichment/loss in every phase of the workflow. Aliquots of the homogenate (50 µL), post-nuclear supernatant (PNS; 50 µL), post-mitochondrial supernatant (Cr. Cyto; 100 µL) and filtered cytosol (Filt. Cyto; 300 µL) were taken for these tests, along with the resuspended and enriched mitochondria (EMF; 120 µL).

3.6 Fractioned magnetic isolation: MACS kit

MACS utilizes the principles of immunoprecipitation and magnetically activated cell sorting via magnetized retention columns, condensed into a simple and robust commercial kit. The kit consistently delivers isolates of high purity, yet minimal and highly variable yields have been reported in different sample types when applying the manufacturer protocol (Franko *et al.*, 2013; Hubbard *et al.*, 2019). In that regard, initial MACS parameters had to be tested and established

for skeletal muscle, as no published optimizations for this tissue exists. Hubbard *et al.* (2019) identified key steps in the methodology to be optimized for increasing mitochondrial yield, accordingly, initial optimizations were aimed at the i) ratio of tissue weight to buffer volume, ii) antibody-to-tissue ratio and iii) final elution steps. The final established MACS protocol, as published in Van der Walt and Louw (2020), is summarised in Figure 3-3.

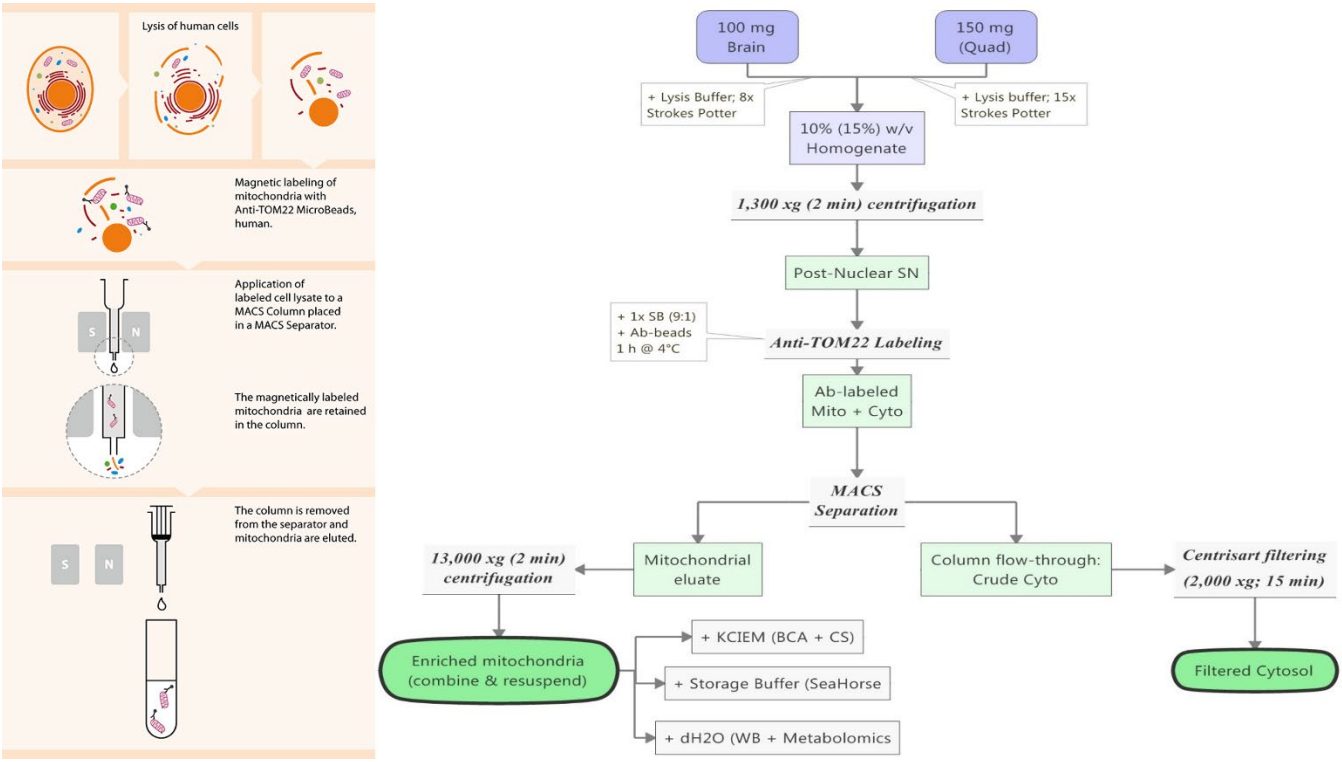


Figure 3-3: Established MACS workflow for mitochondrial & cytosolic purification. The flowchart summarizes each step performed during the MACS methodology established, while the excerpt image (left) illustrates the principles underlying the homogenization, antibody (Ab) labelling and mitochondrial separation steps, respectively. *Adapted and reprinted from Hornig-Do et al. (2009), as permitted by the Creative Commons Attribution License (CC BY 4.0).*

3.6.1 Instrumentation

The same Potter homogenizer and refrigerated centrifuge listed for DC isolation in section 3.5.1 was used. A MidiMACS™ magnetic separator and MACS MultiStand (#130-094-872) was purchased from Miltenyi Biotec (DEU) for performing magnetic separation.

3.6.2 Established and standardized MACS methodology

Sub-cellular fractions were prepared at 4°C using the MACS Mitochondria Extraction Kit for mouse tissue (#130-096-946, Miltenyi Biotec, DEU) with slight variations to manufacturer instructions (Hornig-Do *et al.*, 2009). Obtained quadricep or brain tissue, cut finely using sterile scalpel blades while kept on ice (Section 3.2.4.), was weighed off for homogenization. From the

100 mg brain isolates (or 150 mg quadriceps muscle), a 10% (or 15%) w/v tissue lysate was prepared in 1 mL ice-cold lysis buffer, supplied with the kit. While the exact constituency of the buffer is unknown, the prototypic publication of the kit (Hornig-Do *et al.*, 2009) lists the initial makeup thereof as phosphate-buffered saline (PBS) containing a standard protease inhibitor cocktail. Our own NMR analyses thereof confirm the presence of ethanol and glycerol (37 µM). Regardless, this buffer presents an isotonic isolation environment adequate for mitochondrial isolation. Brief centrifugation at 1,300 x*g* (2 minutes) followed, to remove nuclei and large debris, producing 750 – 950 µL supernatant. The post-nuclear supernatant was diluted 10x (v/v) in 1x MACS separation buffer (SB), preceding magnetic enrichment. Hornig-Do *et al.* (2009) states their prototype of the SB as PBS (adjusted to pH 7.2), containing 2 mM EDTA and 0.5% bovine serum albumen (BSA), while in-house NMR analyses confirmed the presence of protein, and 4 mM EDTA. It is suspected that this buffer is also modelled after similar sugar-free buffers as utilized by Corcelli *et al.* (2010) and Pan *et al.* (2018), maintaining isotonicity and mitochondrial membrane stability throughout.

Mitochondria were labelled with anti-TOM22 Microbeads (1.5 µL/mg brain tissue; 0.5 µL/mg tissue for quadriceps muscle) for 1 hour at 4°C, with continuous agitation applied by a platform shaker at 30 rotations/minute (rpm). This defining step of the methodology utilizes recombinant antibodies specific to a translocase of the outer mitochondrial membrane (TOM-22) conjugated to paramagnetic beads, which become magnetized following exposure to a strong magnetic field. After preparing the column by applying 3 mL 1x SB, the suspension was loaded onto a MACS LS (LS-M) column, containing similar paramagnetic beads, which amplify magnetic forces. This was placed in a MACS Separator setup, in a cold room, maintained at 4 °C, supplying the magnetic field that retains the anti-TOM22 Microbeads, with the immunologically bound mitochondria. Up to 3 mL could be applied at a time, flowing through the column while immunoprecipitated mitochondria become magnetically entangled in the mesh of beads.

The flow-through from the column was regarded as a crude cytoplasmic fraction. 2.5 mL thereof was subjected to centrifugal filtering through pre-rinsed Centrisart® 100 kDa centrifugal cut-off filters, identical to the above-mentioned method for preparing DC cytosolic fractions. Labelled mitochondria were eluted from the LS-M column in 1x SB after three successive wash steps to remove any further impurities by running 3 mL 1x SB through the column. Removal from the magnet, addition of 1.5 mL 1x SB and a firm ejection of content using the supplied column plunger, constituted the elution process, which was repeated thrice for each sample. The eluates (4.5 mL total) were split to 3 separate microcentrifuge tubes and centrifuged at 13,000 x*g* for 2 minutes (4 °C), the supernatant discarded, and the EMF stored at -80°C. Before further analysis, the antibody-conjugated mitochondrial pellets were combined and resuspended in a

final volume of 120 µL solvent (MACS storage buffer for Seahorse respirometry, KCIEM for spectrophotometric comparison, Milli-Q water for protein blotting or water containing the selected internal standards for metabolomics, as stated in section 3.9). The isolation procedure took approximately 90 minutes from tissue homogenization to mitochondrial elution.

In phase A, fractions obtained between every successive step were sampled to track mitochondrial enrichment/loss in every subsequent step. Aliquots of the homogenate (50 µL), post-nuclear supernatant (PNS; 50 µL), diluted and antibody-labelled PNS (Label mix; 250 µL), LS column flow-through (Cr. Cyto; 1,000 µL), crude mitochondrial eluate (CR. Mito), post-mitochondrial centrifugal supernatant (Mito SN; 1,000 µL) and filtered cytoplasm (Filt. Cyto; 300 µL) were taken for these tests, along with the resuspended EMF (120 µL).

3.7 Comparison of analytical efficiency

3.7.1 BCA Protein quantification

A prerequisite to obtaining comparable enzyme activity results or protein enrichment during western blotting, is normalization to tissue mass (i.e., µg protein or homogenate volume, given that a consistent mass-to-volume ratio is used during homogenization). Therefore, the total protein content of the mitochondrial and cytosolic fractions was quantified using the bicinchoninic acid (BCA) assay, first described by Smith *et al.* (1985) as standardized at the Mitochondria Research Laboratory (NWU). This was done following DC or MACS isolation, as a prerequisite test for CS assay and WB normalization. The BCA assay involves two distinct reactions that include the reduction of cupric ions (Cu^{2+}) to Cu^{+} by the protein peptide bonds. During this (biuret) reaction, the product Cu^{+} ions are produced relative to the amount of peptide bonds (thus protein) in a sample, to chelate with BCA molecules in a 1:2 ratio. A purple complex is produced, with a strong absorbance maximum at 562 nm. Therefore, the measured absorbance is directly proportional to the protein content of the sample (Smith *et al.*, 1985).

3.7.1.1 Instrumentation and software

For this spectrophotometric assay, a Synergy™ HT Multi-detection microplate reader (Biotek® Instruments), and Gen5™ Data Analysis software (v 1.11.5) was used.

3.7.1.2 Methodology

The BCA assay was performed according to the kit manufacturer's instructions in a 96-well UV microtiter plate with a final reaction volume of 220 µL per well. First, duplicate reactions of a bovine serum albumin (BSA) protein standard dilution series (0 µg to 20 µg) were plated in increments of 4 µg. Thereafter, the samples were added in triplicate to the appropriate wells,

with volumes determined to be efficient for each specific fraction (0.5 µL for homogenate, PNS or EMF; 3 µL for Cr. Cyto and MACS Cr. Mito or Mito SN; 10 µL for Filt. Cyto). After being topped up to a final volume of 20 µL with Milli-Q® H_2O, the biuret reaction was initiated by adding 200 µL BCA reagent [1:50 ratio of copper(II)sulphate ($CuSO_4.5H_2O$) to BCA] to each well and incubating the plate (37 °C, 30 minutes) until reaction endpoints were reached. Thereafter, the absorbance was measured at 562 nm and the protein content (µg) per well was determined from the BSA standard curve ($R^2 > 0.99$) via least mean-squares linear regression. Finally, the protein concentration [Prot] in µg/µL was calculated (as shown in Equation 3-1) by dividing the protein content measured (P_M) by the effective sample volume per well (V_{eff}).

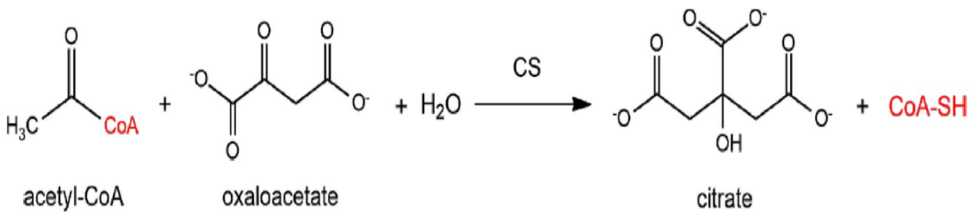
Equation 3-1: Determining protein concentration from BCA output.

$$[Prot] = \frac{P_M}{V_{eff}}$$

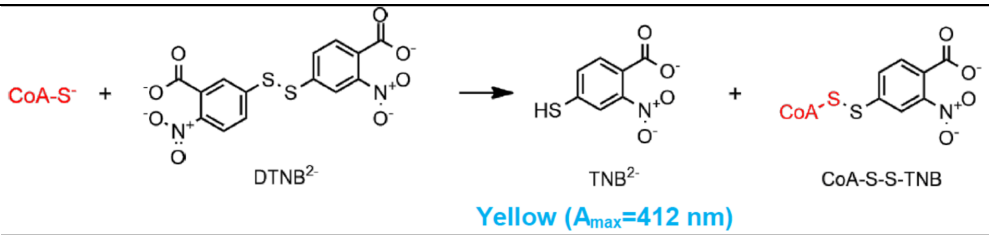
3.7.2 Yield interrogation via CS recovery

Citrate synthase (EC 2.3.3.1) is commonly used as a quantitative mitochondrial marker, as the catalytically active form is exclusive to the mitochondrial matrix. Therefore, the activity of this enzyme was measured and quantified as an indicator of mitochondrial mass/content. During initial optimizations, a small aliquot of each DC or FMMS sample and intermediary fraction was set aside after subsequent steps for CS assays according to established protocols (Shepherd & Garland, 1969). The assay involves two coupled reactions, which include the CS catalysed production of free CoA-SH from the condensation of oxaloacetate with acetyl-coenzyme A (acetyl-CoA) (Reaction 3-1), and the secondary detection of CoA-SH sulfhydryl groups via reaction with DNTB (2,2'-dinitro-5,5'-dithiobenzoic acid) yielding the yellow-coloured product, TNB (2-nitro-5-thiobenzoic acid) (Reaction 3.2), with absorbance maximum at 412 nm.

Reaction 3-1: CoA formation by CS catalysis.



Reaction 3-2: TNB formation from CoA-SH and DTNB.



3.7.2.1 Instrumentation and Software

For CS assays, absorbance was measured by the Synergy™ HT Multi-detection microplate reader (Biotek Instruments), quantified by Gen5™ Data analysis software (Biotek Instruments) and processed in Microsoft Excel (2016).

3.7.2.2 Methodology

The assay was performed at 30 °C with triplicate reactions for each sample in a 96-well UV microtiter, at a final reaction volume of 200 µL per well. A CS master mixture was prepared, consisting of 60 µM acetyl-CoA, 0,1 mM 2,2'-dinitro-5,5'-dithiobenzoic acid (DTNB) and 0,04 % (v/v) Triton™X-100, while 5 mM oxaloacetate was preheated to 33 °C in a water bath. Samples were added in appropriate volumes to each well; 0,5 µL (as 10 µL of a 1:20 dilution in Milli-Q water) for the homogenate, PNS and EMF's, 5 µL (topped to 10 µL with Milli-Q water) or 10 µL (all other fractions). The prepared master mix was added (140 µL) to each well and the plate incubated for 10 minutes at 30 °C. The pre-heated oxaloacetate (50 µL)was immediately and simultaneously added to all wells to initiate the reaction, producing Ac-CoA that reacts stoichiometrically with DTNB to produce the measured TNB chromophore.

TNB was kinetically measured at 412 nm in 1-minute intervals for 5 minutes to produce a pseudo-first order reaction velocity. As this velocity should remain constant if substrate levels do not become depleted, a mean velocity (V_{Mean}) is automatically calculated by the software from the linear slope produced between 3 or more successive measurements, the only variable differing between successive samples being the amount of active enzyme units present.

3.7.2.3 Data analysis and processing

All fraction activities were normalized to their respective volumes (µmol/minute/µL), as standardizing tests revealed that the amount of protein added by the MACS buffers and the immunoglobulins in the microbeads cannot be consistently accounted for by BCA, thus inferring differential amounts of exogenous protein in each successive sample. Since these samples (DC and MACS) were all fractionations of the same original homogenate dilution, measured concomitantly in one plate, this relative units of citrate synthase (UCS) expression (rUCS) was deemed an adequate normalization for relative expressions of enzyme enrichment.

Using the molar extinction coefficient for TNB absorbance in a 200 µL reaction (ε = 7465 mAbs/mM, as previously determined by several analyses of substrate standard series under the given reaction conditions), these normalized activities could be converted to an expression of

enzyme unit abundance (Equation 3-2). For determining fraction enrichment, this value for each DC or MACS fraction is expressed as a percentage of that measured in the homogenate preceding both methods (Equation 3-3).

Equation 3-2: Calculating normalized CS activity.	$$UCS = \frac{V_{Mean}}{\varepsilon \,.\, V_{Load}} \,.\, V_{Total}$$
Equation 3-3: Calculating CS enrichment (yield).	$$\%Yield = \frac{UCS}{UCS_{Homog}} \,.\, 100$$

3.7.3 Confirmation of MACS purity via Western blot

Western blotting (WB) serves as a means of investigating the purity of the final fractions as the presence/depletion of compartment-specific proteins. This technique was, therefore, utilized to quantify the relative depletion of lysosome content (lysosome-associated membrane protein; LAMP-2B) from the mitochondrial fractions produced by DC and MACS, and similarly the efficient depletion of residual mitochondrial matrix content (heat-shock protein; Hsp60) from the final cytosolic fractions. Samples from the homogenate were used as a positive control for comparing protein enrichment/depletion. Standard protocols for SDS-PAGE (sodium dodecylsulphate polyacrylamide gel electrophoresis) and WB of the NWU Mitochondrial Research Laboratory, as adapted by Mereis (2017), were applied. Minor modifications were introduced, pertaining to protein extraction and specific optimal reaction conditions for each antibody.

3.7.3.1 Instrumentation and software

For SDS-PAGE and Western blotting, the T100 Thermocycler (#186-1096, Bio-Rad, ZAF), Heraeus™ Multifuge™ X3R Centrifuge (#75004516, Thermo Scientific, USA), Soniprep™ 150 Ultrasonicator (#687, MSE, FRA), Savant ISS110 SpeedVac™ concentrator (#12612735, Thermo Scientific, USA), Mini-PROTEAN® Tetra cell kit (#16584, Bio-Rad, ZAF), TransBlot® Turbo blotting system (#1704155, Bio-Rad, ZAF), ChemiDoc™ MP Imaging system (#170-8280, Bio-Rad, ZAF) and ImageLab (v.5.2.1) imaging software (Bio-Rad, ZAF) was used. All chemicals and reagents are listed in full detail in Annexure A.

3.7.3.2 Fraction-specific sample preparation

Enriched mitochondria and filtered cytosol fractions were prepared for SDS-PAGE as first described by Laemmli (1970). Preliminary trials emphasized the necessity of thorough organelle disruption, protein release and centrifugal removal of antibody containing OMM debris to obtain viable and repeatable electrophoresis results. Therefore, mitochondrial and homogenate samples to be used for blotting underwent three cycles of rapid freeze-thawing via liquid nitrogen – interjected by vortex mixing at maximum speed and rough pipette mixing. Sonication for 30 seconds at high power using a clean pipette tip over the sonication needle for each sample followed to ensure thorough shearing of all membranes. The filtered cyto samples were voided of any molecules > 100 kDa, the protein content of each sample was more than an order of magnitude too low (< 0,2 µg/µL, determined by BCA) to obtain a per-well protein content (10-20 µg) on the gel within the limits of detection for the given blotting and imaging protocol. For that reason, filtered cytosol samples were first concentrated 10x on a SpeedVac sample concentrator at low dry rate and room temperature (3 hours).

Samples containing 15 µg total protein (12 µg for cyto samples) were thereafter prepared for SDS-PAGE, according to the strategy first developed by Laemmli (1970). Fraction samples were incubated in 4x Laemmli buffer (#161-0747, Bio-Rad, ZAF) containing 5% [v/v] 2-mercaptoethanol for 5 minutes at 100 °C. The sulphur group of 2-mercaptoethanol reduces inter-peptide disulphide bonds, while the LDS (a similar detergent to SDS, conjugated to a lithium cation) in the Laemmli buffer binds to hydrophilic amino acid sidechains, linearizing and denaturizing the proteins. All samples were briefly centrifuged at 16,000 x*g* (2 minutes) to pellet any remaining membrane debris and antibody beads, and the supernatant carefully removed for SDS-PAGE.

3.7.3.3 SDS-PAGE separation

Sample proteins were separated in TGX Stain-Free™ FastCast™ Acrylamide gels before being transferred to 0.2 µm Mini-format polyvinylidene difluoride (PVDF) membranes. For that purpose, a 1 mm SDS-PAGE gel (consisting of a 10% resolving gel with a 2-3 cm 4% stacking gel cast on top) was prepared in 1x Tris/Glycine/SDS buffer and left to set (45 minutes) in the Mini-PROTEAN® Tetra Cell setup. Samples were then added to the relevant wells of the SDS-PAGE gel, at 25 µL volumes. Mitochondrial samples were grouped on one side, while the cytosolic samples were applied to the opposing side of the same gel. Additionally, 20 µL of a molecular weight marker [containing 9.6% (v/v) Precision Plus Protein™ WesternC™ Blotting Standard, 1x Laemmli sample buffer and Milli-Q® H_2O] was loaded on both sides of the samples and the gel was run at 300 V (22 min). As the LDS remains in its anionic form when

bound to the protein, the Laemmli buffer thus also conferred each polypeptide with a negative charge. They then migrate towards the anode, while separating by virtue of their molecular mass. The gel was run until the electrophoretic dye front (indicated by bromophenol blue) had reached 1 cm from the bottom of the glass plates.

3.7.3.4 Blotting and imaging

The separated proteins were then transferred to a 0.2 µm PVDF membrane for 30 minutes by using the Trans-Blot® Turbo™ Blotting System. During this procedure, a 25 V current was passed at right angles to the gel, causing the protein bands in the gel to migrate towards the anode and onto the membrane. This blot was imaged using the ChemiDoc™ MP system to indicate total transferred protein content per well as normalization factor for the quantified target proteins. The blots were halved between the mito and cyto sample lanes, all blocking and wash steps to follow were performed applying constant agitation on a platform shaker. Every succeeding step was followed by washing the blot three times, for 5 minutes each in 1x TBS + 1% (w/v) casein and 0.1% (v/v) Tween®20 (TBS/T). Protein blots were blocked in TBS/T for 1.5 hours to cover up the remaining hydrophobic sites on the PVDF membrane and prevent unwanted protein binding. Thereafter, they were incubated overnight at 4 °C and constant shaking in the indicated primary antibody combination (all raised in rabbits) for each blot half. For the mitochondrial fractions, LAMP-2B/C (1:1,000) and β-Actin (1:4,000) as loading control was diluted in 10 mL TBS/T. Similarly, for the blot half containing cyto fractions, Hsp60 (1:10,000) and β-Actin (1:4,000) was prepared. Although β-Actin is generally considered a cytosolic protein marker, sufficient evidence exists that it also serves as structural protein in the mitochondria (Reyes *et al.*, 2011; Xie *et al.*, 2018), supporting its application as a loading control for both fractions.

On the following day, the blot halves were incubated for 1.5 hours in TBS/T containing the secondary antibody directed against the primary antibodies (at a 1:10,000 dilution; 1:1,000 for cyto samples). A goat polyclonal horse radish peroxidase (HRP)-conjugated antibody, reactive to rabbit IgG, was used. Following a final wash in 1x TBS for 5 minutes to remove the Tween®20, blot halves were individually covered by chemiluminescence (ECL) Substrate and imaged. The ECL contains a 1:1 solution of H_2O_2 and luminol/enhancer. During this reaction, the HRP enzyme oxidises luminol in the presence of its substrate, H_2O_2, to produce light, while the enhancer serves to increase the longevity and intensity of the emission. Following 1 minute of incubation, the blot was photographed using the ChemiDoc™ MP system and Image Lab software (v5.2.1). A Chemi Hi-Resolution protocol was set up, and the image was obtained using signal accumulation mode (SAM) for 3 minutes.

Band intensities of the loading controls were compared to validate equal protein transfer. Target protein band intensities were normalized to total protein content for each lane, as obtained from the unstained blot, in ImageLab (v 5.2.1). For mitochondrial LAMP-2 bands, this normalized value was expressed as a percentage of the LAMP-2 intensity in the control lane correlating to the homogenate. Cytosolic Hsp-60 results were also expressed as such.

3.7.4 Probing mitochondrial integrity by respiratory coupling via Seahorse respirometry

Mitochondria were isolated by both DC and MACS methods from the same split homogenate as detailed in Sections 3.5 and 3.6 on the day of analysis, only interjected by CS assay of the EMFs as a condition for effective sample dilution and comparison. The Seahorse XF^e96 Extracellular Flux Analyzer and XF^e96 Flux Assay Kit was used to measure oxygen consumption rates (OCR) of these mitochondria, using previous methods with slight modifications (Aucamp *et al.*, 2017; Hubbard *et al.*, 2019). A manufacturer provided "coupling assay" (www.Seahorsebio.com/resources/tech-writing/iso-mito-xf96.pdf) evaluates coupling between O_2 consumption and ATP phosphorylation in the OXPHOS system, and expresses mitochondrial function as the respiratory steady-states defined by Chance and Williams (1955).

A typical Seahorse respiratory coupling assay (Figure 3-4) starts with measuring basal respiration (BR), being the rate of O_2 consumption in the presence of substrates only. This is achieved by specific oxygen-reactive, fluorometric probes dotted on every stylus of the sensor cartridge to be inserted in a single well during analysis, which gives real-time feedback on O_2 depletion and thus respiration. Other respiratory states are then successively measured as compounds are injected in a specific order: 1) ADP to initiate state 3_{ADP} (maximal phosphorylating respiration), 2) ATP synthase inhibitor (oligomycin) to initiate state 4_o (non-phosphorylating basal respiration), 3) uncoupler (carbonyl cyanide-p-trifluoro-methoxyphenyl hydrazine; FCCP) to initiate State 3_u (maximal non-phosphorylating respiration) and 4) ETC complex inhibitors (antimycin A and rotenone) to allow non-mitochondrial (NM) respiration to be measured. The latter constitutes residual oxygen consumption after complete inhibition of the ETC by high-affinity inhibitors (Brand & Nicholls, 2011) and is subtracted from all rates to reflect only mitochondrial respiration.

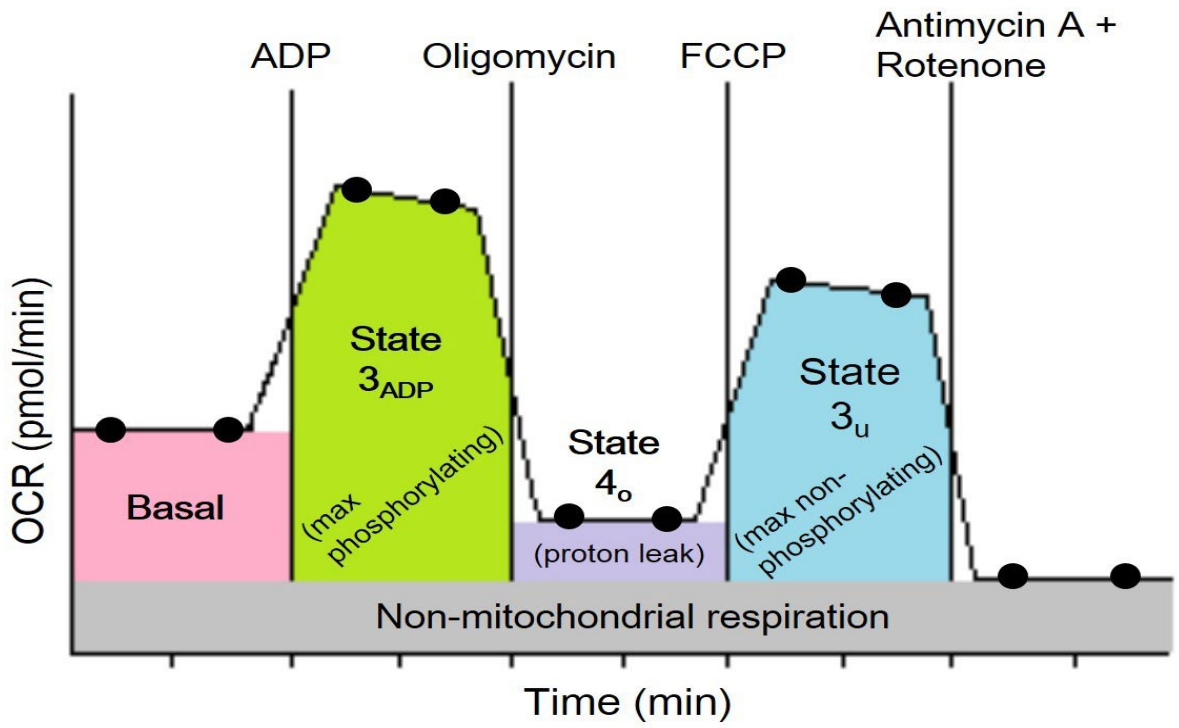


Figure 3-4: Typical OCR vs time graph obtained from XFe96 coupling assay summarizing the different respiratory states measured after each subsequent compound injection. Dots on the graph represent duplicate measurements of oxygen consumption rate (OCR, pmol/minute) *versus* time of measurement before each subsequent injection.

The respiratory control ratio (RCR), defined as state 3-ADP divided by state 4o, indicates the tightness of mitochondrial coupling; that is, how tightly electron transport and oxygen consumption are controlled by phosphorylation occurring at ATP synthase (Bhaskaran *et al.*, 2018; Brand & Nicholls, 2011). A disrupted IMM will dissipate the proton gradient required to drive this coupling and significantly lower the RCR. Similarly, higher RCR values suggest a greater ability of mitochondria to oxidize substrates, a greater ATP turnover capacity and/or a lower proton leak (i.e., a more intact IMM). Given the absence of biological variation, as all samples are diluted from the same homogenate in similar buffer environments, this value thus comments specifically on differential membrane coupling and IMM integrity between DC or MACS samples (Hubbard *et al.*, 2019). RCRs are used in a relative context since absolute values vary with substrates and tissues.

3.7.4.1 Instrumentation and software

The Heraeus™ Multifuge™ X3R Centrifuge, Seahorse XF^{e}96 Analyzer (Agilent Technologies, USA) and XF^{e} Wave Desktop V2.2 software (Seahorse Bioscience, USA) was used.

3.7.4.2 Protocol

Mitochondrial assay buffer was prepared beforehand (MAS; 105 mM sucrose 330 mM mannitol, 15 mM KH_2PO_4, 7,5 mM $MgCl_2$, 3 mM HEPES, 1,5 mM EGTA, 0,3% (w/v) BSA. Stocks of 100 mM were prepared in water for succinate, malate and glutamate, respectively. Stocks (2.5 mM) of FCCP, rotenone, oligomycin and antimycin A were prepared in dimethyl sulfoxide (DMSO). The pH of stocks and buffers were adjusted to 7.2 at 37°C with KOH, aliquoted and stored (-20°C). The sensor cartridge was hydrated overnight at 37 °C according to manufacturer instructions. On the day of analysis, 100 mM pyruvate and 250 mM ADP stocks were prepared fresh and pH adjusted to 7.2 as described above. Before loading, the injection stocks were diluted appropriately in MAS (already containing 10mM pyruvate or 5 mM malate, adjusted to pH 7.2) and 25 µL loaded in each injection port to achieve final concentrations of 6 mM ADP (Port A), 4 µM oligomycin A (Port B), 4 µM FCCP (Port C) and 3 µM rotenone/6 mM Antimycin A (Port D) in each respiration chamber.

Freshly prepared DC or MACS mitochondria were diluted in MAS based on their respective, pre-determined CS activities (Section 3.7.2). Eight 25 µL replicates for each dilution range (2-8 nmol/minute/µL CS activity) was loaded in each well of a Seahorse Standard $X^{Fe}96$ assay plate, kept on ice throughout. Four background correction wells were left open at each corner of the plate. The assay plates were centrifuged at 2,000 x*g* for 20 minutes at 4°C to adhere the mitochondria to the bottom of the wells. During this time, the sensor cartridge was placed into the Seahorse XF^e96 Flux Analyzer for automated calibration. After centrifugation, 150 µL of MAS (pre-incubated in a water bath to 37°C) was added to obtain a final volume of 175 µL per well and the loaded assay plate inserted for analysis. A pre-programmed mix-and-measure protocol, described by Rogers *et al.* (2011), was run at 37°C. This involved cyclic steps of mixing, sequential injections of substrates and inhibitors via Ports A through D, equilibration and duplicate measurements of the oxygen consumption rate (OCR) after each injection.

The XFe96 Wave software automatically applies the AKOS algorithm, described by Gerencser *et al.* (2009), to correct for oxygen diffusion and background noise and to calculate OCRs. Raw kinetic data was visualised as OCR values (pmol/minute/well) at the relevant time points during the study, correlating to the successive injections, for each well.

3.7.4.3 Data analysis

Respiratory rates were calculated by using the first measurement after injection for BR, state 3_{ADP} and state 3_u while the last measurement was used for state 4_o and non-mitochondrial respiration to ensure maximal inhibition. Untrustworthy measurements were firstly identified and

removed using Tukey's test for outliers (data points falling outside 1.5 interquartile ranges below the 25th percentile or above the 75th percentile for the given measurement). Non-mitochondrial respiration for each well was subtracted from all values before further processing. Mean respiratory rates of the eight replicates ± standard deviation (SD) was calculated at each timepoint to comment on the reliability of measurement. In the cleaned data set, respiratory control ratios (RCR) were calculated by dividing the baseline-corrected OCR obtained from State 3_{ADP} by the similarly corrected OCR values obtained during State 4_o measurement. Thereafter, the average and measurement precision (%CV) was calculated for each well, and expressed as the average RCR for each of the DC/MACS dilution levels investigated.

3.8 *Ndufs4* KO Metabolomics workflow overview

In the following section, instrumentation and methodologies for the GC-TOF-MS, ^{1}H-NMR and LC-MS/MS analyses applied to the pilot and final mitochondrial and cytosolic samples, are described. A full detailed list of chemicals and reagents used is to be found in Annex A. While these applied parameters are widely the same for all analyses, minor alterations in sample preparation and data processing differentiate the final methodologies of the standard trial WT mice and final comparison of *Ndufs4* KO and WT compartment metabolomics. In that regard, the global methodology will be detailed for each platform, respectively, where sample specific variations in protocol are stipulated at each relevant section. As the analyses of pure chemical reference standards in MACS buffer environment and distilled water published under authorship of the candidate in Paper 1 already form part of two NWU dissertations (Du Plessis, 2019; Willemse, 2019), the methods used are briefly described at the end of the section.

Given the limited amount of sample available (120 µL mitochondrial and ~300 µL cytosolic), a workflow was designed to partition these samples to the three different metabolomic platforms utilized, as to gain the maximum information from these small volumes. Figure 3-5 depicts the workflow for mitochondrial samples, while the methodology adapted for cytosolic extracts differs only in allocated volumes and internal standard composition. Samples analyzed by ^{1}H-NMR (which is inherently non-destructive with minimal alteration) were thus recollected post-analysis for subsequent LC-MS/MS amino acid and acylcarnitine profiling, while 55 µL of sample was stored for future GC-MS organic acid profiling (outside the scope of this study).

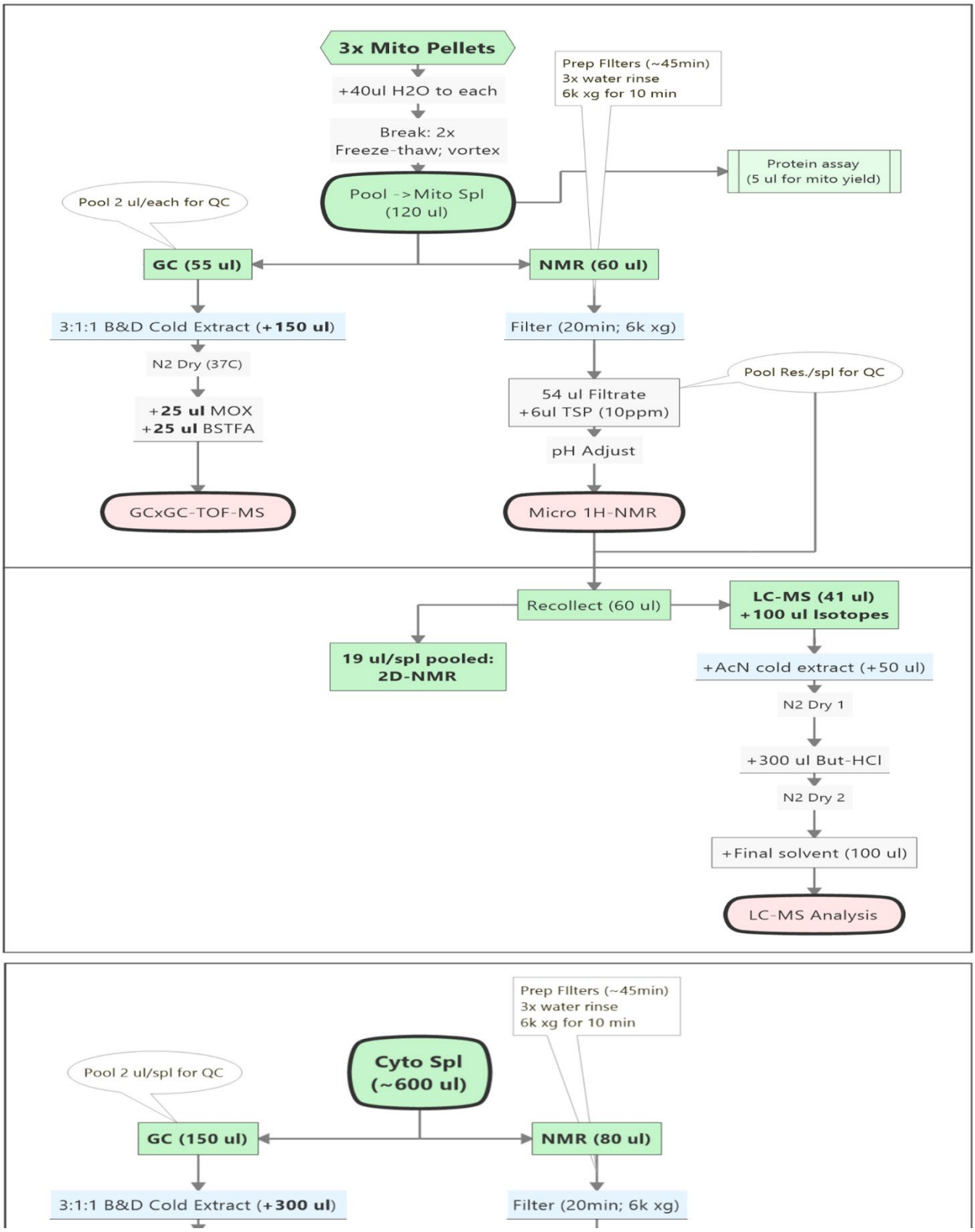


Figure 3-5: Final multi-platform metabolomic workflow for mitochondrial isolates and cytosolic filtrates indicating the fraction preparation as in section 3.6.2., sample volume allocation to each platform and a summary of the preparative process. Only the first part of the cytosolic workflow is shown, as the following steps are identical to that shown for the mitochondrial workflow. B&D: Bligh & Dyer metabolite extraction, But-HCL: Butanolic hydrochloric acid, MOX: Methoxamine-HCL, BSTFA: N,O-bis-trimethylsilyl trifluoroacetamide, TSP: trimethylsilyl propionic acid.

3.8.1 Internal standard preparation and addition prior to all analyses

In metabolomics, pure chemical reference compounds known as internal standards (IS) are typically added to each biological sample during metabolome extraction to account for biases (Type A) that arise during the metabolite extraction, derivatization and analysis process. Several internal standards were tested for applicability to GC-TOF-MS and ^{1}H-NMR analyses in the highly buffered MACS environment. As no single compound served as an acceptable IS in this environment for all three platforms (Section 4.3.2), a mixture of those serving best for each respective platform was added to each entire sample prior to aliquoting for each separate leg of analyses shown in Figure 3.5. 3-Phenylbutyric acid (3-PBA) was added, as a historically effective internal standard for GC-TOF-MS. N,N-dimethylphenylalanine (DMPA) was selected for the ^{1}H-NMR and LC-MS/MS portion of the workflow, because it has been shown to be effective as an IS for these platforms (Mason *et al.*, 2018; Terburgh *et al.*, 2019).

Separate DMPA and 3-PBA stock solutions (2,000 ppm) were prepared by dissolving 20 mg of the selected pure salt in 10 mL Milli-Q H_2O. The final internal standard mixture was prepared in 2 mL Milli-Q H_2O (containing both 735 ppm DMPA and 3-PBA) and added in a fixed volume specific to either sample matrix, allowing analysis of equivalent final IS concentrations across all samples for a given platform (Table 3.2). These dilutions were calculated to give a final concentration of 35 ng/µL DMPA analyzed in all ^{1}H-NMR samples, while resulting in 32 ng DMPA on-column for all LC samples, and 46 ng 3-PBA in GC samples. This was achieved through adding the needed amount of IS mixture (5.0 µL) to each thawed cytosolic sample on the day of analyses, before splitting the sample volume for ^{1}H-NMR and GC-TOF-MS analyses. In the mitochondrial samples, this was achieved by adding the IS mixture (5.7 µL / 120 µL) to the water used for resuspending the post-MACS mitochondrial pellets (refer to section 3.6.2).

Table 3-2 : IS details and analyzed amounts across all samples and platforms

Analytical platform	Sample matrix	Total sample volume analyzed (ul)	IS added (ul)	[IS] Analyzed (ppm)	Mass IS (ng) on-column
GC-MS (3-PBA)	Cyto	150	5	46	46
	Mito	55	5.7	46	46
NMR (DMPA)	Cyto	100	5	35	N/A
	Mito	60	5.7	35	N/A
LC-MS/MS (DMPA)	Cyto	41	-	13	32
	Mito	41	-	13	32

3.9 GC-TOF-MS analyses

The untargeted gas chromatography time-of-flight mass spectrometry (GC-TOF-MS) techniques used were initially described by Lindeque *et al.* (2013), having recently been adapted for *Ndufs4* KO muscle tissue (Terburgh *et al.*, 2019).

3.9.1 Instrumentation and Software

Heraeus™ Multifuge™ X3 centrifuge (Thermo Fisher Scientific, USA), Dri-Block® heater and sample concentrators from Techne® (GBR). The GC-TOF-MS system consisted of an Agilent© (USA) 7890A series gas chromatograph with Agilent© 7693 autosampler, coupled to a LECO (USA) Pegasus HT time-of-flight (TOF) mass analyzer with an electron impact (EI) ionization source. ChromaTOF® software (v 4.5x, LECO, USA) was used for data acquisition and extraction. Spectral matching was done using the NIST11 commercial library and an in-house mass spectral library to identify the measured compounds.

3.9.2 Sample preparation

Sub-cellular fractions were thawed and diluted as per section 3.6.2. A derivation of the Bligh–Dyer metabolite extraction method (Gullberg *et al.*, 2004) was applied, utilizing a monophasic mixture of methanol, water and chloroform (3:1:1), as described by Wu *et al.* (2008). This adjusted solvent ratio allows for rapid, repeatable extraction of both hydrophilic and lipophilic compounds in a single phase. Additionally, the cold methanol within the buffer effectively reduces the solubility of proteins to aid sample deproteinization, as whole polypeptides can severely interfere with analyses or even damage the installed capillary column. The standard compounds utilized for buffer testing, as well as the sub-cellular isolates, were diluted in a pre-made mixture of the Bligh-Dyer solvent (200 µL).

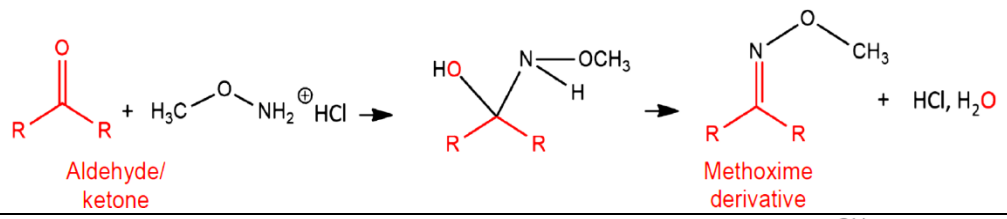
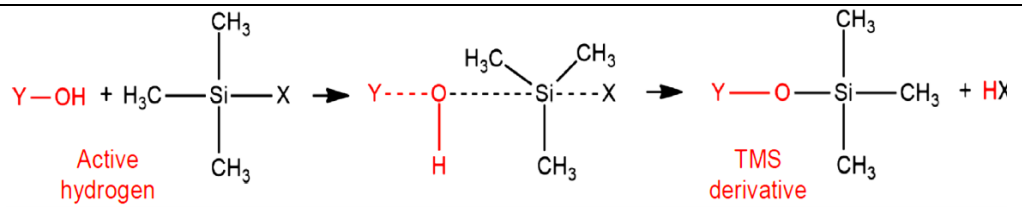
Mitochondrial and cytosolic isolates were aliquoted in equivalent amounts for GC-TOF-MS and NMR; hence, 55 µL of the 120 µL total EMF for each tissue sample was used for GC-MS, along with 150 µL of the accompanying filtered cytosol. To these samples, the allotted amount of extraction solvent (150 µL or 300 µL for mitochondria and cytosolic samples, respectively) was added, the mixture rigorously vortexed (1 minute) and incubated on ice (10 minutes) to aid protein precipitation. All samples were then centrifuged at 20,000 x*g* (10 minutes; 4 °C) to sediment the insoluble proteins, while the metabolite containing supernatants were transferred to 2 mL glass microvials (Agilent©, USA).

3.9.2.1 Quality control samples

For each separate analyses, quality control (QC) samples were included into all sample batches to monitor metabolomic data integrity. These were prepared by pooling a small volume of all mitochondrial (or cytosolic) samples. The QC samples were then aliquoted, stored (−80 °C) and prepared in the same manner as the other samples. The purpose of the QC samples is to indicate inter- and intra-day variations in machine response (Broadhurst *et al.*, 2018).

3.9.2.2 Derivatization

All samples were subjected to drying under nitrogen gas stream (37 °C) to remove water molecules that severely interfere with derivatization. The purpose of the derivatization steps is to shield off the polar groups of metabolites with large inert groups to increase their volatility and thermal stability. This aids in obtaining more reproducible chromatographic results (by improving peak shape and separation) but also assists in compound identification via existing spectral libraries (Dunn *et al.*, 2013). Derivatization was achieved via a two-step reaction; oximation and silylation. Oximation adds methoxamine groups to aldehyde and ketone functional groups (Reaction 3-3), breaking the CO-double bond, which prevents keto-enol tautomerization and the formation of multiple peaks for a single compound. Silylation adds trimethylsilyl (TMS) groups from N,O-bis(trimethylsilyl) trifluoroacetamide (BSTFA) to polar moieties containing active hydrogens (e.g. -COOH, -OH, -NH, and -SH), resulting in volatile metabolite-TMS-ethers, -esters, -amines or –sulphides (Reaction 3-4).

Reaction 3-3: Oximation of ketone groups by methoxamine-HCl	
Reaction 3-4: Silylation of active hydrogen groups by BSTFA	

Derivatization reagents were prepared freshly on the day of the analysis. To oximate the samples, a 20 mg/mL solution of methoxyamine hydrochloride in pyridine (EMF: 25 µL ; 50 µL for all other samples) was added and the samples were vortex mixed (1 minute) to dissolve and oximate the dried compounds. The samples were incubated at 60 ºC for 1 hour. Thereafter, BSTFA (EMF: 25 µL; 50 µL for all other samples) already containing 1 % (v/v)

trimethylchlorosilane (TMCS; catalyst for silylation reaction) was added and incubated at 60 ºC for 1 hour. The final sample volume (50 or 100 µL) was then transferred to 250 µL pulled point glass inserts, placed back in the vial and capped tightly. Finally, each vial was loaded onto an Agilent© 7693 autosampler for GC-TOF-MS analysis.

3.9.3 Analysis parameters

All sample batches were randomized prior to analysis. QC samples were analyzed in the beginning, after every 10 samples, and at the end of each batch. The GC-TOF-MS protocol described by Lindeque *et al.* (2013) was slightly modified for this study. Chromatographic separation was done with an RTX-5MS column (Restek, 30 m x 0.25 mm x 0.25 µm), utilizing an apolar, fused silica solid phase. Derivatized samples (1 µL) were injected in splitless mode (purge hold 30 seconds) and the inlet temperature set at 250 °C throughout the entire run. A splitless, single-taper, deactivated FocusLiner® with glass wool (Phenomenex, outside Ø 6.3 mm, inside Ø 4.0 mm, length 78.5 mm) was used. The initial GC oven temperature was held at 70 ˚C for 1 minute. Thereafter, the oven temperature was increased by 7 °C/minute to 120 °C, then by 10 °C/minute to 230 °C and finally by 13 °C/minute to 300 °C where the temperature was held for 1 minute before cooling to 70 °C in a total run time of ~ 25.5 minutes. Helium was used as carrier gas, with a pressure-programmed constant flow rate of 1.5 mL /minute. Transfer line and ion source temperatures were held throughout at 225 °C and 200 °C, respectively. Universal EI (electron impact ionization) settings were used for fragmenting compounds prior to spectral collection, while the detector was operated at 50 V above tune voltage. After an acquisition (solvent) delay of 330 seconds, data were acquired at a rate of 20 spectra/second using a mass-to-charge (m/z) ratio range of 50–900 amu. Peaks with 5 apexing masses were detected using an expected peak width of 3 seconds and a signal-to-noise (S/N) ratio of > 20.

3.10 ^{1}H-NMR analyses

Untargeted measurement of sub-cellular fractions obtained from brain and quadricep tissues of *Ndufs4* KO and WT mice were performed according to a recent miniaturized ^{1}H-NMR spectroscopy protocol applicable to mouse models of MD (Mason *et al.*, 2018; Terburgh *et al.*, 2019). This method has been proven in limited volume samples down to 60 µL with sufficient statistical method equivalency to the standard methodology.

3.10.1 Instrumentation and Software

NMR measurements were conducted at 500 MHz on a Bruker (DEU) Avance III HD NMR spectrometer equipped with a SampleXpress autosampler and 5 mm triple resonance inverse (TXI; ^{1}H, ^{15}N, ^{13}C) probe head optimized for ^{1}H observation. Bruker Topspin (V3.5) and AMIX

(V3.9.14), softwares were used for data processing and annotation The eVol® NMR digital syringe equipped with a 100 µL syringe and a 180-mm-long bevel-tipped needle was used for sample and buffer transfer. The Heraeus™ Multifuge™ X3 centrifuge (Thermo Fisher Scientific) was also utilized again.

3.10.2 TSP chemical shift standard and sample preparation

Additional to the DMPA and 3-PBA added as described in section 3.8.1, deuterated 3-(trimethylsilyl) propionic acid (TSP) as a standard NMR IS was prepared for serum/tissue extracts (Dona *et al.*, 2014) and added during the appropriate step of sample preparation. Although initial tests deemed TSP as inadequate for metabolite quantification over different concentration ranges in the MACS buffer (Section 4.3.3), it still serves as chemical shift and peak-width calibration standard for ensuring sharp spectra and overall data integrity. A 20 mM stock solution of TSP was prepared in deuterated water (D_2O) and stored at -80 °C in between analyses. On the day of analyses, 250 µL of this stock was diluted with fresh D_2O to obtain the 5 mM working solution. The use of the standard phosphate-based pH buffer component was disregarded in this instance, as the MACS buffers already contain components that serve the same function. Addition of any further buffer salts potentially endangers the quality of subsequent chromatographic separation, ionization efficiency and mass spectral analyses of the post-mitochondrial sample (Liu & Xu, 2018).

Sample preparation mainly entailed removing proteins and other macromolecules, which may show heavy interference on the observed spectra. The aliquots of mitochondrial (60 µL) and cytosolic fractions (150 µL) designated for ^{1}H-NMR analyses (as per Section 3.8) were prepared. Firstly, the Centrifree 30 kDa cut-off filters were pre-rinsed with Milli-Q water through three successive rounds of centrifugation (12,000 x*g*, 5 minutes). This timeous yet necessary step removes any residual glycerol from the filter membrane coating, which produces large spectral interference in the observed data. After the samples were centrifugally filtered (12,000 x*g*; 20 minutes) through the 30 kDa membrane at room temperature (25 °C), 54 µL was transferred to a 2 mm NMR tube. A programmed sequence of the digital syringe was used to transfer the filtrate, before adding 6 µL phosphate-buffered TSP internal standard, to obtain the 10:90% ratio of D_2O:H_2O as per standard protocol. Following aspiration and purging of the whole volume for mixing purposes, the needle was flushed by three successive cycles of aspirating and purging 100 µL of Milli-Q water.

The 2 mm NMR tube was inserted into the gripper-adaptor of the Bruker MATCH system, which fits in the standard 10 mm spinner, before each MATCH assembly was loaded onto the autosampler conveyor for analysis.

3.10.3 Quality control samples, batch structure and run details

Pooled quality control (QC) samples were included in each batch, containing a mixture of all the samples analyzed in the batch to monitor data integrity. To prepare these samples, the remaining filtrate in the Centrifree filter cup (after 54 µL is removed for analysis) is taken and pooled (thus, one pooled mitochondrial QC containing both WT and KO brain and quadricep samples, and one such QC for the cytosolic batch of samples). Four separate 54 µL aliquots were taken from this pooled sample and further subjected to the same process as the samples, as described in Section 3.10.2.

Cytosol samples from all groups could be analyzed in a single batch of 32 samples (and 4 QCs), while the mitochondria formed their own analytically independent batch with separate QC samples. These samples, therefore, only provide information on intra-day variation in machine response for all the features investigated. Samples were randomized within their respective batches, with one QC sample being run at the start of each batch, after every 10^{th} sample, and at the very end. Due to equipment or consumable failure, both batches were interrupted during their initial run. During the maintenance period, all samples were stored within their NMR tubes in present state at 4 °C and re-ran within 24 hours after the initial interruption.

3.10.4 Analysis parameters

For ^{1}H-NMR analyses, all batches were randomized, and QCs were analyzed intermittently as described above. Sample spectra were collected at 500 MHz. Briefly, ^{1}H spectra were acquired as 128 transients in 32K data points with a spectral width of 6000 Hz (12,0 ppm). The H_2O resonance at 4.70 ppm was suppressed using the pulse sequence programme NOESY-presat, which presaturates the H_2O resonance by single-frequency irradiation during a relaxation delay of 4 seconds, with a 90° excitation pulse of 10 microseconds. The acquisition time and receiver gain were set for 2.7 and 64 seconds, respectively. Each sample was analyzed during a 15.75-minute run time, consisting of 4 dummy scans and 128 scans. These settings follow those given by established SOPs (Mason *et al.*, 2018), and resulted in a total runtime of 9.75 hours per batch. Each sample was automatically shimmed on the deuterium signal, locked, probe tuned and matched, and pulse calibrated using Bruker Topspin (V3.5), with further processing conducted using Bruker AMIX (V3.9.14).

As an added level of confidence in feature identification, a pooled aliquot from each post-NMR sample was pooled and subjected to 2D correlation spectroscopy (COSY) and 2D J-resolved spectroscopy (JRES) on the same NMR system (Dona *et al.*, 2016).

3.10.5 Sample recollection

As ^{1}H-NMR represents a non-destructive analytical method wherein minimal chemical change is affected upon the sample metabolome during preparation or analysis, the post-NMR samples were re-collected for high-sensitivity LC-MS/MS analyses. The eVol® digital syringe, was again used to ensure that consistently accurate volumes are transferred from the narrow and fragile NMR Tube. The programmed sequence of the digital syringe aspirated 60 µL of sample from the tube to be dispensed in a corresponding marked 1.5 mL microcentrifuge tube. The needle was flushed by three successive cycles of aspirating and purging 100 µL of Milli-Q water.

Of the recollected samples, 41 µL of each was transferred to separate microcentrifuge tubes for LC-MS analyses, while the approximately 19 µL remainder was pooled for each tissue matrix (brain and quadriceps cytosol, brain and quadriceps mitochondria), designated for 2D-NMR metabolite identity confirmation as described above.

3.11 LC-MS/MS Analyses

LC-MS/MS amino-acid and acylcarnitine profiling was performed on the post-NMR samples as described for murine model tissue samples (Terburgh *et al.*, 2019) with minor modifications to better suit the post-MACS mitochondrial and cytosolic sample matrices.

3.11.1 Instrumentation and Software

The LC-MS/MS system consisted of an Agilent© 1200 series HPLC front end, with temperature-controlled column compartment. Samples were introduced through a thermostat-regulated autosampler compartment, while solvents were managed through a binary solvent pump and vacuum degasser. The column compartment couples to an Agilent© 6410 series triple quadrupole mass analyzer with electrospray ionization (ESI) source. The Agilent© MassHunter Workstation Software (v B02.01; Data acquisition for 6400 Series Triple Quadrupole) was used for data acquisition in the multiple reaction monitoring (MRM) configuration setting for maximum sensitivity, while data extraction was done using the Agilent© MassHunter Workstation software (v B09.00; Qualitative Analysis and Quantitative Analysis).

3.11.2 Isotope-labelled reference standard and Sample preparation

In addition to the DMPA and 3-PBA added as described in section 3.8.1, an internal standard mixture consisting of several deuterium-labelled versions of selected target compounds (2.5 ppm) was to be added before LC-MS/MS sample preparation. These compounds are added to account for some of the biases (Type B) that arise due to differential extraction, derivatization and ionization during data processing, as outlined in Section 3.12. The isotope mixture

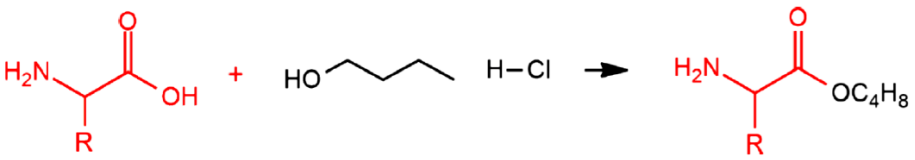
contained amino acid (valine_d8, isoleucine_d10, phenylalanine_d5, lysine_d4) and acylcarnitine (acetylcarnitine_d3, octanoylcarnitine_d3, octadecanoylcarnitine_d3) in water, which were originally prepared from individual isotope stock solutions (500 ppm) in methanol.

The post-NMR extracts (41 µL) were transferred to LC-certified, 2 mL glass vials (Agilent©). After adding 100 µL of the isotope reference standard mixture to each sample, 300 µL of ice-cold acetonitrile was added. Metabolite separation from any remaining macromolecules in the sample that will interfere with LC-MS/MS analyses proceeded, by allowing the samples to stand on ice for 10 minutes before 10-minute centrifugation (20,000 x*g* at 4°C). As the cold acetonitrile presents the proteins with an immiscible environment (similar to methanol in Section 3.9.2), the proteins are thereby pelleted, while the metabolite-containing supernatant was dried under a stream of nitrogen gas and stored (−80 °C) for derivatization on the day of analysis.

3.11.2.1 Derivatization

On the day of analysis, samples were derivatized by butylation, during which active hydrogens on COOH functional groups are replaced with a butyl (-C_4H_8) group, resulting in the formation of butyl esters of amino acids (Reaction 3-5) and acyl-carnitines. This step, which effectively reduces the polarity of these compounds, is necessary to better retain the polar amino acids and carnitines on the apolar C18 reverse-phase column and achieve acceptable chromatographic separation in the allotted runtime. To derivatize the samples, 300 µL butanolic hydrochloric acid [4:1 (v/v) 1-butanol and acetyl chloride, prepared fresh and used within 2 days] was added and the samples were incubated at 50 °C for 1 hour. Thereafter, the butylated samples were evaporated to dryness under a stream of nitrogen gas at 37 °C. Finally, the dried residue was reconstituted in a final volume of 100 µL water:acetonitrile (50:50, v/v). The samples were thoroughly vortex mixed to dissolve the dried compounds in the final volume, before being transferred to 250 µL pulled point glass inserts, placed back in the sample vial and loaded onto an Agilent© 1200 series autosampler for LC-MS/MS analysis.

Reaction 3-5: Butylation of active hydrogen groups by butanolic-HCl



Amino acid

3.11.3 QC samples, batch structure and run details

Pooled quality control (QC) samples were included in each batch, containing a mixture of all the samples analyzed in the batch to monitor data integrity. For the two respective batches of LC-MS/MS samples (consisting of all the cytosolic and mitochondrial fractions, respectively), QC samples were prepared from the recollected NMR QC's, again pooled and split into six identical 41 µL aliquots (technical errors in recollection lead to only 5 cytosolic QC aliquots being recovered), which were prepared for LC-MS/MS analyses identically to the samples.

Cytosol samples from all groups could be analyzed in a single batch of 32 samples (and 5 or 6 QCs for the cytosol and mitochondria, respectively), while the mitochondria formed their own analytically independent batch, thus these samples only provide information on intra-day variation in machine response for all the features investigated. For the LC-MS/MS analyses, an in-house mixture of pure reference standards for all compounds analyzed was included in technical duplicate at the end of each batch, providing absolute confirmation on metabolite identity. The samples were randomised within their respective batches, with one QC sample run at the start of each batch, after every 6^{th} – 10^{th} sample, and at the very end, for five or six total QC repeats. Due to technical errors and stops in the run overnight, the cytosol sample run finally took another day above the initially calculated time. Similar technical errors and unavailability of access to the system for a long period, lead to the mitochondrial sample run having to be repeated 1 month after initial preparation. As butylated derivatives are known to be stable over long periods at -80 °C, all sample vials were recapped, sealed with parafilm and stored under ultra-refrigeration for final analyses. On the day, these samples were thawed, re-randomized and analyzed as described in the following section.

3.11.4 Analysis parameters

For separation, a Zorbax SB-Aq reverse phase column (Agilent,USA: 150 mm x 2.1 mm outer diameter; 3.5 µm internal diameter), with bonded apolar alkyl (C18) solid phase, was used. The column was kept at 30°C during the entire run. A sample volume of 2.5 µL was injected, as an injection volume shows maximal metabolite detection plateauing between 1.5 and 2,5 µL injections. A mobile phase gradient was used to enhance metabolite separation. The chromatographic gradient started at 100% solvent A (water with 0.1 % formic acid) and 0% solvent B (acetonitrile with 0.1% formic acid) with a flow of 0.3 mL /minute, maintained for 1 minute, before ramping the gradient to the original method starting point (5% solvent B) over 1 minute. This modification attempts to purge as much of the highly polar buffer salts within the sample matrix as possible, as this can severely interfere with retention, ionization and compromise the ion source or detector (Corcelli *et al.*, 2010). Thus, the first minute of

chromatographic eluent was directed to waste, as preliminary test runs indeed indicated a significant amount of ion suppression of early eluting compounds if this first 0.3 mL of eluate is allowed on-column. Thereafter, solvent B was increased to 20% over a period of 2 minutes, where it was then kept constant for 3 minutes. Thereafter, it was increased linearly to 100% solvent B over 7 minutes. Over this period, the flow was linearly increased to 0.35 mL /minute (between 14 and 14.1 minutes). After maintaining these conditions for 5 minutes, the gradient was decreased to 5% solvent B at 19.5 minutes and kept constant for 1.5 minutes. A post-run of 8 minutes was allowed to ensure equilibration of the column to give a total run time of 29 minutes per sample, and a total run time of 22.5 hours per batch.

Mass spectrometry was operated in the positive ionization mode, set on multiple reaction monitoring (MRM) detection mode, targeting the mass transitions of target amino acids, derivatives, acylcarnitines and reference standards indicated in Table 3.3. The ESI source gas (nitrogen) temperature was kept at 300 °C, with a flow rate of 7.5 L/minute. Nebuliser pressure was kept at 30 psi and the capillary voltage at 3500 V.

Table 3-3: MRM Parameters for metabolites and internal standards monitored

Metabolite name	~R.T. (min)	Transition precursor ion (m/z)	Transition product ion (m/z)	Dwell time (s)	Fragmentor voltage (V)	Collision energy (eV)
Amino acids and derivatives						
2-Aminoadipic acid	12.9	274.2	98.1	45	113	24
3-Methyl Histidine	1.2	226.4	96.2	45	130	25
4-Hydroxyproline	3.0	188.1	68.1	45	120	35
Alanine	3.0	146.1	44.2	45	80	15
Arginine	1.3	231.2	70.1	45	103	40
Asparagine	1.9	189.1	144.1	45	89	8
Aspartic acid	12.4	246.2	144.1	45	98	12
β-Aminoisobutyrate	4.7	160.1	86.1	45	100	10
Beta-Alanine	2.8	146.2	72.1	45	90	10
Citrulline	3.5	232.2	70.1	45	89	32
Creatine	5.4	188.1	90.1	45	104	16
Cystathionine	9.3	335.2	190.1	45	127	16
Dimethylglycine	2.8	160.3	58.2	45	90	20
Gamma-Aminobutyric acid	4.7	160.1	87.1	45	79	8
Glutamic acid	12.7	260.2	84.1	45	89	24
Glutamine[a]	2.5	203.1	84.1	45	89	20

Table 3-3 (continued)

Metabolite name	~R.T. (min)	Transition precursor ion (m/z)	Transition product ion (m/z)	Dwell time (s)	Fragmentor voltage (V)	Collision energy (eV)
Glycine	1.9	132.1	76.1	45	65	4
Histidine	1.2	212.1	110.1	45	89	16
Homocysteine	7.1	192	90	45	161	12
Isoleucine__d10	10.9	198.2	96.2	45	108	12
Isothreonine / Threonine[b]	2.8	176.1	74.1	45	94	12
Leucine_Isoleucine[c]	11.2	188.2	86.2	45	89	8
Lysine[a]	1.2	203.2	84.1	45	89	20
Lysine__4,4,5,5__d4	1.2	207.2	88.2	45	118	16
Methionine	9.5	206.1	104.1	45	94	8
N,N-Dimethylphenylalanine	12.6	250.1	148.1	45	103	20
N-Acetylaspartate	14.1	288.2	144.1	45	98	16
N-Acetylglutamate	14.2	302.2	186.1	45	113	12
Ornithine	1.1	189.2	70.2	45	74	20
Phenylalanine	12.0	222.2	120.1	45	108	16
Phenylalanine__ring__d5	12.0	227.2	125.1	45	108	16
Pipecolic acid	7.9	186.1	84.1	45	108	16
Proline	5.2	172.1	70.2	45	94	20
Pyroglutamic acid		186.1	84.1	45	108	16
Sarcosine	2.9	146.1	44.2	45	80	15
Serine	2.0	162.1	60.1	45	94	12
Threonine	2.8	176.1	74.1	45	94	5
Trimethylglycine	4.0	174.2	58.2	45	130	45
Tryptophan	12.5	261.2	244.1	45	94	8
Tyrosine	9.9	238.2	136.1	45	94	12
Valine	8.9	174.2	72.2	45	89	12
Valine__d8	8.9	182.2	80.2	45	103	12
Acylcarnitines						
(C0) Free Carnitine	4.9	218.2	103	45	132	16
(C2) Acetyl-carnitine__d3	9.3	263.2	85	45	100	20

Table 3-3 (continued)

Metabolite name	~R.T. (min)	Transition precursor ion (m/z)	Transition product ion (m/z)	Dwell time (s)	Fragmentor voltage (V)	Collision energy (eV)
(C2) Acetyl-carnitine	9.4	260.2	85.1	45	122	24
(C3) Propionyl-carnitine	11.3	274.2	85.1	45	127	20
(C4) Butyryl-carnitine	12.4	288.2	85.1	45	110	20
(C5) Isovaleryl-carnitine	13.0	302.2	85.1	45	105	24
(C6) Hexanoyl-carnitine	13.5	316.2	85.1	45	137	24
(C8) Octanoyl-carnitine	14.2	344.3	85.1	45	115	28
(C8) Octanoyl-carnitine__d3	14.2	347.3	85.1	45	136	24
(C10) Decanoyl-carnitine	14.7	372.3	85.1	45	125	28
(C12) Dodecanoyl-carnitine	15.3	400.3	85.1	45	155	28
(C14) Myristoyl-carnitine	16.6	428.4	85.1	45	150	28
(C16) Palmitoyl-carnitine	16.2	456.4	85.1	45	160	36
(C18) Stearoyl-carnitine	16.7	484	85.1	45	155	36
(C18) Stearoyl-carnitine__d3	16.7	487.5	85.1	45	160	36

[a]Compounds with abundant isotopes having identical mass transitions, deconvoluted by pure reference standard mixture R.T. match.

[b]Isothreonine and threonine with overlapping R.T. and identical mass transitions could not be separated under current chromatographic conditions

[c]MRM metabolite identity confirmed as Leucine through pure reference standard mixture R.T. match.

3.12 Metabolomics data extraction, processing and statistical analyses

Within this section, the full bioinformatics pipeline for data obtained from the final *Ndufs4* KO and WT ^{1}H-NMR and LC-MS/MS metabolomics is described in detail.

3.12.1 Biological samples: Data extraction and quality inspection

Data acquired from sub-cellular fractions and tissue isolates were treated similarly. After metabolomic analyses were performed, the raw spectral data from each platform were

automatically baseline corrected, aligned and extracted into matrices using the instrument software (Agilent MassHunter or Bruker Topspin).

Along with the final extracted data, a separate dataset, including the unprocessed spectral bins detected and quantified in each sample, was extracted. Total useful signal (TUS) was calculated from all identified metabolite-containing spectral bins, by summating these raw measurements for each sample. This was used as a final normalization factor for all datasets as it better captures discrepancies in the total metabolite content due to all sources of variation (from the starting tissue weight to metabolomics preparation) than normalization, with the IS compounds that were added later (Section 5.4.7), although the corrective power is directly proportional to the amount of compounds measured (Li *et al.*, 2016).

A standard data quality check was performed as detailed in Annexure D. This included: i) manual data inspection with regards to correct peak picking and chromatographic quality; ii) visual inspection of multivariate data clustering (including QC samples) via principal component analysis (PCA) to identify any biases in the data due to intra-batch effects; and univariate inspection of iii) metabolite intra-batch coefficient of variation (QC-CV) distributions, as well as iv) scatter plots of relative intensity vs run order for each batch of samples analyzed. Altogether, the data proved to be of good quality, with no obvious batch effects visible.

3.12.2 Data pre-processing

A “clean” data matrix was produced, corrected for certain sources of uninduced variation due to sample preparation and analysis, in the form of normalized peak areas that reflect the relative intensities of metabolites. Excel 2021 (Microsoft) was used for this clean-up, and included data filtering, missing value imputation and normalization. Data filtering was done to identify and remove variables in the dataset that were unreliable or unstable. First, a missing value (or 50% zero) filter was applied to remove features that were not detected in more than 50% of both *Ndufs4* KO/ and WT group samples (per tissue). Second, a QC variance filter was applied to remove features from the dataset with a CV-value above 50% in the QC samples. Since QC’s are identical samples prepared and analyzed throughout, high variance features in these samples represent unstable metabolites or unreliable detection thereof on the given platform (Dunn *et al.*, 2012). QC samples were normalized to the selected IS’s (as described later in this section) prior to QC-CV filtering.

Missing value imputation followed, as too many missing data points cause difficulties for multivariate statistical tools. Missing value imputation was done by replacing all empty data points with a small value (random values around one fifth of the minimum positive value in the

original data), assumed to be the lower detection limit. This assumption underlies the limitation of this method, as zero values may represent other effects than low-abundance metabolites alone, although it has been shown to not significantly affect the final list of discriminatory features in comparative studies of limited-volume biological samples (Terburgh *et al.*, 2019).

Lastly, sample normalization was done to adjust for differences due to technical variation among samples and improve sample comparability. ^{1}H-NMR results were normalized to the TUS calculated as per section 3.13.1. LC-MS/MS data were first normalized to the stable isotopes added immediately prior to butylation; where available, each measured amino acid or acylcarnitine was normalized to its own isotope standard – otherwise to the standard to which it showed the strongest linear correlation in peak area across all QC samples within a batch. Pearson correlations used in that regard were calculated in SPSS (IBM, v.28). These values were finally normalized to the NMR-TUS value calculated for each sample as described above- as a total sample signal for semi-targeted MRM measurements (LC-TUS) are biased towards only the probed amino acid and acylcarnitine content of the samples and less accurately represent the total metabolome content. All data were normalized to the relative added IS compounds added to the samples before their respective platform preparations (DMPA for both platforms' data; TSP and LC-TUS, respectively) as well, to motivate the implemented NMR-TUS approach (Section 5.5).

3.12.3 Data pre-treatment

The data were pre-treated, further adjusting the clean data set to a suitable and comparable scale for multivariate analyses. Data pretreatment was done in MetaboAnalyst 4.0 (Chong *et al.*, 2018) and involved data transformation and data-centering techniques. First, generalized logarithm (glog) transformation was done (Equation 3-4). This helps obtain a data distribution closer to normal by correcting for heteroscedasticity, while also conferring a pseudo-scaling effect to reduce the difference between low and high abundance features and make them more comparable (van den Berg *et al.*, 2006). Next, pareto scaling was done (according to Equation 3-5) to convert metabolite concentrations to fluctuations around zero, instead of around the mean, further reducing the offset between high and low abundant metabolites while keeping the original unit of measurement. These techniques leave only the relevant variation for analysis (van den Berg *et al.*, 2006). Finally, outlier samples were corrected using principal component analysis (PCA) and inspection of contribution to average group variation.

Equation 3-4: Generalized logarithm transformation.	$x_{\log} = \log_{10} x$
Equation 3-5: Pareto scaling of metabolomics data.	$x_{PS} = \frac{x - \bar{x}}{\sqrt{Stdev}}$

3.12.4 Univariate and multi-variate statistics

To understand the full impact of data, it is essential to investigate both statistical significance and practical significance. Statistical significance examines, at an *a priori* defined level of confidence, whether findings are likely to be due to chance, whereas practical significance helps to understand the magnitude of the differences found (relative to the uninduced natural variation of the compared groups of measurements) and correlate back to the biological question (Sullivan & Feinn, 2012).

Significantly discriminatory features between *Ndufs4* KO and WT metabolic profiles were determined via univariate analyses applied to the untransformed dataset, after data extraction and pre-processing as described above. Testing of the assumptions for normality (Kolmogorov-Smirnov test) and homoskedasticity (Levene's test) were applied via SPSS to select the most adequate means comparison. Statistically important differences were inspected at a 10% significance (alpha) level ($p < 0.1$) using parametric student's t-test variations for homogenous or non-homogenous variances (automatically determined by SPSS based on Levene's test output) or the non-parametric equivalent, where applicable (Mann-Whitney U test, which compares sample distributions rather than means). The effect size of each univariate comparison was determined in Excel 2021 (Microsoft) according to Cohens' formula of difference in means divided by the pooled standard deviation (Steyn & Ellis, 2003). The cut-off threshold for practical significance was set at an effect size (Cohen's) D-value of ≥ 1.0. While *a priori* power calculations support the chosen D-value cut-off, the selected alpha level[19] reflects the expected variation in the data set due to small pilot group sizes and the large intragroup variation inherent to sub-cellular metabolomics studies (Section 2.11.3). As this largely explorative study aims to emphasize the largest effects deserving of further study, the trade-off of larger Type I error possibility (false positive) for a decreased chance of losing potentially significant features for future reference (Type II error) was deemed acceptable. Features meeting one or the other criteria of significance (but not both) were also reported.

[19] The selected p-value is larger than the generally accepted, although arbitrary, $p < 0.5$ cut-off in biological sciences that indicates a 5% chance of Type I errors (false positive effect).

The data representing these selected features from both platforms were combined and visually investigated on a univariate and multivariate level. The PCA was performed in MetaboAnalyst 4.0 (Chong *et al.*, 2018) on this dataset after autoscaling to inspect the data clustering, covariance and discriminatory power. The identities of the recorded metabolites are of the highest confidence, achieving level 1 designation according to the latest International Metabolomic standards depicted in Figure 3-6 (Schymanski *et al.*, 2014).

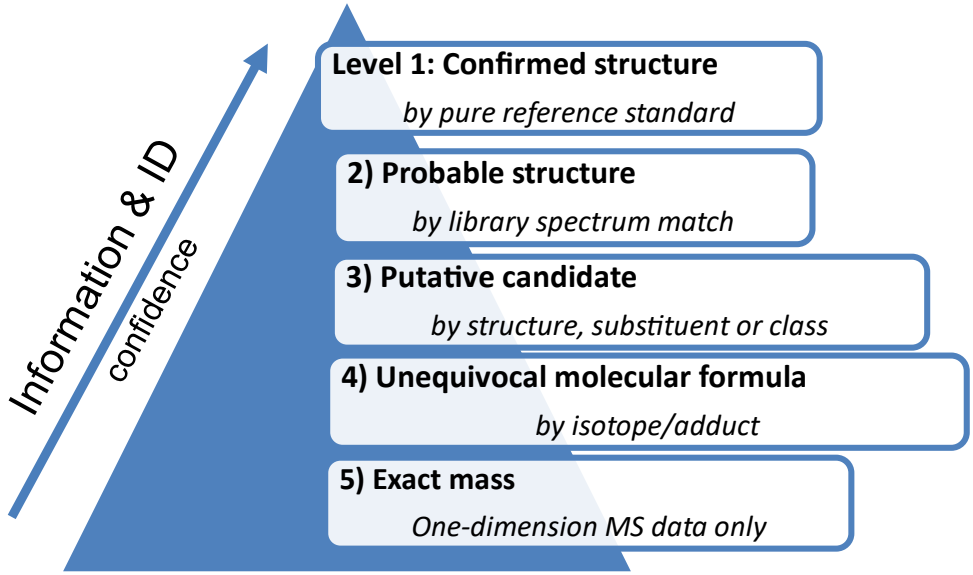


Figure 3-6: Currently accepted metabolite identification confidence levels as reported by Schymanski et al. (2014), with accompanying spectral information criteria for each level from 5 (lowest confidence) to level 1 (highest confidence in identification).

3.13 GC-TOF-MS and ^{1}H-NMR method variations for standard compound mixture analyses

For GC-TOF-MS analyses, ten 150 µL replicates of each of the 6 standard compound groups (50, 250 or 500 µM in Milli-Q water or MACS 1x SB; Section 3.4) were aliquoted to separate 1,5 mL microcentrifuge tubes and subjected to the modified single-phase metabolite extraction protocol as described in Section 3.9.2. Quality control samples were prepared by mixing aliquots of MACS and water-diluted standard compound samples at each concentration range. Similar replicates were aliquoted to separate 1.5 mL microcentrifuge tubes for ^{1}H-NMR analyses. The standard compound solutions designated for NMR analysis already contained the selected internal standards at 750 µM concentration as per Section 3.4.

For the standard compound series, data processing was done using Excel 2013 (Microsoft). Spectral data obtained from the GC-TOF-MS was extracted into matrices by the ChromaTOF® Software. This included automatic baseline removal via the “spanning” tracking method (offset of 1; just above the noise) and auto smoothing, with the software’s Statistical Compare feature used to align peaks. NMR data was extracted as described in Section 3.12.1.

Data matrices were manually inspected (correct peak picking and alignment, batch effect and data integrity) before an 80% zero-filter and 50% QC-CV filter was applied as described in section 3.12.2. No batch corrections were needed as the QCs showed no significant drift effects. Peak intensities from the GC-TOF-MS were normalized to 3-PBA and EDTA in separate attempts to determine the most efficient compound to normalize these samples of non-biological nature. As a stable component present in fixed amounts within the 1x SB, the obtained peak intensities for EDTA showed minimal inter-sample variation and superior stability over the entire duration of analyses, meeting the criteria of a metabolomics reference standard (Dunn *et al.*, 2012). This is, however, only applicable to this sample type, wherein a fixed amount of 1x SB is derivatized in the final sample. For the mitochondrial/cytosolic isolates, the amount of 1x SB (and thus EDTA) in the final sample fluctuates depending on the prevailing factors on each day of analysis, thus rendering this approach ineffective. For ^{1}H-NMR data, normalization and quantification according to TSP, 3-PBA and DMPA was applied to the dataset obtained.

A mean and %CV was calculated for each of the 9 spiked-in compounds over all ten replicates per sample group as indication of measurement precision. Linear coefficients were drawn for each compound at the three concentration ranges, in either water or 1x SB. Relative accuracy expressed as the percentage recovery of the given metabolite in the MACS buffer environment, relative to the aqueous reference samples, was only calculated for ^{1}H-NMR data, as the only platform wherein measurement in both matrices are comparably quantitative.

CHAPTER 4

Novel mitochondrial and cytosolic purification pipeline for compartment-specific metabolomics in mammalian disease model tissues

This chapter was published as

Van der Walt, G. & Louw, R. 2020. Novel mitochondrial & cytosolic purification pipeline for compartment-specific metabolomics in mammalian disease model tissues. *Metabolomics,* 16(7):78.

4.1 Background

Mitochondria are eukaryotic organelles that mediate several compartmentalized reactions, intimately tied to cellular viability (Birsoy *et al.*, 2015; Frezza, 2017; Nunnari & Suomalainen, 2012). As such, emphasis has been placed on the investigation of mitochondrial function and dysfunction (MD) in relation to disease research (Picard *et al.*, 2016). Pathologies of high epidemiological impact such as cancer, diabetes, neurodegenerative diseases (e.g. Parkinson's and Alzheimer's), tuberculosis and HIV have all been shown to be tied to MD in the affected tissues (Patti & Corvera, 2010; Pustylnikov *et al.*, 2018; Tahrir *et al.*, 2018; Tzelepis *et al.*, 2018; Yao *et al.*, 2009).

Metabolomic approaches aim to expose genotype-phenotype correlations in such cases through the detection of several small-molecule biochemical intermediates and their subsequent integration into metabolic pathways/networks (Dunn *et al.*, 2011; Fiehn, 2002). Investigating the urine/serum metabolomes in these MD related complex diseases has revealed unique compound biosignatures, often overlapping on the grounds of bioenergetic perturbations (Esterhuizen *et al.*, 2017; Nagrath *et al.*, 2011; Wu *et al.*, 2007). The frequency and impact of pre-clinical metabolomic studies on isolated target tissues has increased substantially over the last two decades thanks to animal disease models, as the advantage of negating confounding effects from the exometabolome through a tissue-specific approach is amplified by the high genetic and phenotypic homogeneity of laboratory-bred animals (Kruse *et al.*, 2008; Ruggeri *et al.*, 2014). For tissue-specific pathologies linked to whole-body mutations, as presented by the *Ndufs4* KO mouse model of Leigh syndrome, this has provided unprecedented insights into the adaptive mechanisms active only in the tissues that are most affected (Esterhuizen *et al.*, 2017; Terburgh *et al.*, 2019)

When considering the tissue metabolome, however, much of the metabolite contribution from the mitochondrial compartment is still overshadowed by that of the significantly greater cytoplasmic volume (Van Vranken & Rutter, 2016). Despite the absolute nature of the mitochondrial metabolite space being mostly unknown, case-control studies using mitochondrial isolates have unveiled significant alterations in both matrix-specific and more common intracellular pathways that cannot be efficiently interrogated when considering the combined effect of all cellular compartments in whole cell lysates (Chen *et al.*, 2016; García-Sevillano *et al.*, 2015; Pan *et al.*, 2018). Since several metabolite transport and counter transport mechanisms at the interface between the matrix and cytosol are allosterically regulated by diverse cellular conditions such as pH, adenylate charges and nutrient signalling, these effects may pertain to more than just the principal metabolic target of perturbation (Junghans *et al.*,

2019; Palmieri & Monne, 2016). Therefore, organelle-level resolution has become critical to uncovering metabolic aspects involved in the pathogenesis of bioenergetic-linked diseases.

For metabolomics studies at the organelle level, isolating mitochondria of sufficient yield and purity in a buffer environment applicable to all downstream analyses is the key obstacle inhibiting large-scale application of such compartment-specific approaches (Liu & Xu, 2018; Roede *et al.*, 2012). While costly and timeous ultracentrifugation produces higher purity mitochondria (Hubbard *et al.*, 2019), differential centrifugation (DC) promises quick, cheap and robust preparation, with the drawback of decreased fraction purity. Nevertheless, such methods have been successfully applied to elucidate compartment-specific signatures related to gender, metal toxicity and MD (Afanasyeva *et al.*, 2018; Go *et al.*, 2014a; Pan *et al.*, 2018).

Some of these fractionation issues have been partially overcome by fractioned magnetic mitochondrial isolation (FMMS) approaches, wherein magnetically labelled antibodies specific to mitochondrial epitopes are used to bind and retain the organelles in a strong magnetic field. The most analytically sound approach published to date involves producing recombinant mouse strains expressing FLAG-tag epitopes on selected mitochondria alongside custom, recombinant antibody cocktails (Bayraktar *et al.*, 2019; Chen *et al.*, 2016). This approach is complex, labour intensive and expensive, thus not applicable to all laboratories or models. Commercially available alternatives, such as a popular approach using antibodies targeting an abundant translocase of the outer membrane (TOM22) could potentially give laboratories of various financial and analytical status access to these FMMS-based techniques (Hornig-Do *et al.*, 2009). Kit-based methods are known to produce variable mitochondrial yields in different tissues (Franko *et al.*, 2013). The contained buffers may also interfere with downstream analyses, prompting preliminary testing of isolation buffer constituency and applicability for the intended purpose (Corcelli *et al.*, 2010). Significant optimization for specific sample types and experiments is thus required. Furthermore, true quantification is hindered by the rapid turnover time of certain compounds, especially those implicated in the central metabolism (Steinhauser & Lechene, 2013). It is thus imperative that data produced by such methods be viewed in combination with metabolic flux rates through an isotope-dilution strategy to better elucidate temporal effects (Junghans *et al.*, 2019; Lee *et al.*, 2019), as organelle isolation strategies are better suited for a global snapshot of the most pronounced perturbations.

Another important factor to consider is the nature of the sample used, with which to compare the mitochondrial metabolome. While whole-cell lysates have been deemed sufficient comparison for isolated mitochondria, the presence of lysosomes, endosomes, endoplasmic reticuli and other organelles infer possible confounding of the true cytosolic contribution to the observed metabolite levels. Purified cytosolic fractions (devoid of other organelles) could thus home in on

the respective metabolite pool sizes in – and metabolic fluxes between – these two pathologically significant sub-cellular spaces (Go *et al.*, 2014b; Matuszczyk *et al.*, 2015). Given sufficient optimization of mitochondrial and cytosolic fractioning alongside sensitive and reliable analytical platforms, it is reasonable to hypothesize that inexpensive commercial FMMS protocols can be adapted for compartment-specific metabolomics in animal model tissues (Franko *et al.*, 2013; Hubbard *et al.*, 2019; Kappler *et al.*, 2016).

To that end, we established a rudimentary, kit-based FMMS workflow for GC-TOF-MS and ^{1}H-NMR mitochondrial and cytosolic metabolomics in tissue samples obtained from a widely available mouse model of MD. Fractioning was performed using an Anti-TOM22 magnetically activated cell sorting (MACS) kit applied to brain tissue from a Leigh Syndrome mouse model, along with a novel filtering approach for producing purified cytosol. The isolates were analytically compared to DC-enriched mitochondria based on yield (CS enrichment), purity (immunoblotting) and membrane integrity (respirometry). The effect of the kit-based buffers on chemometrics was probed for each platform, respectively, before a pilot analysis of the cellular fractions was performed to illustrate biological applicability to limited-volume samples from model animals.

4.2 Methods and Materials

4.2.1 Spiked standard compounds

Dilutions of nine commercially available metabolites commonly found in brain tissue were prepared as analytical standards for investigating the effect of the selected mitochondrial isolation buffer constitutions on chemical analyses. Pyruvic acid (Pyr), lactic acid (Lac), alanine (Ala), valine (Val), glutamic acid (Glu), aspartic acid (Asp), glycine (Gly), 3-hydroxybutyric acid (3-HB) and 2-hydroxybutyric acid (2-HB) were respectively dissolved in de-ionized water (Millipore®, Merck, USA). A combined stock concentration of 5 mM (of each metabolite) was created in de-ionized water before being diluted to 500, 250 or 50 µM (designated high to low concentration samples) in either water or MACS Separation buffer (#130-096-946), Miltenyi Biotec (DEU), at 1x final dilution (1x SB). All chemical standards were purchased from Sigma-Aldrich (USA).

4.2.2 Animals and Sampling

All protocols used have been approved by the designated authority (AnimCare animal research ethics committee, North-West University) with approval number NWU-00568-19-S5. All animals were maintained, and procedures performed in accordance with the code of ethics in research, training and drug development in South Africa and complied with national legislation. *Ndufs4*

Wildtype (WT) mice (B6.129S4-*Ndufs4*$^{tm1.1Rpa}$/J; Jackson Laboratories, USA) were used. Mice were held under controlled conditions (22 ± 1 °C; 55 ± 10% humidity; 12:12 hour light/dark cycle) on campus at the Vivarium (SAVC reg. no. FR15/13458) of the Pre-Clinical Drug Development Platform (PCDDP; NWU, RSA). The animals were fed a standard laboratory diet with food and water provided ad libitum. Mice were euthanized between P45–P50 to correlate with pre-determined relevant ethical endpoints in *Ndufs4* knock-out studies (Kayser *et al.*, 2016). After euthanasia via cervical dislocation, whole brains were rapidly dissected and immediately processed for mitochondrial isolation via either DC or FMMS workflows, both performed at 0-4°C.

4.2.3 Mitochondrial isolation via differential centrifugation (DC)

The DC protocol was adapted from Pan *et al.* (2018) for downstream GC-MS and NMR analysis. Mitochondria were isolated in optimized mass spectrometry (MS) compatible KClEM isolation buffer [180 mM KCl, 1 mM EDTA and 5 mM MOPS-KOH (pH 7.2)], as first described by Corcelli *et al.* (2010). Briefly, a 10% w/v tissue lysate was made from 100 mg whole brain in ice-cold KClEM buffer via eight strokes in the Potter-Elvehjem homogenizer. Nuclei and large debris were pelleted by subsequently increasing the centrifugal force in a single centrifugation run: 250 x*g* for 2 minutes, 1,000 x*g* for 4 minutes and 1,900 x*g* for 4 minutes. The post-nuclear supernatant was subjected to 8,000 x*g* centrifugation for 15 minutes to pellet mitochondria. Enriched mitochondria were resuspended in KCIEM to 120 µL final volume. Post-mitochondrial supernatants were collected and filtered using Centrisart® 100 kDa centrifugal cut-off filters (#13269E, Sigma Aldrich, USA), accelerated to 2,000 x*g* for 15 minutes at 4 °C to prepare the cytosolic fraction. The whole procedure was performed on ice to minimize mitochondrial damage and post-isolation metabolic fluxes.

4.2.4 Fractioned magnetic mitochondrial separation (FMMS)

Sub-cellular fractions were prepared at 4 °C using the MACS Mitochondria Extraction Kit for mouse tissue (Miltenyi Biotec, DEU) with slight variations to manufacturer instructions (Hornig-Do *et al.*, 2009). Whole brain (150 mg) was cut into small pieces and homogenized in Lysis Buffer (LB) to produce 10% (w/v) lysates, as described above. Brief centrifugation at 1,300 x*g* (2 minutes) followed, to remove nuclei and large debris, before the post-nuclear supernatant was diluted 10x (v/v) in 1x Separation Buffer (SB). For magnetic enrichment, mitochondria were labelled with anti-TOM22 Microbeads (1.5 µL/mg tissue) for 1 hour at 4 °C. The suspension was loaded onto an LS-M column, which had been placed in a MACS Separator at 4 °C. Of the flow-through, regarded as a crude cytoplasm, 2.5 mL was subjected to centrifugal filtering identical to the above-mentioned method to prepare the cytosolic fraction. Labelled mitochondria were

eluted from the LS-M column in 1x SB after removal from the magnet; this was repeated three times for each sample. Before further analysis, the eluates were centrifuged at 13,000 x*g* for 2 minutes (4 °C) and the mitochondrial pellets resuspended in a final volume of 120 µL solvent, relative to the specific downstream application. The isolation procedure took approximately 90 minutes from tissue homogenization to mitochondrial elution.

4.2.5 Citrate synthase enzyme activity

During initial optimizations, a small aliquot of each DC or FMMS sample was set aside after subsequent steps for citrate synthase (CS) assays according to established protocols (Shepherd & Garland, 1969). Total protein content for each fraction, as well as the MACS reagents shown to contain protein, was determined via bicinchoninic acid (BCA) assay (Sigma Aldrich). For both BCA and CS, absorbance was measured by the Synergy™ HT Multi-detection microplate reader (Biotek Instruments), quantified by the Gen5™ Data analysis software (Biotek Instruments) and statistical analysis performed in Excel 2013 (Microsoft Inc.). All fraction activities were normalized to their respective volumes (µmol/minute/µL) and expressed as a percentage of that measured in the preceding homogenate.

4.2.6 Western Blotting

Primary antibodies used in this study were all obtained from Abcam (GBR) and are listed by antigen, catalogue number and final working dilution: VDAC1 (ab15895, 1:1,000); Hsp60 (ab46798, 1:10,000), LAMP-2B/C (ab18529, 1:1,000), β-Actin (ab6276, 1:4,000). All equipment, reagents and software were purchased from Bio-Rad (ZAF). Briefly, samples containing 15 µg total protein were incubated in 4x Laemmli buffer (161-0747) containing 5% [v/v] 2-mercaptoethanol for 5 minutes at 100°C. Sample proteins were separated in 10% TGX Stain-Free™ FastCast™ Acrylamide gels (161-0182) before being transferred to 0,2 µm Mini-format PVDF membranes. Protein blots were then blocked in 1x TBS + 1% (w/v) casein (161-0782) for 1.5 hours, before being incubated overnight at 4°C and constant shaking in the indicated primary antibodies, diluted in TBS/T [1x TBS + 1% casein + 0,1% (v/v) Tween20 (166-2404)]. After three 5-minute washing steps in TBS/T, the membranes were incubated for 1 hour at room temperature in horseradish peroxidase-conjugated anti-rabbit IgG antibody solution (Abcam, ab97051), diluted in TBS/T to optimal concentrations for each antibody combination probed. Membranes were incubated in Clarity™ Western ECL Substrate (170-5060) and chemiluminescence signals detected by the ChemiDoc™ MP Imaging system (170-8280) in signal accumulation mode. Images were analyzed, and band intensities normalized to total protein content for the mitochondrial and cytosolic blots, respectively, via ImageLab (v 5.2.1).

4.2.7 Measurement of oxygen consumption and respiratory control ratio (RCR)

The Seahorse XF^{e}96 Extracellular Flux Analyzer (Agilent Technologies, USA) was used to measure oxygen consumption rates (OCR) of isolated mitochondria in the presence of different substrates, inhibitors and uncouplers, using previous methods with slight modifications (Aucamp *et al.*, 2017; Hubbard *et al.*, 2019). Mitochondrial assay buffer was prepared beforehand (MAS; 105 mM sucrose 330 mM mannitol, 15 mM KH_2PO_4, 7.7 mM $MgCl_2$, 3 mM HEPES, 1.5 mM EGTA, 0.3% (w/v) bovine serum albumen). The sensor cartridge was hydrated overnight at 37 °C. Before loading, the injection stocks were diluted appropriately in MAS (already containing 10 mM pyruvate/ 5 mM malate, adjusted to pH 7.2) and 25 µL loaded in each injection port to achieve final concentrations of 6 mM ADP (Port A), 4 µM oligomycin A (Port B), 4 µM FCCP (Port C) and 3 µM rotenone/6 mM antimycin A (Port D) in each respiration chamber. Thereafter, the sensor cartridge was placed into the Seahorse X^{Fe}96 Flux Analyzer for automated calibration. The FMMS or DC mitochondria were diluted in MAS based on CS activity; eight 25 µL samples containing 2-8 nmol/minute/µL CS were loaded in each well of a Seahorse Standard XF^{e}96 assay plate. The assay plates were centrifuged at 2,000 x*g* for 20 minutes at 4 °C to adhere the mitochondria to the bottom of the wells. After centrifugation, 150 µL of MAS (pre-incubated to 37 °C) was added to obtain a final volume of 175 µL per well. After instrument calibration, the loaded assay plate was inserted for analysis. Briefly, it involved cyclic steps of mixing, sequential injections of substrates and inhibitors via Ports A through D, equilibration, and duplicate measurements of the oxygen consumption rate (OCR) through fluorometric optical probes.

Untrustworthy measurements were removed by Tukey's test for outliers at every subsequent measurement. In the cleaned data set, respiratory control ratios (RCR) were calculated by dividing the OCR obtained from State III respiration values (maximal phosphorylating state in the presence of pyruvate, malate and ADP) by State IV respiration values (OXPHOS-inhibited state in the presence of oligomycin).

4.2.8 Complimentary GC-TOF-MS and ^{1}H-NMR Metabolic profiling

Untargeted measurement of standard compound mixtures and sub-cellular fractions obtained from whole brain homogenates of *Ndufs4* (n = 3) WT mice were performed. The analytical techniques used were previously described and comprised untargeted gas chromatography time-of-flight mass spectrometry (GC-TOF-MS) (Lindeque et al., 2013), and miniaturized proton nuclear magnetic resonance (^{1}H-NMR) spectroscopy (Mason et al., 2018). The data obtained in this study (Van der Walt, 2019) can be accessed at the NIH Common Fund's Data Repository

and Coordinating Center (supported by NIH grant) website, the Metabolomics Workbench, http://www.metabolomicsworkbench.org.

4.2.8.1 Extract preparation and derivatization

Quality control (QC) samples were prepared from aliquots of all samples within a batch. Standard compound mixes and muscle extracts for NMR were prepared according to the recently established miniaturized protocol (Mason *et al.*, 2018) as follows: After 12,000 ×*g* centrifugation in Centrifree 30 kDa cut-off filters (Merck/Millipore, USA) at room temperature to remove proteins and other macromolecules, 54 µL of the 60 µL originally loaded (100 µL for standard mixes) remained to be transferred to a 2 mm NMR tube using the eVol® NMR digital syringe (Sigma-Aldrich) equipped with a 100 µL bevelled-tip needle. The programmed pipetting sequence of the digital syringe added phosphate-buffered 3-(trimethylsylil)-propionic acid (98% TSP D4 Na^+-salt; #269913, Merck/MagniSolv™, DEU) and N,N-Dimethyl-L-phenylalanine (99% DMPA; #273910, Sigma-Aldrich) or 3-phenylbutyric acid (98% 3-PBA; #116807, Sigma-Aldrich) internal standard for ^{1}H-NMR; as such that a 10:90% ratio of D_2O:H_2O was maintained as per standard protocol. The 2 mm NMR tube was inserted into the gripper-adaptor of the Bruker MATCH system, before each NMR MATCH assembly was loaded onto a SampleXpress autosampler for NMR analysis.

Metabolite extraction for GC-TOF-MS was achieved using a modified monophasic Bligh–Dyer extraction method (Gullberg et al., 2004) with a solvent ratio of 3:1:1 (methanol:water:chloroform) (chromatography grade, Burdick & Jackson). All extractions were done on ice to minimize further metabolic interactions. The selected standard, 3-PBA was added in a fixed concentration to each sample, consisting of the remaining 60 µL mitochondrial/150 µL cytosolic fractions (or 100 µL standard compound mixture). Tissue extracts/standard compound mixtures were dried under nitrogen. Oximation of the ketone groups in the dried extracts was achieved through incubation in 25 µL of methoxamine hydrochloride [#226904, Aldrich (98%)] (20 mg/mL in pyridine [#270970, Sigma-Aldrich, USA]) at 60 °C for 1.5 hours. Thereafter, 25 µL of a pre-mixed dilution of 1% TMCS in BSTFA [#15238, Sigma (99%), USA] was added before incubation under the same conditions for 1 hour to silylate polar hydrogen containing groups. For the metabolite standards, 50 µL of each derivatization reagent was used. The derivatized samples were subsequently transferred to 250 µL pulled-point inserts, placed back into screw-cap vials and loaded onto the 7693 Autosampler (Agilent, USA).

4.2.8.2 Instrumentation and analysis parameters

NMR measurements were conducted at 500 MHz on a Bruker Avance III HD NMR spectrometer equipped with a 5 mm triple resonance inverse (TXI; ^{1}H, ^{15}N, ^{13}C) probe head optimized for ^{1}H observation. Briefly, ^{1}H spectra were acquired as 128 transients in 32K data points with a spectral width of 6000 Hz (12.0 ppm). The H_2O resonance at 4.70 ppm was suppressed using the pulse sequence programme NOESY-presat. The number of dummy scans (4) and number of scans (128) yielded a run time of 15.765 minutes per sample. These settings follow those given by established SOPs (Mason *et al.*, 2018). Each sample was automatically shimmed on the deuterium signal, locked, probe tuned and matched, and pulse calibrated using Bruker Topspin (V3.5); then further processing was conducted using Bruker AMIX (V3.9.14).

A GC-TOF-MS system, comprising a LECO Pegasus TOF-MS with Agilent A980 front end was used as described (Lindeque et al., 2013). Helium was used as carrier gas at 1.5 mL/minute flow while 1 µL sample was injected in split-less mode (allowing 30 seconds purge delay). The inlet temperature was kept at 250 ˚C. Compounds were separated on an RTX-5MS column (30 m x 0.25 mm x 0.25 µm), with an apolar, fused silica phase (#12623-124, Restek, USA). The transfer line and source temperature were 225 and 200˚C, respectively. A solvent delay of 330 seconds was allowed, whereafter masses (50 – 900 m/z) were recorded at 20 spectra/second. Universal EI (electron impact ionization) settings were used for fragmenting compounds prior to spectral collection, while the detector was operated at 50 V above tune voltage.

4.2.8.3 Data extraction and processing

All data processing was done using Excel 2013 (Microsoft). Spectral data obtained from the analytical platforms were extracted into matrices. For GC-TOF-MS data, this process was preceded by peak alignment and deconvolution (ChromaTOF). Data matrices were manually inspected (correct peak picking and alignment, batch effect and data integrity) before an 80% zero-filter and 50% CV filter were applied. Peak intensities were normalized to 3-PBA (GC-TOF-MS data) or DMPA (^{1}H-NMR data). No batch corrections were needed as the QCs showed no significant drift effects. %CV, linear coefficients and/or percentage recovery was calculated for the standard samples. For the biological samples, %CV was calculated and qualitatively inspected to comment on the applicability of the proposed workflow to each platform. Identities of varied confidence level (Schymanski *et al.*, 2014) were manually assigned to metabolites based on the NIST11 and our own in-house spectral library.

4.3 Results and Discussion

To produce cellular fractions applicable to metabolomics, balance must be achieved between analytical parameters (purity, yield, integrity, etc.) and practical factors, such as time and cost to ensure reproducibility (Liu & Xu, 2018). To that end, we set out to adapt a MACS-based fractioning pipeline to meet these criteria and prove the analytical superiority thereof (compared to a recent DC workflow (Pan *et al.*, 2018)) for downstream metabolomics in animal disease models. Brain tissue was selected for method development, as it presents abundant mitochondria and central involvement in the selected disease phenotype (Lake *et al.*, 2015), also enabling extrapolation of the methodology to mammalian models of more common mitochondria-linked neuropathies (Hall & Roberson, 2012; Jin *et al.*, 2008).

4.3.1 Establishment of MACS-based fractioning workflow for application in mouse tissues

4.3.1.1 Protocol variations produce mitochondrial isolates of sufficient yield

The amount of antibody available per tissue weight has been proven a critical limiting factor to the yield obtained. As such, an optimal dilution (1.5 µL /mg wet tissue) was selected from recently published data (Hubbard *et al.*, 2019) as to find a balance between yield and reagent cost. The mitochondrial elution phase, meant to purge labelled organelles from the demagnetized column post-isolation, also proved to be a significant bottleneck step. Initial trials yielded up to three times more mitochondria based on CS enrichment after flushing the magnetic column three times (Figure 4-4; Section 4.5.1) – compared to a single flush with 1x SB as prescribed by the kit. Hence, this adaptation was included into the final methodology.

For comparing DC and MACS yields, the same homogenate was split immediately before both simultaneously performed isolation strategies to eliminate differences in biological substrate/inhibitor or enzyme concentrations. As citrate synthase is a well-known, definite marker of mitochondrial matrix content, not found in any other compartment, the readout is thus accepted as a qualitative determination of differences in mitochondrial yield for these two methods. Kinetic enzyme analyses were conducted simultaneously on the same reaction plate utilizing optimized and identical substrate concentrations. When comparing DC and FMMS using brain tissue, patterns of mitochondrial distribution differ between the two methods at pivotal points in the fractioning process, indicated by percentage of the matrix-specific CS enzyme from the homogenate present in each fraction (Figure 4-1). For the given parameters, higher relative mitochondrial yields were achieved using the MACS kit (~27%) compared to DC (~14%). This corroborates the data of similar CS enrichment experiments (~19 – 23%) using

MACS-isolated brain mitochondria (Franko *et al.*, 2013; Hubbard *et al.*, 2019), indicating no significant decrease in yield for the given methodological alterations. A large amount of organelles are not bound by the optimized antibody concentration (~11,5%), taking into account that synaptic mitochondria are also lost in the flow-through without disruption of their containing synaptosomes (Brown et al., 2004; Hubbard et al., 2019). Saturating all non-synaptic and synaptic mitochondria is possible, but not feasible for a robust metabolomics workflow, since manual disruption of synaptosomes and up to eight times the manufacturer specified amount of antibody is needed for such application (Hubbard et al., 2019).

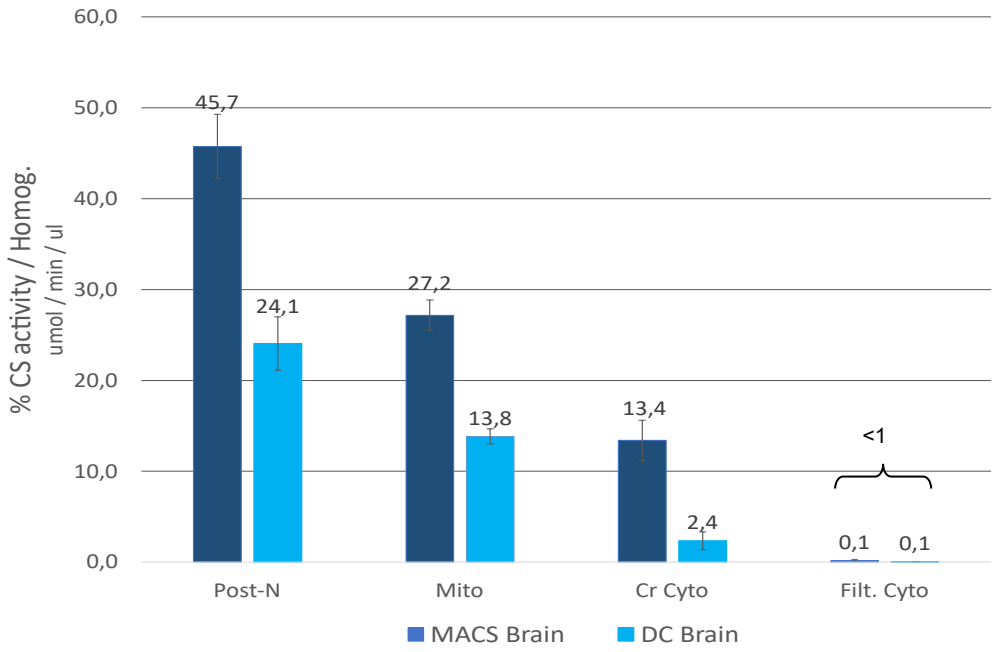


Figure 4-1: Comparison of mitochondrial enrichment from brain tissue for DC and MACS methods (n=3). The CS activity of each fraction is expressed as a % of the CS activity captured from the preceding homogenate. Post-N: Post-nuclear supernatant, Mito: enriched mitochondria, Cr. Cyto: crude cytoplasm, Filt. Cyto: 100kDa filtered cytosol.

The initial nuclear pelleting step accounts for a significant portion (~55 – 75%) of the yield lost, for both methods. Although repelleting and another round of centrifugation could release more of the organelles trapped in the large cell debris for any of the two methods (Liu & Xu, 2018), the single-step approach applied during MACS isolation yields more brain mitochondria than the patented three-step method for DC-enrichment, contradicting the data published for yeast cells (Pan *et al.*, 2018).

Furthermore, preliminary tests using quadricep muscle revealed differential patterns of mitochondrial loss at different steps in the workflow (Figure 4-5; Section 4.5.1), emphasizing the role of tissue-specific confounding factors in optimizing homogenization/fractioning parameters. The highly filamentous nature of skeletal muscle mitochondria likely causes greater obscurement of TOM-22 epitopes from antibody binding than expected for the more dynamic

neural mitochondria (Picard *et al.*, 2013; Vendelin *et al.*, 2005), therefore, substantially more muscle-derived organelles are left unlabelled and end up in the column flow-through.

The limitations in this approach include the effect of even minimal differences in CS inhibitor concentrations present, as well as the inability to accurately probe mitochondrial protein content against the background of antibodies and protein contributed by the 1x SB. The former issue was minimized by utilizing a single split homogenate for every DC and MACS experiment compared. The KCIEM buffer contains no known CS inhibitors, while the MACS buffers are also not stated to contain any such compounds (Hornig-Do *et al.*, 2009). Regardless, minute differences may occur, and without concomitant analyses of a purified enzyme standard in a spectrophotometrically optimized buffer, these results remain majorly qualitative. It must also be stated that volumetric normalization, as used here, is also only valid given the homogeny of the samples analyzed and the comparative nature of the information desired. Issues regarding measurement of protein content in MACS samples, alternative buffer systems and the effect of their constituency on purified CS must, therefore, be addressed for any future experiments that necessitate absolute quantification of CS activity.

4.3.1.2 Novel filtering approach depletes residual organelles to produce cytosolic fractions

The MACS-derived crude cytosolic/cytoplasmic fraction to be used for comparison still contains significant amounts of mitochondria (~13%), which may skew the metabolic profile observed. Specialized centrifugal filters with descending 100 kDa filter membranes were used to remove these and other large organelles whole, as the filter design substantially decreases the risk of membrane blockages and/or resultant rupture of organelles (in comparison to traditional spin columns). Mitochondrial depletion can be visualised as the absence of the matrix-bound chaperone, Hsp 60 (Figure 4-2; raw blot images in Figure 4-6). This indicates that most whole mitochondria were removed. Ruptured organelles would have freed the 60 kDa Hsp to pass through the membrane filter and be detected in the filtered fraction (Cheng *et al.*, 1989). Similarly, the 52 kDa CS enzyme would be able to freely pass the filter (Shepherd & Garland, 1969). Therefore, the minimal (< 0.3%) CS activity we detected in the filtrate (cytosol fraction) also indicates negligible amounts of mitochondrial rupture and efficient depletion of the organelles and their content through this approach.

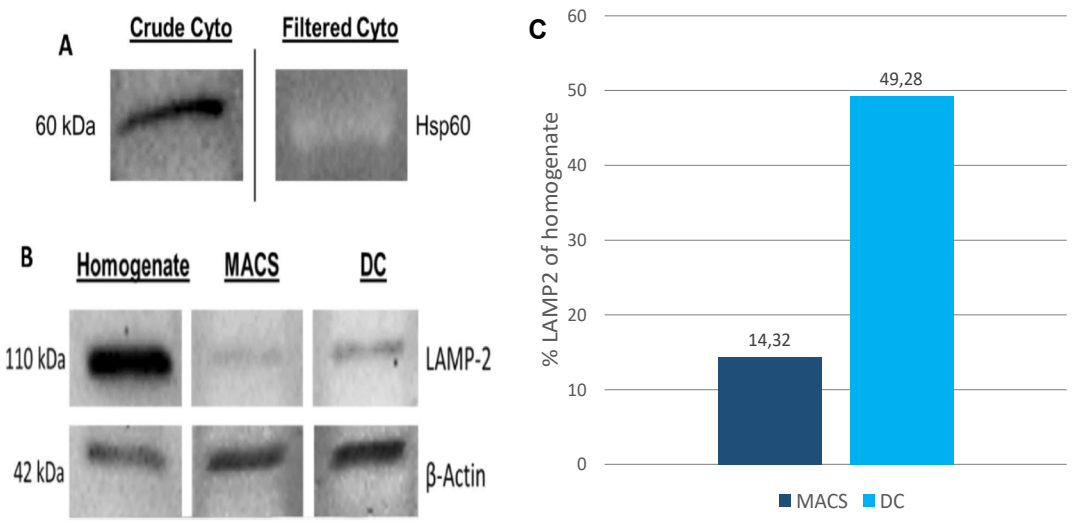


Figure 4-2: Comparison of fraction purity of DC and MACS methods by immunoblotting against compartment-specific proteins. Western blots depicting **A**) a comparison of mitochondrial depletion (Hsp60) in cytosolic fractions pre- and post-filtering and **B**) lysosomal depletion (LAMP-2) in MACS or DC mitochondria, compared to the whole homogenate (with β-actin as loading control); **C**) total-protein normalized LAMP-2 volume, expressed as a percentage of that detected in the preceding homogenate.

4.3.1.3 Mitochondrial purity and integrity unaffected by selected protocol adaptations

Substantial evidence exists regarding the superior purity of MACS mitochondria, compared to DC isolates, where protein-level proof of superior endosomal, nuclear, cytosolic and lysosomal depletion in the final mitochondria has been presented in several cases. (Franko *et al.*, 2013; Hornig-Do *et al.*, 2009; Hubbard *et al.*, 2019; Lee *et al.*, 2019). In that regard, the comparable depletion of LAMP-2 (Lysosomal membrane protein) in our MACS isolates serves as substantial proof that the selected protocol alterations do not negate the previously established purity of the method (Figure 4-2, Figure 4-6). Minute amounts of LAMP-2 detected by western blotting (~14%) corroborates previous results, owing rather to unbound variants of the protein detected than significant presence of the whole organelles (Chen *et al.*, 2016).

A higher respiration control ratio (RCR) is indicative of higher respiratory capacity, less proton leak over the inner-membrane and thus a more intact mitochondrial inner membrane (IMM) (Brand & Nicholls, 2011). Previous respiration experiments on organelles isolated by either MACS or DC have shown comparable RCR's for both methods (Franko *et al.*, 2013; Hubbard *et al.*, 2019). Our findings corroborate this well; an average RCR of 6.14 (CV = 9.47%) and 7.35 (CV = 7.54%) for MACS and DC isolates, respectively, being an acceptable indication of good respiratory coupling and IMM integrity.

The slightly lower RCR for MACS mitochondria, relative to the DC method, might indicate marginally higher mitochondrial uncoupling in these fractions. It is well known that mitochondria uncouple over time, thus the longer MACS isolation process can potentially account for the marginally lower RCR measured in the MACS samples. However, this may also be a purely analytical effect, owing to the differential buffer environment, in which the respective isolates are produced (Franko *et al.*, 2013). Nevertheless, the extensive CS experiments described above deliver further proof on mitochondrial integrity, as the absence of CS activity in the filtered cytosol is indicative of minimal IMM rupture. Furthermore, CS assays of the MACS post-mitochondrial supernatant also reveal minimal to no matrix content leakage (<1% CS) towards the very end of the experimental workflow. Combined, the data presented here provide different levels of substantiation for the analytical purity and integrity of mitochondria isolated via the adapted protocol, as well as the purity of the collected cytosolic fraction.

4.3.2 Effect of MACS buffers on GC-TOF-MS and NMR metabolomics

Previous reports indicate that mitochondrial isolation buffers, typically containing a high concentration of buffer salts, can significantly impact the measured metabolite concentration in isolates (Corcelli *et al.*, 2010; Liu & Xu, 2018; Pan *et al.*, 2018). NMR probing of the MACS kit buffers indicated the presence of ethanol, glycerol, protein and EDTA in either the kit lysis or separation buffers. According to the cornerstone publication of the kit (Hornig-Do *et al.*, 2009), substantial amounts of buffering salts constitute the base of the separation buffer, the predominant feature of the final sample mixture. In that regard, we set out to determine the effect of this buffer environment on the qualitative and/or quantitative analysis of nine commercially available, common metabolic intermediates tandemly, on both selected platforms.

For NMR analysis, effects on absolute quantification were determined by comparison against the same metabolites measured in a water environment, as per universal SOP's (Beckonert *et al.*, 2007; Dona *et al.*, 2014; Mason *et al.*, 2018). In an untargeted GC-MS experiment, however, investigation of precision and quantitative linearity in the MACS buffer were deemed sufficient.

4.3.2.1 GC-TOF-MS analysis of standard compounds in MACS environment

Ten technical replicates of the metabolite standard solutions were analyzed at a low (50 µM), medium (250 µM) and high (500 µM) concentration to determine whether any part of the untargeted metabolomics workflow (i.e., metabolite extraction, derivatization or chemical analyses) is significantly affected by the MACS environment.

4.3.2.1.1 Analytical precision

As an indication of measurement precision, %CV was calculated for each compound at the different concentration levels. These results (Table 4-1) were weighed against the pre-defined 50% limit for variation in GC-MS untargeted metabolomic studies (Dunn 2012). For the majority of metabolites, a variation far below these standards can be seen (CV < 22%; except for aspartic acid), indicating excellent stability of these compounds and their measurement in the buffer environment. The high ionic strength owed by the salts in the buffer seem to confer a stabilizing effect upon alpha-ketoacids such as pyruvate (CV = 4 – 12%), which are known to be notoriously unstable in the GC-MS environment (Mamer *et al.*, 2013; Tsai, 1967). However, this iconicity does incur drawbacks as well, as indicated by the measured values for aspartate. The ionic environment may induce salt adducts during ionization, possibly even linking salt bridges between other free amino acids or those present in the buffer-based protein (Bissantz *et al.*, 2010; Luo *et al.*, 1999). Thus, it is proposed that the same standard analyses be completed for specific compound classes of interest in subsequent experiments.

Table 4-1: Precision and quantitative linearity of selected standards in MACS buffer environment, analyzed by GC-TOF-MS. Variance is expressed as %CV for EDTA-normalized measurements at each concentration level, while the R2 value indicates linearity.

%CV	Low (50µM)	Med (250µM)	High (500µM)	Linearity (R^2)
Pyruvate	10.0	6.7	7.0	>0.99
Lactate	12.0	7.5	4.4	>0.99
2-Hydroxybutyrate	4.0	4.3	5.1	>0.99
3-Hydroxybutyrate	3.7	4.8	5.8	>0.99
Glycine	9.4	18.9	21.6	>0.99
Alanine	6.6	13.3	4.6	>0.99
Valine	4.3	4.9	6.7	>0.99
Aspartate	60.3	32.6	19.3	>0.99
Glutamate	N.D.	19.9	6.1	0.85
3-Phenylbutyrate	47.6	49.4	36.4	
EDTA	8.04	6.16	7.29	

It should be noted that the selected internal standard, 3-PBA, has consistently been shown to perform poorly in the MACS buffer for GC-TOF-MS (CV = 36.4 – 49.4% in comparison to < 15% for most other compounds) and NMR analyses (see section 4.3.2.2.). Due to the lack of an

efficient internal standard at the time of analyses, a stable component in the buffer itself was utilized for normalization, as all samples were diluted in the same concentration of the separation buffer prior to analyses, EDTA was selected as the measured amount showed excellent inter- and intragroup consistency (6 – 8% CV intragroup and <3% difference in means between groups). Thus, for the purposes of these standard compound mixtures only, it fulfilled the criteria for an applicable internal standard, correcting for differences in extraction, derivatization, injection and/or chemometrics. Henceforth the selection of internal standards for subsequent experiments should also be based upon critical analysis of their stability and applicability to specific subsequent experiments (Chen *et al.*, 2016).

4.3.2.1.2 Linearity

Linear least squares regression was applied to the normalized intensities for each sample. A linearity coefficient cut-off of > 0.95 was selected as criteria for determining the performance of measurement over increasing concentration; these results are also described in Table 4-1. Almost all compounds show excellent linearity (>0.99), except for glutamate, which was not detectable at the lowest concentration (Figure 4-7). Glutamic acid is known to spontaneously convert to pyroglutamic acid, which might explain the generally lower amounts thereof measured at every concentration and the linear increase in pyroglutamate, although not being an addition of the sample itself. Linearity is expressed for one of three aspartic acid peaks (R.T. = 812s; m/z = 70) observed at different retention and mass-to-charge ratios, since the other related peaks showed poor quantification at the medium and low levels (Figure 4-7). This is most likely also due to differential ionization of extracted aspartate in the highly saline environment. All these confounding chemical factors are to be taken into account and preferentially corrected by similar standard analyses when amino acids or other polyionic compounds are the target of analyses.

4.3.2.2 ^{1}H-NMR analysis of standard compounds in MACS buffer vs SOP aqueous environment

NMR is known to be a far more precise platform than mass spectral methods, this enables absolute quantification of compounds using a stable internal standard, as virtually no chemical modification of samples are necessary (Beckonert *et al.*, 2007). We set out to determine the effects of the MACS buffers on quantification via a recently developed miniaturized ^{1}H-NMR protocol for limited-volume samples (Mason *et al.*, 2018). The aim here was to evaluate the same parameters as in the GC—TOF-MS analyses (precision & linearity). The additional parameter of measurement accuracy, relative to samples analyzed strictly via SOP in a water

environment, was also investigated to emphasize the applicability of NMR analyses as a valuable quantitative extension to the workflow.

Since the analytical stability of the internal standard is a critical criterion for enabling absolute quantification, lessons learned from the GC—TOF-MS analyses instigated an evaluation of different internal standards in the given sample matrix (Figure 4-8). Traditional TSP standard was shown to be affected by the high ionic environment in a concentration-dependant manner, while 3-PBA quantities are exaggerated similarly at all three levels. This resulted in lower precision (CV > 30%) and variable recoveries that do not coincide with the given sensitivity of NMR. Contrarily, DMPA performed adequately in this environment, leading to acceptable precision, accuracy and linearity. Thus, this compound was selected as internal standard for all subsequent analyses, in line with previous studies (Terburgh *et al.*, 2019; Van Aardt *et al.*, 2016).

4.3.2.2.1 Analytical precision

A precision cut-off point was determined at each concentration (5% and 10% for high and medium concentrations, respectively, while 15% was deemed sufficient at the lower concentrations that lie close to the limit of detection). These values are below the 15% or 20% (low concentration) FDA standards for targeted analyses (FDA, 2001) and far below the 50% cut-off for untargeted studies (Dunn *et al.*, 2012). As indicated in Table 4-2, all metabolites performed within these chosen bounds of precision, with the exception of aspartate and glutamate at the lowest concentration. This effect can be seen in both MACS and water-based samples, and rather owes to the instability of these compounds at concentrations close to detection limits, as also indicated by the coincidental GC-TOF-MS analyses. Researchers conducting further studies along this line should also take possible chemical shifts in a high-ionic environment into account, as other electrolytes may induce changes in resonant frequency absorbed/measured for certain chemical groups (Lindon *et al.*, 1999; Wang & Bax, 1993). These results once again emphasize the need for compiling and analysing a mixture of standard compounds applicable to the intended goal of any subsequent study.

Table 4-2: Comparison of precision (%CV) and relative recovery of standard compounds analyzed via ^{1}H-NMR in either MACS buffer environment or pure water (SOP) at low, medium and high concentrations (n = 10). Relative recovery (MACS buffer quantity vs water) is indicated in parentheses.

%CV and %Rel. recovery	Low (50 µM)		Medium (250 µM)		High (500 µM)	
	MACS	dH_20	MACS	dH_20	MACS	dH_20
Pyruvate	10.6	6.3	1.2	1.4	1.3	1.3
	(83-104)	(93-119)	(103-107)	(95-100)	(97-101)	(98-103)
Lactate	14.9	8.7	1.9	1.9	0.8	1.8
	(99-115)	(96-112)	(100-106)	(97-103)	(98-101)	(97-104)
2-Hydroxybutyrate	14.0	12.4	3.2	4.0	1.0	2.2
	(107-119)	(92-108)	(99-109)	(90-105)	(97-101)	(96-103)
3-Hydroxybutyrate	9.2	8.9	2.0	4.0	0.8	1.7
	(80-106)	(87-120)	(97-103)	(94-106)	(98-101)	(97-104)
Glycine	9.4	14.5	10.1	5.0	3.0	2.2
	(137-245)	(89-162)	(87-114)	(88-105)	(97-106)	(96-102)
Alanine	12.0	8.1	2.3	1.7	0.9	1.5
	(104-115)	(89-120)	(109-117)	(108-114)	(108-111)	(110-115)
Valine	7.5	7.8	2.0	1.8	1.0	1.0
	(100-114)	(94-118)	(99-106)	(96-103)	(97-101)	(100-103)
Aspartate	34.4	27.7	14.3	17.2	4.6	8.2
	(99-249)	(61-199)	(78-138)	(52-111)	(93-107)	(85-113)
Glutamate	25.1	23.1	7.6	8.5	3.0	4.1
	(97-203)	(74-139)	(92-110)	(93-107)	(95-106)	(93-107)

4.3.2.2.2 Relative accuracy

As an indication of the buffer's effect on the inherent quantitative power of the platform, all measurements were expressed as a percentage of the measured average for a given compound in the SOP water environment (Table 4-2), this average value being designated as 100% recovery. Acceptance criteria were set as 80 – 120%, in line with previous similar studies

(Chan *et al.*, 2004; Mason *et al.*, 2018). Excellent relative accuracy was shown for the DMPA-normalized compounds, with aspartate once again being the sole outlier at all three concentrations. Glutamate and Glycine also fall outside these bounds, only at the lowest concentration; most likely due to spectral noise having a larger impact on measurements close to the lower limit of detection (LLOD). The value of investigating both parameters is evident from glycine, as high precision and low accuracy measurements may occur for certain compounds, impacting quantification unbeknownst to the analyst only equipped with one of these criteria.

4.3.2.2.3 Quantitative linearity

Linear regression was applied to each compound at the three concentration levels, similar to that described in Section 4.3.2.1.2. In this case, the linearity graph for each compound in MACS buffer was overlayed with that for the same analyte in the SOP water environment (Figure 4-9). All compounds performed with acceptable linearity ($R^2 > 0.99$), although the ionic effects upon aspartate, glutamate and glycine as described above clearly influence quantification, indicated by the offset of the MACS linearity graph from that of the water-based SOP in these three compounds. Overall, it can be concluded that NMR analyses in MACS buffer performs acceptably on the grounds of precision, linearity and accuracy relative to SOP conditions, although the value of investigating quantitative effects upon metabolites of interest for further studies are emphasized by these results.

4.3.3 Applicability of selected methodology to mouse model tissues

The following objective entailed a pilot application of the developed methodology on mouse models of disease, specifically WT mice from the complex I-deficient *Ndufs4* cohort. To prove that the methodology can be extrapolated to other genetic animal models, 100 mg whole brain from a single animal was subjected to the developed fractioning workflow, after which the mitochondrial and cytosolic samples were split for limited-volume analysis on either GC-TOF-MS or NMR, to probe the number of features visible, as well as their analytical performance. It should be noted that a 90-minute isolation procedure inevitably incurs metabolite turnover, as the quickest metabolic processes still proceed, albeit at much slower rates, even at the 0-4 °C temperatures applied throughout. Each isolation was, however, performed in an experientially fixed timespan of 90 minutes and all metabolite extractions were performed in small batches, with minimal time elapsing between each sample. Thus, metabolite turnover in each sample was accepted to be equivalent, and given that only comparisons between different fractions of each sample were of importance, these parallel changes yielded no considerable changes in analysis repeatability.

4.3.3.1 Pilot GC-TOF-MS analysis of mitochondria and cytosol

Of the ~120 µL mitochondrial extract, 60 µL was subjected to metabolite extraction and derivatization, as described in Section 4.2.8.1., 150 µL of the voluminous cytosolic extract was prepared similarly. After analysis (technical triplicates of each fraction), peaks showing unstable measurement in the QC's (CV > 50%) were removed. Features attributed solely to the buffer environment were subtracted from the matrix. Feature IDs were assigned by automatic spectral database matching done by the ChromaTOF software, before being manually annotated and curated. Known derivatization/ionization artefacts and products of overdeconvolution were also removed to deliver a final list of 29 confirmed metabolites [levels 1 to 3, according to Schymanski *et al.* (2014)] for the mitochondrial and cytosol, respectively. Variation < 50% for all compounds indicates the repeatability and precision of these measurements, as an average CV of 16.7% and 19.6% was achieved in the mitochondria and cytosol, respectively.

Seventeen peaks of sufficient signal to noise ratio and spectral match for annotation were shown to be common to the two fractions (Figure 4-3), while 12 compounds unique to each respective fraction were also detected and annotated with sufficient confidence. Diligent annotation with more specialised libraries or larger sample volumes could clarify the unknown features detected, however, they may represent novel compounds to our libraries. In that regard, further analyses of applicable metabolite standards may be a pre-requisite for subsequent studies. Of the features positively identified, several metabolites commonly perturbed in bioenergetics dysfunction were found (Esterhuizen *et al.*, 2017; Gielisch & Meierhofer, 2015).

A list of metabolites found in this study, and their ID confidence levels, are available (Table 4-3). Compounds present in both fractions included organic acids such as lactic-, malic-, oxalic- and octadecanoic acid. The sugar alcohols erythritol and myo-inositol, along with amino acids such as alanine, aspartate, glycine, glutamate and 3-methyltyrosine were also detected as common features. Fraction specific compounds detected (Table 4-4), include proline, serine, threonine and cytosine norleucine in the mitochondria; and succinate, urea and 5-hydroxytryptophan in the cytosol. Despite only confirming ±30 features, possibly due to minute sample volumes approaching the inherent detection limits of the GC-TOF-MS system, this trial analysis proves the possibility of identifying several compounds of significance in limited-volume samples of purified cytosol and mitochondria from disease model animals. Strategies for sample concentration or consideration of more sensitive techniques such as 2D-GC-TOF-MS may serve to overcome this issue.

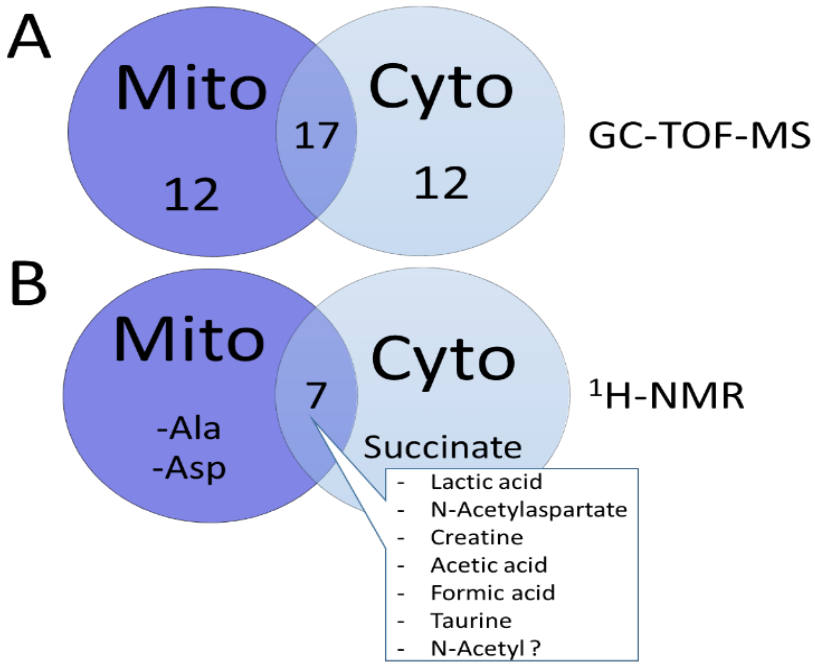


Figure 4-3: Comparison of features detected in the mitochondrial (n = 1; 3 replicates) and cytosolic (n = 1; 3 replicates) fractions of *Ndufs4* WT mouse brain by **A**) untargeted GC-TOF-MS and **B**) ^{1}H-NMR. Text in the circles represents features unique to each fraction, while that in the intersection represents the positively identified compounds common to both.

4.3.3.2 Probing the applicability of a limited-volume ^{1}H-NMR protocol

The application of precise and repeatable ^{1}H-NMR spectroscopy compliments more comprehensive but variable mass spectrometry analyses by being able to quantitatively confirm significant effects found by MS (Dunn *et al.*, 2011). As such, the remaining 60 µL mitochondrial sample and triplicates of the remaining cytosol were subjected to minimum-prep ^{1}H-NMR investigation designed for limited-volume extracts (Mason *et al.*, 2018). An untargeted approach was followed, wherein deproteinized and buffered samples were analyzed and the resulting metabolite spectra quantified over 376 spectral bins of 2 ppm each (excluding the water region).

Nine compounds were quantified with high relative accuracy in the brain mitochondria of the animal, while eight were detected with sufficient precision (CV < 10%) in the cytosol (Figure 4-3). Taurine is the only exception, at 13% CV, however, this compound is known to be more unstable than most under conditions of NMR analysis (Hohmann *et al.*, 2014). Metabolites significant in studies of bioenergetics-related diseases, such as lactate, succinate, creatine, alanine and aspartate, were detected. The presence of lactate in the mitochondrial fraction confirms the recently theorised notion that this common metabolite is not only found in the cytosol but can be readily imported and utilized in the mitochondria of certain tissues (de Bari & Atlante, 2018; Passarella & Schurr, 2018). An important intermediate of brain metabolism, N-

acetylaspartate, was detected (Moffett *et al.*, 2007; Tsai & Coyle, 1995), as well as an unidentified N-acetyl compound, indicating a possible novel compound for study. Although these compounds are few in numbers, they indicate the possibility of application in further studies as a complimentary quantitative measurement for the most abundant compounds in a given sample.

To our knowledge, this is the first successful application of NMR sub-cellular metabolomics to limited-volume extracts from small disease model animals, generally thought to be impractical due to the platform's inherent insensitivity. Indeed, our initial trial runs using the manufacturer supplied tissue protocol and quadricep muscle from *Ndufs4* WT mice did not detect any compounds at all; however, upon application of the described yield increasing optimizations, six mitochondrial compounds could be detected even in these tissues (Figure 4-10), known to possess far fewer mitochondria than the neural matrix (Esterhuizen *et al.*, 2017; Paul & Sperling, 1952). Far more sensitive setups, than the general 500 MHz machine used here, exist; 1.2 GHz spectroscopes have been developed, and cryoprobe technology also allows up to a tenfold increase in sensitivity (Fratila & Velders, 2011; Glaves *et al.*, 2014). Laboratories with access to such setups will naturally detect far more compounds; thus, this study exists only as an indication of future possibilities in this line of enquiry.

4.4 Conclusion

Here we outline a novel adaptation of commercially available FMMS-based mitochondrial isolation and cytosol filtering for sub-cellular metabolomics in a mouse model of MD, contributing to the currently restricted arsenal that investigators have at their disposal for determining compartment-specific effects in diseases related to altered mitochondrial metabolism. The selected MACS methodology outperforms standard DC methods on the grounds of brain mitochondria yield (~60% more) and purity (~35% LAMP-2 depletion), as indicated by CS assays and western blotting, respectively. MACS mitochondria show comparable integrity to the DC isolates, with RCR's of 6 and 7 being indicative of sufficient IMM coupling (Franko *et al.*, 2013). The significant addition of a simple and cheap filtering method for purifying the cytoplasm of remaining organelles to produce a cytosolic fraction (<0,1% CS) will allow a true comparison of pools and fluxes between these organelles, and the perturbation thereof in disease. For further application, our results have indicated the homogenization and preliminary debris-clearing centrifugation steps as critical targets for further optimization as they display tissue-specific patterns of yield loss.

Through the measurement of nine standard compounds, commonly found in brain tissue, the effects of the MACS buffers were shown to not be of significant detriment to chemical analyses,

as is often the case for metabolomics in highly ionic isolation buffers (Liu & Xu, 2018). GC-TOF-MS analysis in this environment proves applicable for most compounds, as indicated by high measurement precision (CV < 22%) and linearity over three concentration ranges (R^2 > 0.99). Similarly, for NMR analyses, precision (CV < 10%, or 15% at low levels) and quantitative linearity (R^2 > 0.99) was achieved in the buffered samples at acceptable limits for this highly precise platform. Recovery between 80–120% for most compounds infers high relative measurement accuracy, further proving the quantitative value of NMR analyses in compartment-specific studies. However, it is evident that metabolites of various chemical nature are differentially affected by the buffers, including internal standards such as 3-PBA and TSP. Therefore, no future study should proceed without in-depth evaluation of analytical standards for the compound classes in question, and their performance on the selected platforms.

The developed workflow was applied to a healthy control of a PMD mouse model to indicate applicability of the methodology to tissue-based studies in disease research. GC-TOF-MS analysis detected 60-70 compounds of sufficient stability (CV < 22%), encompassing metabolites commonly perturbed in MD, as well as some unidentified features that may represent novel targets for study. The unprecedented application of miniaturized ^{1}H-NMR metabolomics to limited-volume sub-cellular extracts also opens new possibilities for complimentary quantitative data in compartment-specific studies, as our relatively low sensitivity setup could measure six to ten abundant metabolites with high relative accuracy (1–15% CV) in these fractions. It should, however, be noted that it is not possible to accurately measure mitochondrial protein content against the background of antibodies and protein contributed by the 1x SB, thus, normalization of metabolomics data to protein content is not possible. Therefore, other normalization strategies should be followed, like the use of internal standards as utilized in this study or even MS total useful signal (MSTUS) normalization (Warrack *et al.*, 2007).

This study is by no means analytically perfect but serves as a template pipeline to laboratories of every financial and analytical status. It extends the usefulness of MACS technology to application in sub-cellular metabolomics, providing a midway between expensive recombinant immunopurification techniques and rudimentary centrifugal methods, while also proposing a simple solution to producing comparable cytosolic fractions. A combination of simple and robust workflow, inexpensive commercially available fractioning equipment and standard metabolomic platforms is intended to inspire increased outputs in compartment-specific metabolomics universally, to grow and refine this niche field of research substantially in the coming years.

4.5 Supplementary Results

4.5.1 Detailed CS yield and protein results

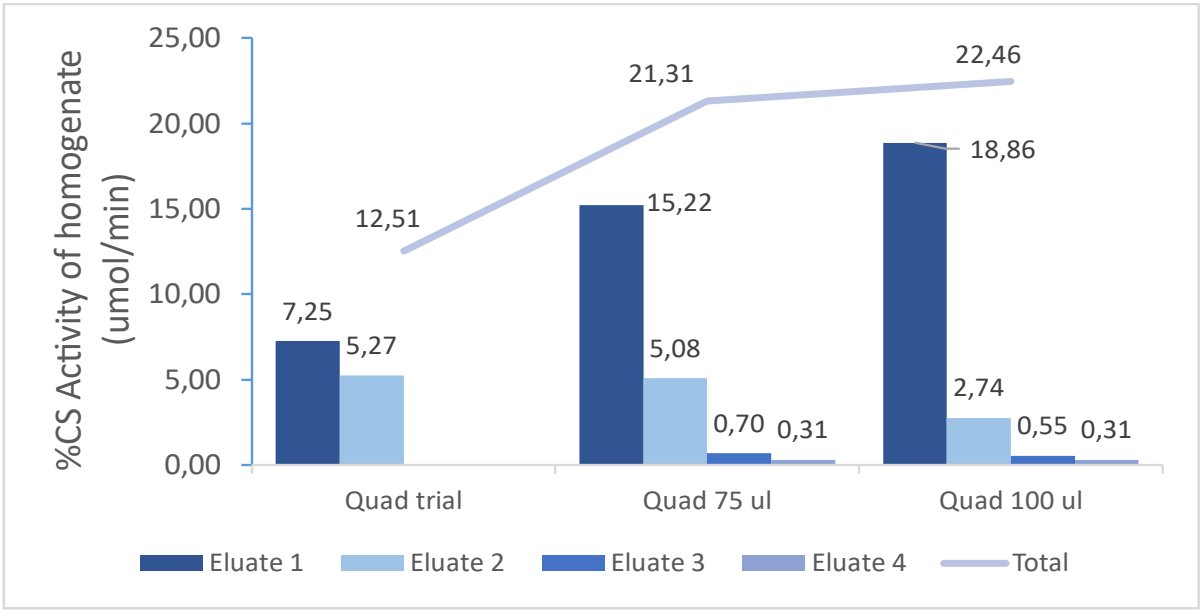


Figure 4-4: Selection of antibody dilution and mitochondrial elution parameters for quadricep muscle tissues (150 mg). The graph shows the effect of increasing the number of times mitochondria are flushed from the column post-isolation, as well as increasing the amount of antibody used for the same tissue weight. Yields are expressed as percentages of total citrate synthase (CS) activity, defined by the measured value for the homogenate, captured during each subsequent elution. From this, it can clearly be seen that a plateau in yield increase is seen after 3x elution and 75 µL antibody. This inspired keeping the 3x elution principle for all subsequent analyses, as well as focusing on the antibody to tissue ratio as a key parameter for optimization.

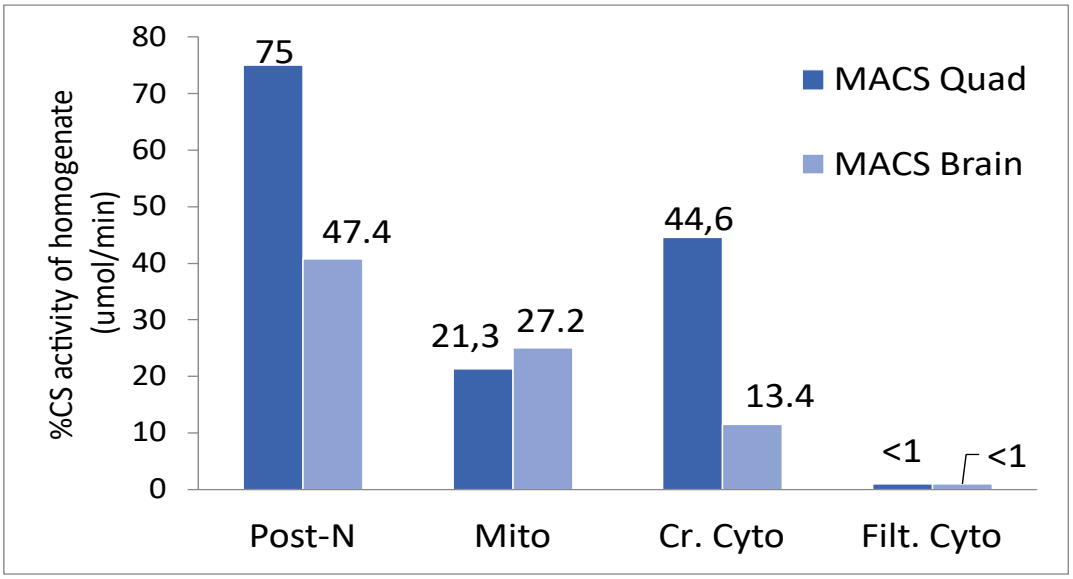


Figure 4-5: Comparison of CS distribution during various steps of the fractioning workflow for whole-brain and quadricep tissues. Yields are expressed as percentage CS of the homogenate present in each fraction. This graph emphasizes the tissue-specific caveats to consider for future optimization. Substantial amounts of brain mitochondria are lost during the initial debris-clearing

centrifugation step, while most muscle mitochondria are lost in the column flow-through, evidently not being labelled and bound in the magnetic field.

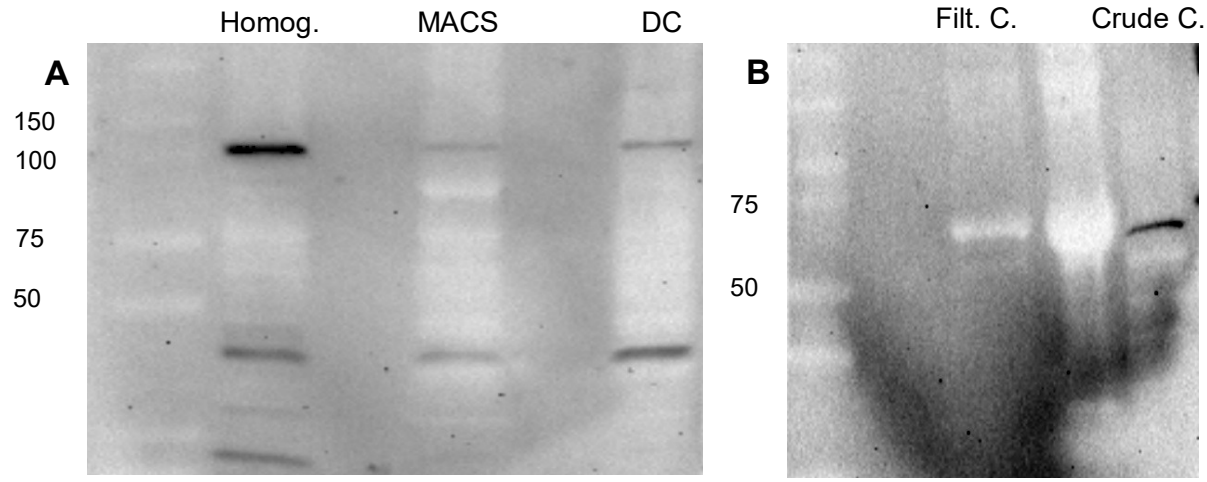


Figure 4-6: Unprocessed Western Blot results for **A**) DC and MACS mitochondrial fractions and **B**) crude and filtered cytoplasmic samples. The mitochondrial fractions were stained with LAMP-2b (110 kDa) lysosomal marker primary antibody, as well as b-Actin (42 kDa) as a loading control. The cytosolic fractions were stained with Hsp60 (60 kDa) mitochondrial matrix marker antibody.

4.5.2 Additional GC-TOF-MS and ^{1}H-NMR results

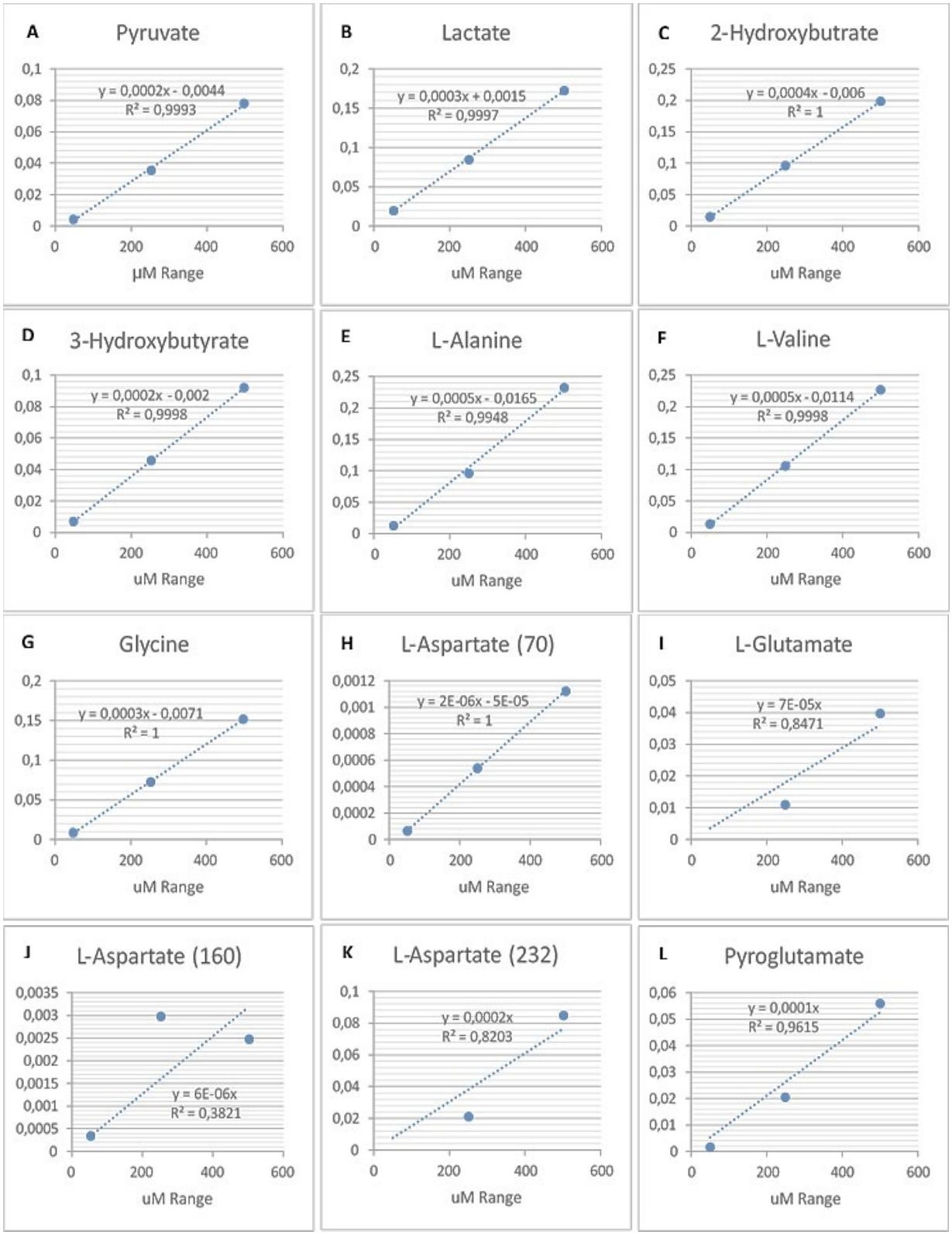


Figure 4-7: Linearity graphs for the selected nine standards in MACS buffer, analyzed via GC-TOF-MS (A – I) with accompanying line formulae and linearity coefficients, as well as for the other observed (unstable) Asp peaks (**J, K**) and pyroglutamic acid (**L**). Measurements are expressed as raw peak area arbitrary units (AU) normalized to EDTA in each sample.

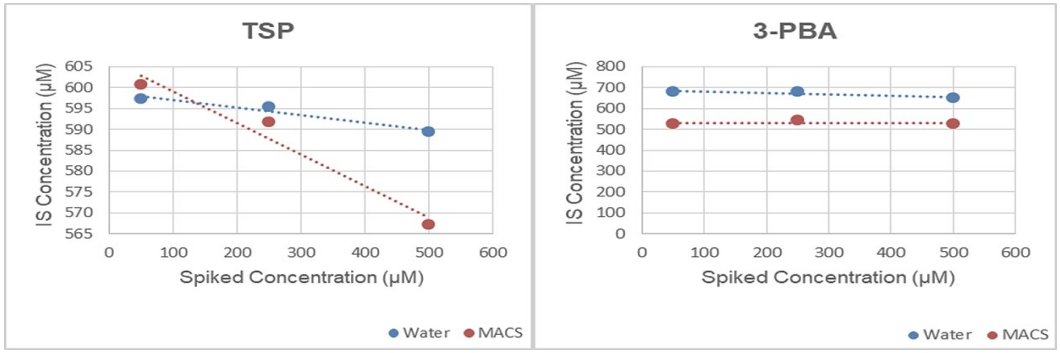


Figure 4-8: Fig. S5 Visualization of other selected NMR internal standards A) TSP and B) 3-PBA, at 750 uM true concentration, and their unreliability in the high-ionic MACS environment. Measured concentrations are plotted for every dilution of metabolites investigated (50, 250, 500 uM). TSP is clearly affected by the iconicity of the sample mixture in a concentration dependant way, while measured 3-PBA concentrations were consistently lower than the added amount.

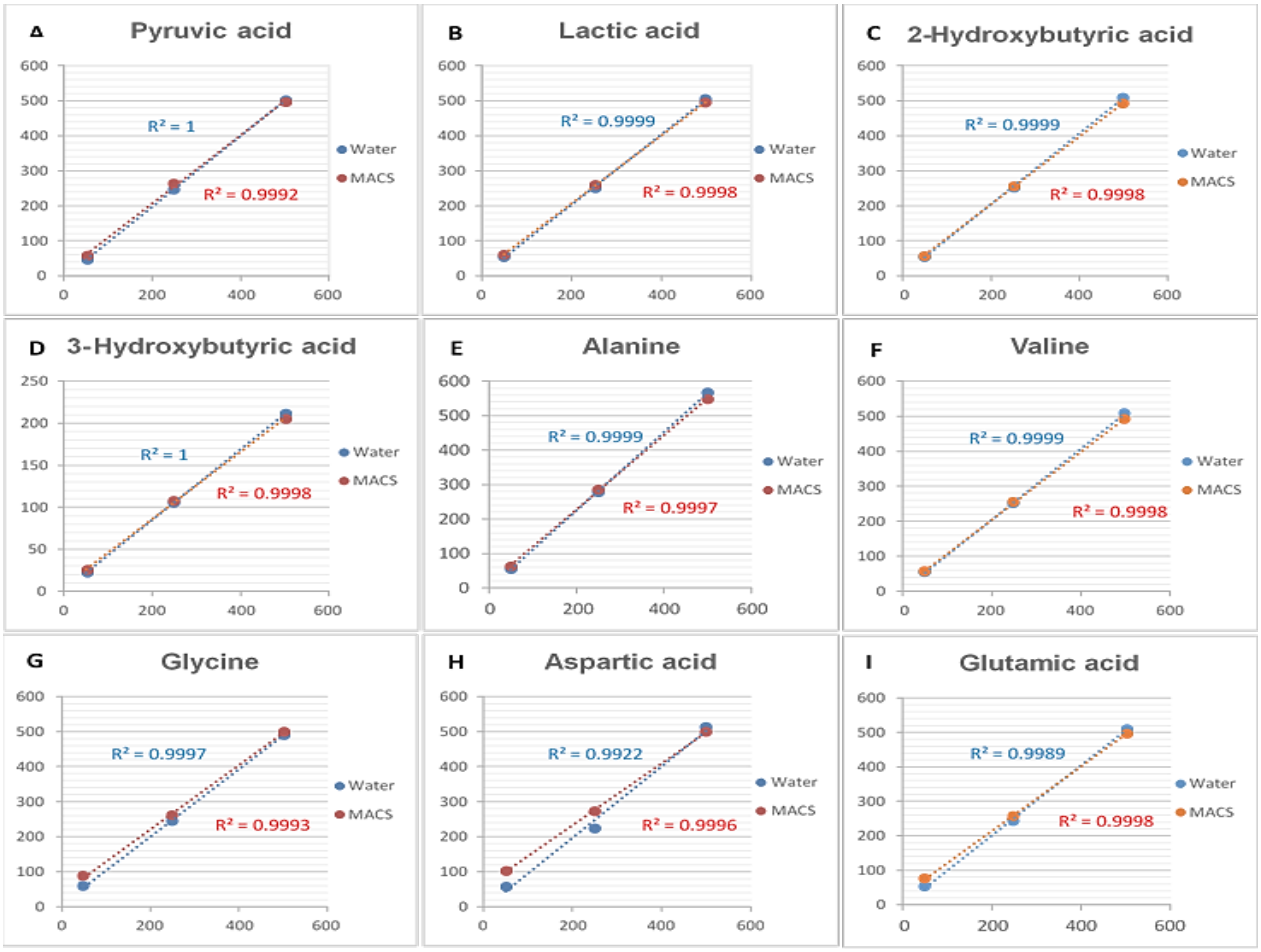


Figure 4-9: Comparison of linearity for the ^{1}H-NMR measured compounds in MACS environment and water. Quantified concentrations are plotted against true concentration for each level (50µM, 250µM, 500µM; n = 10).

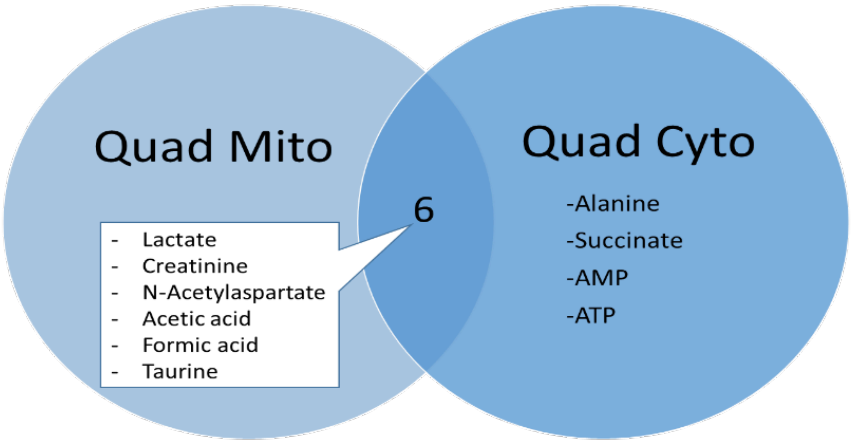


Figure 4-10: Compounds detected via ^{1}H-NMR in mitochondrial and cytosolic fractions of mouse quadricep muscle. The number in the intersection indicates the number of features common to both fractions.

Table 4-3: List of filtered and annotated compounds detected by GC-TOF-MS as common features in both brain mitochondrial and cytosolic extracts. Compound names as assigned by manual spectral library comparison as well as level of ID confidence (in brackets) are shown. Detected fragment mass and average retention times (n =3) are also given.

Confirmed feature (level)	Mass (m/z)	Ave R.T.(s)
Unknown	105	341.3
Lactic acid (1)	117	424.2
Methyl glycolate, benzyldimethylsilyl ether (unknown)	89	437.2
Alanine (1)	116	465.1
Glycine (1)	102	481.9
Sarcosine (1)	116	485.3
Oxalic acid (3)	133	505.7
Dithioerythritol (3)	73	568.7
Glycine (1)	174	667.8
Malic acid (1)	73	823.0
Aspartic acid (1)	232	848.2
Pyroglutamic acid (1)	156	851.4
GABA (3)	174	853.7
2-MethylTyrosine (3)	232	853.9
Glutamic acid (1)	246	920.2

Table 4-3 (continued)

Confirmed feature (level)	Mass (m/z)	Ave R.T.(s)
Biotransformed N-methylmalonamic acid (unknown)	158	949.0
Myo-inositol (2)	217	1224.3
Creatinine (enol) (3)	115	878.0
C16:0 (1)	117	1182.5
C18:0 (1)	117	1282.4

Table 4-4: List of filtered and annotated compounds detected by GC-TOF-MS as features unique to brain mitochondrial and cytosolic extracts, respectively. Compound names as assigned by manual spectral library comparison as well as level of ID confidence (in brackets) are shown. Detected fragment mass and average retention times (n =3) are also given.

Mitochondrial fraction			Cytosolic fraction		
Confirmed feature (level)	**Mass (m/z)**	**Average R.T. (s)**	**Confirmed feature (level)**	**Mass (m/z)**	**Average R.T. (s)**
Norleucine (1)	158	634.5	Hexanoic acid (3)	173	435.5
Glycerol (1)	218	639.1	Pyruvate (2)	75	458.4
Norleucine (3)	158	655.8	Tartaric acid (3)	89	516.8
Proline (1)	142	659.5	Urea (1)	171	643.4
Serine (1)	204	716.8	Succinic acid (1)	147	672.2
Cytosine (3)	240	734.6	Decanoic acid (3)	117	710.5
threonine (1)	73	740.7	Cytosine (3)	240	734.8
Oxalic acid (3)	73	798.5	Maleic acid (3)	245	866.3
Glycerol-1-P (1)	299	1023.2	2-aminoethylphosphate (3)	100	1036.4
2-aminoethylphosphate (3)	100	1036.2	5-Hydroxytryptophan (3)	290	1348.4
3-Hexendioic acid (3)	73	1059.3	5-Hydroxytryptophan (3)	288	1375.5
C18:1 (1)	55	1271.4	Cholest-5-ene (3)	129	1484.4

CHAPTER 5

Sub-cellular metabolomics contributes mitochondria-specific metabolic insights to a mouse model of Leigh Syndrome

This chapter was published as

Van der Walt, G., Lindeque, J.Z., Mason, S. & Louw, R. 2021. Sub-Cellular Metabolomics Contributes Mitochondria-Specific Metabolic Insights to a Mouse Model of Leigh Syndrome. *Metabolites,* 11(10):658.

5.1 Introduction

Throughout more than a century of mitochondrial research, science has ascertained at least this much regarding mitochondrial function: (i) it is critical to many facets of cellular health; (ii) it is a highly dynamic and adaptable role player in global and tissue-specific biology; and (iii) it maintains spatiotemporal compartmentalization of core metabolic/signalling networks. Mitochondria orchestrate these processes towards cellular homeostasis.

Through tightly regulated coordination with other intracellular spaces, mitochondria participate in several key energy-producing and biosynthetic pathways (Aouacheria *et al.*, 2017; Nunnari & Suomalainen, 2012; Shaughnessy *et al.*, 2014). Furthermore, complex metabolic and signal transduction pathways integrate nutrient, stress state and cell cycle cues at the mitochondrial level to elicit whole-cell responses following any change in environment or physiological needs (Quirós *et al.*, 2016; Wasilewski *et al.*, 2017). Concordantly, mitochondria have been implicated in multiple complex pathologies, from cancer to COVID-19 (Eysert *et al.*, 2020; Saleh *et al.*, 2020; Stepien *et al.*, 2017; Wallace, 2012). Central to our understanding of the mitochondrial contribution to pathology, however, is the study of primary mitochondrial disease (PMD), which results from deleterious mutations in core mitochondria-related genes (Craven *et al.*, 2017; Ylikallio & Suomalainen, 2012). Specifically, disorders of the first and foremost contributing enzyme of the respiratory chain (RC)- NADH:ubiquinone oxidoreductase (complex I, CI), are the most prevalent, with multiple nDNA or mtDNA mutations contributing to the observed CI-deficient (CID) phenotypes (Ghezzi & Zeviani, 2018; Triepels *et al.*, 2001). Deletion of the iron–sulfur CI protein subunit, *Ndufs4*, leads to subsequent CID, and a progressive encephalomyopathy, with severe musculoskeletal symptoms and poor prognosis known as Leigh syndrome (LS) (Lake *et al.*, 2015; Quintana *et al.*, 2010). The underlying whole-body knock-out (KO) paradoxically only leads to tissue-specific deterioration and metabolic reprogramming, implicating multiple biological systems in the observed mosaic.

Metabolomics has proven to be indispensable towards capturing changes in the small-molecule intermediates of metabolism that underlie bioenergetic, anabolic and signaling pathways intimately related to multiple mitochondria-related disease states (Nagrath *et al.*, 2011; Newgard, 2017; Priori *et al.*, 2013). Mouse models for PMD, such as the synthesized *Ndufs4* KO strain studied here (Kruse *et al.*, 2008; Leong *et al.*, 2012), serve as adequate *in vivo* models for CI-related LS and have contributed substantially to our understanding of the underlying tissue-specific deficits and potential treatment options (Esterhuizen *et al.*, 2017; Johnson *et al.*, 2013). In these mice, as in patients, it is known that whole-body *Ndufs4* KO leads to graded, region-specific neurodegeneration and metabolic alteration, which has convincingly been shown to be the driving force of the total LS phenotype (Emmerzaal *et al.*,

2020; Johnson *et al.*, 2020; Terburgh *et al.*, 2021). Oxidative and glycolytic muscles also show fibre type-specific metabolic alterations relating to the atrophy and locomotive defects in late-stage LS model mice and patients (Finsterer, 2008; Terburgh *et al.*, 2019). Both LS nervous and muscle tissues present features of perturbed metabolic and signalling pathways evident of differential catabolic/anabolic switching. These pathways are intertwined in the cascade of multi-organelle signalling molecules that facilitate an integrated stress response (ISR) during chronic mitochondrial stress (Emmerzaal *et al.*, 2020).

Adaptive bioenergetic responses aimed at controlling the redox state while supplementing the tricarboxylic acid (TCA) cycle and RC-derived ATP synthesis are evident from the metabolite alterations in *Ndufs4* KO brain and skeletal muscle tissues (Terburgh *et al.*, 2019; Terburgh *et al.*, 2021). Features related to perturbed anabolic shifts are also prevalent, seemingly in line with the prerequisites of the ISR (Johnson *et al.*, 2013; Khan *et al.*, 2017). Concurrently, alterations in core amphibolic substrate levels, such as glutamine, glutamate and α-ketoglutarate, are apparent even in lesser affected and pre-symptomatic neural/muscular *Ndufs4*$^{-/-}$ samples. Unlike in perturbed neural cells, which are supplemented by several neuron-glial metabolite shuttles (Liu *et al.*, 2017; Mason, 2017), this anabolic shift is presumably far less sustainable in the comparably mitochondria-lacking glycolytic muscle tissues (Schiaffino & Reggiani, 2011) and eventually leads to a global depletion of core metabolic intermediates. As such, induction of an amino acid restriction response has also been strongly correlated with RC inhibition in muscle fibres (Johnson *et al.*, 2014; Tyynismaa *et al.*, 2010). Evidently, multiple contributing and often conflicting metabolic switches are triggered during RC dysfunction, which require even deeper, more reductive and integrated approaches to fully grasp the metabolic dysfunction during *Ndufs4* KO, LS and PMD overall.

Despite decades of study around the causes and effects of mitochondrial dysfunction, only recently has technology allowed us to observe the related metabolic effects inside mitochondria, specifically (Liu & Xu, 2018). Mitochondria maintain a separate chemical milieu to the surrounding cytosol and organelles, with the abundance of multiple unique, inter- and trans-compartmental reactions. Mitochondria rely on tight membrane coupling to drive the proton gradient necessary for oxidative phosphorylation and ATP synthesis; thus, metabolite exchanges are highly coordinated by multiple substrate-specific, allosterically regulated, inner mitochondrial membrane transporter proteins, of which many are still being discovered and elucidated (Hewton *et al.*, 2021; Palmieri, 2013). Finally, even in the most mitochondria-rich tissues, the total mitochondrial matrix volume is substantially smaller than the cytosolic space (Kaasik *et al.*, 2007), leading to significant compartment-specific changes often being buried in the total cellular metabolome. This underlies the recent interest in metabolomic methods, which

can elucidate spatiotemporal compartmentalization of the implicated trans-cellular reactions and how this contributes to the observed whole-cell phenotype. Two complementary approaches underlie compartmental metabolomic studies: (1) Isotope-labelled metabolite flux measurements can follow the spatiotemporal distribution and the fate of certain targeted chemical precursors (Gravel *et al.*, 2014; Wiechert, 2001); (2) organelle isolation and metabolite fingerprinting offer a greater metabolic resolution and have concurrently delivered accurate sub-cellular insights on effects related to sex, age, fasting state, tumorigenesis and heavy metal toxicity (Go *et al.*, 2014a; Goodman *et al.*, 2018; Kiebish *et al.*, 2009; Roede *et al.*, 2012). While still scarce in volume, studies utilizing these methods in cell culture models of RC dysfunction have unequivocally proven mitochondria-level metabolite changes, which cannot be deduced from whole-cell samples alone (Chen *et al.*, 2016; Gravel *et al.*, 2014; Pan *et al.*, 2018).

These techniques are still only finding their footing in the field of *in vivo* disease modelling at a handful of institutions (Bayraktar *et al.*, 2019) and, to the best of our knowledge, have yet to be applied to an *in vivo* model of genetic CID. We thus hypothesized that a rudimentary immunopurification-based organelle isolation and compartment-specific metabolomic strategy (Van der Walt & Louw, 2020) could reveal mitochondria-specific metabolic insights that were not visible at the whole cell level. Comparative, multiplatform metabolomics was performed on the brain and skeletal muscle mitochondria and cytosol of late-stage *Ndufs4* KO mice alongside wildtype (WT) control mice (Figure 5-1). The significantly altered features that were reported underline current *Ndufs4* KO metabolomic knowledge, while indeed illuminating compartment-specific effects that went unseen in whole-cell studies of these tissues.

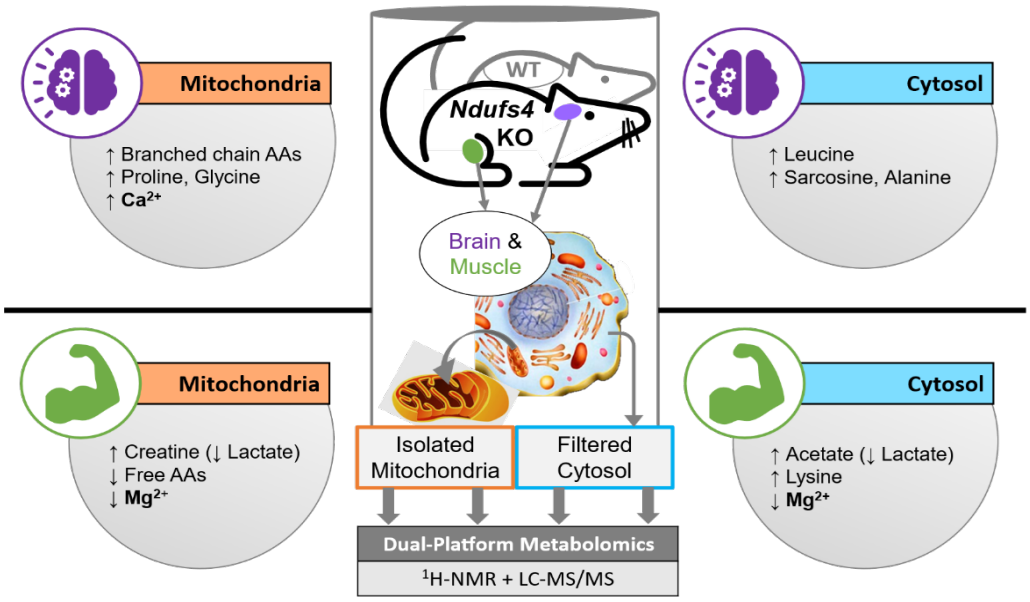


Figure 5-1: Graphical abstract summarizing experimental rationale and core results of the *Ndufs4* KO *versus* WT sub-cellular metabolomics study.

5.2 Results

5.2.1 Experimental rationale and data quality

To elaborate on the current metabolic knowledge of *Ndufs4*-linked LS, we performed ^{1}H-NMR and LC-MS/MS metabolomics on purified brain and quadricep muscle mitochondria and cytosols from male *Ndufs4* KO mice (n = 8), as well as age- and sex-matched controls (n = 8). The genotype was confirmed by an established PCR genotyping method. *A priori* sample calculations deemed these group sizes sufficient for detecting the most prominent metabolic effects in the current pilot (Cohen's D ≥ 1.0 at 80% power; G*-Power 3 R-package (Faul *et al.*, 2007)).

An established adaptation of the ubiquitous Miltenyi MACS murine mitochondrial isolation kit for *in vivo* metabolomics was applied (Van der Walt & Louw, 2020), alongside cost-efficient, robust minimal-volume ^{1}H-NMR and LC-MS/MS methods (Mason *et al.*, 2018; Mels *et al.*, 2011; Terburgh *et al.*, 2019), emphasizing the feasibility of mitochondrial metabolomics in more resource-restricted research settings. To maximize the information gained, post-NMR samples were subjected to LC-MS/MS analyses, rather than splitting the already limited sample volume (Figure 5-2A). WT and KO means were compared in each sample matrix, whereafter the statistically significant metabolite alterations were interpreted across compartments for each tissue (Figure 5-2B,C). Absolute metabolite identity confirmation was provided by 2D-NMR

techniques (JRES and COSY), as well as spectral matching to pure metabolite reference standards included for each mass transition probed by LC-MS/MS.

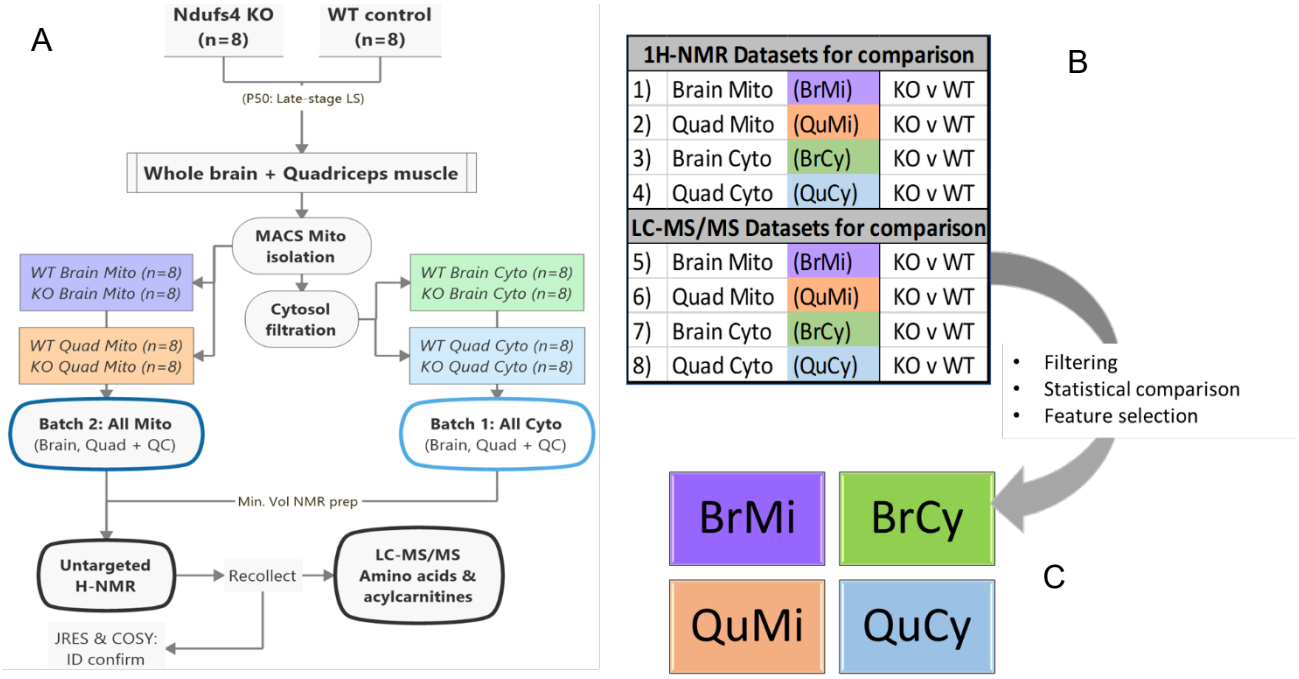


Figure 5-2: Summarized workflow for the study. *Ndufs4* KO and control mouse quadriceps and whole brains were subjected to MACS mitochondrial isolation and cytosolic filtering, before subsequent ^{1}H-NMR and LC-MS/MS analyses (A). Datasets were extracted as such that *Ndufs4* KO and WT were compared in each matrix (B) before data processing and statistical feature selection. Thereafter, the combined significant feature (VIP) datasets for each tissue and compartment were further processed and interpreted (C). BrCy/Mi: Brain cytosol or mitochondria, QuCy/Mi: quadriceps cytosol or mitochondria.

Data quality was controlled by monitoring univariate variance in quality control sample (QC) technical replicates throughout each batch, as well as variance of IS compounds uniformL y added to each sample. From the relative standard deviation, or percent coefficient of variance (%CV) reported for each compound (Figure 5-3A–D), the analytical accuracy of NMR or LC-MS measurements within these minimum-volume, buffered samples was well within acceptable precision limits for untargeted metabolomics (Dunn *et al.*, 2012). Average QC-CV% values across all platforms were even below the FDA-stipulated 20% limit for targeted chemical analyses close to lower quantification limits (FDA, 2001), while no more than two compounds were removed from each dataset based on the selected 30% QC-CV filter applied here. From the NMR mitochondrial dataset, dimethylamine and dimethylformamide (possibly methylamine artefacts) were removed with a high %CV, while only alanine was excluded from analysis in the cytosolic NMR data. QC samples showed similar analytical performances in the LC-MS/MS batches, with only threonine being filtered from the cytosolic dataset, and none from the mitochondrial dataset. Upon exclusion of these four compounds, QC-CV values across all batches did not exceed 10%.

Finer technical variance, as inferred by IS compound %CVs across all samples per batch (Figure 5-3E,F), also averaged at ~10% for both cytosolic and mitochondrial batches, with no compound exceeding 20% CV. From the total signal scatterplots generated before and after data normalization (Figures 5-8, 5-9), the sample-wise normalization strategy applied did not exacerbate the QC signal variance while also being able to correct for certain levels of technical variance in the separate sample groups analyzed in each batch. Therefore, it can be concluded that the metabolomic methods applied were of sufficient precision for metabolite abundance measurement, while minimizing the inherent technical variance of low-volume mitochondrial metabolomics.

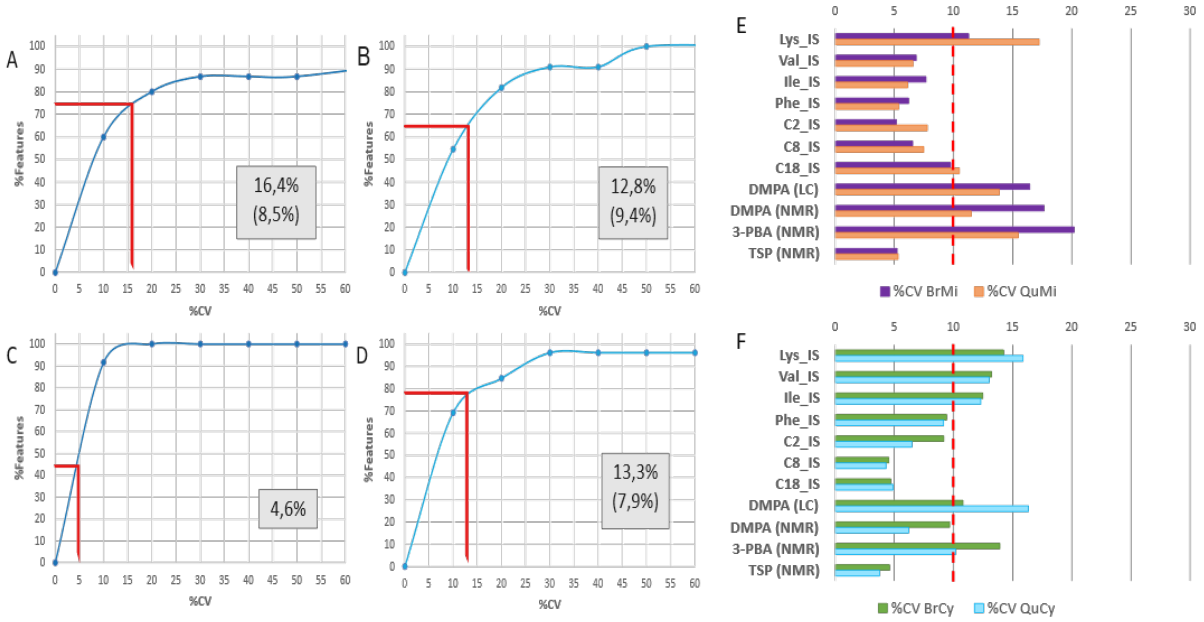


Figure 5-3: Technical variance and data quality for each ^{1}H-NMR and LC-MS/MS batch. (A) Cumulative percentage features plotted over coefficient of variance (%CV) intervals, from QC sample technical replicates within ^{1}H-NMR mitochondrial and (B) cytosolic sample batches. The same is plotted for (C) LC-MS/MS mitochondrial and (D) cytosolic batches as well. Enclosed numbers indicate mean %CV values across all viable features in each dataset, where individual unstable features were filtered, the number in brackets indicates the adjusted mean %CV after filtering. Measured IS compound variance as %CV in each tissue matrix, (E) for the mitochondrial and (F) cytosolic samples. Deuterium-labelled standards: C2_IS: d3-acetylcarnitine, C8_IS: d3-octanoylcarnitine, C18_IS: d3-stearoylcarnitine, Ile_IS: d10-isoleucine, Lys_IS: d4-lysine, Phe_IS: d5-phenylalanine, Val_IS: d3-valine.

5.2.2 Metabolome coverage and data clean-up

Given current uncertainty regarding the exact mitochondrial metabolome and compartmentalization of ambiguous metabolite pools (Chen *et al.*, 2016; Liu & Xu, 2018), we first established LC-MS/MS and ^{1}H-NMR profiles for the accurately identified and quantifiable compound averages across each sample matrix. Untargeted ^{1}H-NMR, following a binning approach, could identify and measure 14 compounds at various levels across all samples, while LC-MS/MS delivered 35 such viable compounds from the 54 metabolites originally targeted by

MRM (Figure 5-4A,B). It should be noted that the LC-MS/MS methodology is biased towards amino acid and acylcarnitine analyses, targeting only mass transitions for a predefined set of metabolites from these classes.

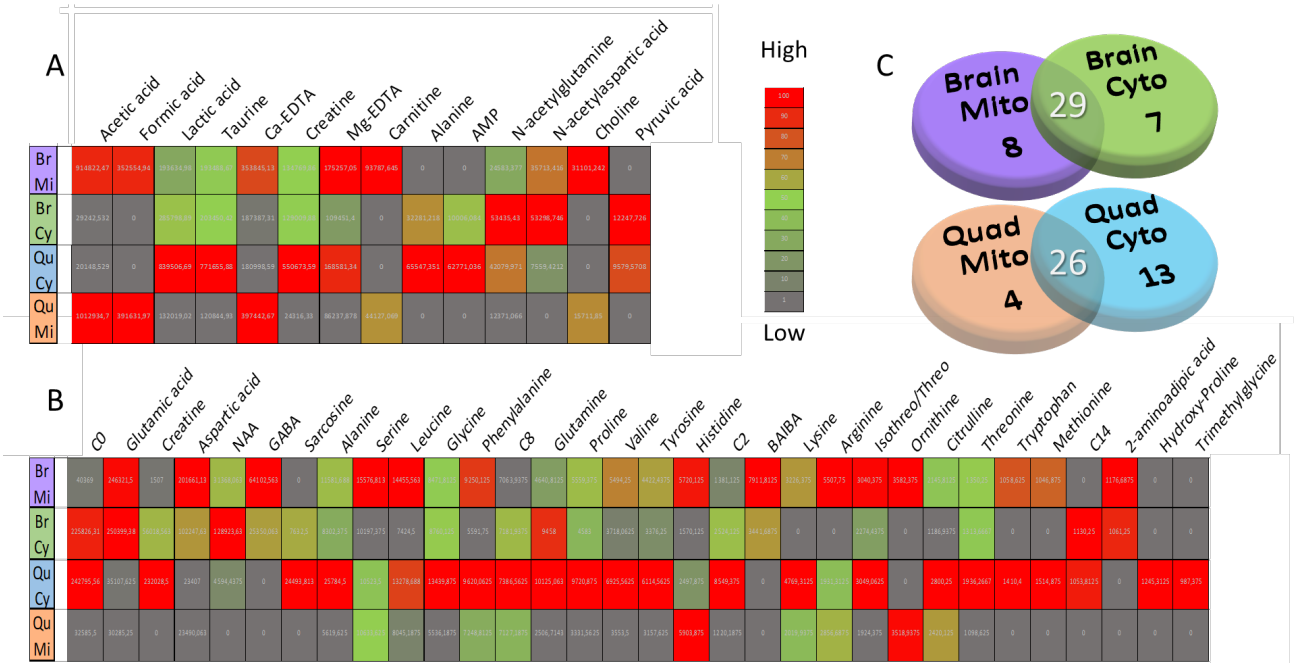


Figure 5-4: Comparison of viable metabolite presence and gross abundance across sample matrices. Heatmaps of average matrix raw peak abundances, contrasted by Euclidian between-mean distances, are presented for the (A) total viable ^{1}H-NMR and (B) LC-MS/MS features. Venn diagrams in (C) summarize the number of metabolites viably detected above the noise level in mitochondria, cytosols and both compartments for the whole-brain and quadricep matrices, separately.

From a tissue-specific perspective, whole-brain mitochondria and cytosols, respectively, delivered eight and seven compartment-specific compounds, and 29 across both compartments (Figure 5-4C). Similarly, four uniquely mitochondrial compounds were viably detected in the quadriceps, alongside 13 cytosolic and 26 cross-compartment metabolites. Detected and quantifiable features are listed according to total median spectral signal abundance and QC measurement stability in Table 5-2. The most abundant features across all matrices were glutamic acid, aspartic acid, carnitine, formic acid and lactic acid. Expectedly, several features were identified and analyzed in one compartment, while not being present above baseline/detection levels in the other, as evident from the compartment-specific distributions of sarcosine, hydroxyproline, ornithine and formic acid, among others. This emphasizes the value of the reported approach in measuring metabolites at a mitochondrial level that are either ubiquitous in the total cell volume or diluted beyond detection limits therein.

Several MS feature peaks were removed due to being below the reliable signal/noise area range of 10^{3} mAu before the generation of the heatmaps shown in Figure 5-4. Thereafter, a 50% zero filter was applied, excluding compounds detected at < 1000 mAu in more than 8/16

samples. Finally, the 30% QC-CV data filter was applied as described in Section 5.2.1. These steps ensured only the most stable metabolites, and the most relevant patterns in the variation were preserved for statistical analyses.

5.2.3 Compartment-specific, significant *Ndufs4* KO metabolite alterations

The selected variables of importance (VIPs) showing significant statistical ($p < 0.1$) and/or practical ($D > 1.0$) differences between WT and KO mitochondria and cytosols are reported in Table 5-1. The clean and normalized datasets were subjected to univariate tests for significant differences in means; *t*-test statistics and Cohen's D values were calculated in SPSS, automatically accounting for formula derivations per feature based on their differential normality and homogeneity of variance criteria.

Significance limits stricter than the a priori power calculations infer, assure a greater preference for type II statistical errors (rejecting potentially significant changes), while minimizing type I errors (reporting non-significant changes as significant) (Akobeng, 2016; Vinaixa *et al.*, 2012). Although this assures that the few metabolites reported are indeed of significant value, many possibly significant alterations may be lost. Notably, three compounds approached the cut-off for significance in the whole-brain samples ($p < 0.15$; $D > 0.8$), while none but the reported quadricep-derived metabolites showed borderline significant differences in means. Alanine, glutamine and sarcosine are thus included in the discussion of whole-brain metabolic perturbations. Altogether, these VIPs reflect known bioenergetic and anabolic perturbations related to mitochondrial distress.

Table 5-1: VIP compounds identified by univariate statistical and practical significance testing. Common metabolite names (Level 1 identity) are reported with the direction of means change (↑ and ↓ arrows representing KO vs WT mean increases or decreases, respectively). T-test p-values and Cohen's D values in the cytosol, alongside the correlating mitochondrial KO vs. WT comparison are shown in each tissue. The metabolomics platform from which each significant feature was derived is also shown. N.S.: non-significant statistical test result, N.Q.: not quantified due to being filtered from dataset, N.D.: not detected above baseline level.

Quadricep Muscle							
Cytosol				Mitochondria			
Metabolite (Level 1)	**KO Δ (vs. WT)**	***p***	***D***	**KO Δ (vs. WT)**	***p***	***D***	**Platform**
Lactic acid	↓	0.04	1.2	↓	0,04	1,1	^{1}H-NMR
Mg(II)-EDTA	↓	0.10	0.9	↓	0,09	0,9	^{1}H-NMR
Threonine	N.Q.			↓	0.04	1.1	LC-MS/MS
Glycine	N.S.			↓	0.05	1.1	LC-MS/MS

Table 5-1 (Continued)

Cytosol				Mitochondria			
Metabolite (Level 1)	**KO Δ (vs. WT)**	***p***	***D***	**KO Δ (vs. WT)**	***p***	***D***	**Platform**
Creatine	N.S.			↑	0.05	1.0	^{1}H-NMR
Histidine	N.S.			↓	0.07	1.0	LC-MS/MS
Tyrosine	N.S.			↓	0.07	1.0	LC-MS/MS
Ornithine	N.D.			↓	0.08	1.0	LC-MS/MS
Leucine	N.S.			↓	0.10	0.9	LC-MS/MS
Hydroxyproline	↓	0.01	1.8	N.Q.			LC-MS/MS
Citrulline	↓	0.07	1.0	N.S.			LC-MS/MS
Acetylcarnitine	↑	0.09	0.9	N.S.			LC-MS/MS
Lysine	↑	0.10	0.9	N.S.			LC-MS/MS
Whole Brain							
Cytosol				***Mitochondria***			
Metabolite (Level 1)	**KO Δ (vs. WT)**	***p***	***D***	**KO Δ (vs. WT)**	***p***	***D***	**Platform**
Leucine	↑	0.09	0.9	↑	0,03	1,2	LC-MS/MS
Proline	N.S.			↑	0.03	1.1	LC-MS/MS
Phenylalanine	N.S.			↑	0.03	1.1	LC-MS/MS
Valine	N.S.			↑	0.06	1.0	LC-MS/MS
Octanoylcarnitine	N.S.			↑	0.08	1.0	LC-MS/MS
Glycine	N.S.			↑	0.08	0.9	LC-MS/MS
Ca(II)-EDTA	N.S.			↑	0.09	0.9	^{1}H-NMR
Alanine[1]	↑	0.10	0.9	↑	0,13	0,8	LC-MS/MS
Glutamine[1]	N.S.			↓	0.12	0.8	LC-MS/MS
Sarcosine[1]	↑	0.11	0.8	N.D.			LC-MS/MS

[1] Metabolites approaching statistical and practical significance, yet below defined limits.

PLS-DA projections of the combined VIP datasets for each sample matrix indicate the power of the resulting model to separate WT and KO phenotypes based on the selected features from Table 1 (Figure 5-10). While the power of multivariate analyses is severely restricted by the small number of samples and significant features in each dataset, cross-validation of the PLS-DA model indicates similar maximal model accuracies (~70%) across matrices. Despite the described limitations, these results also support the ability of sub-cellular metabolomics to discern between *Ndufs4* KO and WT metabolic phenotypes.

5.2.4 Amino acids accumulate in whole-brain CI-deficient mitochondria to a greater extent than cytosolic or region-specific metabolomics can fully elucidate

The majority of whole-brain compartment-specific metabolic alterations reported here (Table 5-1, Figure 5-5) pertain to metabolites at the intersections of bioenergetic and anabolic pathways. The overall increase in the branched-chain amino acids (BCAAs) valine and leucine, supports the classic model wherein hyperaccumulated NADH inhibits the NAD^+-dependent enzyme branched-chain keto-acid dehydrogenase (BCKDH), leading to accumulation of its BCAA precursors (Arany & Neinast, 2018; Bifari & Nisoli, 2017; Esterhuizen *et al.*, 2017). These BCAA increases were more prominent at the mitochondrial level than previously detected in the lesser-affected anterior cortex, thus indicating a possibly predictive mitochondrial BCAA accumulation that whole-cell metabolic profiles cannot sufficiently convey (Terburgh *et al.*, 2021). A significant increase in proline was seen only at the whole-brain mitochondrial level. This concurs proline accumulation observed in all *Ndufs4* KO brain regions (Oka *et al.*, 2013; Terburgh *et al.*, 2021), in line with the prominent role of mitochondrial-cytosolic proline shuttling in buffering redox and adenylate charge ratios (Krishnan *et al.*, 2008; McDonald *et al.*, 2018). These results accentuate hypotheses regarding bioenergetic buffering during RC dysfunction, while implicating spatial compartmentalization in these pathways.



Figure 5-5: Compartment−specific metabolite alterations in *Ndufs4* KO whole brain, identified by ^{1}H−NMR and LC−MS/MS. Histograms indicate mean differences with size and directionality, graphed as Cohen's D values, while boxplots summarize the sample value distributions for each compound across the two genotypes and cell compartments analyzed. Statistical significance via Student's t-test is indicated as (*) for $p < 0.1$ or (**) for $p < 0.05$. Abbreviations: Ala: alanine, C8-carn: octanoylcarnitine, Ca(2+): Calcium(II)-EDTA, Gln: glutamine, Gly: glycine, Leu: leucine, Phe: phenylalanine, Pro: proline, Src: sarcosine, Val: valine.

Mitochondrial glycine levels were significantly increased (Figure 5-11), while the same effect was not observed in the cytosolic samples or in whole-cell metabolite extracts from affected *Ndufs4* KO brain regions (Johnson *et al.*, 2020; Terburgh *et al.*, 2021). As a key role player in several metabolic pathways in animal cells (Razak *et al.*, 2017; Wang *et al.*, 2013), multiple probable explanations exist, which require further study. One such explanation involves one-carbon (1C) metabolism and its complex roles in mediating catabolic/anabolic shifts (Ducker & Rabinowitz, 2017; Yang *et al.*, 2020). This notion is supported by an observed concomitant increase in cytosolic sarcosine levels, as an alternative 1C-related glycine precursor. Further amino acid increases appear obscure in isolation, but collectively, also support a general anabolic upregulation in these neural tissues (Johnson *et al.*, 2020). The accumulation of alanine across both compartments and increased mitochondrial phenylalanine support a general increase in amino acid liberation for energy metabolism or protein synthesis (Johnson *et al.*, 2014; McDonald *et al.*, 2018), while all amino acid increases reported here may also support this hypothesis. Increased octanoylcarnitine (C8-carnitine) may correlate with a general dysregulation of fatty acid metabolism and neuroinflammation concurrent with the *Ndufs4* KO phenotype (Liu *et al.*, 2017; Quintana *et al.*, 2010), although these studies reported a greater dysregulation in acylcarnitines larger than C8-carnitine. In support of the glutamine perturbation reported here, the prominent involvement of the glutamine/glutamate/ketoglutarate axis in the concurrent *Ndufs4* KO brain's metabolic shifts is well described, enacting substrate-level coordination of key amphibolic pathways (Chen *et al.*, 2018; Johnson *et al.*, 2020). Furthermore, some of these amino acid increases serve as potent stimulants of anabolic shifts, where leucine and proline specifically upregulate the function of the mitochondrial target of rapamycin (mTORC1) signalling pathways towards greater protein and nucleic acid synthesis (Phang, 2019; Son *et al.*, 2020). While sparsely spread across all these pathways, these results preliminarily support perturbed anabolic signalling and metabolism, as hypothesized by current *Ndufs4* KO brain studies (Emmerzaal *et al.*, 2020; Johnson *et al.*, 2020; Terburgh *et al.*, 2021).

Altogether, the isolated whole-brain mitochondria from *Ndufs4* KO animals displayed patterns in metabolite perturbation that resemble the combined metabolic footprints of multiple brain regions previously measured in these mice while showing a greater perturbation at the mitochondria-specific level.

5.2.5 Differential depletion of quadriceps mitochondrial and cytosolic metabolites related to CID muscle metabolic reprogramming

Mitochondrial and cytosolic VIP compounds point to known perturbed bioenergetic pathways in *Ndufs4* KO glycolytic skeletal muscle fibres (Table 5-1, Figure 5-6). A decrease in lactic acid across both compartments was detected, in line with existing *Ndufs4* KO whole-cell quadricep

metabolic data (Terburgh *et al.*, 2019). While sequestration of glycolytic units for NAD^+ regeneration via mitochondrial glycerol-3-phosphate cycling stands as a convincing explanation for lactate decrease at the whole cell level (McDonald *et al.*, 2018), concomitant mitochondria-level decreases also implicate biologically significant mitochondrial lactate import and oxidation towards TCA anaplerosis (Brooks, 2020; Passarella *et al.*, 2008). In that regard, a lesser-described mitochondrial lactate dehydrogenase (mLDH) seemingly plays an important role in skeletal muscle energy buffering during energetic stress (Young *et al.*, 2020). An increase in acetylcarnitine (C2-carnitine), as reported here, is known to be a repercussion of acetyl-CoA accumulation due to RC blockage (Karamanlidis *et al.*, 2013). Accumulated mitochondrial creatine contradicts the decrease in whole-cell Cr previously described in *Ndufs4* KO quadriceps. This indicates perturbation of the mitochondrial-cytosolic creatine shuttle and differential functionalities of compartment-specific creatine kinases (CK)(Schlattner *et al.*, 2006).

Significant depletion of select amino acids is also reminiscent of recent hypotheses supporting a cellular focus on alternate RC fueling pathways. Decreased 4-hydroxyproline indicates sequestration of upstream Pro for preferential use in balancing redox restrictions by proline/pyrroline-5-carboxylate cycling, while it may also correlate with disturbed collagen proteostasis (Oka *et al.*, 2013; Schwörer *et al.*, 2020). Increased cytosolic lysine levels also indicate a shift in its interrelated metabolic pathways aimed at preserving cellular $NADH/NAD^+$ ratios, restricting its mitochondrial catabolism to 2-aminoadipate (Terburgh *et al.*, 2019).

The measured ornithine and citrulline implicate compartmentalized perturbation of muscle urea cycling (Figure 5-12). While a decrease in these compounds supports a hypothesized increased channelling of ornithine towards the proline and/or CK shuttles as described above, distinct compartment-specific perturbations, as reported here, were not seen in a previous whole-cell *Ndufs4* KO quadriceps study (Terburgh *et al.*, 2019). Glycine was found significantly decreased in *Ndufs4* KO muscle mitochondria while showing no significant difference in cytosolic samples. Threonine levels followed the same trend, as threonine catabolizes through glycine back to pyruvate, their concomitant depletions are likely related.

Decreased leucine, histidine and tyrosine levels were also observed in the muscle mitochondria (Figure 5-12), indicative of perturbed amphibolic pathways. Other than being a critical energy source for the skeletal muscle, leucine also serves to increase whole-body energy availability by stimulating the muscle-liver Cahill cycle and subsequent hepatic gluconeogenesis (Bifari & Nisoli, 2017; Sarabhai & Roden, 2019), at the expense of muscle lactate and glutamate. Classic histidine catabolism ultimately leads to replenishment of glutamate and donation of methyl units to the 1C cycle; thus, its decrease may lie up-, or downstream of RC-induced perturbations in these pathways (Holeček, 2020). While the role of lesser-expressed tyrosine catabolic enzymes

towards TCA anaplerosis is prominent in oncogenic muscle deterioration (cachexia) (Cui *et al.*, 2019), significant perturbations in tyrosine pools were not previously found at the cytosolic or whole cell level in MD mice (Esterhuizen *et al.*, 2017; Terburgh *et al.*, 2019).

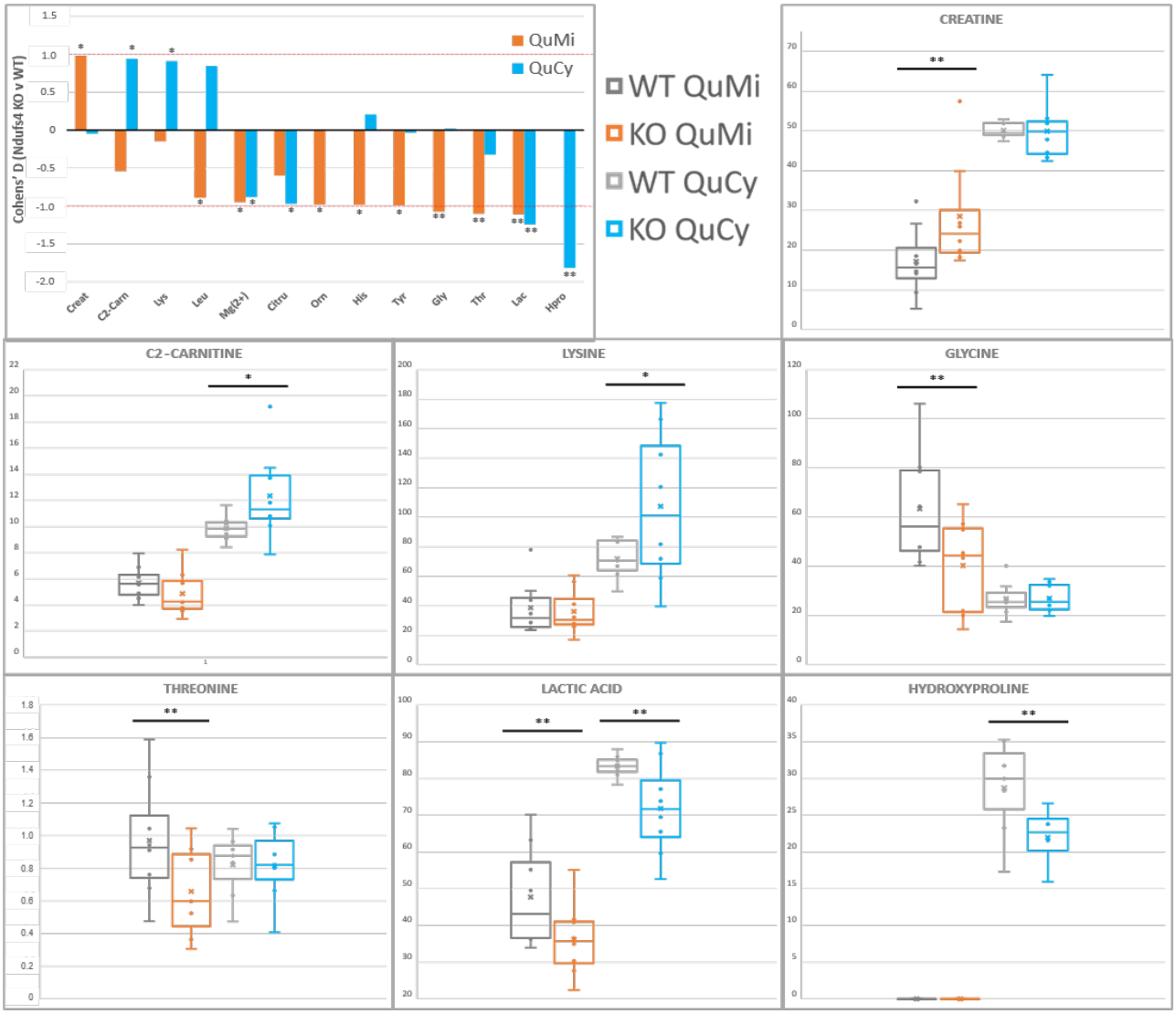


Figure 5-6: Compartment-specific metabolite alterations in *Ndufs4* KO quadriceps muscle, identified by ^{1}H-NMR and LC-MS/MS. Histograms indicate mean differences with size and directionality, graphed as Cohen's D values, while boxplots summarize the sample value distributions for each compound across the two genotypes and cell compartments analyzed. Statistical significance via Student's t-test is indicated as (*) for $p < 0.1$ or (**) for $p < 0.05$. Abbreviations: C2-carn: ace-tylcarnitine, Citru: citrulline, Creat: creatine, Gly: glycine, His: histidine, Hpro: 4-hydroxyproline, Lac: lactic acid, Leu: leucine, Lys: lysine, Mg(2+): Mg(II)-EDTA, Orn: ornithine, Src: sarcosine, Thr: threonine, Tyr: tyrosine.

Despite all the pathways described, the observed amino acid depletion is probably related to differential dysregulation of mitochondrial and cytosolic protein turnover during PMD (Ross-Inta *et al.*, 2008; Tyynismaa *et al.*, 2010). Notably, this supports the hypothesis wherein the sparse, glycolytic muscle fibre mitochondrial network cannot sustain similar stress responses as induced in the brain and ultimately leads to an amino acid restriction response (Johnson *et al.*,

2014; Schiaffino & Reggiani, 2011). In summary, the described compartment-specific metabolite perturbations highlight several well-supported hypotheses regarding metabolic distress in CID glycolytic muscle fibres, while clearly homing in on effects beyond the discernment ability of whole-cell metabolomics.

5.2.6 First report of tissue and compartment-specific bivalent cation measurement in *Ndufs4* KO mice highlights role of metal homeostasis in integrated stress responses

During ^{1}H-NMR analyses, we exploited a recently developed procedure for quantifying bivalent metal cations through their chelation with ethylenediaminetetraacetic acid (EDTA) (Hafer *et al.*, 2020; Mathuthu *et al.*, 2021). As the sub-cellular samples contain a molar excess of EDTA as part of the isolation buffer environment (Hornig-Do *et al.*, 2009; Van der Walt & Louw, 2020), chelated calcium (Ca-EDTA) and magnesium (Mg-EDTA) concentrations are representative of the relative amounts of the cations present. Here, we report the first direct measurement (to our knowledge) of altered compartment-specific metallostasis in affected LS model tissues (Figure 5-7).

A significant increase in brain mitochondrial Ca^{2+} levels was observed, with virtually no difference in its cytoplasmic concentrations due to *Ndufs4* KO. This is in line with mitochondria-endoplasmic reticulum (ER) coupling and subsequent mitochondrial Ca^{2+} influx during ER stress responses to RC insult (Emmerzaal *et al.*, 2020; Koshenov *et al.*, 2021; Nunnari & Suomalainen, 2012). This buffering mechanism serves to upregulate multiple Ca^{2+}-dependent metabolic enzymes, independently of cytosolic calcium pools. The skeletal muscle Mg^{2+} levels were significantly lower over both cell compartments. Although no present direct explanation suffices, lowered Mg^{2+} levels are also involved in bioenergetic feedback signalling during the mitochondrial stress responses (Barbagallo *et al.*, 2021; Huskisson *et al.*, 2007). This may also reflect alterations in protein turnover as described in the preceding section, as Mg^{2+} readily serves as a co-factor in multiple enzyme complexes, most notably in ATP-consuming proteins; however, whole-body Mg^{2+} decreases are often associated with decreased intestinal absorption and renal reabsorption due to energy deficiency (Heidari *et al.*, 2018).

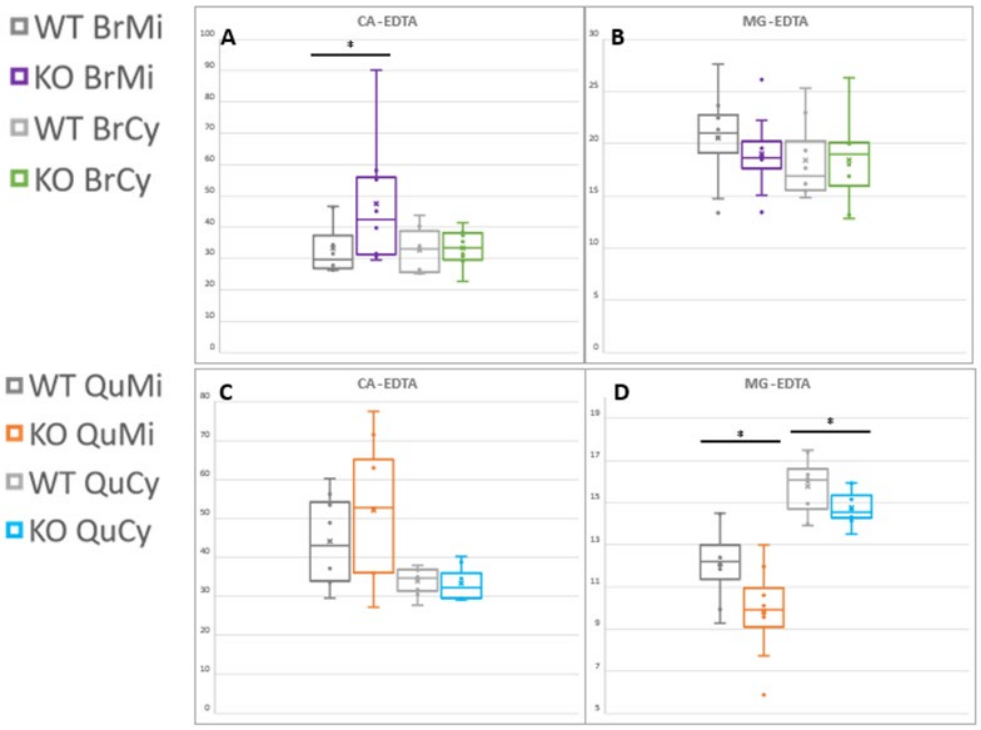


Figure 5-7: Compartment-specific magnesium and calcium levels, detected as EDTA chelates by ^{1}H-NMR. (A) Brain mitochondrial Ca-EDTA and (B) Mg-EDTA, as well as (C) quadricep muscle Ca-EDTA and (D) Mg-EDTA levels are shown. Statistical significance via Student's t-test is indicated as (*) for $p < 0.1$ or (**) for $p < 0.05$. Ca-EDTA: Ca(II)-ethylenediaminetetraacetate, Mg-EDTA: Mg(II)-ethylenediaminetetraacetate.

5.3 Discussion

5.3.1 Contribution towards *in vivo Ndufs4* KO Model and *in vitro* CID knowledge base

The reported mitochondrial and cytosolic metabolites from these LS model tissues highlight current metabolomic hypotheses underlying *in vivo* pathogenic and adaptive responses to *Ndufs4* KO (Esterhuizen *et al.*, 2017; Quintana *et al.*, 2010). Central to the problem addressed by this study are detected metabolite alterations at mitochondrial level in neural and glycolytic muscles that their correlated whole-cell and cytosolic samples do not reveal (Alam *et al.*, 2015; Johnson *et al.*, 2020; Terburgh *et al.*, 2019; Terburgh *et al.*, 2021). The whole-brain VIPs support the reported role of multiple bioenergetic and anabolic pathways at the core of the LS phenotype. In the related glycolytic muscle, differential patterns of metabolic change were observed across both compartments; however, all of them related to the presumed depletion of similar pathways to those upregulated in whole-brain tissues.

Both tissues clearly reflect redox perturbations and the upregulation of pathways that attempt to restore reductant pools (McDonald *et al.*, 2018). BCAA, Pro (Arany & Neinast, 2018; Schwörer *et al.*, 2020), lactate and creatine perturbations support this, with a greater visible effect in the

mitochondrial samples. Most notably, the reported results indicate the roles of lesser-described mitochondrial mLDH and mCK isoforms, emphasizing the value of organelle-level resolution in these core classic bioenergetic pathways (Bonilla *et al.*, 2021; Brooks, 2020; Schlattner *et al.*, 2006). As mitochondrial NADH pools are presumably affected to a greater extent than the accompanying cytosolic pool (Goodman *et al.*, 2018; Lewis *et al.*, 2014), the greater observed perturbation of redox-related pathways at the sub-cellular level was expected. These results also further implicate core biosynthetic and anaplerotic pathways, as dysregulated anabolic signalling is a core feature and therapeutic target for CID (Johnson *et al.*, 2013; Khan *et al.*, 2017). Presumably, this shift attempts to replenish proteins that mediate cellular responses to energetic stress via mito-nuclear signalling and the ISR (Quirós *et al.*, 2016). Specifically, altered levels of leucine, proline, glycine and other 1C substrates underlie this statement (Ducker & Rabinowitz, 2017; Phang, 2019; Son *et al.*, 2020), although the tight correlation between amino acid availability and protein synthesis may insinuate a direct correlation of all the reported amino acids with dysregulated protein turnover (Ross-Inta *et al.*, 2008). In contrast, increased liberation of free amino acids towards energy metabolism and concurrent RC/TCA cycle congestion may also viably underlie the overall amino acid accumulation described here (Terburgh *et al.*, 2019; Yang *et al.*, 2020). Regardless, mitochondrial proteostasis is regulated both separately and in unison with whole-cell levels (Johnson *et al.*, 2014); therefore, the study of mitochondria-specific amino acid perturbations may well serve to deconvolute their differential metabolic fates under various conditions.

Very few studies to date have provided sub-cellular metabolomic data on RC distress; however, similar pathway perturbations and compartment-specific adaptations have been reported for *in vitro* CID models (Chen *et al.*, 2016; Gravel *et al.*, 2014; Pan *et al.*, 2018). Ac-CoA and Lys accumulation, glutamate disturbances, and Pro and urea cycle upregulation have been reported in human and murine cells after CI inhibition by rotenone, but with cell type-specific patterns (Chen *et al.*, 2016; Gravel *et al.*, 2014). Our application of sub-cellular methods to a living mouse model thus also capitulates the value of extending these techniques to *in vivo* studies, by factoring in tissue-specific effects and considering systemic metabolic contributions. Overall, whole-brain VIPs presented amphibolic pathway substrates that may drive the catabolic/anabolic shifts at the core of the phenotype (Johnson *et al.*, 2020). In accordance, increased mitochondrial Ca^{2+} levels without a concomitant cytosolic increase indicate ER–mitochondrial contact, a key feature of ISR induction (Koshenov *et al.*, 2021; Szibor *et al.*, 2020). *In vivo* neural metabolomics, however, presents unique challenges regarding specialized, intercellular metabolic shuttles. For instance, astrocytic leucine serves as a key carbon source for neuronal TCA anaplerosis when this axis is depleted (Yudkoff, 2017), while lactate and fatty acid shuttling between microglia and neurons is a key neuroinflammatory

feature in late-stage LS (Liu *et al.*, 2017; Mason, 2017). Furthermore, the role of aromatic amino acids and glycine in neurotransmitter metabolism must be considered (Johnson *et al.*, 2020; Neurauter *et al.*, 2008). Glutamatergic neurons, however, are of predominant focus in LS models, implicating perturbed glutamate related metabolism within their mitochondria (Quintana *et al.*, 2010; Yudkoff, 2017).

The most striking contrast seen in the KO quadricep tissue remains a global depletion of intermediates relating to the same pathways deemed increased in the *Ndufs4* KO brain. Urea, creatine and lactate metabolic derangements were also unique to the muscle samples, in agreement with the current metabolic knowledge on mitochondria-related myopathies (Nikkanen *et al.*, 2016; Terburgh *et al.*, 2019; Tyynismaa *et al.*, 2010). Lactate and Leucine depletion also implicate the muscle-liver Cahill cycle alongside the intracellular pathways described (Bifari & Nisoli, 2017; Sarabhai & Roden, 2019). Of note, magnesium, and not calcium, was determined as the perturbed cation in this tissue. As a key co-factor for ATP-utilizing enzymes and an indicator of healthy protein turnover (Barbagallo *et al.*, 2021; Huskisson *et al.*, 2007), this is a significant effect deserving of further study. Again, non-muscle metabolic contributions should also be considered, as the Mg^{2+} depletion may also be related to reduced renal reabsorption or intestinal reabsorption due to energy deficits in these tissues (Finsterer, 2008; Heidari *et al.*, 2018).

In conclusion, rudimentary sub-cellular, mitochondria-targeted metabolomics captures known alterations in *in vivo* LS model mice while granting the ability to further elucidate minor tissue-specific and major mitochondrial responses to *Ndufs4* KO at a sub-cellular level. Herein lies the value of sub-cellular metabolomics for mitochondria-related research, as these effects were not detectable in whole-cell studies of the same tissues.

5.3.2 Limitations and future directions

Without the direct interrogation of several of the intermediates related to all the pathways discussed here, no mechanistic conclusions, as to the full underlying significance of these effects, can be established. In the face of many practical issues regarding technical variation in metabolomics studies using isolated mitochondria (Liu & Xu, 2018), the statistical selection criteria were set very strictly in comparison to the statistical power-lacking small sample groups employed here. The purpose of this was to exclude the possibility of type I errors (false positives), while accepting the loss in information from an increased chance of type II error (falsely excluding positive correlations) (Akobeng, 2016; Vinaixa *et al.*, 2012), and thus focus on only the most prominent and abundant intergroup variation in this study.

Metabolic intermediates of significant interest, but higher subjectivity to technical variance, were thus not able to be quantified, while they are indirectly implicated in many of the implicated pathways. Concurrently, accurate analysis of compartmentalized glutamine, glutamate, serine and aspartate would deliver excellent insights on the LS pathology as these amino acids are critical intermediates to TCA cycle anaplerosis, transamination reactions, urea cycling, 1C metabolism, biosynthetic pathways, cellular senescence and neurotransmitter metabolism. The quantification of 1C-related transsulfuration and methylation intermediates (cystine, cystathionine, methionine, etc.) would also serve to complement or rule out many of the hypothesized metabolic shifts described here. The methodological advancements published in the late course of this study allow even more targeted mitochondrial immunopurification techniques that promise interrogation of highly specified mitochondrial sub-populations from tissue matrices (Bayraktar *et al.*, 2019; Hubbard *et al.*, 2019), while novel proteomics-based mitochondrial content assays may enable more accurate quantitative studies (McLaughlin *et al.*, 2020). Regardless, the outcomes of this study accentuate the ability of sub-cellular metabolomics to further clarify the compartmentalized nature of pathways currently implicated in LS and other RC-related disease. Mitochondrial neuromyopathy research and clinical interventions thus stand to gain much from further targeted *in vivo* study of compartmentalized metabolic intermediate concentrations and fluxes for these anabolic and bioenergetic pathways.

5.4 Materials and methods

5.4.1 Animals and sampling

Male mice harboring a homozygous *Ndufs4* truncation (KO) were used for this study, along with age- and sex-matched healthy controls (WT). Only males were included in this study to minimize known differences in sex-related metabolic variation which might obscure interpretation of the results (Ruoppolo *et al.*, 2018; Wells *et al.*, 2016). KO mice were born from heterozygous crosses (*Ndufs4*$^{-/+}$; B6.129S4-*Ndufs4*$^{tm1.1Rpa/J}$) obtained from Jackson Laboratory (JAX stock #027058, USA). *Ndufs4* genotypes were confirmed by polymerase chain reaction using tailsnips. The animals were bred and housed at the specific pathogen-free unit of the Vivarium (SAVC reg. no. FR15/13458) of the Pre-Clinical Drug Development Platform (PCDDP; NWU, RSA). This study was ethically approved (NWU-00568-19-A5) and governed by the Animal Research Ethics Committee of the NWU. Animals were housed under controlled conditions: temperature (22 ± 1 °C), humidity (55 ± 10%) and light (12:12 hour light/dark cycle), with standard laboratory chow (Rodent Breeder, #RM1845, LabChef, Nutritionhub, ZAF) and water provided *ad libitum*.

Based on survival curves and phenotypic analyses described in Miller et al. (Miller *et al.*, 2021), mice of the post-natal age of 45–50 days (P45–50) were selected for the study, as they phenotypically resemble the late stage of LS in patients. Mice were euthanized between P45 and 50 via cervical dislocation at the same time of day. Whole-brain and quadricep femoris tissues were removed and rinsed with ice-cold saline solution (SABAX PBS; 0.9% NaCl (*w*/*v*), #7634, Adcock Ingram, ZAF) to remove the surrounding blood and hair. These tissues were immediately processed for mitochondrial isolation.

5.4.2 Mitochondrial isolation and cytosol preparation

To produce mitochondrial and cytosolic fractions of sufficient purity for metabolomics analysis, fractionated magnetic mitochondrial separation (FMMS) and cytosolic reverse filtration were performed according to a recently established kit-based method (Van der Walt & Louw, 2020)(Chapter 4). The process was performed at 4 °C using the MACS Mitochondria Extraction Kit for mouse tissue (Miltenyi Biotec, DEU) with slight variations from the manufacturer's instructions (Hornig-Do *et al.*, 2009). Brain (100 mg) and quadricep muscles (150 mg) were finely cut and homogenized in MACS lysis buffer to produce 10% and 15% (*w*/*v*) homogenates for the brains and muscles, respectively. Brief centrifugation at 1,300 x*g* (2 minutes) followed, before the post-nuclear supernatant was diluted 10x (v/v) in 1x separation buffer (SB).

For magnetic enrichment, mitochondria were labelled with anti-TOM22 microbeads (1.5 and 0.5 µL /mg tissue for brain and muscle samples, respectively) for 1 hour at 4 °C. The suspension was loaded onto a magnetized LS-M column, in a MACS Separator at 4 °C to retain labelled mitochondria. Of the flow-through, regarded as a crude cytoplasm, 2.5 mL was subjected to centrifugal filtering to prepare the cytosolic fraction. Centrisart® 100 kDa centrifugal cut-off filters (#13269E, Sigma Aldrich, USA), accelerated to 2,000 x*g* for 15 minutes at 4 °C, were utilized for the centrifugal filtering. Labelled mitochondria were eluted from the LS-M column in 1x SB after removal from the magnet; this was repeated three times for each sample. Before further analysis, the eluates were centrifuged at 13,000 x*g* for 2 minutes (4 °C), and the mitochondrial pellets were resuspended in 120 µL chromatography-grade water (Burdick & Jackson, USA) containing the selected internal standard (IS) compounds described in Section 5.4.4. The mitochondria isolation procedure took approximately 90 minutes from tissue homogenization to mitochondrial elution.

5.4.3 Metabolomics group structure and preparation for multiplatform studies

Established untargeted proton nuclear magnetic resonance (^{1}H-NMR) and semi-targeted liquid chromatography-tandem mass spectrometry (LC-MS/MS) metabolomics methodologies (Mason

et al., 2018; Terburgh *et al.*, 2019) were applied to each mitochondrial and cytosolic sample produced from the quadriceps and whole-brain homogenates of each *Ndufs4* KO (n = 8) or WT (n = 8) animal. To maximize the information gained from the small sample volumes available, samples were first analyzed with ^{1}H-NMR, which requires minimal sample preparation, before preparing and analyzing the recollected samples on LC-MS/MS. All cytosolic samples were analyzed together as a batch on each platform, while the mitochondria were analyzed as their own separate batch on each platform.

5.4.4 Internal standards and quality control samples

The IS compounds N,N-dimethyl-L-phenylalanine (DMPA; Sigma-Aldrich) and 3-phenylbutyric acid (3-PBA; Sigma-Aldrich) were added during the resuspension of the mitochondrial fractions as described above, while a small volume of the mixed stock solution thereof was added to each cytosolic fraction prior to metabolomic sample preparations to obtain similar concentrations of each IS across all samples. For each batch analyzed, a quality control (QC) sample (consisting of pooled aliquots from each sample therein) was periodically re-analyzed to monitor technical variation, while a single sample composed of pure chemical reference standards for each targeted LC-MS/MS feature was also analyzed at the end of each LC batch to aid metabolite identification. Unless otherwise stated, all solvents used were of chromatography grade or equivalent purity.

5.4.5 Untargeted ^{1}H-NMR spectroscopy

Mitochondrial and cytosolic samples were prepared according to the recently established miniaturized ^{1}H-NMR protocol (Mason *et al.*, 2018) as follows: Samples were centrifugally filtered using Centrifree 30 kDa cut-off filters (Merck/Millipore, USA) at 12,000 x*g* and room temperature to remove proteins and other macromolecules, before 54 µL filtrate was transferred to a 2 mm NMR tube using the eVol® NMR digital syringe (Sigma Aldrich, USA). The programmed pipetting sequence added the selected chemical shift standard for ^{1}H-NMR (3-(trimethylsylil)-propionic acid (TSP; Merck/MagniSolv™, DEU in deuterated water (D_2O)), such that a 10:90% ratio of D_2O/H_2O was maintained as per the standard protocol. The 2 mm NMR tube was inserted into the gripper adaptor of the Bruker MATCH system, before each NMR MATCH assembly was loaded onto a SampleXpress autosampler for NMR analysis.

Analysis proceeded at 500 MHz on a Bruker (DEU) Avance III HD NMR system, equipped with a 5 mm TXI probe head optimized for ^{1}H observation. Briefly, ^{1}H spectra were acquired as 128 transients in 32 K data points with a spectral width of 6000 Hz (12.0 ppm). The H_2O resonance at 4.70 ppm was suppressed using the pulse sequence programme NOESY-presat. The

number of dummy scans = 4 and the number of scans = 128 yielded a run time of 15.75 minutes per sample. Each sample was automatically shimmed on the deuterium signal, locked, probe tuned and matched; and pulse calibrated using Bruker Topspin (V3.5), before further processing was conducted using Bruker AMIX (V3.9.14).

NMR samples were recollected post-analyses for LC-MS/MS preparation, as the applied NMR methodology is innately non-destructive. Of the recollected samples, 41 µL of each was transferred to separate microcentrifuge tubes for LC-MS/MS analyses, while the approximately 19 µL remainder was pooled for each tissue matrix (brain and quad cytosol, brain and quad mitochondria) to perform additional 2D correlation spectroscopy (COSY) and 2D J-resolved spectroscopy (JRES) to confirm metabolite identification (Dona *et al.,* 2016).

5.4.6 LC-MS/MS amino acid and acylcarnitine profiling

LC-MS/MS amino acid and acylcarnitine profiling was performed according to the methodology previously described in *(Terburgh et al., 2019)* for murine model tissue samples, with minor modifications to better suit the post-MACS mitochondrial and cytosolic sample matrices.

To each post-NMR extract (41 µL), an internal standard mixture consisting of several deuterium-labelled versions of selected target compounds (2.5 ppm per compound) was added before LC-MS/MS sample preparation (valine_d8, isoleucine_d10, phenylalanine_d5, lysine_d4, acetylcarnitine_d3, octanoylcarnitine_d3, stearoylcarnitine_d3; all from Cambridge Isotope Laboratories). Metabolites were extracted in a molar excess (~300 µL) of acetonitrile at 4 °C (10 minutes) before 10-minute centrifugation (20,000 ×*g* at 4 °C). Thereafter, metabolite-containing supernatant was dried under nitrogen gas stream. Metabolites were butylated via a reaction with 4:1 (v/v) 1-butanol (Sigma-Aldrich, USA)/acetyl chloride (Fluka Analytical, CHE) and heat block incubation at 50 °C for 1 hour. Samples were again dried under nitrogen stream, before being reconstituted in a final volume of 100 µL water/acetonitrile (50:50, *v*/*v*; Burdick & Jackson, USA) and transferred to 250 µL pulled point glass vial inserts.

The LC-MS/MS system consisted of an Agilent© 1200 series HPLC front end, coupled to an Agilent© 6410 series triple quadrupole mass analyzer with an electrospray ionization (ESI) source, operated in the positive ionization mod. Analytes were separated on a C18 Zorbax SB-Aq reverse phase column (Agilent©, USA: 150 mm x 2.1 mm x 3.5 µm) kept at 30 °C. A sample volume of 2.5 µL was separated using a mobile phase gradient. The chromatographic gradient started at 100% solvent A (water with 0.1% formic acid (Sigma-Aldrich)) and 0% solvent B (acetonitrile with 0.1% formic acid), with a flow of 0.3 mL/minute, maintained for 1 minute, before ramping to 5% solvent B over 1 minute. Thereafter, solvent B was increased to 20% over

a period of 2 minutes, where it was then kept constant for 3 minutes. Thereafter, it was increased linearly to 100% solvent B over 7 minutes. Over this period, the flow was linearly increased to 0.35 mL/minute (between 14 and 14.1 minutes). After maintaining these conditions for 5 minutes, the gradient was decreased to 5% solvent B at 19.5 minutes and kept constant for 1.5 minutes. A post-run of 8 minutes was allowed to ensure equilibration of the column between samples, capping the 29-minute total run time. The ESI source gas (nitrogen) temperature was kept at 300 °C, with a flow rate of 7.5 L/minute. Nebulizer pressure was kept at 30 psi, and the capillary voltage at 3,500 V. The Agilent© MassHunter Workstation Software (v B09.00) was used for data acquisition and extraction.

5.4.7 Data processing

Spectral data were extracted into matrices, where an extra NMR data matrix reporting only the untargeted spectral bin sums for each sample was also extracted for calculation of a total useful NMR signal (NMR-TUS) normalization factor, as none of the selected IS compounds could accurately represent the variance due to pre-metabolomics tissue sampling and MACS isolation procedures. All datasets were individually inspected for data quality, through correct peak picking, alignment and batch precision (Section 5.2.1) as IS and QC coefficients of variance (CV%), and pre-processed (50% QC-CV% filtering, missing value imputation via randomized ¼ minimum area replacement and normalization).

Metabolites were normalized to tissue mass through normalization with NMR-TUS as the most applicable factor for the data reported here (Figures 5-8, 5-9). For LC-MS/MS data, metabolites were normalized to their own isotope (where possible) or the isotope showing the strongest linear correlation thereto, based on the analyte peak area (Pearson's r correlation analyses) prior to the above-mentioned normalizations. No significant batch effects were evident; thus, no batch corrections were performed.

Finally, data pre-treatment (glog transformation and Pareto scaling) and outlier detection (PCA Hotelling's T2 ellipses, loadings plot and biplots) were conducted. Data processing was conducted using Excel 2013 (Microsoft), SPSS Statistics (v.25.0; IBM) and MetaboAnalyst 5.0 (Pang et al., 2021). The metabolomics data obtained in this study (file name: Gunter007dekok_20210916_012612) can be accessed at the Common Fund's National Metabolomics Data Repository (NMDR) website, the Metabolomics Workbench (https://www.metabolomicsworkbench.org (accessed on 18 September 2021)), where it has been assigned the Data Track ID 2843.

5.4.8 Statistical analyses

Univariate analyses were used to determine significant discriminatory features between *Ndufs4* KO and WT sub-cellular metabolic profiles. Comparisons were performed between genotypes (WT vs. KO) in each separate tissue compartment dataset only, with only the results of these tests being compared between compartments and tissues.

An independent, two-sample Student *t*-test was carried out on the unpretreated, NMR-TUS-normalized datasets to identify compounds with significantly altered intensities between diseased mice and controls (VIPs). In line with power calculations performed (G* Power 3; Universität Dusseldorf) at the inception of this study, a t-statistic with a *p*-value of <0.1 was considered statistically significant, while effect sizes (Cohen's D value; D) of ≥1.0 were considered practically significant and used complimentary to the *t*-test (Faul *et al.*, 2007). Principal component analysis (PCA) and partial least squares discriminant analyses (PLS-DA) were used to visually investigate the clustering, covariance and discriminatory power of the univariately selected VIPs. This was performed in MetaboAnalyst 5.0 (Pang *et al.*, 2021) on a log-transformed and Pareto-scaled dataset comprising only the important metabolites identified on each platform.

Dataset features were identified via spectral and retention time matching, using the analyzed pure chemical reference standards, and commercial and in-house spectral libraries, together with public databases, and metabolite identities were assigned to spectral features, all with the highest (Level 1) confidence (Schymanski *et al.*, 2014).

5.5 Supplementary results

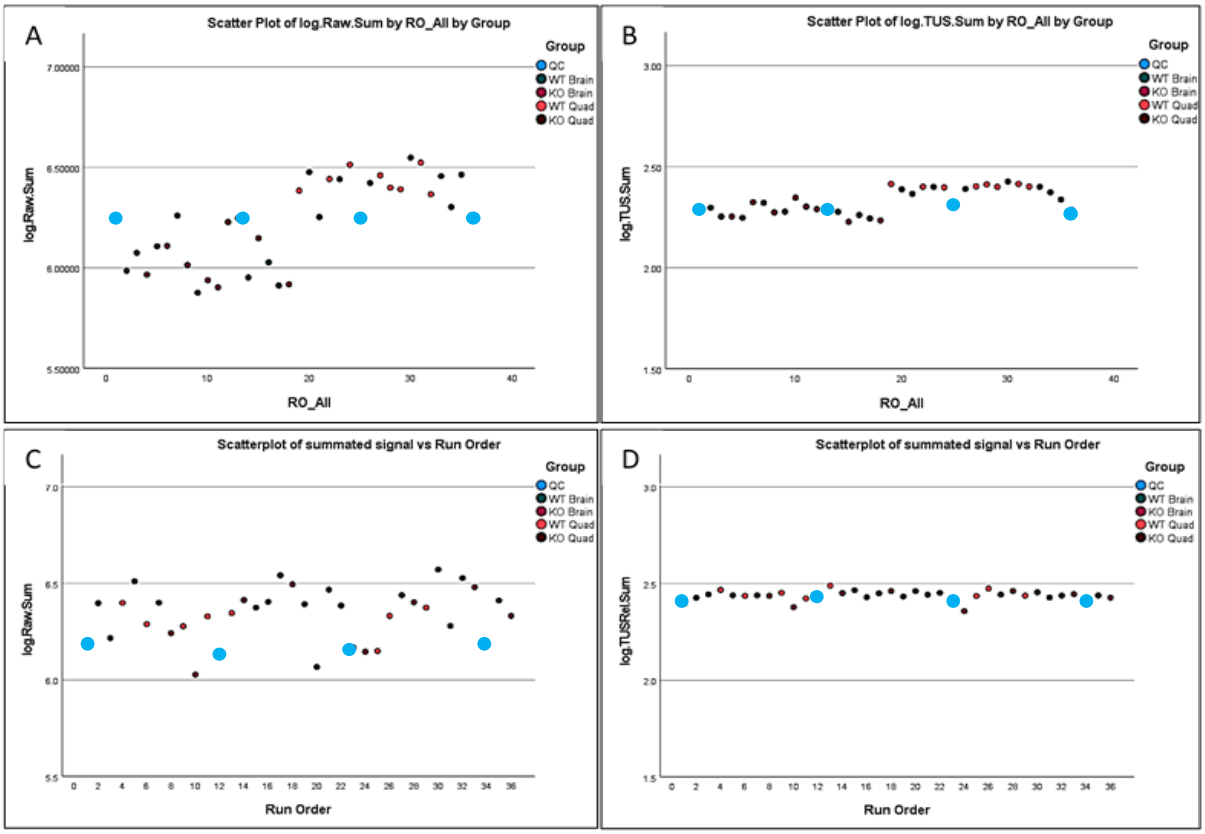


Figure 5-8: Scatterplots of raw and TUS normalized total feature sum vs run order per NMR batch, indicating applicability of the applied normalization strategy. (A) and (B) depict the total sample signal for the unnormalized and TUS normalized cytosol samples, respectively. (C) and (D) illustrates the same unnormalized and TUS normalized sample sums, respectively, for the mitochondrial sample batches. Large blue dots indicate QC replicates throughout each batch.

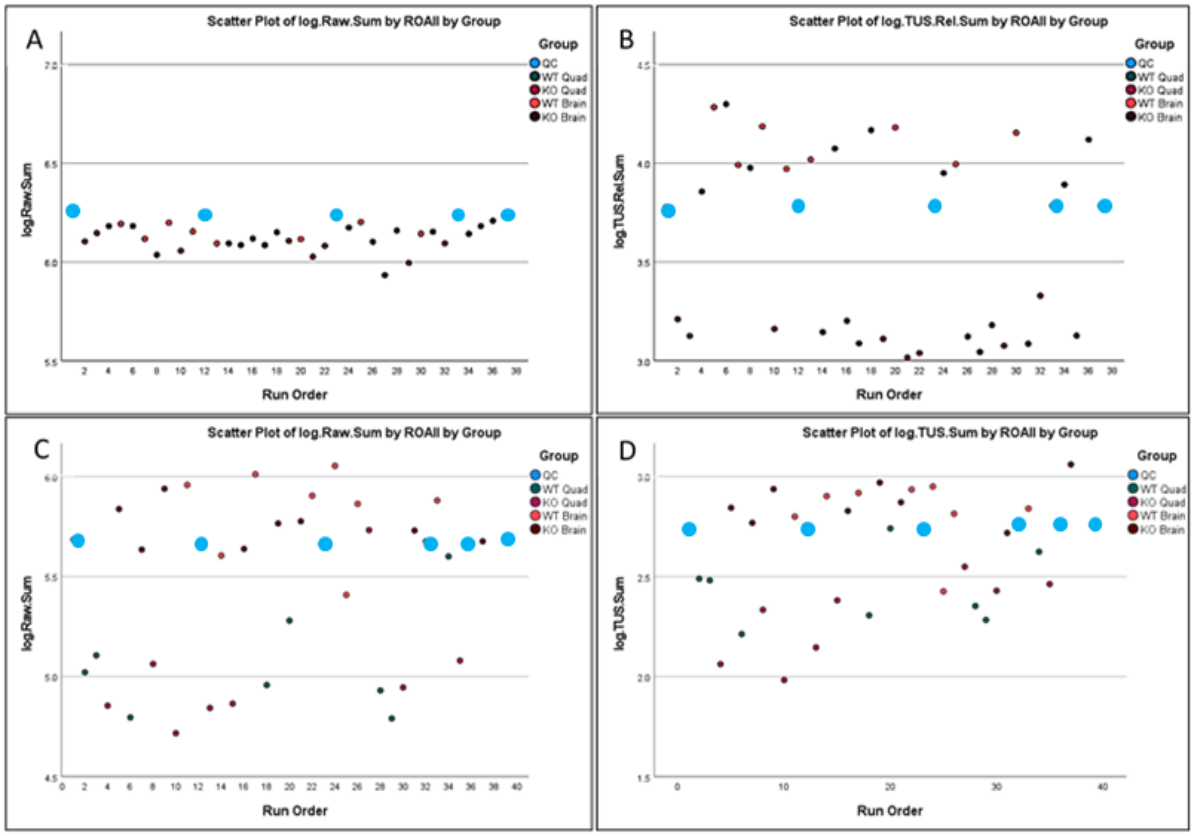


Figure 5-9: Scatterplots of raw and TUS normalized total feature sum vs run order per LC-MS/MS batch, indicating applicability of the applied normalization strategy. (A) and (B) depict the total sample signal for the unnormalized and TUS normalized cytosol samples, respectively. (C) and (D) illustrates the same unnormalized and TUS normalized sample sums, respectively, for the mitochondrial sample batches. Large blue dots indicate QC replicates throughout each batch.

Table 5-2: Positively detected features by LC-MS/MS and ^{1}H-NMR sorted from highest to lowest detected area signal (unprocessed). Measurement stability is indicated by %CV values for each compound in the separate batches, where N.A. indicates compounds not present above noise level in the specified QC samples.

Metabolite (Level 1)	Med Signal (log amu)	%QC-CV Mito	%QC-CV Cyto
LC-MS/MS			
Carnitine (C0)	5.34	N.A.	3.27
Glutamic acid	5.15	1.48	3.33
Creatine	5.15	N.A.	4.63
Aspartic acid	4.94	2.27	3.72
N-Acetylaspartic acid	4.74	3.49	7.99
γ-Aminobutyric acid	4.65	6.85	3.22
Sarcosine	4.21	N.A.	10.23

Table 5-2 (Continued)

Metabolite (Level 1)	Med Signal (log amu)	%QC-CV Mito	%QC-CV Cyto
Alanine	4.11	3.23	7.73
Serine	4.07	1.02	3.13
Leucine	4.03	1.79	2.59
Glycine	3.96	3.50	9.11
Phenylalanine	3.90	2.41	5.02
Octanoyl-carnitine (C8)	3.86	5.91	38.39
Glutamine	3.87	7.49	4.65
Proline	3.76	12.98	6.50
Valine	3.69	1.23	1.89
Tyrosine	3.63	2.81	3.24
Histidine	3.63	11.06	11.34
Acetylcarnitine (C2)	3.53	2.82	3.11
β-Aminoisobutyric acid	3.75	4.44	5.29
Lysine	3.52	1.94	9.17
Arginine	3.54	5.80	19.39
Isothreo/Threo	3.41	5.34	5.07
Ornithine	3.55	3.67	N.A.
Citrulline	3.33	5.68	17.85
Threonine	3.15	22.30	174.00
Tryptophan	3.09	3.69	N.A.
Methionine	3.11	N.A.	N.A.
Myristoyl-carnitine (C14)	3.04	N.A.	29.81
2-aminoadipic acid	3.05	N.A.	N.A.
4-Hydroxyproline	3.10	N.A.	N.A.
Trimethylglycine	2.99	N.A.	N.A.
^{1}H-NMR			
Acetic acid	5.69	11.13	13.82
Formic acid	5.57	27.28	N.A.
Lactic acid	5.56	1.82	3.53
Taurine	5.51	8.78	7.93
Ca(II)-EDTA	5.45	8.06	3.22
Creatine	5.32	3.00	1.19
Mg(II)-EDTA	5.13	9.02	2.58
Carnitine	4.84	8.44	N.A.

Table 5-2 (Continued)

Metabolite (Level 1)	Med Signal (log amu)	%QC-CV Mito	%QC-CV Cyto
Alanine	4.69	N.A.	50.04
Adenosine monophosphate	4.64	N.A.	20.92
N-acetylglutamine	4.52	8.48	10.51
N-acetylaspartic acid	4.51	18.01	4.08
Choline	4.37	13.07	N.A.
Pyruvic acid	4.04	N.A.	31.69

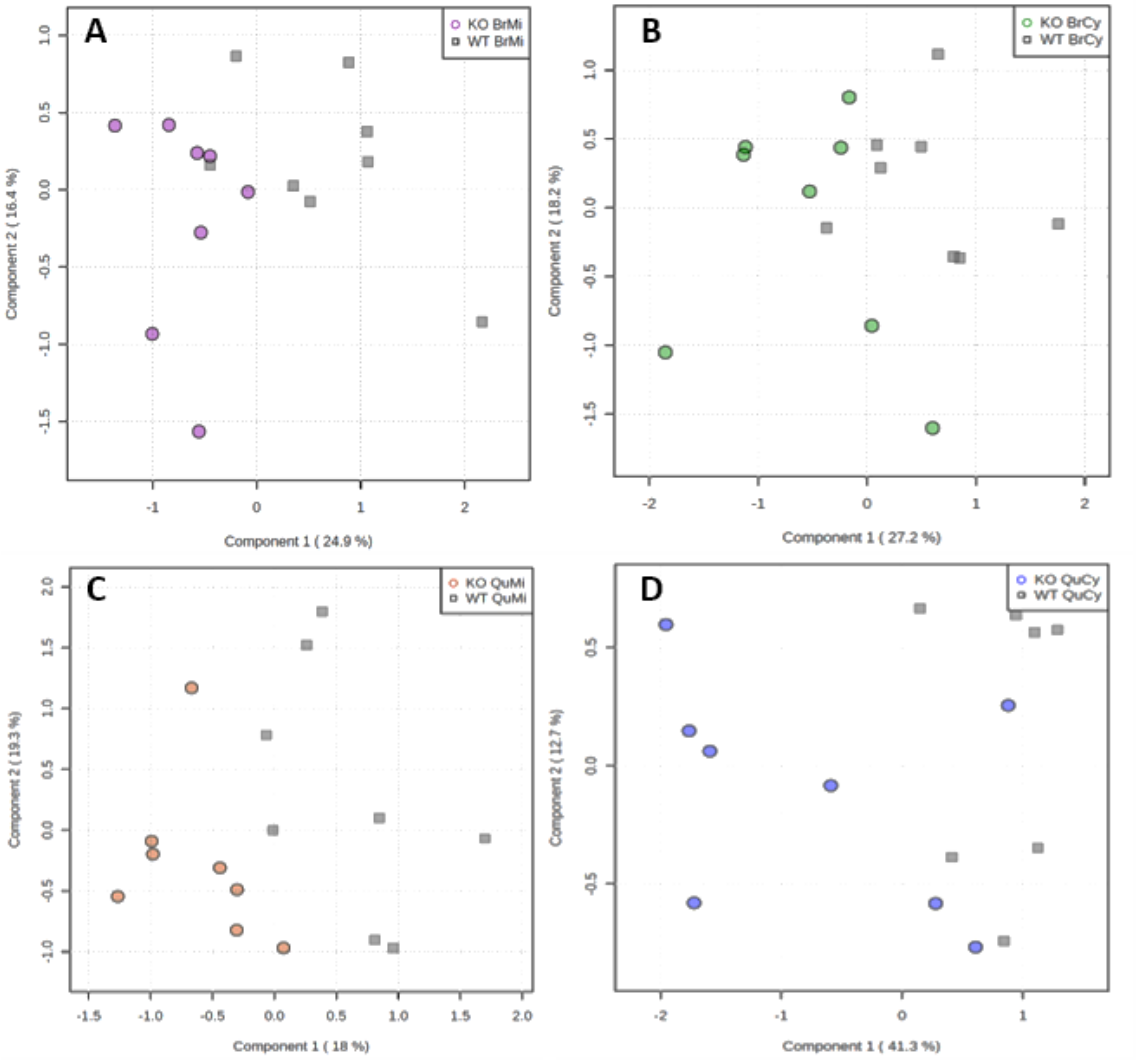


Figure 5-10: PLS-DA projections of the univariately selected VIP features for each tissue or cell-compartment sample matrix. Figures (A) and (B) represent the PLS model for *Ndufs4* KO (colour dots) and WT (grey squares) supervised group separation in whole-brain mitochondria and cytosol VIP datasets, respectively. Similarly, (C) and (D) indicate the PLS plots for quadricep mitochondrial and cytosolic VIP plots, respectively.

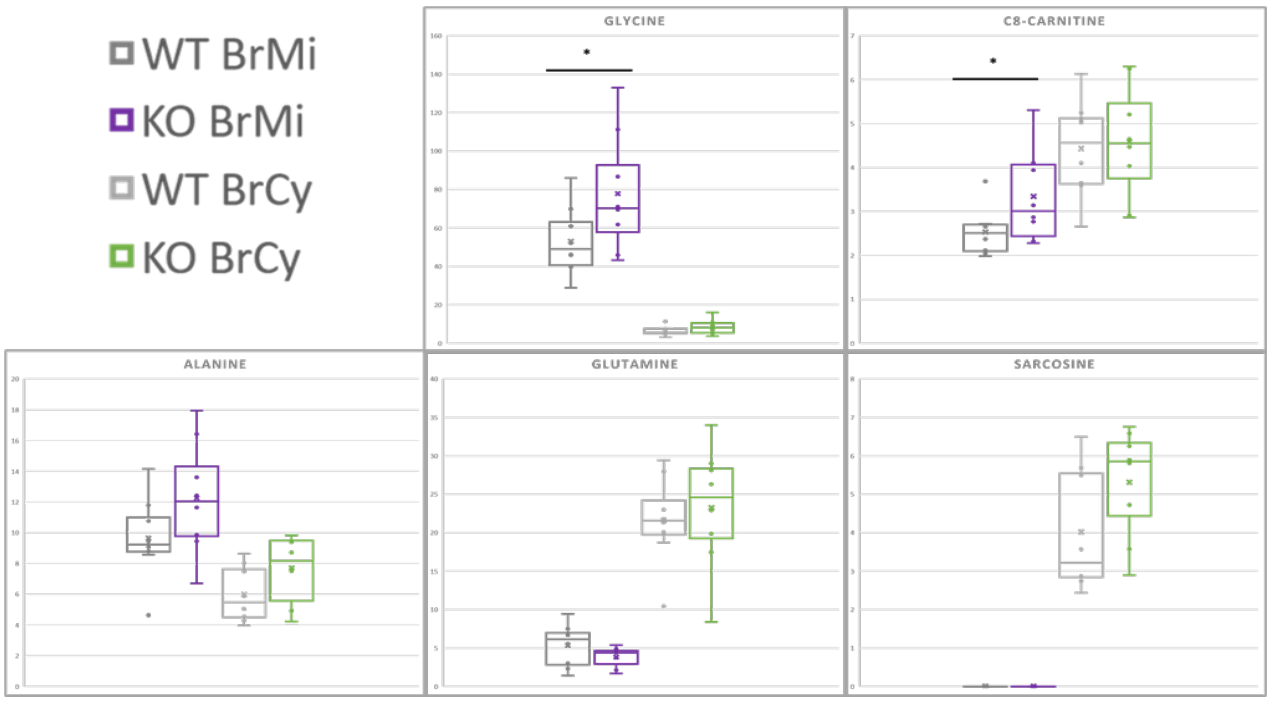


Figure 5-11: Additional compartment-specific metabolite alterations in *Ndufs4* KO whole-brain, identified by ^{1}H-NMR and LC-MS/MS. Boxplots indicate normalized value range descriptives across all analyzed whole-brain matrices. Statistical significance as t-test probabilities is indicated as (*) for $p < 0.1$ or (**) for $p < 0.05$.

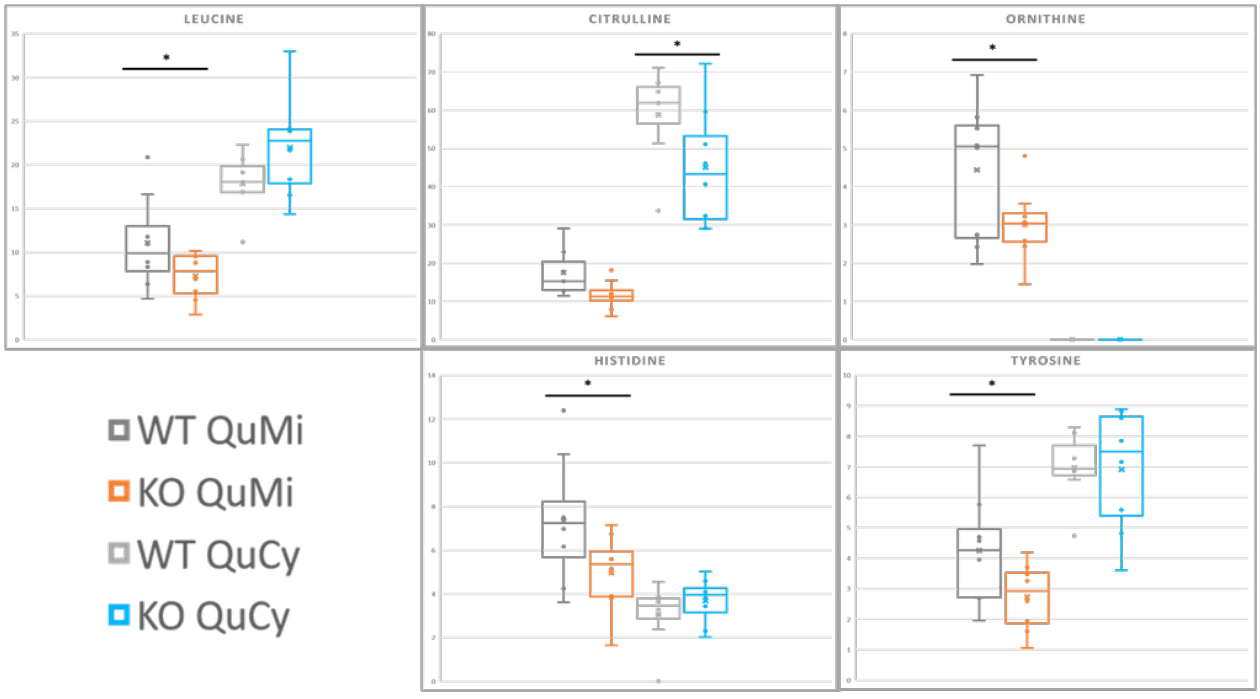


Figure 5-12: Additional compartment-specific metabolite alterations in *Ndufs4* KO quadricep muscle, identified by ^{1}H-NMR and LC-MS/MS. Boxplots indicate normalized value range descriptives across all analyzed quadricep matrices. Statistical significance as t-test probabilities is indicated as (*) for $p < 0.1$ or (**) for $p < 0.05$.

CHAPTER 6

Summary, conclusions and recommendations

6.1 Introduction

Being the most common and diverse pathology associated with Complex I disease (CID), Leigh Syndrome (LS) cases have set a benchmark for understanding pathogenic mitochondrial dysfunction. Despite the knowledge of unambiguous pathogenic mutation targets (such as the *Ndufs4* truncation investigated here), research is impeded by the complex genetic, epigenetic and metabolic repercussions of such mutations, thus diagnostic and treatment options are still scarce and of limited effectivity. Although the neuromuscular pathology of *Ndufs4*-deficient LS mouse models is known to be neurologically driven, recent studies have identified severe muscle metabolic disturbances that implicate multi-organ bioenergetic regulation. A core factor in this regard remains the contribution of mitochondria-specific metabolism in these tissues, given that distinct mitochondrial abundance, morphology and functions underlie the respective tissues' metabolic responses to energy deprivation. To date, this compartment-targeted philosophy has not been applied to mammalian models of genetic mitochondrial disease (MD), although its value has been proven in several other pathological and pharmacological models.

This study aimed to address this research gap by contributing compartment-specific knowledge of metabolic perturbations due to CID. This was achieved by adapting and implementing a highly specific, widely available immunochemistry driven magnetically activated cell sorting (MACS) method for mitochondrial isolation, cytosolic purification and downstream metabolomics of these cell fractions from *Ndufs4* KO and WT mouse brain and skeletal muscle. Towards this aim, several objectives divided into three distinct experimental phases had to be met. While the results thereof are expansively discussed in chapter 4 and 5 (and published after peer review as indicated by annexure C and D), this chapter provides a summary of the conclusions derived therefrom before discussing the strengths and limitations of each phase. Chapter 6 is concluded with potential prospects for further application of this sub-cellular metabolomic strategy in mitochondria-related diseases, specifically towards better understanding, diagnosing and treating CID-related LS.

6.2 Summary and conclusions

6.2.1 Sample collection phase

Breeding of heterozygous *Ndufs4*$^{+/-}$ mice and collection of the predefined amounts of knockout (KO) and wildtype control (WT) animals for this study was successfully completed (**Objective 1.1**), with the details of individual animals summarized in Annexure B. *Post mortem* genotype confirmation of the selected animals confirmed their WT or KO grouping (initially determined by PCR upon weening) as accurate (**Objective 1.3**), with results corresponding to those of

Valsecchi *et al.* (2012). Finally, tissue collection was performed successfully and rapidly for all the stated animals, with whole-brain and quadricep muscles being excised, kept on ice and processed for mitochondrial isolation within 30 minutes of euthanasia (**Objective 1.2**).

6.2.2 Phase A: Establishing a suitable MACS methodology for mitochondrial and cytosolic fraction preparation from *Ndufs4* KO mice

The first phase of the study commenced with adapting the manufacturers' MACS methodology to obtain enough intact mitochondria for metabolomics applications (**Objective 2.1).** Up to 3-fold more mitochondria (observed as enrichment of matrix-specific citrate synthase enzyme activity compared to the homogenate) could be obtained from quadricep tissue by adjusting the ratio of antibody to tissue and repeating the elution of magnetically retained mitochondria three times instead of just once (Franko *et al.*, 2013; Hubbard *et al.*, 2019). Notably, both the mitochondrial and cytosolic fractions delivered viable ^{1}H-NMR features after these adjustments, where no metabolite was present above baseline trials using the original protocol. The entire fractioning procedure consistently took 90 minutes, and the timeframe could be standardized as such.

The superiority of MACS, compared to differential centrifugation (DC) as the most widely applied isolation method, was successfully demonstrated on the grounds of mitochondrial yield and fraction purity. Of the total mitochondrial content, 25–27% could be isolated from the brain tissue (roughly double the DC yield; **Objective 2.2**), in line with the maximum reported yield for kit-based MACS methods. Greater depletion of LAMP-2 (an indication of lysosomal membrane contamination) in MACS mitochondria was shown by quantitative Western blot analyses, indicating greater depletion of lysosomal contamination and thus higher fraction purity in the MACS-derived fractions (**Objective 2.3**). Furthermore, the integrity of the isolated mitochondria, expressed as respiratory coupling of the IMM via Seahorse respirometry, was equivalent and acceptable for both DC and MACS isolates (**Objective 2.4**). Western blots also confirmed the ability of our cytosolic filtering approach to remove any residual organelles to produce a purely cytosolic fraction, as the total absence of matrix-derived Hsp-60 protein (abundant small matrix-specific protein) was observed in the cytosolic filtrates. This was also shown by CS yield measurements, as the residual CS activity in the crude cytoplasmic fractions (13%) was depleted below detection levels after filtration. In summary, the described approach could produce MACS mitochondria with yield, purity and integrity comparable to the best adaptations published to date (Chen *et al.*, 2016; Franko *et al.*, 2013; Hornig-Do *et al.*, 2009; Hubbard *et al.*, 2019), while the novel filtering approach delivered the most comparable, organelle-free cytosolic fraction described in literature thus far (Afanasyeva *et al.*, 2018; Matuszczyk *et al.*, 2015), effectively meeting the stated objectives of this phase.

6.2.3 Phase B: Probing the viability of metabolomics in the MACS buffer environment and the produced tissue fractions

NMR analyses of the MACS buffers confirmed the absence of interfering sugars, showing only a large amount (~4 mM) of EDTA that could be exploited for bivalent cation analyses in the final samples. To visualize the effects of the buffers' salt content on NMR, chromatography, and mass spectrometry, pure reference standards of abundant mammalian metabolites were analyzed within and without the MACS buffer environment (**Objective 3.1** and **3.2**), showing minimal effect on analytical performance for most compounds. Measurement precision (expressed as coefficient of variance percentage over ten analytical replicates) was found to be < 20% for most compounds at low, medium and high concentration levels on GC-TOF-MS and ^{1}H-NMR platforms, well below the 30% CV cut-off typically utilized for targeted metabolomics. Notably, the ionic environment improved GC-MS analysis of organic acids such as pyruvate and lactate, showing greater stability in the MACS environment than in pure water. The analytical accuracy of ^{1}H-NMR measurement was shown by comparing metabolite recovery in MACS buffer to that in the nascent NMR medium (water). Most compounds showed 80-120% recovery, indicating acceptable accuracy for NMR measurement in this medium. On both platforms, the linearity of metabolite measurements over the three concentration ranges were excellent (R^2 > 0.99), indicating no concentration-dependant analytical effects. The only exceptions to these precision, accuracy and linearity results were aspartate and glutamate, as these compounds are known to spontaneously degrade during preparation. It is thus imperative to investigate the performance of individual compounds in subsequent studies; however, these results prove an acceptable quality of most metabolite measurement in MACS buffers.

The activities of phase A and B concluded with a pilot application of GC-TOF-MS and ^{1}H-NMR analyses on MACS-derived mitochondria and cytosol from a *Ndufs4* WT mouse (**Objective 3.3**), showing that i) a viable number of metabolites could be detected with high confidence identification and ii) these metabolites can be measured with high precision over three technical replicates. GC-TOF-MS analyses could identify and measure 29 compounds in the obtained fractions, with 12 unique mitochondrial features and 17 common to mitochondrial and cytosolic samples. These metabolites were measured with high precision (< 20% CV) and confident annotation (level 1-3 identities, according to Schymanski *et al.* (2014)). An unprecedented application of relatively insensitive ^{1}H-NMR to small-volume sub-cellular samples also delivered eight to ten metabolites with high-confidence identification, with an average %CV below 10% for each compound. Many of the detected metabolites represent features related to bioenergetic processes that are commonly perturbed in MD (Emmerzaal *et al.*, 2020; Esterhuizen *et al.*, 2017), including amino acids such as aspartate, leucine, sarcosine, glycine and N-

acetylaspartate; organic acids such as lactate, succinate and malonic acid, and lipid derivatives such as glycerol, hexadecenoic and octadecanoic acid. In summary, the MACS buffer environment does not majorly affect the analytical performance of metabolomic platforms for most biologically important metabolites and many of these compounds can be detected in mitochondrial and cytosolic fractions with high confidence and precision, thus achieving the objectives defined for this phase.

6.2.4 Phase C: First application of sub-cellular metabolomics towards the elucidation of *Ndufs4* KO mitochondrial metabolic alterations

The preceding phases provided a foundation for performing valid mitochondrial and cytosolic metabolomics on brain and muscle tissues from the *Ndufs4* KO mouse model. The authors embraced the opportunity to extend the applicability of MACS-derived isolates by performing amino acid and acylcarnitine targeted LC-MS/MS analysis on these fractions as well (**Objective 4.1**). ^{1}H-NMR and LC-MS/MS analyses (**Objective 4.2**), after data clean-up and processing (**Objective 4.3**), delivered compound measurements with %CV's below 10% across QC samples and all-sample IS measurements, indicating high-fidelity analyses and trustworthy data. Importantly, normalisation using the total useful signal from the NMR analyses outperformed the use of any IS for sample-wise data normalisation, as this approach most accurately conveys any affecting analytical factors from tissue collection to metabolomics analyses, while the ISs only represent technical variation introduced post fractioning.

Multivariate statistical analyses preliminarily showed the ability of the sub-cellular metabolite profiles to discern between WT and *Ndufs4* KO mice, while univariate statistical analyses revealed several phenotype-defining metabolite alterations in each tissue (**Objective 4.4**). Of the 10 metabolites altered in *Ndufs4* KO brain cell compartments, the majority showed increase in KO animals, with a far greater effect visible at the mitochondria-specific level. Biological interpretation (**Objective 4.5**) of these compounds corroborated the role of redox perturbation and adaptive responses aimed at restoring physiological redox ratios, alternative supplementation of respiratory activity in the absence of CI activity, and aberrant anabolic reactions mediated by one-carbon (1C) metabolism and mTORC1 signalling during the integrated stress response (Johnson *et al.*, 2020; Terburgh *et al.*, 2021). The most novel result, however, remained the utilization of bivalent cation EDTA chelate measurement to identify a significant increase in mitochondrial calcium levels that the cytosolic samples did not show. As mitochondrial calcium levels are a well-defined indicator of energetic stress and concomitant stress responses (Aouacheria *et al.*, 2017; Palmieri *et al.*, 2010), this result may pave the way for extensive future research. Analyses of *Ndufs4* KO quadricep samples revealed strikingly different compartment-specific alterations in 13 metabolites previously implicated in this tissue's

reaction to CI ablation. An overall depletion of key metabolic intermediates emphasizes the notion that glycolytic muscles do not possess sufficient mitochondrial content to fuel many of these adaptive pathways continually and successfully (Schiaffino & Reggiani, 2011; Terburgh *et al.*, 2019). Decreased urea cycle intermediates and hydroxyproline with compartment-specific patterns indicate disturbed proteostasis (Johnson *et al.*, 2014; Ross-Inta *et al.*, 2008), which likely relates to the observed muscle atrophy and hypotonia in LS. Decreased mitochondrial lactate, alongside concomitant increases in mitochondrial creatine, implicate mitochondria-specific lactate dehydrogenase and creatine kinase activity (Kazak & Cohen, 2020; Young *et al.*, 2020), emphasizing the value of this approach in elucidating compartment-specific alterations within even the most thoroughly studied bioenergetic processes. Decreased magnesium levels in both compartments also links this co-factor's important role in energetic stress to the muscle metabolic changes of *Ndufs4* KO mice.

In conclusion, this study presents a viable methodology representing a midway between the most efficient yet expensive, and the most routine yet crude mitochondrial isolation methods (Van der Walt & Louw, 2020). Application thereof, as described in this study's seminal publication (Van der Walt *et al.*, 2021), unequivocally supports the main hypotheses and met the overarching aim of the study, by reporting metabolic alterations within the mitochondria and cytosol of *Ndufs4* KO tissues that were not seen in comprehensive tissue metabolic profiling studies of whole brain and skeletal muscles from these animals or LS patients to date.

6.3 Strengths and limitations of the present study

6.3.1 *Ndufs4* KO and WT mouse breeding and sampling

Ndufs4 KO mice remain a viable model for studying LS, as small patient cohorts with variable phenotypic expressions confound large-scale study of the underlying biochemical alterations, and cell cultures from patients do not convey the physiological nuances of systemic contributions (Quintana *et al.*, 2010; Torraco *et al.*, 2015). The ability to isolate both brain and muscle tissues from these mice, a practical impossibility in human cases, exponentially accelerates our understanding of tissue-specific effects in disease. However, the main advantage animal models confer are their highly similar genetic background, environmental conditions and diet, effectively minimizing background variation in the cohort and enabling the use of less animals to achieve statistically significant results. Concurrently, the group sizes used here were deemed to be adequate for uncovering the most pronounced genotype-related effects, while exceeding the cohort sizes employed in sub-cellular evaluation of RCD to date (Chen *et al.*, 2016; Gravel *et al.*, 2014; Pan *et al.*, 2018)

The main limitation in this approach pertains to the long and expensive breeding programme required. This is attributed to i) low genetic probability of obtaining KO animals from heterozygous breeding pairs[20], ii) the use of only male mice which halves the amount of useful animals from each litter and substantially lengthens the sample collection period, iii) the advanced age that mice must reach before sampling and iv) the high cost of maintaining adequate numbers of breeding pairs. Despite the genetic similarity of the sampled mice, significant phenotypic variance among late-stage mice is common, while differences in feeding and social habits between sick and healthy mice at this stage have recently been shown to play a greater role in the final phenotypes than previously expected (Foriel *et al.*, 2018), thus euthanasia criteria based on post-natal age alone will not suffice in all contexts. Lastly, this study is limited in only evaluating male mice, as sex-specific metabolic differences may confound the results (Ruoppolo *et al.*, 2018).

6.3.2 MACS mitochondrial isolation and cytosol filtration

The MACS method applied conveys significant strengths to this study, as the kit-based components are widely available, cost-effective, easy to use and adapt to new tissues. Anti-TOM22 antibodies purify mitochondria from other cellular constituents more effectively than any centrifugal method, while keeping the IMM intact and yielding enough material for multi-platform metabolomics. The centrifugal filtering approach is rapid and efficiently removes any cellular structure (organelle) larger than 100 kDA. The smartest adaptation is the filter's mechanism of action: opposite centrifugal force and filtration directions significantly reduce the probability of rupturing organelles as they are not forced against a membrane but rather the membrane descends upon the content and gently filters extra organellar fluid through it.

The most significant drawback of any mitochondrial isolation method remains the inability to isolate all mitochondria present in a sample, as even the most specific and rapid recombinant isolation system to date can only isolate 20 – 30% thereof (Liu & Xu, 2018). Tracing the mitochondrial enrichment in each step of the fractioning process emphasized the need to consider tissue-specific milieus of mitochondrial sub-populations, as their cellular contexts detriment different steps of the fractioning process. The most important experimental factor to optimize in future studies utilizing this methodology, however, is the significant duration of the labelling and separation steps and the low throughput of the basic MACS system (one LS column and sample at a time). This inevitably increases the likelihood of confounding metabolite

[20] Mendelian genetics suggest that a 25% mutant yield should follow heterozygous crosses, however, it has been shown that far less KO mice are viably delivered for study, possibly due to infant mortality or germline selection against the mutation after multiple generations (Mereis, 2017).

turnover or IMM uncoupling during the fractioning procedure itself or during the different storage periods of the first and last collected samples before analyses (Liu & Xu, 2018). The cytosolic filtering approach, although very effective, is limited by the maximum volume a single filter can contain, as only 2,5 mL of the approximately 9 mL dilute cytosolic column flow-through can be filtered; possibly contributing to the low abundance of cytosolic metabolites observed.

6.3.3 Cell fraction quality control

Our isolation method was shown to be effective on the grounds of the three most important mitochondrial isolate quality parameters identified in previous sub-cellular studies (Kappler & Lehmann, 2019; Liu & Xu, 2018). Most importantly, the combination of enzyme enrichment, targeted protein immunoblotting and respirometry assays present three heterogeneous lines of evidence to confirm the quality of mitochondrial and cytosolic isolates, the most significant strength of the described methodology. CS enrichment stands as a rapid and high-throughput method to gauge both mitochondrial yield and their depletion from compared cytosolic fractions, while also identifying the critical steps in the workflow where future optimizations should be targeted. Immunoblotting against protein markers of common contaminating organelles is ubiquitous in such methodologies and lysosomal protein markers, as the most common mitochondrial co-precipitant, have consistently been shown to be the greatest indicator of fraction purity. Assaying the respiratory coupling ratio (RCR) of isolated mitochondria is a viable interrogation of intact mitochondria, as any IMM disruption that leads to metabolite leakage would also severely disrupt the proton motive force and impede respiration.

While expressing mitochondrial content as %CS enrichment has been a staple in mitochondrial research for decades, recent evidence reveals that it is not the most robust and sensitive indicator thereof, as several biological and experimental factors may influence the spectrophotometrically observed CS activity (McLaughlin *et al.*, 2020). Furthermore, the presence of bead-conjugated antibodies and the very diluted cytosolic samples, impedes spectrophotometric protein quantification and normalisation of CS activity to protein content, thus yields could only be expressed relative to the homogenate. When evaluating the purity of compartment fractions, the most prudent method would be to assay both compartment-specific proteins and metabolites from multiple organelles, however, the remaining uncertainty surrounding the definite mitochondrial metabolome leaves protein-based purity assessments as the most trustworthy (Liu & Xu, 2018). Western blotting was performed only against the most representative mitochondrial purity marker (lysosomal LAMP2 protein) and matrix marker for cytosolic purity (Hsp-60), while proteins from lesser contaminants such as the reticular organelles, nuclei and endosomes were not considered. Although RCR's are a proven indication of an intact IMM, several experimental and biological factors may also affect

respiratory coupling without necessarily leading to mitochondrial rupture. A need for reliable compartment-specific metabolite and protein measurement in the produced fractions is thus again emphasized.

6.3.4 Multi-platform metabolomics of mitochondrial and cytosolic isolates

The ability to apply multiple metabolomic platforms to the produced samples is a key strength, as the use of several platforms targeting different chemical classes greatly improves the resolution and thus information gained from metabolomics. Concurrently, no other studies to date have combined the precise ^{1}H-NMR and sensitive, targeted LC-MS/MS platforms or utilized the sample group sizes as large as reported here for sub-cellular metabolomics of MD tissues. The non-destructive nature of the miniaturized NMR workflow (Mason *et al.*, 2018) allowed the recollection and LC-MS/MS analyses of the minimal sample volumes; further maximizing the information gained from only 120 µL of sample. Although the high salt content necessitated multiple adaptations to our in-house metabolomic protocols, the results of phase B indeed showed the viability of most metabolite measurements in the MACS buffer environment. A large advantage of phase C was the ability to confidently identify all the metabolites in our LC-MS/MS (via MRM targets and analyzed reference standards for each transition) and ^{1}H-NMR datasets (via 2D-NMR structural information from the recollected, pooled samples).

The inherent limitations of this method, however, remains the minute amounts of metabolites in these low-volume samples, as even the most sensitive platform could only detect a fraction of the known metabolome, with many compounds bordering the lower detection and quantification limits, thus presenting with greater instability in measurement. The timeous nature of the entire workflow may incur uninduced biological variation due to metabolic turnover. Bioinformatics of metabolomics data remains an issue in pilot-type studies such as this, as no standardized pipelines exist, and a data driven approach is usually followed (van den Berg *et al.*, 2006). This is even more problematic for sub-cellular studies, as the low compound abundance, buffer interference and many unknown features complicate the application of existing workflows. Missing value imputation can significantly affect the number and significance scores of important variables, yet previous studies have shown that the most pronounced intergroup changes remain relatively consistent when applying small-value (20% of lower quantification limits) replacement as used here *versus* more statistically driven methods, such as the XERp strategy (Terburgh *et al.*, 2019). As described in section 6.2.4., no ideal normalisation method could be identified in the current study, as neither the selected internal standards or the NMR bin approach used here could correct for technical variation equivalently across all the analyzed batches and platforms. All these factors, as well pilot group sizes and inherent phenotypical variation within KO and WT groups, cumulate as the limited amount of VIPs detected. This

amount of uninduced variation necessitated the use of a p-value cut-off (< 0.1) higher than the 0.05 alpha level typically used in biological studies. The lower statistical power observed here renders standard multiple testing corrections (such as false discovery rate or FDR corrections) inapplicable towards the end of identifying the most pronounced intergroup effects – as all the identified VIPs fell below the selected significance when applying FDR. Despite all these confounding factors, the reported results still corroborate several MD and sub-cellular studies, while being able to contribute viable, novel compartment-specific effects for further study.

6.4 Recommendations and prospects for future research

6.4.1 MACS-based metabolomic applications to mitochondria-related disease

Towards more efficient metabolomic studies of MACS-derived fractions from animal models, a few key factors must still be greatly optimized. Firstly, obtaining larger sample cohorts in a shorter timeframe by optimizing breeding programs would be critical for targeted or confirmatory studies. To that end, this pilot serves as an adequate starting point for further power calculations and group size estimations. Background biological variation should be better controlled in subsequent studies by using phenotypic scoring sheets for endpoint determination (rather than age alone) and closely monitoring feeding habits to minimize metabolic variation due to possible differences in eating patterns (Foriel *et al.*, 2018). By increasing sample group sizes and reducing phenotypic variation, the statistical power and confidence levels can be greatly Improved - allowing more discriminative statistical cut-offs (such as the standard $p < 0.05$ alpha level for means comparisons). In adequately powered future studies, controlling the increased probability for Type I statistical errors due to multiple testing via FDR or similar methods is greatly recommended as to assure all reported VIPs indeed convey significant intergroup differences.

Future study should include female mice and thoroughly deconvolute gender related metabolic differences towards a full understanding of pathology related metabolism. Furthermore, high-resolution proteomics of mitochondria-specific proteins, as shown by McLaughlin *et al.* (2020) after completion of the experimental work described here, gives the most robust indication of total mitochondrial yield and purity, thus potentially presenting a rapid quality control measure and the soundest factor for normalizing metabolomics data to individual sample content. Selecting either more targeted quantitative metabolomics methods or more sensitive comprehensive profiling platforms such as GCxGC-MS or cryoprobe NMR would be the crux of further sub-cellular studies, although investigating the analytical performance of each measured compound in the low-volume, ionic environments would remain imperative. Without the availability of greatly more sensitive metabolomics platforms, compartment isolation from in vivo

models and sub-cellular analyses would not be applicable to smaller tissue samples, such as isolated brain regions, smaller muscles or invertebrate model tissues. This methodology would, however, be recommended in any study of bioenergetics-related diseases involving larger vertebrate disease models or an adequate amount of cultured cells. Finally, as more validated sub-cellular datasets become available, computational training thereof would contribute greatly towards establishing standards in bioinformatics pipelines for compartment-specific metabolomics.

6.4.2 Sub-cellular resolution of Leigh syndrome and Complex I disfunction

Targeted analyses of all the implicated pathways' intermediates would be the logical next step towards fully understanding the involved metabolism (Johnson *et al.*, 2013; Terburgh *et al.*, 2019; Terburgh *et al.*, 2021). Upon the availability of suitable methods, GC-MS profiling of apolar metabolites and direct compartment-specific redox state measurement would also clarify some of the remaining metabolism-related questions. Assessing compartment-specific lactate and creatine related enzymes would help understand the mitochondria-specific adaptations in ATP/ADP and redox balance resulting from sustained CID. Finally, regarding the complex, disease driving neural metabolic profiles, isolating and studying cell-type specific mitochondria to elucidate their role in astrocyte-neuron, glial and synaptosomal metabolite shuttles implicated here and in previous benchmark studies, would be advantageous. All factors considered; sub-cellular metabolomics can contribute vastly towards more precise LS research and eventually improve diagnosis, prognosis and treatment options for patients.

ANNEXURE A

Chemical and reagent information

Table A: Reagents and chemicals used, organized by experimental section.
Common/abbreviated names of each regent (full chemical name in brackets, where applicable) is listed alphabetically for each experimental method. The supplier and catalogue number is listed for each. Where reagents were used in more than one methodology, it is listed in the relevant section describing its first chronological application, according to Chapter 3.

Reagent	Cat. #	Company
PCR Genotyping		
Quick-DNA Miniprep plus genomic DNA isolation kit	ZR-D4069	Inqaba Biotec, ZAF
Proteinase K and storage buffer		
Solid tissue buffer		
Genomic binding buffer		
gDNA Pre-wash buffer		
gDNA Wash buffer		
gDNA Elution buffer		
Zymo-Spin columns and collection tubes		
2x Phire Direct PCR mastermix	F170L	Thermo Scientific, USA
NDUFS4 1060 Forward primer	S32E6	Inqaba Biotec, ZAF
NDUFS4 Reverse primer	S3424	Inqaba Biotec, ZAF
Nuclease-free water	129114	Qiagen, DEU
Agarose	8100	Thermo Scientific, US
Ethidium bromide	46065	Sigma Aldrich, USA
10x Bionic™ buffer	B6185	Sigma Aldrich, USA
GeneRuler 100bp DNA ladder	SM0241	Thermo Scientific, USA
GeneRuler 6x DNA Loading dye	SM0242	Thermo Scientific, USA
Homogenization and fractioning		
Centrisart 100 kDa Centrifugal cut-off filters	13269E	Sigma Aldrich, USA
EDTA [Ethylenediaminetetraacetic acid]	ED2P-100G	Sigma Aldrich, USA
KCL [Potassium chloride]	504200	UniLab, DEU
KOH [Potassium hydroxide]	8.14353.100	Merck, DEU
MACS Mitochondria Isolation kit, mouse tissue	130-094-872	Miltenyi Biotech, DEU
Tissue lysis buffer		
10x Separation Buffer		
Anti-TOM22 IgG-conjugated paramagnetic beads		
LS paramagnetic separation column		
MOPS [3-(N-morpholino) propanesulfonic acid]	M-3183	Sigma Aldrich , USA
BCA Assay		
BCA [Bicinchoninic acid]	B9643	Sigma Aldrich, USA
BSA standard [Bovine serum albumen] 1µg/µL	P0914	Sigma Aldrich, USA

Reagent	Cat. #	Company
$CuSO_4$.$5H_2O$ [Copper(II) sulphate]	C2284	Sigma Aldrich, USA
Citrate Synthase Assay		
Acetyl-Coenzyme A [Li^+]	A218	Sigma Aldrich, USA
DTNB [2,2-dinitro-5,5-dithiobenzoic acid]	D8130	Sigma Aldrich, USA
OAA [Oxaloacetic acid]	O4126	Sigma Aldrich, USA
Triton™ X-100	T9284	Sigma Aldrich, USA
SDS-PAGE & Western blot		
1˚ β-Actin Antibody (Polyclonal Rabbit anti-mouse)	ab6276	Abcam, GBR
1° Hsp60 Antibody (Monoclonal Rabbit anti-mouse)	ab46798	Abcam, GBR
1° LAMP2 Antibody (Monoclonal Rabbit anti-mouse)	ab18529	Abcam, GBR
2° HRP-conjugated anti-rabbit IgG Antibody (Polyclonal goat)	ab97051	Abcam, GBR
APS (Ammonium Persulfate)	A3678	Sigma Aldrich, USA
β-Mercaptoethanol	M-3148	Sigma Aldrich, USA
Clarity Western ECL Substrate	170-5060	Bio-Rad, ZAF
Peroxide solution		
Luminol/enhancer solution		
LaemmL i solution (4x) [65,8mM Tris-HCl; 26,3% w/v glycerol; 2,1% Li-dodecylsulphate; 0,01% bromophenol blue; pH=6,28]	161-0747	Bio-Rad, ZAF
Precision Plus Protein™ Dual Xtra Prestained Protein Standards	161-0377	Bio-Rad, ZAF
TBS (10x) [Tris buffered saline]	170-6435	Bio-Rad, ZAF
TBS (1x) [Tris buffered Saline] and (1% w/v Casein)	161-0782	Bio-Rad, ZAF
TEMED (N,N,N′,N′-Tetramethylethylenediamine)	T7024	Sigma Aldrich, USA
TGX Stain-Free™ FastCast™ Acrylamide 1 Starter Kit, 10%	1610182	Bio-Rad, ZAF
TransBlot Turbo Transfer Pack, Mini format (0.2 µm PVDF, Single Application)	170-4156	Bio-Rad, ZAF
Tris/Gly/SDS (10x) [25mM Tris; 192mM glycine; 0,1% w/v LDS; pH=8,3]	1610732	Bio-Rad, ZAF
Tween20 (10%)	1662404	Bio-Rad, ZAF
Seahorse XFe96 Respirometry		
Seahorse XFe96 FluxPaks	102416-100	Agilent, USA[21]
XF Calibrant solution		
XFe96 sensor cartridges		
XF96 microplates		
Seahorse XF Mito Stress Test Kit	103015-100	Agilent, USA
Antimycin A		

[21] Company names are subject to change due to acquisitions and mergers. Catalogue numbers, however, have stayed the same for attributability's sake

Reagent	Cat. #	Company
FCCP [Carbonyl cyanide 4-(trifluoromethoxy) phenylhydrazone]		
Oligomycin A		
Rotenone		
ADP [≥95%; adenosine diphosphate]	A2754	Sigma Aldrich, USA
DMSO [dimethyl sulphoxide]	D2650	Sigma Aldrich, USA
EGTA [Ethylene glycol-bis(2-aminoethylether)-N,N,N',N'-tetra acetic acid]	E4378	Sigma Aldrich, USA
L-Glutamic acid.H_2O [≥99%; K^+]	G1501	Sigma Aldrich, USA
HEPES [4-(2-Hydroxyethyl) piperazine-1-ethanesulfonic acid]	H3375	Sigma Aldrich, USA
L-Malic acid [≥95%; $2Na^+$]	M9138	Sigma Aldrich, USA
D-Mannitol	M9546	Sigma Aldrich, USA
$MgCl_2$ [Magnesium chloride]	M2670	Sigma Aldrich, USA
Pyruvic acid [≥99%; Na^+]	P2256	Sigma Aldrich, USA
Sucrose	S7903	Sigma Aldrich, USA
Metabolite standards		
C0: L-carnitine [≥ 98%; HCl]	C0283	Sigma Aldrich, USA
C2: Acetyl-L-carnitine [99%; HCl]	360929	Sigma Aldrich, USA
C3: Propionyl-L-carnitine [≥ 97%]	42602	Sigma Aldrich, USA
C4: Butyryl-L-carnitine [≥ 97%]	42623	Sigma Aldrich, USA
C5: Isovaleryl-L-carnitine [≥ 97%]	51371	Sigma Aldrich, USA
C6: Hexanoyl-L-carnitine [≥ 97%]	07439	Sigma Aldrich, USA
C8: Octanoyl-L-carnitine [≥ 97%]	50892	Sigma Aldrich, USA
C10: Decanoyl-L-carnitine [≥ 97%]	50637	Sigma Aldrich, USA
C12: Dodecanoyl-L-carnitine [≥ 97%]	39953	Sigma Aldrich, USA
C14: myristoyl-L-carnitine [≥ 97%]	61367	Sigma Aldrich, USA
C16: Palmitoyl-L-carnitine [≥ 97%]	61251	Sigma Aldrich, USA
C18: Stearoyl-L-carnitine [≥ 97%]	61229	Sigma Aldrich, USA
L-Alanine [≥ 99%; L-Alanine]	5130	Fluka Analytical, CHE
B-Alanine [≥ 99%]	37009	BDH Biochem, ARE
L-2-aminoadipic acid [≥ 98%]	A7275	Sigma Aldrich, USA
L-Arginine [≥ 99%]	11010	Fluka Analytical, CHE
L-Asparagine [≥ 99%; anhydrous]	11150	Fluka Analytical, CHE
L-Aspartic acid [≥ 99%; L-Aspartate]	11190	Fluka Analytical, CHE
BAIBA: D/L-β-aminoisobutyric acid [≥ 98%]	8290	Fluka Analytical, CHE
L-Citrulline [≥ 99%]	27510	Fluka Analytical, CHE
Creatine [≥ 99%; monohydrate]	27900	Fluka Analytical, CHE
Cystathionine [≥ 98%]	30055	Fluka Analytical, CHE

Reagent	Cat. #	Company
Cysteine [≥ 99%]	30090	Fluka Analytical, CHE
Cystine [≥ 99%]	30200	Fluka Analytical, CHE
N,N-dimethylglycine [≥ 99%]	D1156	Sigma Aldrich, USA
GABA: γ-aminobutyric acid [≥ 99%]	A5835	Sigma Aldrich, USA
D-Glucose [≥ 99,5%]	G8270	Sigma Aldrich, USA
L-Glutamine [≥ 99%]	49419	Fluka Analytical, CHE
Glycine [≥ 99%]	G7126	Sigma Aldrich, USA
L-Histidine [≥ 99%]	53320	Fluka Analytical, CHE
L-Homocysteine [≥ 98%]	H6010	Sigma Aldrich, USA
2-Hydroxybutyrate [97%; Na^+]	220116	Sigma Aldrich, USA
3-Hydroxybutyric acid [95%; 1,126 g/mL EtOH]	166898	Sigma Aldrich, USA
4-Hydroxy-L-proline [≥ 99%]	41875	Sigma Aldrich, USA
D/L-Isoleucine [99%]	298689	Sigma Aldrich, USA
Isothreonine	H6515	Sigma Aldrich, USA
L-Lactate [Na^+]	L7022	Sigma Aldrich, USA
L-Leucine [≥ 98%]	L8000	Sigma Aldrich, USA
L-Lysine [≥ 98%]	62840	Fluka Analytical, CHE
L-Methionine [≥ 99%]	64320	Fluka Analytical, CHE
1-Methyl-L-histidine [≥ 98%]	67520	Sigma Aldrich, USA
3-Methyl-L-histidine	M9005	Sigma Aldrich, USA
NAA: N-acetylaspartic acid [≥ 99%]	00920	Sigma Aldrich, USA
NAG: N-acetyl-L-glutamic acid [99%]	855642	Sigma Aldrich, USA
L-Ornithine [99%; HCl]	O830-5	Sigma Aldrich, USA
L-Phenylalanine [≥ 99%]	78019	Sigma Aldrich, USA
L-Pipecolic acid [99%]	P2519	Sigma Aldrich, USA
L-Proline [≥ 99%]	P0380	Sigma Aldrich, USA
L-Pyroglutamic acid [99%]	F-3634	Sigma Aldrich, USA
L-Sarcosine [98%]	S9881	Sigma Aldrich, USA
L-serine [99%]	84960	Fluka Analytical, CHE
Taurine [≥ 99%]	86330	Fluka Analytical, CHE
L-Threonine [≥ 98%]	89180	Fluka Analytical, CHE
Trimethylglycine [≥ 98%; anhydrous]	61962	Fluka Analytical, CHE
L-Tyrosine [≥ 99%]	93830	Fluka Analytical, CHE
L-Valine [≥ 98%]	V0500	Sigma Aldrich, USA
GC-TOF-MS Metabolomics		
3-Phenylbutyric acid [98%]	116807	Sigma Aldrich, USA
BSTFA [N,O-Bis(trimethylsylil)trifluoroacetamide] containing 1%	33027	Supelco, USA

Reagent	Cat. #	Company
TMCS [Trimethylchlorosilane]		
Chloroform	049-4	Burdick Jackson, USA
Disposable glass Pasteur pipettes	612-1701	VWR, USA
Hexane needle wash	52766	Sigma Aldrich, USA
Methanol, HPLC grade	230-4	Burdick Jackson, USA
Methoxamine hydrochloride	226904	Sigma Aldrich, USA
Pyridine anhydrous [99.8%]	270970	Sigma Aldrich, USA
TMCS [98%; trimethylchlorosilane]		Fluka Analytical, CHE
Water, HPLC grade	365-4	Burdick Jackson, USA
^{1}H-NMR Metabolomics		
Centrisart® Centrifree 30 kDa micro-volume cut-off filters	4104	Merck, DEU
D_2O [99.9%; Deuterium oxide]	435767	Merck, DEU
DMPA [99%; N,N-Dimethyl-L-phenylalanine]	273910	Sigma Aldrich, USA
KH_2PO_4 [Potassium phosphate]	229806	Sigma Aldrich, USA
NaN_3 [≥ 99.5%; Sodium azide]	S2002	Sigma Aldrich, USA
TSP [98%; 3-(Trimethylsylil)propionic acid; D_4, $2Na^+$]	269913	Merck, DEU
LC-MS/MS Metabolomics		
Acetonitrile, HPLC grade [>99%]	BJ015CS	Burdick Jackson, USA
Acetyl chloride [≥ 99%]	00990	Fluka Analytical, CHE
1-Butanol [99.8%]	281549	Sigma Aldrich, USA
Formic acid [98%]	06440	Sigma Aldrich, USA
LC-MS/MS: Deuterium(d)-labelled metabolite standards		
Acetyl-L-carnitine_d_3	N.A.	VUmc[22], NLD
L-Isoleucine-d_{10} [98%]	DLM-141	Cambridge IL, USA
L-Lysine-4,4,5,5_d_4 [96-98%]	DLM-2640	Cambridge IL, USA
Octanoyl-L-carnitine-8,8,8_d_3	N.A.	VUmc, NLD
Stearoyl-L-carnitine-18,18,18_d_3	N.A.	VUmc, NLD
L-Phenylalanine_ring_d_5 [98%]	E151P	Euriso-top, FRA
L-Valine_d_8 [99%]	E161P	Euriso-top, FRA

[22] Acylcarnitine standards were synthesized and gifted by Dr Brink of the Vrije Universiteit medical centre.

ANNEXURE B

Sampled animal details

Table B: Identification, euthanasia and sampling details for each *Ndufs4* mouse used. Animal IDs assigned on weening (P21), as well as the litter number and confirmed genotype are listed for each animal used in each study phase. Date of euthanasia, animal age upon sampling and used sample weights in milligram are also listed.

Sampling date	Litter #	Mouse ID	Genotype	Age	Brain used (mg)	Quad used (mg)
Mice used for method establishment (Phase A + B)						
2019/04/24	GLP[23]	10	(WT)	65		115,0
2019/05/09	GLP	17	(WT)	80		Pool 350,0
2019/05/09	GLP	18	(WT)	80		
2019/05/22	GLP	36	(WT)	45		150,0
2019/06/04	GLP	38	(WT)	67		478,0
2019/07/16	7n	46	(HET)	40		150,0
2019/09/05	7n	60	(WT)	44	213,5	
2019/09/13	7n	54	(KO)	52	192,6	134,6
2019/09/18	7n	55	(HET)	57	105,3	154,2
2019/10/22	7n	65	(WT)	62	202,5	
2019/10/29	7n	68	(WT)	69	216,0	
2020/06/04	7o	21	(HET)	143	Pool 349,2	
2020/06/04	7o	22	(HET)	143		
2020/06/04	7o	23	(HET)	143		
Mice used for Disease/control study (Phase C)						
2019/09/12	7n	62	WT: *Ndufs4*$^{+/+}$	51	100,6	101,1[24]
2020/02/05	7o	14		47	101,9	152,8
2020/02/06	7o	13		48	101,6	154,2
2020/03/03	7o	26		50	101,4	151,4
2020/06/15	7o	57		49	100,6	151,8
2020/06/30	7o	61		49	103,6	150,0
2020/07/01	7o	64		50	108,1	156,2
2020/07/21	7o	65		49	100,5	150,8
2019/10/09	7n	74	KO: *Ndufs4*$^{-/-}$	49	105,3	142,7
2019/10/09	7n	75		49	108,0	112,1
2019/12/10	7o	6		50	100,4	145,4
2019/12/10	7o	10		50	102,0	152,2
2020/02/04	7o	15		46	100,0	151,4
2020/04/29	7o	32		50	104,5	149,9
2020/06/29	7o	62		48	101,1	147,9
2020/07/20	7o	69		48	100,0	153,8

[23] Mice bred outside the specific pathogen free area, for general use.
[24] Homogenization buffer volumes were adjusted to obtain the standardized 15% (w/v) homogenate.

ANNEXURE C

Published peer-reviewed paper I

Metabolomics (2020) 16:78
https://doi.org/10.1007/s11306-020-01697-9

ORIGINAL ARTICLE

Novel mitochondrial and cytosolic purification pipeline for compartment-specific metabolomics in mammalian disease model tissues

Gunter van der Walt[1] · Roan Louw[1]

Received: 21 December 2019 / Accepted: 13 June 2020
© Springer Science+Business Media, LLC, part of Springer Nature 2020

Abstract

Introduction Mitochondria represent an important milieu for studying the pathogenesis of several major diseases. The need for organelle-level metabolic resolution exists, as mitochondrial/cytosolic metabolites are often diluted beyond detection limits in complex samples. Compartment-specific studies are still hindered by the lack of efficient, cost-effective fractioning methods—applicable to laboratories of all financial/analytical standing.

Objectives We established a novel mitochondrial/cytosolic purification pipeline for complimentary GC-TOF–MS and ^{1}H-NMR metabolomics using robust, commercially available fractionation strategies.

Methods Magnetic based mitochondria isolation kits (MACS) were adapted for this purpose, accompanied by cytosolic filtering. Yield was assessed through the percentage recovery of citrate synthase (CS; a mitochondrial marker), purity by immunoblotting against compartment-specific proteins and integrity interrogated through the respiratory coupling ratio (RCR). The effects of the kit-based buffers on MS/NMR analyses of pure metabolite standards were evaluated. Finally, biological applicability to mammalian disease models was shown using *Ndufs4* mouse brain tissue.

Results With minor modifications, MACS produced around 60% more mitochondria compared to a differential centrifugation method. Less than 15% of lysosomal LAMP-2 protein was found in the MACS isolates, confirming relative purity—while RCR's above 6 indicate sufficient mitochondrial integrity. The filtering approach effectively depleted mitochondria from the cytosolic fraction, as indicated by negligible Hsp60 and CS levels. Our GC–MS pilot yielded 60–70 features per fraction, while NMR analyses could quantify 6–10 of the most abundant compounds in each fraction.

Conclusion This study provides a simple and flexible solution for mitochondrial and cytosolic metabolomics in animal model tissues, towards large-scale application of such methodologies in disease research.

Keywords Mitochondria · Cytosol · Compartment-specific metabolomics · MACS · Gas chromatography time-of-flight mass spectrometry (GC-TOF–MS) · Proton nuclear magnetic resonance (^{1}H-NMR)

1 Background

Mitochondria are eukaryotic organelles that mediate several compartmentalized reactions, intimately tied to cellular viability (Birsoy et al. 2015; Frezza 2017; Nunnari and Suomalainen 2012). As such, emphasis has been placed on the investigation of mitochondrial function and dysfunction (MD) in relation to disease research (Picard et al. 2016). Pathologies of high epidemiological impact such as cancer, diabetes, neurodegenerative diseases (e.g. Parkinson's and Alzheimer's), tuberculosis and HIV have all been shown to be tied to MD in the affected tissues (Patti and Corvera 2010; Pustylnikov et al. 2018; Tahrir et al. 2018; Tzelepis et al. 2018; Yao et al. 2009).

Electronic supplementary material The online version of this article (https://doi.org/10.1007/s11306-020-01697-9) contains supplementary material, which is available to authorized users.

✉ Roan Louw
Roan.Louw@nwu.ac.za

[1] Human Metabolomics, Faculty of Natural and Agricultural Sciences, North-West University (Potchefstroom Campus), Private Bag X6001, Potchefstroom, South Africa

Published online: 23 June 2020

Metabolomics approaches aim to expose genotype–phenotype correlations in such cases through the detection of several small-molecule biochemical intermediates and their subsequent integration into metabolic pathways/networks (Dunn et al. 2011; Fiehn 2002). Investigating the urine/serum metabolomes in these MD related complex diseases has revealed unique compound biosignatures, often overlapping on the grounds of bioenergetic perturbations (Esterhuizen et al. 2017; Nagrath et al. 2011; Wu et al. 2007). The frequency and impact of pre-clinical metabolomics studies on isolated target tissues has increased substantially over the last two decades thanks to Animal disease models—as the advantage of negating confounding effects from the exometabolome through a tissue-specific approach is amplified by the high genetic and phenotypic homogeneity of laboratory-bred animals (Kruse et al. 2008; Ruggeri et al. 2014). For tissue-specific pathologies linked to whole-body mutations, as presented by the *Ndufs4* mouse model of Leigh syndrome, this has provided unprecedented insights into the adaptive mechanisms active only in the tissues most affected (Esterhuizen et al. 2017; Terburgh et al. 2019).

When considering the tissue metabolome, however, much of the metabolite contribution from the mitochondrial compartment is still overshadowed by that of the significantly greater cytoplasmic volume (Van Vranken and Rutter 2016). Despite the absolute nature of the mitochondrial metabolite space being mostly unknown, case–control studies employing mitochondrial isolates have unveiled significant alterations in both matrix-specific and more common intracellular pathways that cannot be efficiently interrogated when considering the combined effect of all cellular compartments in whole cell lysates (Chen et al. 2016; García-Sevillano et al. 2015; Pan et al. 2018). Since several metabolite transport and counter transport mechanisms at the interface between the matrix and cytosol are allosterically regulated by diverse cellular conditions such as pH, adenylate charges and nutrient signalling– these effects may pertain to more than just the principal metabolic target of perturbation (Junghans et al. 2019; Palmieri and Monne 2016). Organelle-level resolution has therefore become critical to uncovering metabolic aspects involved in the pathogenesis of bioenergetics-linked diseases.

For metabolomics studies at the organelle level, isolating mitochondria of sufficient yield and purity in a buffer environment applicable to all downstream analyses is the key obstacle inhibiting large-scale application of such compartment-specific approaches (Liu and Xu 2018; Roede et al. 2012). While costly and timeous ultracentrifugation produces higher purity mitochondria (Hubbard et al. 2019), differential centrifugation (DC) promises quick, cheap and robust preparation, with the drawback of decreased fraction purity. Nevertheless, such methods have been successfully applied to elucidate compartment-specific signatures related to gender, metal toxicity and MD (Afanasyeva et al. 2018; Go et al. 2014a; Pan et al. 2018).

Some of these fractionation issues have been partially overcome by fractioned magnetic mitochondrial isolation (FMMS) approaches, wherein magnetically-labelled antibodies specific to mitochondrial epitopes are used to bind and retain the organelles in a strong magnetic field. The most analytically sound approach published to date involves producing recombinant mouse strains expressing FLAG-tag epitopes on selected mitochondria alongside custom, recombinant antibody cocktails (Bayraktar et al. 2019; Chen et al. 2016). This approach is complex, labour intensive and expensive, thus not applicable to all laboratories or models. Commercially available alternatives—such as a popular approach using antibodies targeting an abundant translocase of the outer membrane, TOM22 (Hornig-Do et al. 2009) could potentially give laboratories of various financial and analytical status access to these FMMS-based techniques. Kit-based methods are known to produce variable mitochondrial yields in different tissues (Franko et al. 2013). The contained buffers may also interfere with downstream analyses—prompting preliminary testing of isolation buffer constituency and applicability for the intended purpose (Corcelli et al. 2010). Significant optimization for specific sample types and experiments is thus required. Furthermore, true quantification is hindered by the rapid turnover time of certain compounds, especially those implicated in the central metabolism (Steinhauser and Lechene 2013). It is thus imperative that data produced by such methods be viewed in combination with metabolic flux rates through an isotope-dilution strategy to better elucidate temporal effects (Junghans et al. 2019; Lee et al. 2019)—as organelle isolation strategies are better suited for a global snapshot of the most pronounced perturbations.

Another important factor to consider is the nature of the sample used to compare the mitochondrial metabolome to. While whole-cell lysates have been deemed sufficient comparison for isolated mitochondria, the presence of lysosomes, endosomes, endoplasmic reticuli and other organelles infer possible confounding of the true cytosolic contribution to the observed metabolite levels. Purified cytosolic fractions (devoid of other organelles) could thus hone in on the respective metabolite pool sizes in—and metabolic fluxes between—these two pathologically significant subcellular spaces (Go et al. 2014b; Matuszczyk et al. 2015). Given sufficient optimization of mitochondrial and cytosolic fractioning alongside sensitive and reliable analytical platforms—it is reasonable to hypothesize that inexpensive commercial FMMS protocols can be adapted for compartment-specific metabolomics in animal model tissues (Franko et al. 2013; Hubbard et al. 2019; Kappler et al. 2016).

To that end, we established a rudimentary, kit-based FMMS workflow for GC-TOF–MS and ^{1}H-NMR

mitochondrial and cytosolic metabolomics in tissue samples obtained from a widely available mouse model of MD. Fractioning was performed using an Anti-TOM22 magnetically activated cell sorting (MACS) kit applied to brain tissue from a Leigh Syndrome mouse model, along with a novel filtering approach for producing purified cytosol. The isolates were analytically compared to DC-enriched mitochondria based on yield (CS enrichment), purity (immunoblotting) and membrane integrity (respirometry). The effect of the kit-based buffers on chemometrics was probed for each platform respectively, before a pilot analyses of the cellular fractions was performed to illustrate biological applicability to limited-volume samples from model animals.

2 Methods and materials

2.1 Spiked standard compounds

Dilutions of nine commercially available metabolites commonly found in brain tissue were prepared as analytical standards for investigating the effect of the selected mitochondrial isolation buffer constitutions on chemical analyses. Pyruvic acid (Pyr), lactic acid (Lac), alanine (Ala), valine (Val), glutamic acid (Glu), aspartic acid (Asp), Glycine (Gly), 3-hydroxybutyric acid (3-HB) and 2-hydroxybutyric acid (2-HB) were respectively dissolved in de-ionized water (Millipore®, Merck, MA, USA). A combined stock concentration of 5 mM (of each metabolite) was created in de-ionized water before being diluted to 500, 250 or 50 µM (designated high to low concentration samples) in either water or MACS Separation buffer (#130–096-946), Miltenyi Biotec, Gladsbach, GER) at 1 × final dilution (1 × SB). All chemical standards were purchased from Sigma-Aldrich (GER).

2.2 Animals and sampling

All protocols used have been approved by the designated authority (AnimCare animal research ethics committee, North-West University) with approval number NWU-00568-19-S5. All animals were maintained and procedures performed in accordance with the code of ethics in research, training and drug development in South Africa and complied with national legislation. *Ndufs4* Wildtype (WT) mice (B6.129S4-*Ndufs4*$^{tm1.1Rpa}$/J; Jackson Laboratories, Maine, USA) were used. Mice were held under controlled conditions (22 ± 1 °C; 55 ± 10% humidity; 12:12-h light/dark cycle) on campus at the Vivarium (SAVC reg. no. FR15/13458) of the Pre-Clinical Drug Development Platform (PCDDP; NWU, RSA). The animals were fed a standard laboratory diet with food and water provided ad libitum. Mice were euthanized between P45–P50 to correlate with pre-determined relevant ethical endpoints in *Ndufs4* knock-out studies (Kayser et al. 2016). After euthanasia via cervical dislocation, whole brains were rapidly dissected and immediately processed for mitochondrial isolation via either DC or FMMS workflows, both performed at 0–4 °C.

2.3 Mitochondrial isolation via differential centrifugation (DC)

The DC protocol was adapted from Pan et al. (2018) for downstream GC–MS and NMR analysis (Refer to Online Resource). Mitochondria were isolated in optimized mass spectrometry (MS) compatible KClEM isolation buffer [180 mM KCl, 1 mM EDTA and 5 mM MOPS-KOH (pH 7.2)], as first described by Corcelli et al. (2010). Briefly, a 10% w/v tissue lysate was made from 100 mg whole brain in ice-cold KClEM buffer via 8 strokes in the Potter–Elvehjem homogenizer. Nuclei and large debris were pelleted by subsequently increasing the centrifugal force in a single centrifugation run: 250×*g* for 2 min, 1000×*g* for 4 min and 1900×*g* for 4 min. The post-nuclear supernatant was subjected to 8000 × *g* centrifugation for 15 min to pellet mitochondria. Enriched mitochondria were resuspended in KCIEM to 120 µl final volume. Post-mitochondrial supernatants were collected and filtered using Centrisart® 100 kDa centrifugal cut-off filters (#13269E, Sigma Aldrich), accelerated to 2000×*g* for 15 min at 4 °C to prepare the cytosolic fraction. The whole procedure was performed on ice to minimize mitochondrial damage and post-isolation metabolic fluxes.

2.4 Fractioned magnetic mitochondrial separation (FMMS)

Sub-cellular fractions were prepared at 4 °C using the MACS Mitochondria Extraction Kit for mouse tissue (Miltenyi Biotec) with slight variations to manufacturer instructions (Hornig-Do et al. 2009). Whole brain (150 mg) was cut into small pieces and homogenized in Lysis Buffer (LB) to produce 10% (w/v) lysates as described above. Brief centrifugation at 1300×*g* (2 min) to remove nuclei and large debris followed, before the post-nuclear supernatant was diluted 10× (v/v) in 1 × Separation Buffer (SB). For magnetic enrichment, mitochondria were labelled with anti-TOM22 Microbeads (1,5 µl/mg tissue) for 1 h at 4 °C. The suspension was loaded onto an LS column, which had been placed in a MACS Separator at 4 °C. Of the flow-through, regarded as a crude cytoplasm—2,5 ml was subjected to centrifugal filtering identical to the above mentioned method to prepare the cytosolic fraction. Labelled mitochondria were eluted from the LS column in 1 × SB after removal from the magnet—this was repeated 3 × for each sample. Before further analysis, the eluates were centrifuged at 13,000×*g* for 2 min (4 °C) and the mitochondrial pellets resuspended

in a final volume of 120 µl solvent—relative to the specific downstream application. The isolation procedure took approximately 90 min from tissue homogenization to mitochondrial elution.

2.5 Citrate synthase enzyme activity

During initial optimizations, a small aliquot of each DC or FMMS sample was set aside after subsequent steps for citrate synthase (CS) assays according to established protocols (Shepherd and Garland 1969). Total protein content for each fraction—as well as the MACS reagents shown to contain protein—was determined via bicinchoninic acid (BCA) assay (Sigma Aldrich). For both BCA and CS, absorbance was measured by the Synergy™ HT Multi-detection microplate reader (Biotek Instruments), quantified by the Gen5™ Data analysis software (Biotek Instruments) and statistical analysis performed in Excel 2013 (Microsoft Inc.). All fraction activities were normalised to their respective volumes (umol/min/µl) and expressed as a percentage of that measured in the preceding homogenate.

2.6 Western blotting

Primary antibodies used in this study were all obtained from Abcam (Cambridge, UK) and are listed by antigen, catalogue number and final working dilution: VDAC1 (ab15895, 1:1000); Hsp60 (ab46798, 1:10,000), LAMP-2B/C (ab18529, 1:1000), β-Actin (ab6276, 1:4000). All equipment, reagents and software were purchased from Bio-Rad (Pretoria, ZA). Briefly, samples containing 15ug total protein were incubated in 4 × Laemmli buffer (161–0747) containing 5% [v/v] 2-mercaptoethanol for 5 min at 100 °C. Sample proteins were separated in 10% TGX Stain-Free™ FastCast™ Acrylamide gels (161–0182) before being transferred to 0,2 um Mini-format PVDF membranes. Protein blots were then blocked in 1 × TBS + 1% (w/v) casein (161–0782) for 1,5 h, before being incubated overnight at 4 °C and constant shaking in the indicated primary antibodies, diluted in TBS/T [1 × TBS + 1% casein + 0,1% (v/v) Tween20 (166–2404)]. After three 5 min washing steps in TBS/T, the membranes were incubated for 1 h at room temperature in horseradish peroxidase-conjugated anti-rabbit IgG antibody solution (Abcam, ab97051), diluted in TBS/T to optimal concentrations for each antibody combination probed. Membranes were incubated in Clarity™ Western ECL Substrate (170–5060) and chemiluminescence signals detected by the ChemiDoc™ MP Imaging system (170–8280) in signal accumulation mode. Images were analysed, and band intensities normalized to total protein content for the mitochondrial and cytosolic blots, respectively via ImageLab (v 5.2.1).

2.7 Measurement of oxygen consumption and respiratory control ratio (RCR)

The Seahorse $X^{Fe}96$ Extracellular Flux Analyzer (Agilent Technologies, USA) was used to measure oxygen consumption rates (OCR) of isolated mitochondria in the presence of different substrates, inhibitors and uncouplers, using previous methods with slight modifications (Aucamp et al. 2017; Hubbard et al. 2019). Mitochondrial assay buffer was prepared beforehand (MAS; 105 mM sucrose 330 mM mannitol, 15 mM KH_2PO_4, 7.7 mM $MgCl_2$, 3 mM HEPES, 1.5 mM EGTA, 0,3% (w/v) bovine serum albumen). The sensor cartridge was hydrated overnight at 37 °C. Before loading, the injection stocks were diluted appropriately in MAS (already containing 10 mM pyruvate/5 mM malate, adjusted to pH 7.2) and 25 µl loaded in each injection port to achieve final concentrations of 6 mM ADP (Port A), 4 µM oligomycin A (Port B), 4 µM FCCP (Port C) and 3 µM rotenone/6 mM antimycin A (Port D) in each respiration chamber. Thereafter, the sensor cartridge was placed into the Seahorse $X^{Fe}96$ Flux Analyzer for automated calibration. The FMMS or DC mitochondria were diluted in MAS based on CS activity; eight 25 µl samples containing 2–8 nmol/min/µl CS was loaded in each well of a Seahorse Standard $X^{Fe}96$ assay plate. The assay plates were centrifuged at 2000×*g* for 20 min at 4 °C to adhere the mitochondria to the bottom of the wells. After centrifugation, 150 µl of MAS (pre-incubated to 37 °C) was added to obtain a final volume of 175 µl per well. After instrument calibration, the loaded assay plate was inserted for analysis. Briefly, it involved cyclic steps of mixing, sequential injections of substrates and inhibitors via Ports A through D, equilibration, and duplicate measurements of the oxygen consumption rate (OCR) through fluorometric optical probes. Untrustworthy measurements were removed by Tukey's test for outliers at every subsequent measurement. In the cleaned data set, respiratory control ratios (RCR) were calculated by dividing the OCR obtained from State III respiration values (maximal phosphorylating state in the presence of pyruvate, malate and ADP) by State IV respiration values (OXPHOS-inhibited state in the presence of oligomycin).

2.8 Complimentary GC-TOF–MS and ^{1}H-NMR metabolic profiling

Untargeted measurement of standard compound mixtures and sub-cellular fractions obtained from whole brain homogenates of *Ndufs4* (n = 3) WT mice were performed. The analytical techniques used were previously described and comprised of untargeted gas chromatography time-of-flight mass spectrometry (GC-TOF–MS) (Lindeque et al. 2013), and miniaturized proton nuclear magnetic resonance (^{1}H-NMR) spectroscopy (Mason et al. 2018). The data

obtained in this study can be accessed at the NIH Common Fund's Data Repository and Coordinating Center (supported by NIH grant,) website, the Metabolomics Workbench, https://www.metabolomicsworkbench.org.

2.8.1 Extract preparation and derivatisation

Quality control (QC) samples were prepared from aliquots of all samples within a batch. Standard compound mixes and muscle extracts for NMR were prepared according to the recently established miniaturized protocol (Mason et al. 2018) as follows: After 12,000×*g* centrifugation in Centrifree 3 kDa cut-off filters (Merck/Millipore, MA, USA) at room temperature to remove proteins and other macromolecules, 54 µl of the 60 µl originally loaded (100 µl for standard mixes) remained to be transferred to a 2 mm NMR tube using the eVol® NMR digital syringe (Sigma-Aldrich) equipped with a 100 µl bevelled-tip needle. The programmed pipetting sequence of the digital syringe added phosphate-buffered 3-(trimethylsylil)-propionic acid (98% TSP D4 Na^+-salt; #269913, Merck/MagniSolv™) and *N*,*N*-Dimethyl-*L*-phenylalanine (99% DMPA; #273910, Sigma-Aldrich) or 3-phenylbutyric acid (98% 3-PBA; #116807, Sigma-Aldrich) internal standard for ^{1}H-NMR; as such that a 10:90% ratio of D_2O:H_2O was maintained as per standard protocol. The 2 mm NMR tube was inserted into the gripper-adaptor of the Bruker MATCH system, before each NMR MATCH assembly was loaded onto a SampleXpress autosampler for NMR analysis.

Metabolite extraction for GC-TOF–MS was achieved using a modified monophasic Bligh–Dyer extraction method (Gullberg et al. 2004) with a solvent ratio of 3:1:1 (methanol: water: chloroform) (chromatography grade, Burdick and Jackson). All extractions were done on ice to minimize further metabolic interactions. The selected standard, 3-PBA was added in a fixed concentration to each sample—consisting of the remaining 60 µl mitochondrial/150 µl cytosolic fractions (or 100 µl standard compound mixture). Tissue extracts/standard compound mixtures were dried under nitrogen.

Oximation of the ketone groups in the dried extracts was achieved through incubation in 25 µl of methoxamine hydrochloride [#226904, Aldrich (98%)] (20 mg/ml in pyridine [#270970, Sigma-Aldrich]) at 60 °C for 1.5 h. Thereafter, 25 µl of a pre-mixed dilution of 1% TMCS in BSTFA [#15238, Sigma (99%)] was added before incubation under the same conditions for 1 h to silylate polar hydrogen containing groups. For the metabolite standards, 50 µl of each derivatization reagent was used. The derivatized samples were subsequently transferred to 250 µl pulled-point inserts, placed back into screw-cap vials, and loaded onto the 7693 Autosampler (Agilent).

2.8.2 Instrumentation and analysis parameters

NMR measurements were conducted at 500 MHz on a Bruker Avance III HD NMR spectrometer equipped with a 5 mm triple resonance inverse (TXI; ^{1}H, ^{15}N, ^{13}C) probe head optimized for ^{1}H observation. Briefly, ^{1}H spectra were acquired as 128 transients in 32 K data points with a spectral width of 6000 Hz (12.0 ppm). The H_2O resonance at 4.70 ppm was suppressed using the pulse sequence program NOESY-presat. The number of dummy scans = 4 and number of scans = 128, yielded a run time of 15 min and 45 s per sample. These settings follow those given by established SOPs (Mason et al. 2018). Each sample was automatically shimmed on the deuterium signal, locked, probe tuned and matched, and pulse calibrated using Bruker Topspin (V3.5), and further processing conducted using Bruker AMIX (V3.9.14).

A GC-TOF–MS system, comprising a LECO Pegasus TOF–MS with Agilent A980 front end was used as described (Lindeque et al. 2013). Helium was used as carrier gas at 1.5 ml/minute flow while 1 µl sample was injected in splitless mode (allowing 30 s purge delay). The inlet temperature was kept at 250 °C. Compounds were separated on a RTX-5MS column (30 m × 0.25 mm × 0.25um) employing an apolar, fused silica phase (#12623–124, Restek, PA, USA). The transfer line and source temperature were 225 and 200 °C, respectively. A solvent delay of 330 s was allowed where after masses (50–900 m/z) were recorded at 20 spectra/second. Universal EI (electron impact ionization) settings were used for fragmenting compounds prior to spectral collection, while the detector was operated at 50 V above tune voltage.

2.8.3 Data extraction and processing

All data processing was done using Excel 2013 (Microsoft). Spectral data obtained from the analytical platforms were extracted into matrices. For GC-TOF–MS data, this process was preceded by peak alignment and deconvolution (ChromaTOF). Data matrices were manually inspected (correct peak picking and alignment, batch effect and data integrity) before an 80% zero-filter and 50% CV filter was applied. Peak intensities were normalised to 3-PBA (GC-TOF–MS data) or DMPA (^{1}H-NMR data). No batch corrections were needed as the QCs showed no significant drift effects. %CV, linear coefficients and/or percentage recovery was calculated for the standard samples. For the biological samples, %CV was calculated and qualitatively inspected to comment on the applicability of the proposed workflow to each platform. Identities of varied confidence level (Schymanski et al. 2014) were manually assigned to metabolites based on the NIST11 and our own in-house spectral library.

3 Results and discussion

To produce cellular fractions applicable to metabolomics, balance must be achieved between analytical parameters (purity, yield, integrity, etc.) and practical factors such as time and cost to ensure reproducibility (Liu and Xu 2018). To that end, we set out to adapt a MACS-based fractioning pipeline to meet these criteria and prove the analytical superiority thereof (compared to a recent DC workflow (Pan et al. 2018)) for downstream metabolomics in animal disease models. Brain tissue was selected for method development, as it presents abundant mitochondria and central involvement in the selected disease phenotype (Lake et al. 2015)—also enabling extrapolation of the methodology to mammalian models of more common mitochondria-linked neuropathies (Hall and Roberson 2012; Jin et al. 2008).

3.1 Establishment of MACS-based fractioning workflow for application in mouse tissues

3.1.1 Protocol variations produce mitochondrial isolates of sufficient yield

The amount of antibody available per tissue weight has been proven a critical limiting factor to the yield obtained. As such, an optimal dilution (1.5 µl/mg wet tissue) was selected from recently published data (Hubbard et al. 2019) as to find a balance between yield and reagent cost. The mitochondrial elution phase—meant to purge labelled organelles from the demagnetized coloumn post-isolation—also proved to be a significant bottleneck step. Initial trials yielded up to 3 × more mitochondria based on CS enrichment after flushing the magnetic column three times (Online Resource)—compared to a single flush with 1 × SB as prescribed by the kit. Hence this adaptation was included into the final methodology for brain analyses as well.

For comparing DC and MACS yields, the same homogenate was split immediately before both simultaneously performed isolation strategies to eliminate differences in biological substrate/inhibitor or enzyme concentrations. As citrate synthase is a well-known, definite marker of mitochondrial matrix content, not found in any other compartment, the readout is thus accepted as a qualitative determination of differences in mitochondrial yield for these two methods. Kinetic enzyme analyses were conducted simultaneously on the same reaction plate utilizing optimized and identical substrate concentrations. When comparing DC and FMMS using brain tissue, patterns of mitochondrial distribution differ between the

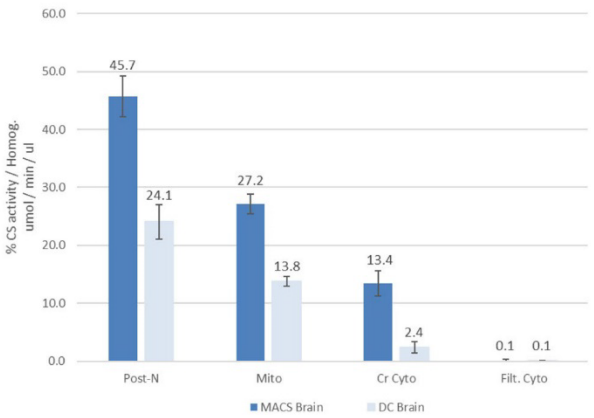


Fig. 1 Comparison of mitochondrial enrichment from brain tissue for DC and MACS methods (n = 3). The CS activity of each fraction is expressed as a % of the CS activity captured from the preceding homogenate. *Post-N* post-nuclear supernatant, *Mito* enriched mitochondria, *Cr. Cyto* crude cytoplasm, *Filt. Cyto* 100 kDa filtered cytosol

two methods at pivitol points in the fractioning process, indicated by percentage of the matrix-specific CS enzyme from the homogenate present in each fraction (Fig. 1). For the given parameters, higher relative mitochondrial yields were achieved using the MACS kit (~ 27%) compared to DC (~ 14%). This corroborates the data of similar CS enrichment experiments (~ 19–23%) using MACS-isolated brain mitochondria (Franko et al. 2013; Hubbard et al. 2019), indicating no significant decrease in yield for the given methodological alterations. A large amount of organelles are not bound by the optimized antibody concentration (~ 11.5%), taking into account that synaptic mitochondria are also lost in the flow-through without disruption of their containing synaptosomes (Brown et al. 2004; Hubbard et al. 2019). Saturating all non-synaptic and synaptic mitochondria is possible, but not feasible for a robust metabolomics workflow—since manual disruption of synaptosomes and up to 8 × the manufacturer specificied amount of antibody is needed for such application (Hubbard et al. 2019).

The initial nuclear pelleting step accounts for a significant portion (~ 55–75%) of the yield lost, for both methods. Although repelleting and another round of centrifugation could release more of the organelles trapped in the large cell debris for any of the two methods (Liu and Xu 2018), the single-step approach employed during MACS isolation yields more brain mitochondria than the patented three-step method for DC-enrichment, contradicting the data published for yeast cells (Pan et al. 2018).

Furthermore, preliminary tests using quadriceps muscle revealed differential patterns of mitochondrial loss at different steps in the workflow (Online Resource), emphasizing

the role of tissue-specific confounding factors in optimizing homogenization/fractioning parameters. The highly filamentous nature of skeletal muscle mitochondria likely infers greater occlusion of TOM-22 epitopes from antibody binding than expected for the more dynamic neural mitochondria (Picard et al. 2012; Vendelin et al. 2005), therefor substantially more muscle-derived organelles are left unlabelled and end up in the column flow-through.

The limitations in this approach include the effect of even minimal differences in CS inhibitor concentrations present, as well as the inability to accurately probe mitochondrial protein content against the background of antibodies and protein contributed by the 1×SB. The former issue was minimised by utilising a single split homogenate for every DC and MACS experiment compared. The KCIEM buffer contains no known CS inhibitors, while the MACS buffers are also not stated to contain any such compounds (Hornig-Do et al. 2009). Regardless, minute differrences may occur, and without concomitant analyses of a puriified enzyme standard in a spectrophotometrically optimised buffer, these results remain majorly qualitative. It must also be stated that volumetric normalisation, as used here, is also only valid given the homogeny of the samples analysed and the comparative nature of the information desired. Issues regarding measurement of protein content in MACS samples, alternative buffer systems and the effect of their constituency on purified CS must therefore be addressed for any future experiments that necessitate absolute quantification of CS activity.

3.1.2 Novel filtering approach depletes residual organelles to produce cytosolic fractions

The MACS-derived crude cytosolic/cytoplasmic fraction to be used for comparison still contains significant amounts of mitochondria (~13%), which may skew the metabolic profile observed. Specialized centrifugal filters with descending 100 kDa filter membranes were used to remove these and other large organelles whole, as the filter design substantially decreases the risk of membrane blockages and/or resultant rupture of organelles (in comparison to traditional spin columns). Mitochondrial depletion can be visualised as the absence of the matrix-bound chaperone Hsp 60 (Fig. 2). This indicates that the majority of whole mitochondria were removed. Ruptured organelles would have freed the 60 kDa Hsp to pass through the membrane filter and be detected in the filtered fraction (Cheng et al. 1989). Similarly, the 52 kDa CS enzyme would be able to freely pass the filter (Shepherd and Garland 1969). Therefore, the minimal (<0.3%) CS activity we detected in the filtrate (cytosol fraction) also indicates negligible amounts of mitochondrial rupture and efficient depletion of the organelles and their content through this approach.

3.1.3 Mitochondrial purity and integrity unaffected by selected protocol adaptations

Substantial evidence exists regarding the superior purity of MACS mitochondria, compared to DC isolates, where protein-level proof of superior endosomal, nuclear, cytosolic and lysosomal depletion in the final mitochondria has been presented in several cases. (Franko et al. 2013; Hornig-Do et al. 2009; Hubbard et al. 2019; Lee et al. 2019). In

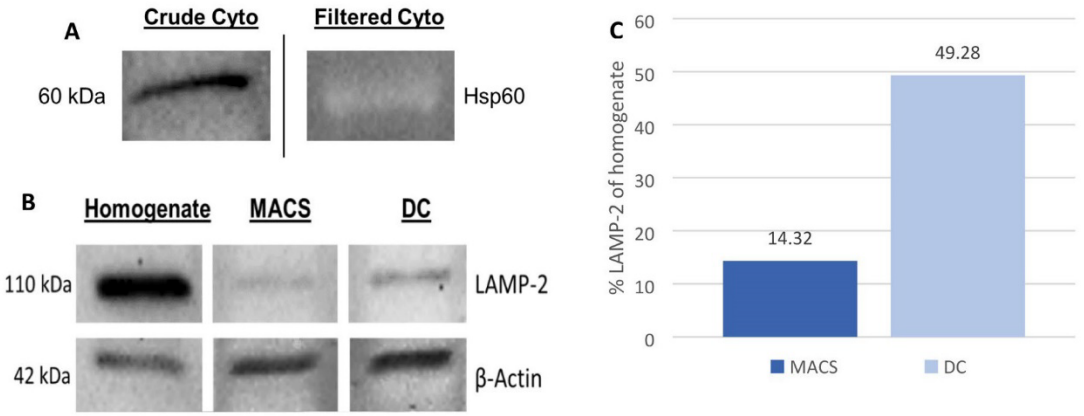


Fig. 2 Comparison of fraction purity of DC and MACS methods by immunoblotting against compartment-specific proteins. Western blots depicting **a** a comparison of mitochondrial depletion (Hsp60) in cytosolic fractions pre- and post-filtering and **b** lysosomal depletion (LAMP-2) in MACS or DC mitochondria, compared to the whole homogenate (with β-actin as loading control). **c** Total-protein normalized LAMP-2 volume, expressed as a percentage of that detected in the preceding homogenate

that regard, the comparable depletion of LAMP-2 (Lysosomal membrane protein) in our MACS isolates serves as substantial proof that the selected protocol alterations do not negate the previously established purity of the method (Fig. 2). Minute amounts of LAMP-2 detected by western blotting (~ 14%) corroborates previous results—owing rather to unbound variants of the protein detected than significant presence of the whole organelles (Chen et al. 2016).

A higher respiration control ratio (RCR) is indicative of higher respiratory capacity, less proton leak over the inner-membrane and thus a more intact mitochondrial inner membrane (MIM) (Brand and Nicholls 2011). Previous respiration experiments on organelles isolated by either MACS or DC has shown comparable RCR's for both methods (Franko et al. 2013; Hubbard et al. 2019). Our findings corroborate this well; an average RCR of 6.14 and 7.35 for MACS and DC isolates, respectively, being an acceptable indication of good respiratory coupling and MIM integrity.

The slightly lower RCR for MACS mitochondria, relative to the DC method, might indicate marginally higher mitochondrial uncoupling in these fractions. It is well known that mitochondria uncouple over time—thus the longer MACS isolation process can potentially account for the faintly lower RCR measured in the MACS samples. However, this may also be a purely analytical effect, owing to the differential buffer environment wherein the respective isolates are produced (Franko et al. 2013). Nevertheless—the extensive CS experiments described above deliver further proof on mitochondrial integrity, as the absence of CS activity in the filtered cytosol is indicative of minimal MIM rupture. Furthermore, CS assays of the MACS post-mitochondrial supernatant also reveal minimal to no matrix content leakage (< 1% CS) towards the very end of the experimental workflow. Combined, the data presented here provide different levels of substantiation for the analytical purity and integrity of mitochondria isolated via the adapted protocol—as well as the purity of the collected cytosolic fraction.

3.2 Effect of MACS buffers on GC-TOF–MS and NMR metabolomics

Previous reports indicate that mitochondrial isolation buffers, typically containing high concentration of buffer salts, can significantly impact the measured metabolite concentration in isolates (Corcelli et al. 2010; Liu and Xu 2018; Pan et al. 2018). NMR probing of the MACS kit buffers indicated the presence of ethanol, glycerol, protein and EDTA in either the kit lysis or separation buffers. According to the cornerstone publication of the kit (Hornig-Do et al. 2009), substantial amounts of buffering salts constitute the base of the separation buffer—the predominant feature of the final sample mixture. In that regard, we set out to determine the effect of this buffer environment on the qualitative and/or quantitative analysis of nine commercially available, common metabolic intermediates tandemly on both selected platforms.

For NMR analysis, effects on absolute quantification were determined by comparison against the same metabolites measured in a water environment, as per universal SOP's (Beckonert et al. 2007; Dona et al. 2014; Mason et al. 2018). In an untargeted GC–MS experiment, however, investigation of precision and quantitative linearity in the MACS buffer were deemed sufficient.

3.2.1 GC-TOF–MS analysis of standard compounds in MACS environment

Ten technical replicates of the metabolite standard solutions were analysed at a low (50 µM), medium (250 µM) and high (500 µM) concentration to determine whether any part of the untargeted metabolomics workflow (i.e. metabolite

Table 1 Precision and quantitative linearity of selected standards analysed by GC-TOF–MS

%CV	Low (50 µM)	Med (250 µM)	High (500 µM)	Linearity (R^2)
Pyruvate	10.0	6.7	7.0	> 0.99
Lactate	12.0	7.5	4.4	> 0.99
2-Hydroxybutyrate	4.0	4.3	5.1	> 0.99
3-Hydroxybutyrate	3.7	4.8	5.8	> 0.99
Glycine	9.4	18.9	21.6	> 0.99
Alanine	6.6	13.3	4.6	> 0.99
Valine	4.3	4.9	6.7	> 0.99
Aspartate	60.3	32.6	19.3	> 0.99
Glutamate	N.D	19.9	6.1	0.85
3-Phenylbutyrate	47.6	49.4	36.4	
EDTA	8.04	6.16	7.29	

Variance is expressed as %CV for EDTA-normalized measurements at each concentration level, while the R^2 value indicates linearity

extraction, derivatization or chemical analyses) is significantly affected by the MACS environment.

3.2.1.1 Analytical precision As an indication of measurement precision, %CV was calculated for each compound at the different concentration levels. These results (Table 1) were weighed against the pre-defined 50% limit for variation in GC–MS untargeted metabolomics studies (Dunn et al. 2012). For the majority of metabolites, a variation far below these standards can be seen (CV < 22%; except for aspartic acid), indicating excellent stability of these compounds and their measurement in the buffer environment. The high ionic strength owed by the salts in the buffer seem to confer a stabilizing effect upon alpha-ketoacids such as pyruvate (Pyr) (CV = 4–12%) which are known to be notoriously unstable in the GC–MS environment (Mamer et al. 2013; Tsai 1967). This iconicity does, however, infer drawbacks as well—as indicated by the measured values for aspartate (Asp). The ionic environment may induce salt adducts during ionization, possibly even linking salt bridges between other free amino acids or those present in the buffer-based protein (Bissantz et al. 2010; Luo et al. 1999). It is thus proposed that the same standard analyses be completed for specific compound classes of interest in subsequent experiments.

It should be noted that the selected internal standard, 3-PBA, has consistently been shown to perform poorly in the MACS buffer for GC-TOF–MS (CV = 36.4–49.4% in comparison to < 15% for most other compounds) and NMR analyses (see Sect. 3.2.2). Due to the lack of an efficient internal standard at the time of analyses, a stable component in the buffer itself was utilized for normalisation, as all samples were diluted in the same concentration of the separation buffer prior to analyses. EDTA was selected as the measured amount showed excellent inter- and intragroup consistency (6–8% CV intragroup and < 3% difference in means between groups). Thus, for the purposes of these standard compound mixtures only, it fulfilled the criteria for an applicable internal standard—correcting for differences in extraction, derivatization, injection and/or chemometrics. Henceforth the selection of internal standards for subsequent experiments should also be based upon critical analysis of their stability and applicability to specific subsequent experiments (Chen et al. 2016).

3.2.1.2 Linearity Linear least squares regression was applied to the normalised intensities for each sample. A linearity coefficient cut-off of > 0.95 was selected as criteria for determining the performance of measurement over increasing concentration—these results are also described in Table 1. Almost all compounds show excellent linearity (> 0.99), except for Glu—which was not detectable at the lowest concentration (Online Resource). Glutamic acid (Glu) is known to spontaneously convert to pyroglutamic acid, which might explain the generally lower amounts of Glu measured at every concentration and the linear increase in pyroglutamate, although not being an addition of the sample itself. Linearity is expressed for a single one of three aspartic acid (Asp) peaks (R.T = 812 s; m/z = 70) observed at different retention and mass-to-charge ratio's—since the other related peaks showed poor quantification at the medium and low levels (Online Resource). This is most likely also due to differential ionization of extracted Asp in the highly saline environment. All of these confounding chemical factors are to be taken account and preferentially corrected for by similar standard analyses when amino acids or other polyionic compounds are the target of analyses.

3.2.2 ^{1}H-NMR analysis of standard compounds in MACS buffer versus SOP aqueous environment

NMR is known to be a far more precise platform than mass spectral methods—this enables absolute quantification of compounds using a stable internal standard, as virtually no chemical modification of samples are necessary (Beckonert et al. 2007). We set out to determine the effects of the MACS buffers on quantification via a recently developed miniaturized ^{1}H-NMR protocol for limited-volume samples (Mason et al. 2018). The aim here was to evaluate the same parameters as in the GC–TOF–MS analyses (precision and linearity). The additional parameter of measurement accuracy—relative to samples analysed strictly via SOP in a water environment—was also investigated to emphasize the applicability of NMR analyses as a valuable quantitative extension to the workflow.

Since the analytical stability of the internal standard is a critical criteria for enabling absolute quantification, lessons learned from the GC–TOF–MS analyses instigated an evaluation of different internal standards in the given sample matrix (Online Resource). Traditional TSP standard was shown to be affected by the high ionic environment in a concentration-dependant manner, while 3-PBA quantities are exaggerated similarly at all three levels. This resulted in lower precision (CV > 30%) and variable recoveries which do not coincide with the given sensitivity of NMR. Contrarily, DMPA performed adequately in this environment, leading to acceptable precision, accuracy and linearity. This compound was thus selected as internal standard for al subsequent analyses, in line with previous studies (Terburgh et al. 2019; Van Aardt et al. 2016).

3.2.2.1 Analytical precision A precision cut-off point was determined at each concentration (5% and 10% for high and medium concentrations, respectively—while 15% was deemed sufficient at the lower concentrations which lie close to the limit of detection) These values are below

Table 2 Comparison of precision (%CV) and relative recovery (in parentheses) of nine standard compounds analysed via ^{1}H-NMR in either MACS buffer environment or pure water (SOP) at low, medium and high concentrations (n = 10)

	Low (50 µM)		Medium (250 µM)		High (500 µM)	
	MACS	dH_20	MACS	dH_20	MACS	dH_20
Pyruvate	10.6	6.3	1.2	1.4	1.3	1.3
	(83–104)	(93–119)	(103–107)	(95–100)	(97–101)	(98–103)
Lactate	14.9	8.7	1.9	1.9	0.8	1.8
	(99–115)	(96–112)	(100–106)	(97–103)	(98–101)	(97–104)
2-Hydroxybutyrate	14.0	12.4	3.2	4.0	1.0	2.2
	(107–119)	(92–108)	(99–109)	(90–105)	(97–101)	(96–103)
3-Hydroxybutyrate	9.2	8.9	2.0	4.0	0.8	1.7
	(80–106)	(87–120)	(97–103)	(94–106)	(98–101)	(97–104)
Glycine	9.4	14.5	10.1	5.0	3.0	2.2
	(137–245)	(89–162)	(87–114)	(88–105)	(97–106)	(96–102)
Alanine	12.0	8.1	2.3	1.7	0.9	1.5
	(104–115)	(89–120)	(109–117)	(108–114)	(108–111)	(110–115)
Valine	7.5	7.8	2.0	1.8	1.0	1.0
	(100–114)	(94–118)	(99–106)	(96–103)	(97–101)	(100–103)
Aspartate	34.4	27.7	14.3	17.2	4.6	8.2
	(99–249)	(61–199)	(78–138)	(52–111)	(93–107)	(85–113)
Glutamate	25.1	23.1	7.6	8.5	3.0	4.1
	(97–203)	(74–139)	(92–110)	(93–107)	(95–106)	(93–107)

the 15% or 20% (low concentration) FDA standards for targeted analyses (FDA 2001) and far below the 50% cut-off for untargeted studies (Dunn et al. 2012). As indicated in Table 2, all metabolites performed within these chosen bounds of precision, with the exception of Asp and Glu at the lowest concentration. This effct can be seen in both MACS and water-based samples, and rather owes to the instability of these compounds at concentrations close to detecton limits, as also indicated by the coincidental GC-TOF–MS analyses. Researchers conducting further studies along this line should also take into account possible chemical shifts in a high-ionic environment, as other electrolytes may infer changes in resonant frequency absorbed/measured for certain chemical groups (Lindon et al. 1999; Wang and Bax 1993). These results once again emphasize the need of compiling and analyzing a mixture of standard compounds applicable to the intended goal of any subsequent study.

3.2.2.2 Relative accuracy As an indication of the buffer's effect on the inherent quantitative power of the platform, all measurements were expressed as a percentage of the measured average for a given compound in the SOP water environment (Table 2)—this average value being designated as 100% recovery. Acceptance criteria were set as 80–120%, in line with previous similar studies (Chan et al. 2004; Mason et al. 2018). Excellent relative accuracy was shown for the DMPA-normalised compounds—with Asp once again being the sole outlier at all three concentrations. Glu and Gly also fall outside these bounds only at the lowest concentration; most likely due to spectral noise having a larger impact on measurements close to the lower limit of detection (LLOD). The value of investigating both parameters is evident from Gly, as high precision and low accuracy measurements may occur for certain compounds, impacting quantification unbeknownst to the analyst only equipped with one of these criteria.

3.2.2.3 Quantitative linearity Linear regression was applied to each compound at the three concentration levels, similar to that described in Sect. 3.2.1. In this case, the linearity graph for each compound in MACS buffer was overlayed with that for the same analyte in the SOP water environment (Online Resource). All compounds performed with acceptable linearity ($R^2 > 0.99$)—although the ionic effects upon Asp, Glu and Gly as described above clearly influence quantification, indicated by the offset of the MACS linearity graph from that of the water-based SOP in these three compounds. Overall it can be concluded that NMR analyses in MACS buffer performs acceptably on the grounds of precision, linearity and accuracy relative to SOP conditions—although the value of investigating quantitative effects upon metabolites of interest for further studies are emphasized by these results.

3.3 Applicability of selected methodology to mouse model tissues

The following objective entailed a pilot application of the developed methodology on mouse models of disease—specifically WT mice from the complex I-deficient *Ndufs4*

cohort. To prove that the methodology can be extrapolated to other genetic animal models, 100 mg whole brain from a single animal was subjected to the developed fractioning workflow—where after the mitochondrial and cytosolic samples were split for limited-volume analysis on either GC-TOF–MS or NMR to probe the amount of features visible, as well as their analytical performance. It should be noted that a 90 min isolation procedure inevitably infers metabolite turnover—as the quickest metabolic processes still proceed, albeit at much slower rates, even at the 0–4 °C temperatures applied throughout. Each isolation was, however, performed in an experientially fixed timespan of 90 min and all metabolite extractions performed in small batches, with minimal time elapsed between each sample. Metabolite turnover in each sample was thus accepted to be equivalent, and given that only comparisons between different fractions of each sample were of importance, these parallel changes yielded no considerable changes in analysis repeatability.

3.3.1 Pilot GC-TOF–MS analysis of mitochondria and cytosol

Of the ~ 120 µl mitochondrial extract, 60 µl was subjected to metabolite extraction and derivatization as described in Sect. 2.8., 150 µl of the voluminous cytosolic extract was prepared similarly. After analysis (technical triplicates of each fraction), peaks showing unstable measurement in the QC's (CV > 50%) were removed. Features attributed solely to the buffer environment were subtracted from the matrix. Feature ID's were assigned by automatic spectral database matching done by the ChromaTOF software, before being manually annotated and curated. Known derivatization/ionization artefacts and products of overdeconvolution were also removed to deliver a final list of 29 confirmed metabolites [levels 1–3, according to Schymanski et al. (2014)] for the mitochondrial and cytosol, respectively. Variation < 50% for all compounds indicates the repeatability and precision of these measurements—as an average CV of 16.7% and 19.6% was achieved in the mitochondria and cytosol, respectively.

Seventeen peaks of sufficient signal to noise ratio and spectral match for annotation were shown to be common to the two fractions (Fig. 3), while 12 compounds unique to each respective fraction were also detected and annotated with sufficient confidence. Diligent annotation with more specialised libraries or larger sample volumes could clarify the unknown features detected, however they may represent novel compounds to our libraries. In that regard, further analyses of applicable metabolite standards may be a prerequisite for subsequent studies. Of the features positively identified, several metabolites commonly perturbed in bioenergetics dysfunction were found (Esterhuizen et al. 2017; Gielisch and Meierhofer 2015).

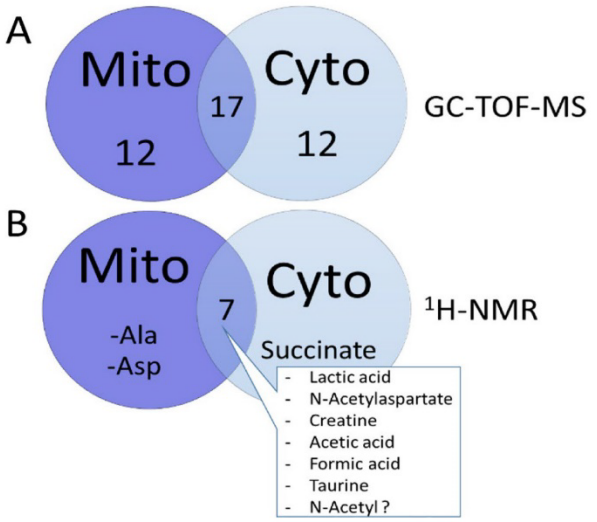


Fig. 3 Comparison of features detected in the mitochondrial (n = 1; 3 replicates) and cytosolic (n = 1; 3 replicates) fractions of Ndufs4 mouse brain by (*A*) untargeted GC-TOF–MS and (*B*) ^{1}H-NMR. Text in the circles represent features unique to each fraction—while that in the intersection represents the positively identified compounds common to both

A list of metabolites found in this study and their ID confidence levels are available (Online Resource). Compounds present in both fractions included organic acids such as lactic-, malic-, oxalic- and octadecanoic acid. The sugar alcohols erythritol and myo-inositol, along with amino acids such as Ala, Asp, Gly, Glu and 3-methyltyrosine were also detected as common features. Fraction specific compounds detected include: Pro, Ser, Thr, cytosine norleucine in the mitochondria, and succinate, urea, 5-hydroxytryptophan in the cytosol. Despite only confirming ± 30 features—possibly as a result of the minute sample volumes approaching the inherent detection limits of the GC-TOF–MS system, this trial analysis proves the possibility of identifying several compounds of significance in limited-volume samples of purified cytosol and mitochondria from disease model animals. Strategies for sample concentration or consideration of more sensitive techniques such as 2D-GC-TOF–MS may serve to overcome this issue.

3.3.2 Probing the applicability of a limited-volume ^{1}H-NMR protocol

The application of precise and repeatable ^{1}H-NMR spectroscopy compliments more comprehensive but variable mass spectrometry analyses by being able to quantitatively confirm significant effects found by MS (Dunn et al. 2011). As such, the remaining 60 µl mitochondrial sample and triplicates of the remaining cytsosol were subjected to

minimum-prep ^{1}H-NMR investigation designed for limited-volume extracts (Mason et al. 2018). An untargeted approach was followed, wherein deproteinized and buffered samples were analyzed and quantified over 376 spectral bins of 2 ppm each (excluding the water region).

Nine compounds were quantified with high relative accuracy in the brain mitochondria of the animal, while 8 were detected with sufficient precision (CV < 10%) in the cytosol (Fig. 3). Taurine is the only exception, at 13% CV, however this compound is known to be more unstable than most under conditions of NMR analysis (Hohmann et al. 2014). Metabolites significant in studies of bioenergetics-related diseases such as lactate, succinate, creatine, alanine and aspartate were detected. The presence of lactate in the mitochondrial fraction confirms the recently theorised notion that this common metabolte is not only found in the cytosol, but can be readily imported and utilized in the mitochondria of certain tissues (de Bari and Atlante 2018; Passarella and Schurr 2018). An important intermediate of brain metabolism, N-acetylaspartate, was detected (Moffett et al. 2007; Tsai and Coyle 1995) as well as an unidentified N-acetyl compound—indicating a possible novel compound for study. Although these compounds are few in numbers, they indicate the possibility of application in further studies as a complimentary quantitative measurement for the most abundant compounds in a given sample.

To our knowledge, this is the first successful application of NMR sub-cellular metabolomics to limited-volume extracts from small disease model animals, generally thought to be impractical due to the platform's inherent insensitivity. Indeed, our initial trial runs using the manufacturer supplied tissue protocol and quadriceps muscle from *Ndufs4* mice did not detect any compounds at all—though upon application of the described yield increasing optimizations, 6 mitochondrial compounds could be detected even in these tissues (Online Resource), known to posess far fewer mitochondria than the neural matrix (Esterhuizen et al. 2017; Paul and Sperling 1952). Far more sensitive setups than the general 500 MHz machine used here exist; 1.2 GHz spectroscopes have been developed, and cryoprobe technology also allows up to a tenfold increase in sensitivity (Fratila and Velders 2011; Glaves et al. 2014). Laboratories with access to such setups will naturally detect far more compounds, this study thus exists only as an indication of future possibilities in this line of enquiry.

4 Conclusion

Here we outline a novel adaptation of commercially available FMMS-based mitochondrial isolation and cytosol filtering for sub-cellular metabolomics in a mouse model of MD, contributing to the currently restricted arsenal investigators have at their disposal for determining compartment-specific effects in diseases related to altered mitochondrial metabolism. The selected MACS methodology outperforms standard DC methods on the grounds of brain mitochondria yield (~ 60% more) and purity (~ 35% LAMP-2 depletion), as indicated by CS assays and western blotting, respectively. MACS mitochondria show comparable integrity to the DC isolates, with RCR's of 6 and 7 being indicative of sufficient MIM coupling (Franko et al. 2013). The significant addition of a simple and cheap filtering method for purifying the cytoplasm of remaining organelles to produce a cytosolic fraction (< 0.1% CS) will allow a true comparison of pools and fluxes between these organelles—and the perturbation thereof in disease. For further application, our results have indicated the homogenization and preliminary debris-clearing centrifugation steps as critical targets for further optimization as they display tissue-specific patterns of yield loss.

Through the measurement of nine standard compounds, commonly found in brain tissue, the effects of the MACS buffers were shown to not be of significant detriment to chemical analyses—as is often the case for metabolomics in highly ionic isolation buffers (Liu and Xu 2018). GC-TOF–MS analysis in this environment proves applicable for most compounds—as indicated by high measurement precision (CV < 22%) and linearity over three concentration ranges ($R^2 > 0.99$). Similarly, for NMR analyses, precision (CV < 10%, or 15% at low levels) and quantitative linearity ($R^2 > 0.99$) was achieved in the buffered samples at acceptable limits for this highly precise platform. Recovery between 80 and 120% for most compounds infers high relative measurement accuracy—further proving the quantitative value of NMR analyses in compartment-specific studies. It is however evident that metabolites of various chemical nature are differentially affected by the buffers, including traditional internal standards such as 3-PBA and TSP. Therefor no future study should proceed without in-depth evaluation of analytical standards for the compound classes in question, and their performance on the selected platforms.

The developed workflow was applied to a healthy control of a PMD mouse model to indicate applicability of the methodology to tissue-based studies in disease research. GC-TOF–MS analysis detected 60–70 compounds of sufficient stability (CV < 22%), encompassing metabolites commonly perturbed in MD, as well as some unidentified features which may represent novel targets for study. The unprecedented application of miniaturized ^{1}H-NMR metabolomics to limited-volume sub-cellular extracts also opens up new possibilities for complimentary quantitative data in compartment-specific studies—as our relatively low sensitivity setup could measure 6–10 abundant metabolites with high relative accuracy (1–15% CV) in these fractions. It should however be noted that it is not possible to accurately measure mitochondrial protein content against the background of antibodies and protein contributed

by the 1 × SB, thus normalization of metabolomics data to protein content is not possible. Therefore other normilization strategies should be followed, like the use of internal standards as utilized in this study or even MS total useful signal (MSTUS) normalization (Warrack et al. 2007).

This study is by no means analytically perfect, but serves as a template pipeline to laboratories of every financial and analytical status. It extends the usefulness of MACS technology to application in sub-cellular metabolomics—providing a midway between expensive recombinant immunopurification techniques and rudimentary centrifugal methods, while also proposing a simple solution to producing comparable cytosolic fractions. A combination of simple and robust workflow, inexpensive commercially available fractioning equipment and standard metabolomics platforms is intended to inspire increased outputs in compartment-specific metabolomics universally, to grow and refine this niche field of research substantially in the coming years.

Acknowledgements This work is based on the research supported by the National Research Foundation of South Africa (NRF; Grant Numbers 92736 and 117424) and the Technological Innovation Agency of the Department of Science and Technology of South Africa (TIA; Grant Number Metabol.01). Opinions expressed and conclusions arrived at, are those of the authors and are not necessarily to be attributed to the NRF or the TIA. We acknowledge and thank Dr's Shayne Mason and J Zander Lindeque of the NWU, Human Metabolomics, for their invaluable assistance during metabolomics and data analyses, as well as Mr's Luciano WIllemse and Charl du Plessis for helping in acquiring chemometrics data for the chemical standard mixtures investigated in this study.

Author contributions The study was conceived by RL, but planned and executed in equal parts by both authors. Data were acquired predominantly by GV and analysed concomitantly by both authors. The manuscript was compiled by GV under supervision of RL.

Data availability The metabolomics and metadata reported in this paper are available via Metabolomics Workbench, https://www.metabolomicsworkbench.org with unique file identifier Gunter007dekok_20191218_151540 and Data Track ID 1877.

Compliance with ethical standards

Conflict of interest Both authors declare to have no conflicts of interest.

Ethical approval The AnimCare animal research ethics committee of North-West University approved (NWU-00568-19-S5) the animal protocols used here. All animals were maintained and all procedures performed in accordance with the code of ethics in research, training and testing of drugs in South Africa and complied with national legislation.

References

Afanasyeva, M., Ustiugova, A., Golyshev, S., Kopylov, A., Bogolyubova, A., Demin, D., et al. (2018). Isolation of large amounts of highly pure mitochondria for "omics" studies. *Biochemistry (Moscow), 83*, 76–85.

Aucamp, J., Bronkhorst, A. J., Peters, D. L., Van Dyk, H. C., Van der Westhuizen, F. H., & Pretorius, P. J. (2017). Kinetic analysis, size profiling, and bioenergetic association of DNA released by selected cell lines in vitro. *Cellular and Molecular Life Sciences, 74*, 2689–2707.

Bayraktar, E. C., Baudrier, L., Özerdem, C., Lewis, C. A., Chan, S. H., Kunchok, T., et al. (2019). MITO-Tag Mice enable rapid isolation and multimodal profiling of mitochondria from specific cell types in vivo. *Proceedings of the National Academy of Sciences, 116*, 303–312.

Beckonert, O., Keun, H. C., Ebbels, T. M., Bundy, J., Holmes, E., Lindon, J. C., et al. (2007). Metabolic profiling, metabolomic and metabonomic procedures for NMR spectroscopy of urine, plasma, serum and tissue extracts. *Nature Protocols, 2*, 2692.

Birsoy, K., Wang, T., Chen, W. W., Freinkman, E., Abu-Remaileh, M., & Sabatini, D. M. (2015). An essential role of the mitochondrial electron transport chain in cell proliferation is to enable aspartate synthesis. *Cell, 162*, 540–551.

Bissantz, C., Kuhn, B., & Stahl, M. (2010). A medicinal chemist's guide to molecular interactions. *Journal of Medicinal Chemistry, 53*, 5061–5084.

Brand, M. D., & Nicholls, D. G. (2011). Assessing mitochondrial dysfunction in cells. *Biochemical Journal, 435*, 297–312.

Brown, M.R., Sullivan, P.G., Dorenbos, K.A., Modafferi, E.A., Geddes, J.W., & Steward, O. (2004). Nitrogen disruption of synaptoneurosomes: An alternative method to isolate brain mitochondria. *Journal of Neuroscience Methods, 137*, 299–303.

Chan, C. C., Lee, Y., Lam, H., & Zhang, X.-M. (2004). *Analytical method validation and instrument performance verification*. New York: Wiley.

Chen, W. W., Freinkman, E., Wang, T., Birsoy, K., & Sabatini, D. M. (2016). Absolute quantification of matrix metabolites reveals the dynamics of mitochondrial metabolism. *Cell, 166*(1324–1337), e11.

Cheng, M. Y., Hartl, F.-U., Martin, J., Pollock, R. A., Kalousek, F., Neuper, W., et al. (1989). Mitochondrial heat-shock protein hsp60 is essential for assembly of proteins imported into yeast mitochondria. *Nature Communications, 337*, 620.

Corcelli, A., Saponetti, M. S., Zaccagnino, P., Lopalco, P., Mastrodonato, M., Liquori, G. E., et al. (2010). Mitochondria isolated in nearly isotonic KCl buffer: Focus on cardiolipin and organelle morphology. *Biochimica et Biophysica Acta, 1798*, 681–687.

de Bari, L., & Atlante, A. (2018). Including the mitochondrial metabolism of l-lactate in cancer metabolic reprogramming. *Cellular and Molecular Life Sciences, 75*, 2763–2776.

Dona, A. C., Jiménez, B., Schäfer, H., Humpfer, E., Spraul, M., Lewis, M. R., et al. (2014). Precision high-throughput proton NMR spectroscopy of human urine, serum, and plasma for large-scale metabolic phenotyping. *Analytical Chemistry, 86*, 9887–9894.

Dunn, W. B., Broadhurst, D. I., Atherton, H. J., Goodacre, R., & Griffin, J. L. (2011). Systems level studies of mammalian metabolomes: The roles of mass spectrometry and nuclear magnetic resonance spectroscopy. *Chemical Society Reviews, 40*, 387–426.

Dunn, W. B., Wilson, I. D., Nicholls, A. W., & Broadhurst, D. (2012). The importance of experimental design and QC samples in large-scale and MS-driven untargeted metabolomic studies of humans. *Bioanalysis, 4*, 2249–2264.

Esterhuizen, K., van der Westhuizen, F. H., & Louw, R. (2017). Metabolomics of mitochondrial disease. *Mitochondrion, 35*, 97–110.

FDA, U.S. (2001) Guidance for industry, bioanalytical method validation. *Federal Register* 66.

Fiehn, O. (2002). Metabolomics—The link between genotypes and phenotypes. In C. Town (Ed.), *Functional genomics* (pp. 155–171). Dordrecht: Springer.

Franko, A., Baris, O. R., Bergschneider, E., Von Toerne, C., Hauck, S. M., Aichler, M., et al. (2013). Efficient isolation of pure and functional mitochondria from mouse tissues using automated tissue disruption and enrichment with anti-TOM22 magnetic beads. *PLoS ONE, 8*, e82392.

Fratila, R. M., & Velders, A. H. (2011). Small-volume nuclear magnetic resonance spectroscopy. *Annual Review of Analytical Chemistry, 4*, 227–249.

Frezza, C. (2017). Mitochondrial metabolites: Undercover signalling molecules. *Interface Focus, 7*, 20160100.

García-Sevillano, M., García-Barrera, T., Navarro, F., Montero-Lobato, Z., & Gómez-Ariza, J. (2015). Shotgun metabolomic approach based on mass spectrometry for hepatic mitochondria of mice under arsenic exposure. *BioMetals, 28*, 341–351.

Gielisch, I., & Meierhofer, D. (2015). Metabolome and proteome profiling of complex I deficiency induced by rotenone. *Journal of Proteome Research, 14*, 224–235.

Glaves, J., Li, M., Mercier, P., Fahlman, R., & Sykes, B. (2014). High-throughput, multi-platform metabolomics on very small volumes: 1 H NMR metabolite identification in an unadulterated tube-in-tube system. *Metabolomics, 10*, 1145–1151.

Go, Y.-M., Roede, J. R., Orr, M., Liang, Y., & Jones, D. P. (2014a). Integrated redox proteomics and metabolomics of mitochondria to identify mechanisms of cd toxicity. *Toxicological Sciences, 139*, 59–73.

Go, Y.-M., Uppal, K., Walker, D.I., Tran, V., Dury, L., Strobel, F.H., Baubichon-Cortay, H., Pennell, K.D., Roede, J.R. and Jones, D.P. (2014b) Mitochondrial metabolomics using high-resolution Fourier-transform mass spectrometry. In *Mass spectrometry in metabolomics* (pp. 43–73). New York: Springer.

Gullberg, J., Jonsson, P., Nordström, A., Sjöström, M., & Moritz, T. (2004). Design of experiments: An efficient strategy to identify factors influencing extraction and derivatization of Arabidopsis thaliana samples in metabolomic studies with gas chromatography/mass spectrometry. *Analytical Biochemistry, 331*, 283–295.

Hall, A. M., & Roberson, E. D. (2012). Mouse models of Alzheimer's disease. *Brain Research Bulletin, 88*, 3–12.

Hohmann, M., Felbinger, C., Christoph, N., Wachter, H., Wiest, J., & Holzgrabe, U. (2014). Quantification of taurine in energy drinks using 1H NMR. *Journal of Pharmaceutical and Biomedical Analysis, 93*, 156–160.

Hornig-Do, H.-T., Günther, G., Bust, M., Lehnartz, P., Bosio, A., & Wiesner, R. J. (2009). Isolation of functional pure mitochondria by superparamagnetic microbeads. *Analytical Biochemistry, 389*, 1–5.

Hubbard, W. B., Harwood, C. L., Prajapati, P., Springer, J. E., Saatman, K. E., & Sullivan, P. G. (2019). Fractionated mitochondrial magnetic separation for isolation of synaptic mitochondria from brain tissue. *Science Report, 9*, 9656.

Jin, F., Wu, Q., Lu, Y. F., Gong, Q. H., & Shi, J. S. (2008). Neuroprotective effect of resveratrol on 6-OHDA-induced Parkinson's disease in rats. *European Journal of Pharmacology, 600*, 78–82.

Junghans, L., Teleki, A., Wijaya, A. W., Becker, M., Schweikert, M., & Takors, R. (2019). From nutritional wealth to autophagy: In vivo metabolic dynamics in the cytosol, mitochondrion and shuttles of IgG producing CHO cells. *Metabolic Engineering, 54*, 145–159.

Kappler, L., Li, J., Häring, H.-U., Weigert, C., Lehmann, R., Xu, G., et al. (2016). Purity matters: A workflow for the valid high-resolution lipid profiling of mitochondria from cell culture samples. *Scientific Reports, 6*, 21107.

Kayser, E. B., Sedensky, M. M., & Morgan, P. G. (2016). Region-specific defects of respiratory capacities in the Ndufs4(KO) mouse brain. *PLoS ONE, 11*, e0148219.

Kruse, S. E., Watt, W. C., Marcinek, D. J., Kapur, R. P., Schenkman, K. A., & Palmiter, R. D. (2008). Mice with mitochondrial complex I deficiency develop a fatal encephalomyopathy. *Cell Metabolism, 7*, 312–320.

Lake, N. J., Bird, M. J., Isohanni, P., & Paetau, A. (2015). Leigh syndrome: Neuropathology and pathogenesis. *Journal of Neuropathology and Experimental Neurology, 74*, 482–492.

Lee, W. D., Mukha, D., Aizenshtein, E., & Shlomi, T. (2019). Spatial-fluxomics provides a subcellular-compartmentalized view of reductive glutamine metabolism in cancer cells. *Nature Communications, 10*, 1351.

Lindon, J. C., Nicholson, J. K., & Everett, J. R. (1999). *NMR spectroscopy of biofluids* (pp. 1–88). Annual reports on NMR spectroscopy: Elsevier.

Lindeque, J.Z., Hidalgo, J, Louw, R., & van der Westhuizen, F.H. (2013). Systemic and organ specific metabolic differences in metallothionein knockout mice when challenged with exercise. *Metabolomics, 9*, 418–432.

Liu, X., & Xu, G. (2018). Recent advances in using mass spectrometry for mitochondrial metabolomics and lipidomics—A review. *Analytica Chimica Acta, 1037*, 3–12.

Luo, R., David, L., Hung, H., Devaney, J., & Gilson, M. K. (1999). Strength of solvent-exposed salt-bridges. *The Journal of Physical Chemistry B, 103*, 727–736.

Mamer, O., Gravel, S.-P., Choinière, L., Chénard, V., St-Pierre, J., & Avizonis, D. (2013). The complete targeted profile of the organic acid intermediates of the citric acid cycle using a single stable isotope dilution analysis, sodium borodeuteride reduction and selected ion monitoring GC/MS. *Metabolomics, 9*, 1019–1030.

Mason, S., Terburgh, K., & Louw, R. (2018). Miniaturized 1H-NMR method for analyzing limited-quantity samples applied to a mouse model of Leigh disease. *Metabolomics, 14*, 74.

Matuszczyk, J.-C., Teleki, A., Pfizenmaier, J., & Takors, R. (2015). Compartment-specific metabolomics for CHO reveals that ATP pools in mitochondria are much lower than in cytosol. *Biotechnology Journal, 10*, 1639–1650.

Moffett, J. R., Ross, B., Arun, P., Madhavarao, C. N., & Namboodiri, A. M. (2007). N-Acetylaspartate in the CNS: From neurodiagnostics to neurobiology. *Progress in neurobiology, 81*, 89–131.

Nagrath, D., Caneba, C., Karedath, T., & Bellance, N. (2011). Metabolomics for mitochondrial and cancer studies. *Biochimica et Biophysica Acta Bioenergetics, 1807*, 650–663.

Nunnari, J., & Suomalainen, A. (2012). Mitochondria: in sickness and in health. *Cell, 148*, 1145–1159.

Palmieri, F., & Monne, M. (2016). Discoveries, metabolic roles and diseases of mitochondrial carriers: A review. *Biochimica et Biophysica Acta, 1863*, 2362–2378.

Pan, D., Lindau, C., Lagies, S., Wiedemann, N., & Kammerer, B. (2018). Metabolic profiling of isolated mitochondria and cytoplasm reveals compartment-specific metabolic responses. *Metabolomics, 14*, 59.

Passarella, S., & Schurr, A. (2018). l-Lactate transport and metabolism in mitochondria of Hep G2 cells—The cori cycle revisited. *Frontiers in Oncology, 8*, 120.

Patti, M.-E., & Corvera, S. (2010). The role of mitochondria in the pathogenesis of type 2 diabetes. *Endocrine Reviews, 31*, 364–395.

Paul, M. H., & Sperling, E. (1952). Cyclophorase system. XXIII. Correlation of cyclophorase activity and mitochondrial density in striated muscle. *Proceedings of the Society for Experimental Biology and Medicine, 79*, 352–354.

Picard, M., Wallace, D. C., & Burelle, Y. (2016). The rise of mitochondria in medicine. *Mitochondrion, 30*, 105–116.

Picard, M., White, K., & Turnbull, D. M. (2012). Mitochondrial morphology, topology, and membrane interactions in skeletal muscle: A quantitative three-dimensional electron microscopy study. *Journal of Applied Physiology, 114*, 161–171.

Pustylnikov, S., Costabile, F., Beghi, S., & Facciabene, A. (2018). Targeting mitochondria in cancer: Current concepts and immunotherapy approaches. *Transl Res, 202*, 35–51.

Roede, J. R., Park, Y., Li, S., Strobel, F. H., & Jones, D. P. (2012). Detailed mitochondrial phenotyping by high resolution metabolomics. *PLoS ONE, 7*, e33020.

Ruggeri, B. A., Camp, F., & Miknyoczki, S. (2014). Animal models of disease: Pre-clinical animal models of cancer and their applications and utility in drug discovery. *Biochemical Pharmacology, 87*, 150–161.

Schymanski, E. L., Jeon, J., Gulde, R., Fenner, K., Ruff, M., Singer, H. P., et al. (2014). Identifying small molecules via high resolution mass spectrometry: Communicating confidence. *Environmental Science and Technology, 48*, 2097–2098.

Shepherd, D., & Garland, P. (1969). The kinetic properties of citrate synthase from rat liver mitochondria. *Biochemical Journal, 114*, 597–610.

Steinhauser, M. L., & Lechene, C. P. (2013). Quantitative imaging of subcellular metabolism with stable isotopes and multi-isotope imaging mass spectrometry. *Seminars in Cell & Developmental Biology, 24*, 661–667.

Tahrir, F. G., Shanmughapriya, S., Ahooyi, T. M., Knezevic, T., Gupta, M. K., Kontos, C. D., et al. (2018). Dysregulation of mitochondrial bioenergetics and quality control by HIV-1 Tat in cardiomyocytes. *Journal of Cellular Physiology, 233*, 748–758.

Terburgh, K., Lindeque, Z., Mason, S., Van der Westhuizen, F., & Louw, R. (2019). Metabolomics of Ndufs4−/− skeletal muscle: Adaptive mechanisms converge at the ubiquinone-cycle. *Biochimica et Biophysica Acta, 1865*, 98–106.

Tsai, C. (1967). Spontaneous decarboxylation of oxalacetic acid. *Canadian Journal of Chemistry, 45*, 873–880.

Tsai, G., & Coyle, J. T. (1995). N-acetylaspartate in neuropsychiatric disorders. *Progress in Neurobiology, 46*, 531–540.

Tzelepis, F., Blagih, J., Khan, N., Gillard, J., Mendonca, L., Roy, D.G., Ma, E.H., Joubert, P., Jones, R.G., and Divangahi, M. (2018) Mitochondrial cyclophilin D regulates T cell metabolic responses and disease tolerance to tuberculosis. *Science Immunology* 3.

Van Aardt, W. J., Le Roux, J. M., Lindeque, J. Z., Mason, S., & Louw, R. (2016). The effect of temperature on the respiration and metabolism of the African burrowing scorpion (Opistophthalmus latimanus). *Comparative Biochemistry and Physiology Part D: Genomics and Proteomics, 20*, 50–56.

Van Vranken, J. G., & Rutter, J. (2016). The whole (cell) is less than the sum of its parts. *Cell, 166*, 1078–1079.

Vendelin, M., Béraud, N., Guerrero, K., Andrienko, T., Kuznetsov, A. V., Olivares, J., et al. (2005). Mitochondrial regular arrangement in muscle cells: A "crystal-like" pattern. *American Journal of Physiology-Cell Physiology, 288*, C757–C767.

Wang, A. C., & Bax, A. (1993). Minimizing the effects of radio-frequency heating in multidimensional NMR experiments. *Journal of biomolecular NMR, 3*, 715–720.

Warrack, B. M., Hnatyshyn, S., Ott, K. H., Reily, M. D., Sanders, M., Zhang, H., et al. (2007). Normalization strategies for metabonomic analysis of urine samples. *Journal of Chromatography B. Analytical Technologies in the Biomedical and Life Sciences, 877*, 547–552.

Wu, M., Neilson, A., Swift, A. L., Moran, R., Tamagnine, J., Parslow, D., et al. (2007). Multiparameter metabolic analysis reveals a close link between attenuated mitochondrial bioenergetic function and enhanced glycolysis dependency in human tumor cells. *American Journal of Physiology: Cell Physiology, 292*, C125–C136.

Yao, J., Irwin, R. W., Zhao, L., Nilsen, J., Hamilton, R. T., & Brinton, R. D. (2009). Mitochondrial bioenergetic deficit precedes Alzheimer's pathology in female mouse model of Alzheimer's disease. *Proceedings of the National Academy of Sciences of the USA, 106*, 14670–14675.

Publisher's Note Springer Nature remains neutral with regard to jurisdictional claims in published maps and institutional affiliations.

ANNEXURE D

Published peer-reviewed paper II

metabolites

MDPI

Article

Sub-Cellular Metabolomics Contributes Mitochondria-Specific Metabolic Insights to a Mouse Model of Leigh Syndrome

Gunter van der Walt, Jeremie Z. Lindeque, Shayne Mason and Roan Louw *

Human Metabolomics, Faculty of Natural and Agricultural Sciences, North-West University, Potchefstroom 2531, South Africa; gvanderwalt007@gmail.com (G.v.d.W.); zander.lindeque@nwu.ac.za (J.Z.L.); nmr.nwu@gmail.com (S.M.)

* Correspondence: roan.louw@nwu.ac.za

Abstract: Direct injury of mitochondrial respiratory chain (RC) complex I by Ndufs4 subunit mutations results in complex I deficiency (CID) and a progressive encephalomyopathy, known as Leigh syndrome. While mitochondrial, cytosolic and multi-organelle pathways are known to be involved in the neuromuscular LS pathogenesis, compartment-specific metabolomics has, to date, not been applied to murine models of CID. We thus hypothesized that sub-cellular metabolomics would be able to contribute organelle-specific insights to known Ndufs4 metabolic perturbations. To that end, whole brains and skeletal muscle from late-stage Ndufs4 mice and age/sex-matched controls were harvested for mitochondrial and cytosolic isolation. Untargeted ^{1}H-NMR and semi-targeted LC-MS/MS metabolomics was applied to the resulting cell fractions, whereafter important variables (VIPs) were selected by univariate statistics. A predominant increase in multiple targeted amino acids was observed in whole-brain samples, with a more prominent effect at the mitochondrial level. Similar pathways were implicated in the muscle tissue, showing a greater depletion of core metabolites with a compartment-specific distribution, however. The altered metabolites expectedly implicate altered redox homeostasis, alternate RC fueling, one-carbon metabolism, urea cycling and dysregulated proteostasis to different degrees in the analyzed tissues. A first application of EDTA-chelated magnesium and calcium measurement by NMR also revealed tissue- and compartment-specific alterations, implicating stress response-related calcium redistribution between neural cell compartments, as well as whole-cell muscle magnesium depletion. Altogether, these results confirm the ability of compartment-specific metabolomics to capture known alterations related to Ndufs4 KO and CID while proving its worth in elucidating metabolic compartmentalization in said pathways that went undetected in the diluted whole-cell samples previously studied.

Keywords: mitochondria; cytosol; mitochondrial disease; complex I deficiency; Ndufs4; metabolomics; sub-cellular metabolomics; ^{1}H-NMR; LC-MS/MS

Citation: van der Walt, G.; Lindeque, J.Z.; Mason, S.; Louw, R. Sub-Cellular Metabolomics Contributes Mitochondria-Specific Metabolic Insights to a Mouse Model of Leigh Syndrome. *Metabolites* **2021**, *11*, 658. https://doi.org/10.3390/metabo11100658

Academic Editor: James McCullagh

Received: 2 September 2021
Accepted: 22 September 2021
Published: 28 September 2021

Publisher's Note: MDPI stays neutral with regard to jurisdictional claims in published maps and institutional affiliations.

Copyright: © 2021 by the authors. Licensee MDPI, Basel, Switzerland. This article is an open access article distributed under the terms and conditions of the Creative Commons Attribution (CC BY) license (http://creativecommons.org/licenses/by/4.0/).

1. Introduction

Throughout more than a century of mitochondrial research, science has ascertained at least this much regarding mitochondrial function: (i) it is critical to many facets of cellular health; (ii) it is a highly dynamic and adaptable role player in global and tissue-specific biology; and (iii) it maintains spatiotemporal compartmentalization of core metabolic/signaling networks. Mitochondria orchestrate these processes towards cellular homeostasis.

Through tightly regulated coordination with other intracellular spaces, mitochondria participate in several key energy-producing and biosynthetic pathways [1–3]. Furthermore, complex metabolic and signal transduction pathways integrate nutrient, stress state and cell cycle cues at the mitochondrial level to elicit whole-cell responses following any change in environment or physiological needs [4,5]. Concordantly, mitochondria have been implicated in multiple complex pathologies, from cancer to COVID-19 [6–9]. Central

to our understanding of the mitochondrial contribution to pathology, however, is the study of primary mitochondrial disease (PMD), which results from deleterious mutations in core mitochondria-related genes [10,11]. Specifically, disorders of the first and foremost contributing enzyme of the respiratory chain (RC)—NADH:ubiquinone oxidoreductase (complex I, CI)—are the most prevalent, with multiple nDNA or mtDNA mutations contributing to the observed CI-deficient (CID) phenotypes [12,13]. Deletion of the iron–sulfur CI protein subunit, Ndufs4, leads to subsequent CID, and a progressive encephalomyopathy with severe musculoskeletal symptoms and poor prognosis known as Leigh syndrome (LS) [14,15]. The underlying whole-body knock-out (KO) paradoxically only leads to tissue-specific deterioration and metabolic reprogramming, implicating multiple biological systems in the observed mosaic.

Metabolomics has proven to be indispensable towards capturing changes in the small-molecule intermediates of metabolism that underlie bioenergetic, anabolic and signaling pathways intimately related to multiple mitochondria-related disease states [16–18]. Mouse models for PMD, such as the synthesized Ndufs4 KO strain studied here [19,20], serve as adequate in vivo models for CI-related LS and have contributed substantially to our understanding of the underlying tissue-specific deficits and potential treatment options [21,22]. In these mice, as in patients, it is known that whole-body Ndufs4 KO leads to graded, region-specific neurodegeneration and metabolic alteration, which has convincingly been shown to be the driving force of the total LS phenotype [23–25]. Oxidative and glycolytic muscles also show fiber type-specific metabolic alterations relating to the atrophy and locomotive defects in late-stage LS model mice and patients [26,27]. Both LS nervous and muscle tissues present features of perturbed metabolic and signaling pathways evident of differential catabolic/anabolic switching. These pathways are intertwined in the cascade of multi-organelle signaling molecules that facilitate an integrated stress response (ISR) during chronic mitochondrial stress [25].

Adaptive bioenergetic responses aimed at controlling the redox state while supplementing the tricarboxylic acid (TCA) cycle and RC-derived ATP synthesis are evident from the metabolite alterations in Ndufs4 brain and skeletal muscle tissues [24,26]. Features related to perturbed anabolic shifts are also prevalent, seemingly in line with the prerequisites of the ISR [22,28]. Concurrently, alterations in core amphibolic substrate levels—such as glutamine, glutamate and 2-ketoglutarate—are apparent even in lesser affected and pre-symptomatic neural/muscular Ndufs4 samples. Unlike in perturbed neural cells, which are supplemented by several neuron-glial metabolite shuttles [29,30], this anabolic shift is presumably far less sustainable in the comparably mitochondria-lacking glycolytic muscle tissues [31] and eventually leads to a global depletion of core metabolic intermediates. As such, induction of an amino acid restriction response has also been strongly correlated with RC inhibition in muscle fibers [32,33]. Evidently, multiple contributing and often conflicting metabolic switches are triggered during RC dysfunction, which require even deeper, more reductive and integrated approaches to fully grasp the metabolic dysfunction during Ndufs4 KO, LS and PMD overall.

Despite decades of study around the causes and effects of mitochondrial dysfunction, only recently has technology allowed us to observe the related metabolic effects inside mitochondria, specifically [34]. Mitochondria maintain a separate chemical milieu to the surrounding cytosol and organelles, with multiple unique, inter- and trans-compartmental reactions abundant. Mitochondria rely on tight membrane coupling to drive the proton gradient necessary for oxidative phosphorylation and ATP synthesis; thus, metabolite exchanges are highly coordinated by multiple substrate-specific, allosterically regulated, inner mitochondrial membrane transporter proteins- of which many are still being discovered and elucidated [35,36]. Finally, even in the most mitochondria-rich tissues, the total mitochondrial matrix volume is substantially smaller than the cytosolic space [37], leading to significant compartment-specific changes often being buried in the total cellular metabolome. This underlies the recent interest in metabolomics methods which can elucidate spatiotemporal compartmentalization of the implicated trans-cellular reactions and

how this contributes to the observed whole-cell phenotype. Two complementary approaches underlie compartmental metabolomics studies. (1) Isotope-labeled metabolite flux measurements can follow the spatiotemporal distribution and the fate of certain targeted chemical precursors [38,39]. (2) Organelle isolation and metabolite fingerprinting offer a greater metabolic resolution and have concurrently delivered accurate sub-cellular insights on effects related to sex, age, fasting state, tumorigenesis and heavy metal toxicity [40–43]. While still scarce in volume, studies utilizing said methods in cell culture models of RC dysfunction have unequivocally proven mitochondria-level metabolite changes which cannot be deduced from whole-cell samples alone [39,44,45].

These techniques are still only finding their footing in the field of in vivo disease modeling at a handful of institutions [46] and, to the best of our knowledge, have yet to be applied to an in vivo model of genetic CID. We thus hypothesized that a rudimentary immunopurification-based organelle isolation and compartment-specific metabolomics strategy [47] could reveal mitochondria-specific metabolic insights that were not visible at the whole cell level. Comparative, multiplatform metabolomics was performed on the brain and skeletal muscle mitochondria and cytosol of late-stage Ndufs4 mice alongside wildtype (WT) control mice. The significantly altered features reported underline the current Ndufs4 metabolomics knowledge while indeed illuminating compartment-specific effects that went unseen in whole-cell studies of these tissues.

2. Results

2.1. Experimental Rationale and Data Quality

To elaborate on the current metabolic knowledge of Ndufs4-linked LS, we performed ^{1}H-NMR and LC-MS/MS metabolomics on purified brain and quadriceps muscle mitochondria and cytosols from male Ndufs4 KO mice ($n = 8$), as well as age- and sex-matched controls (n = 8). The genotype was confirmed by an established PCR genotyping method. A priori sample calculations deemed these group sizes sufficient for detecting the most prominent metabolic effects in the current pilot (Cohen's $D \geq 1.0$ at 80% power; G*-Power 3 R-package [48]).

An established adaptation of the ubiquitous Miltenyi MACS murine mitochondrial isolation kit for in vivo metabolomics was employed [47]—alongside cost-efficient, robust minimal-volume ^{1}H-NMR and LC-MS/MS methods [26,49,50]—emphasizing the feasibility of mitochondrial metabolomics in more resource-restricted research settings. To maximize the information gained, post-NMR samples were subjected to LC-MS analyses, rather than splitting the already limited sample volume (Figure 1A). WT and KO means were compared in each sample matrix, whereafter the statistically significant metabolite alterations were interpreted across compartments for each tissue (Figure 1B,C). Absolute metabolite identity confirmation was provided by 2D-NMR techniques (JRES and COSY), as well as spectral matching to pure metabolite reference standards included for each mass transition probed by LC-MS/MS.

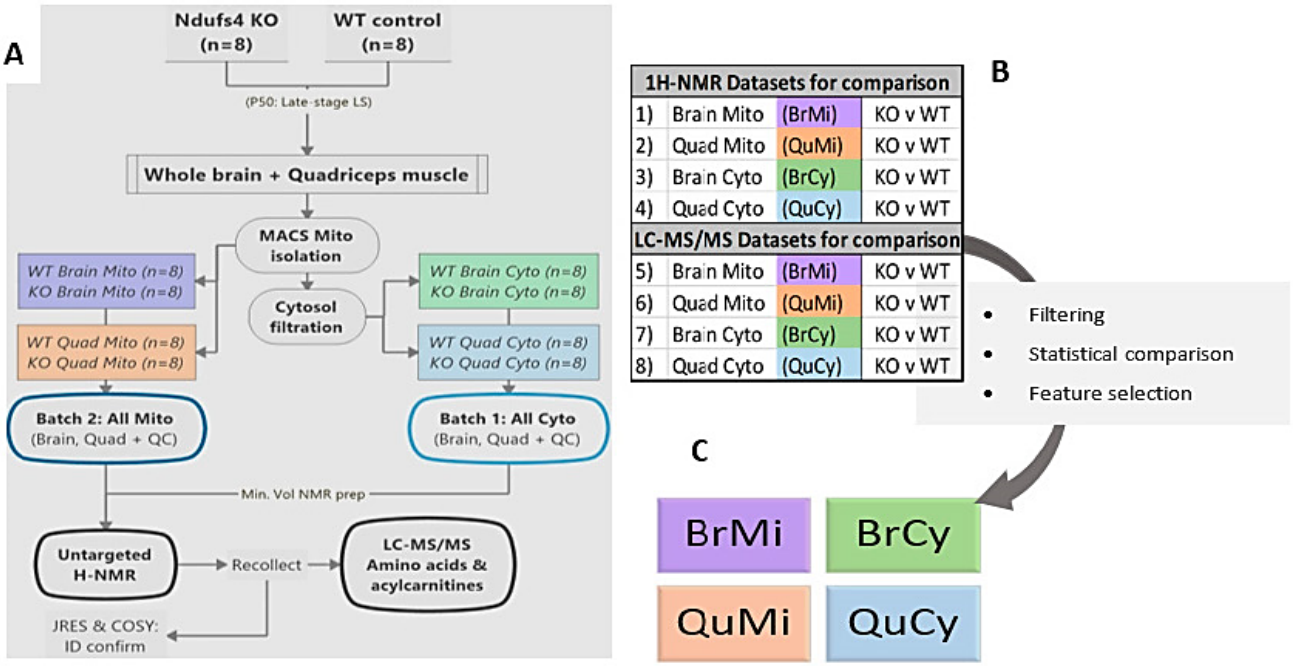


Figure 1. Summarized workflow for the study. Ndufs4 and control mouse quadriceps and whole brains were subjected to MACS mitochondrial isolation and cytosolic filtering, before subsequent ^{1}H-NMR and LC-MS/MS analyses (**A**). Datasets were extracted as such that Ndufs4 KO and WT were compared in each matrix (**B**), before data processing and statistical feature selection. Thereafter, the combined significant feature (VIP) datasets for each tissue and compartment were further processed and interpreted (**C**).

Data quality was controlled by monitoring univariate variance in quality control sample (QC) technical replicates throughout each batch as well as variance of IS compounds uniformly added to each sample. From the relative standard deviation, or percent coefficient of variance (%CV) reported for each compound (Figure 2A–D), the analytical accuracy of NMR or LC-MS measurements within these minimum-volume, buffered samples was well within acceptable precision limits for untargeted metabolomics [51]. Average QC-CV% values across all platforms were even below the FDA-stipulated 20% limit for targeted chemical analyses close to lower quantification limits [52], while no more than two compounds were removed from each dataset based on the selected 30% QC-CV filter employed here. From the NMR mitochondrial dataset, dimethylamine and dimethylformamide (possibly methylamine artefacts) were removed with a high %CV, while only alanine was excluded from analysis in the cytosolic NMR data. QC samples showed similar analytical performances in the LC-MS/MS batches, with only threonine being filtered from the cytosolic dataset, and none from the mitochondrial dataset. Upon exclusion of these four compounds, QC-CV values across all batches did not exceed 10%.

Finer technical variance, as inferred by IS compound %CVs across all samples per batch (Figure 2E,F), also averaged at ~10% for both cytosolic and mitochondrial batches, with no compound exceeding 20% CV. From the total signal scatterplots generated before and after data normalization (Figures S1 and S2), the sample-wise normalization strategy employed did not exacerbate the QC signal variance while also being able to correct for certain levels of technical variance in the separate sample groups analyzed in each batch. Therefore, it can be concluded that the metabolomics methods applied were of sufficient precision for metabolite abundance measurement while minimizing the inherent technical variance of low-volume mitochondrial metabolomics.

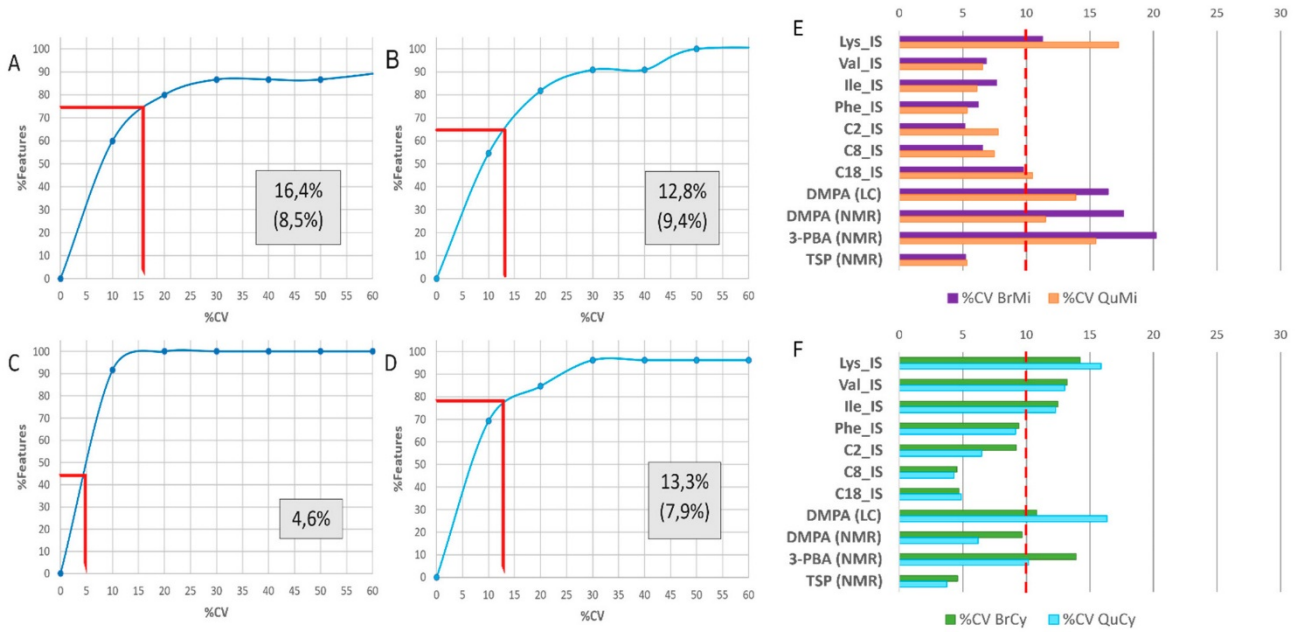


Figure 2. Technical variance and data quality for each ^{1}H-NMR and LC-MS/MS batch. (**A**) Cumulative percentage features plotted over coefficient of variance (%CV) intervals—from QC sample technical replicates within ^{1}H-NMR mitochondrial and (**B**) cytosolic sample batches. The same is plotted for (**C**) LC-MS/MS mitochondrial and (**D**) cytosolic batches as well. Enclosed numbers indicate mean %CV values across all viable features in each dataset—where individual unstable features were filtered, the number in brackets indicates the adjusted mean %CV after filtering. Measured IS compound variance as %CV in each tissue matrix, (**E**) for the mitochondrial and (**F**) cytosolic samples. Deuterium-labeled standards: C2_IS: d3-acetylcarnitine, C8_IS: d3-octanoylcarnitine, C18_IS: d3-stearoylcarnitine, Ile_IS: d10-isoleucine, Lys_IS: d4-lysine, Phe_IS: d5-phenylalanine, Val_IS: d3-valine. Other standards: DMPA: N,N-dimethylphenylalanine, 3-PBA: 3-phenylbutyric acid, TSP: 3-(trimethylsylil) propionic acid.

2.2. *Metabolome Coverage and Data Clean-Up*

Given current uncertainty regarding the exact mitochondrial metabolome and compartmentalization of ambiguous metabolite pools [34,44], we first established LC-MS/MS and ^{1}H-NMR profiles for the accurately identified and quantifiable compound averages across each sample matrix. Untargeted ^{1}H-NMR, following a binning approach, could identify and measure 14 compounds at various levels across all samples, while LC-MS/MS delivered 35 such viable compounds from the 54 metabolites originally targeted by MRM (Figure 3A,B). It should be noted that the LC-MS/MS methodology is biased towards amino acid and acylcarnitine analyses, targeting only mass transitions for a predefined set of metabolites from these classes.

From a tissue-specific perspective, whole-brain mitochondria and cytosols, respectively, delivered 8 and 7 compartment-specific compounds, and 29 across both compartments (Figure 3C). Similarly, 4 uniquely mitochondrial compounds were viably detected in the quadriceps, alongside 13 cytosolic and 26 cross-compartment metabolites. Detected and quantifiable features are listed according to total median spectral signal abundance and QC measurement stability in Table S1. The most abundant features across all matrices were glutamic acid, aspartic acid, carnitine, formic acid and lactic acid. Expectedly, several features were identified and analyzed in one compartment while not being present above baseline/detection levels in the other, as evident from the compartment-specific distributions of sarcosine, hydroxyproline, ornithine and formic acid, among others. This emphasizes the value of the reported approach in measuring metabolites at a mitochondrial level that are either ubiquitous in the total cell volume or diluted beyond detection limits therein.

Several MS feature peaks were removed due to being below the reliable signal/noise area range of 10^3 mAu before the generation of the heatmaps shown in Figure 3. Thereafter, a 50% zero filter was employed, excluding compounds detected at < 1000 mAu in more than 8/16 samples. Finally, the 30% QC-CV data filter was applied as described in Section 2.1. These steps ensured only the most stable metabolites and most relevant patterns in the variation were preserved for statistical analyses.

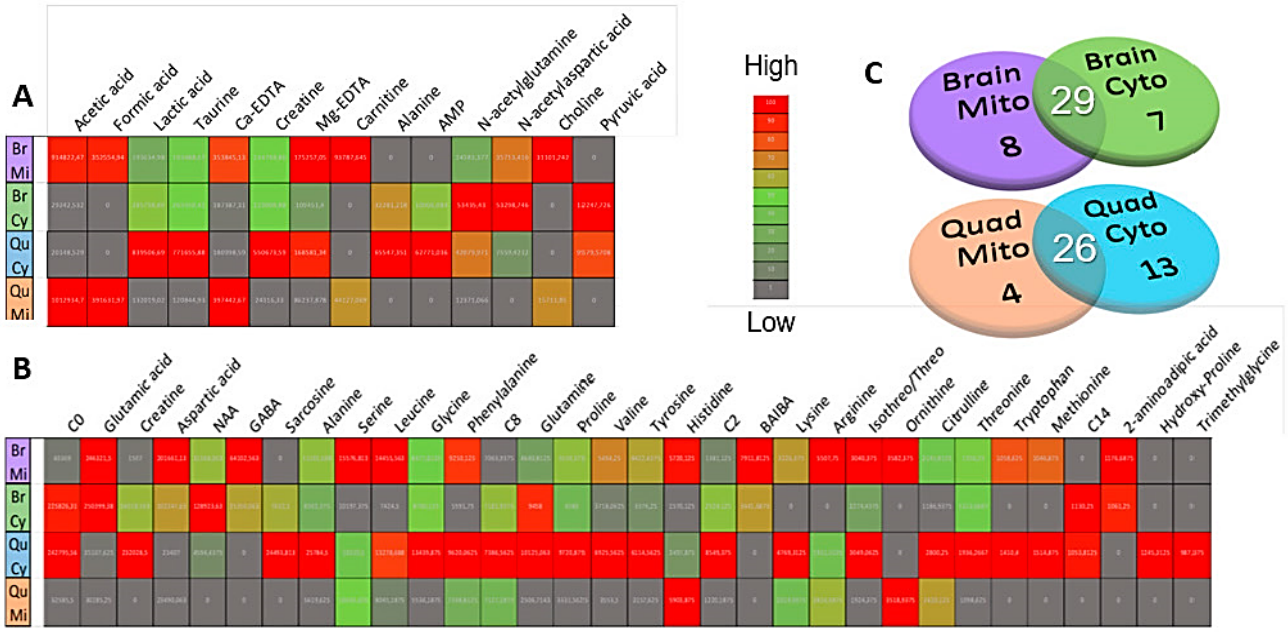


Figure 3. Comparison of viable metabolite presence and gross abundance across sample matrices. Venn diagrams in (**C**) show the number of metabolites viably detected above the noise level in mitochondria, cytosols and both compartments for the whole-brain and quadriceps matrices, separately. Heatmaps of average matrix raw peak abundances, contrasted by Euclidian between-mean distances, are presented for the (**B**) total viable LC-MS/MS and (**A**) ^{1}H-NMR features. Br.C and Br.M abbreviate averages for whole-brain cytosolic and mitochondrial fractions, respectively, and Qu.C and Qu.M indicate quadriceps muscle cytosolic and mitochondrial groups.

2.3. Compartment-Specific, Significant Ndufs4 KO Metabolite Alterations

The selected variables of importance (VIPs) showing significant statistical ($p < 0.1$) and/or practical ($D > 1.0$) differences between WT and KO mitochondria and cytosols are reported in Table 1. The clean and normalized datasets were subjected to univariate tests for significant differences in means; *t*-test statistics and Cohen's D values were calculated in SPSS, automatically accounting for formula derivations per feature based on their differential normality and homogeneity of variance criteria.

Significance limits stricter than the a priori power calculations infer, assure a greater preference for type II statistical errors (rejecting potentially significant changes) while minimizing type I errors (reporting non-significant changes as significant) [53,54]. Although this assures the few metabolites reported are indeed of significant value, many possibly significant alterations may be lost. Notably, three compounds approached the cut-off for significance in the whole-brain samples ($p < 0.15$; $D > 0.8$), while none but the reported quadriceps-derived metabolites showed borderline significant differences in means. Alanine, glutamine and sarcosine are thus included in the discussion of whole-brain metabolic perturbations. Altogether, these VIPs reverberate known bioenergetic and anabolic perturbations related to mitochondrial distress.

PLS-DA projections of the combined VIP datasets for each sample matrix indicate the power of the resulting model to separate WT and KO phenotypes based on the selected features from Table 1 (Figure S3). While the power of multivariate analyses is severely restricted by the small number of samples and significant features in each dataset, cross-validation of the PLS model indicates similar maximal model accuracies (~70%) across matrices. Despite the described limitations, these results also support the ability of sub-cellular metabolomics to discern between Ndufs4 and WT metabolic phenotypes.

Table 1. VIP compounds identified by univariate statistical and practical significance testing. Common metabolite names (Level 1 identity) are reported with the direction of means change (↑ and ↓ arrows representing KO vs WT mean increases or decreases, respectively). *T*-test *p*-values and Cohen's D values in the cytosol—alongside the correlating mitochondrial KO vs. WT comparison are shown in each tissue. The metabolomics platform from which each significant feature was derived is also shown. N.S.: non-significant statistical test result, N.Q.: not quantified due to being filtered from dataset, N.D.: not detected above baseline level.

Quadriceps Muscle							
	Cytosol			***Mitochondria***			
Metabolite (Level 1)	**KO Δ (vs. WT)**	***p***	***D***	**KO Δ (vs. WT)**	***p***	***D***	**Platform**
Lactic acid	↓	0.04	1.2	↓	0.04	1.1	^{1}H-NMR
Mg(II)-EDTA	↓	0.10	0.9	↓	0.09	0.9	^{1}H-NMR
Threonine		N.Q.		↓	0.04	1.1	LC-MS/MS
Glycine		N.S.		↓	0.05	1.1	LC-MS/MS
Creatine		N.S.		↑	0.05	1.0	^{1}H-NMR
Histidine		N.S.		↓	0.07	1.0	LC-MS/MS
Tyrosine		N.S.		↓	0.07	1.0	LC-MS/MS
Ornithine		N.D.		↓	0.08	1.0	LC-MS/MS
Leucine		N.S.		↓	0.10	0.9	LC-MS/MS
Hydroxyproline	↓	0.01	1.8		N.Q.		LC-MS/MS
Citrulline	↓	0.07	1.0		N.S.		LC-MS/MS
Acetylcarnitine	↑	0.09	0.9		N.S.		LC-MS/MS
Lysine	↑	0.10	0.9		N.S.		LC-MS/MS
Whole Brain							
	Cytosol			***Mitochondria***			
Metabolite (Level 1)	**KO Δ (vs. WT)**	***p***	***D***	**KO Δ (vs. WT)**	***p***	***D***	**Platform**
Leucine	↑	0.09	0.9	↑	0.03	1.2	LC-MS/MS
Proline		N.S.		↑	0.03	1.1	LC-MS/MS
Phenylalanine		N.S.		↑	0.03	1.1	LC-MS/MS
Valine		N.S.		↑	0.06	1.0	LC-MS/MS
Octanoylcarnitine		N.S.		↑	0.08	1.0	LC-MS/MS
Glycine		N.S.		↑	0.08	0.9	LC-MS/MS
Ca(II)-EDTA		N.S.		↑	0.09	0.9	^{1}H-NMR
Alanine[1]	↑	0.10	0.9	↑	0.13	0.8	LC-MS/MS
Glutamine [1]		N.S.		↓	0.12	0.8	LC-MS/MS
Sarcosine [1]	↑	0.11	0.8		N.D.		LC-MS/MS

[1] Metabolites approaching statistical and practical significance, yet below defined limits.

2.4. Amino Acids Accumulate in Whole-Brain CI-Deficient Mitochondria to a Greater Extent Than Cytosolic or Region-Specific Metabolomics Can Fully Elucidate

The majority of whole-brain compartment-specific metabolic alterations reported here (Table 1, Figure 4) pertain to metabolites at the intersections of bioenergetic and anabolic pathways. The overall increase in the branched-chain amino acids (BCAAs) valine

(Val) and leucine (Leu) supports the classic model wherein hyperaccumulated NADH inhibits the NAD^+-dependent enzyme branched-chain keto-acid dehydrogenase (BCKDH), leading to accumulation of its BCAA precursors [21,55,56]. These BCAA increases were more prominent at the mitochondrial level than previously detected in the lesser-affected anterior cortex, thus indicating a possibly predictive mitochondrial BCAA accumulation that whole-cell metabolic profiles cannot sufficiently convey [24]. A significant increase in proline (Pro) was seen only at the whole-brain mitochondrial level. This concurs Pro accumulation observed in all Ndufs4 brain regions [24,57], in line with the prominent role of mitochondrial–cytosolic Pro shuttling in buffering redox and adenylate charge ratios [58,59]. These results accentuate hypotheses regarding bioenergetic buffering during RC dysfunction while implicating spatial compartmentalization in these pathways.

Mitochondrial glycine (Gly) levels were significantly increased (Figure S4), while the same effect was not observed in the cytosolic samples or in whole-cell metabolite extracts from affected Ndufs4 brain regions [23,24]. As a key role player in several metabolic pathways in animal cells [60,61], multiple probable explanations exist which require further study. One such explanation involves one-carbon (1C) metabolism and its complex roles in mediating catabolic/anabolic shifts [62,63]. This notion is supported by an observed concomitant increase in cytosolic sarcosine (Src) levels, as an alternative 1C-related Gly precursor. Further amino acid increases appear obscure in isolation but, collectively, also support a general anabolic upregulation in these neural tissues [23]. The accumulation of alanine (Ala) across both compartments and increased mitochondrial phenylalanine (Phe) support a general increase in amino acid liberation for energy metabolism or protein synthesis [32,59], while all amino acid increases reported here may also support this hypothesis. Increased octanoylcarnitine (C8-carnitine) may correlate with a general dysregulation of fatty acid metabolism and neuroinflammation concurrent with the Ndufs4 phenotype [15,29], although these studies reported a greater dysregulation in acylcarnitines larger than C8-carnitine. In support of the glutamine (Gln) perturbation reported here, the prominent involvement of the Gln/Glu/ketoglutarate axis in the concurrent Ndufs4 brain's metabolic shifts is well described, enacting substrate-level coordination of key amphibolic pathways [23,64]. Furthermore, some of these amino acid increases serve as potent stimulants of anabolic shifts, where Leu and Pro specifically upregulate the function of the mitochondrial target of rapamycin (mTORC1) signaling pathways towards greater protein and nucleic acid synthesis [65,66]. While sparsely spread across all these pathways, these results preliminarily reverberate perturbed anabolic signaling and metabolism, as hypothesized by current Ndufs4 brain studies [23–25].

Altogether, the isolated whole-brain mitochondria from Ndufs4 KO animals displayed patterns in metabolite perturbation that resemble the combined metabolic footprints of multiple brain regions previously measured in these mice while showing a greater perturbation at the mitochondria-specific level.

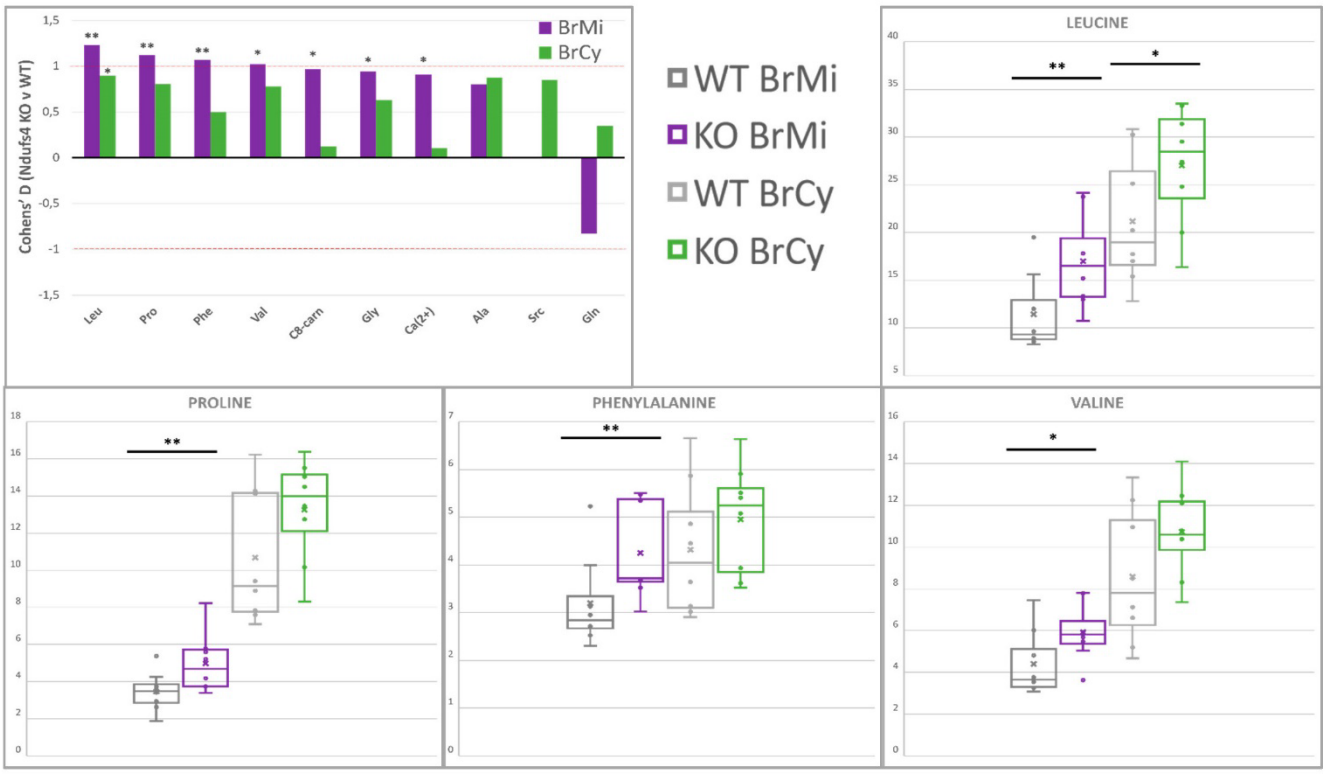


Figure 4. Compartment–specific metabolite alterations in Ndufs4 KO whole brain, identified by ^{1}H–NMR and LC–MS/MS. Histograms indicate mean differences with size and directionality, graphed as Cohen's D values, while boxplots summarize the sample value distributions for each compound across the two genotypes and cell compartments analyzed. Statistical significance via Student's *t*-test is indicated as (*) for $p < 0.1$ or (**) for $p < 0.05$. Abbreviations: Ala: alanine, C8-carn: octanoylcarnitine, Ca(2+): Ca(II)-EDTA, Gln: glutamine, Gly: glycine, Leu: leucine, Phe: phenylalanine, Pro: proline, Src: sarcosine, Val: valine.

2.5. Differential Depletion of Quadriceps Mitochondrial and Cytosolic Metabolites Related to CID Muscle Metabolic Reprogramming

Mitochondrial and cytosolic VIP compounds point to known perturbed bioenergetic pathways in Ndufs4 KO glycolytic skeletal muscle fibers (Table 1, Figure 5). A decrease in lactic acid (Lac) across both compartments was detected, in line with existing Ndufs4 whole-cell quadriceps metabolic data [26]. While sequestration of glycolytic units for NAD^{+} regeneration via mitochondrial glycerol-3-phosphate cycling stands as a convincing explanation for an Lac decrease at the whole cell level [59], concomitant mitochondria-level decreases also implicate biologically significant mitochondrial Lac import and oxidation towards TCA anaplerosis [67,68]. In that regard, a lesser-described mitochondrial Lac dehydrogenase isoform (m-LDH) seemingly plays an important role in skeletal muscle energy buffering during energetic stress [69]. An increase in acetylcarnitine (C2-carnitine), as reported here, is known to be a repercussion of acetyl-CoA accumulation due to RC blockage [70]. Accumulated mitochondrial creatine (Cr) contradicts the decrease in whole-cell Cr previously described

in Ndufs4 KO quadriceps. This indicates perturbation of the mitochondrial–cytosolic creatine shuttle and differential functionalities of compartment-specific creatine kinase (CK) isoforms [71].

Significant depletion of select amino acids is also reminiscent of recent hypotheses supporting a cellular focus on alternate RC fueling pathways. Decreased 4-hydroxyproline (Hpro) indicates sequestration of upstream Pro for preferential use in balancing redox

restrictions by proline/pyrroline-5-carboxylate (P5C) cycling, while it may also correlate with disturbed collagen proteostasis [57,72]. Increased cytosolic lysine (Lys) levels also indicate a shift in its interrelated metabolic pathways aimed at preserving cellular NADH/NAD^+ ratios, effectively restricting its mitochondrial catabolism to 2-aminoadipate [26].

The measured ornithine (Orn) and citrulline (Citru) implicate compartmentalized perturbation of muscle urea cycling (Figure S5). While a decrease in these compounds supports a hypothesized increased channeling of Orn towards the Pro and/or CK shuttles as described above, distinct compartment-specific perturbations, as reported here, were not seen in a previous whole-cell Ndufs4 quadriceps study [26]. Gly was found significantly decreased in Ndufs4 muscle mitochondria while showing no significant difference in cytosolic samples. Threonine (Thr) levels followed the same trend, as Thr catabolizes through Gly back to Pyr—their concomitant depletions are likely related.

Decreased leucine (Leu), histidine (His) and tyrosine (Tyr) levels were also observed in the muscle mitochondria (Figure S5), indicative of perturbed amphibolic pathways. Other than being a critical energy source for the skeletal muscle, Leu also serves to increase whole-body energy availability by stimulating the muscle–liver Cahill cycle and subsequent hepatic gluconeogenesis [55,73], at the expense of muscle Lac and Glu. Classic His catabolism ultimately leads to replenishment of Glu and donation of methyl units to the 1C cycle; thus, its decrease may lie up- or downstream of RC-induced perturbations in these pathways [74]. While the role of lesser-expressed Tyr catabolic enzymes towards TCA anaplerosis is prominent in oncogenic muscle deterioration (cachexia) [75], significant perturbations in Tyr pools were not previously found at the cytosolic or whole cell level in MD mice [21,26].

Despite all the pathways described, the observed amino acid depletion is just as probably related to differential dysregulation of mitochondrial and cytosolic protein turnover during PMD [33,76]. Notably, this supports the hypothesis wherein the sparse, glycolytic muscle fiber mitochondrial network cannot sustain similar stress responses as induced in the brain and ultimately leads to an amino acid restriction response [31,32]. In summary, the described compartment-specific metabolite perturbations highlight several well-supported hypotheses regarding metabolic distress in CID glycolytic muscle fibers while clearly homing in on effects beyond the discernment ability of whole-cell metabolomics.

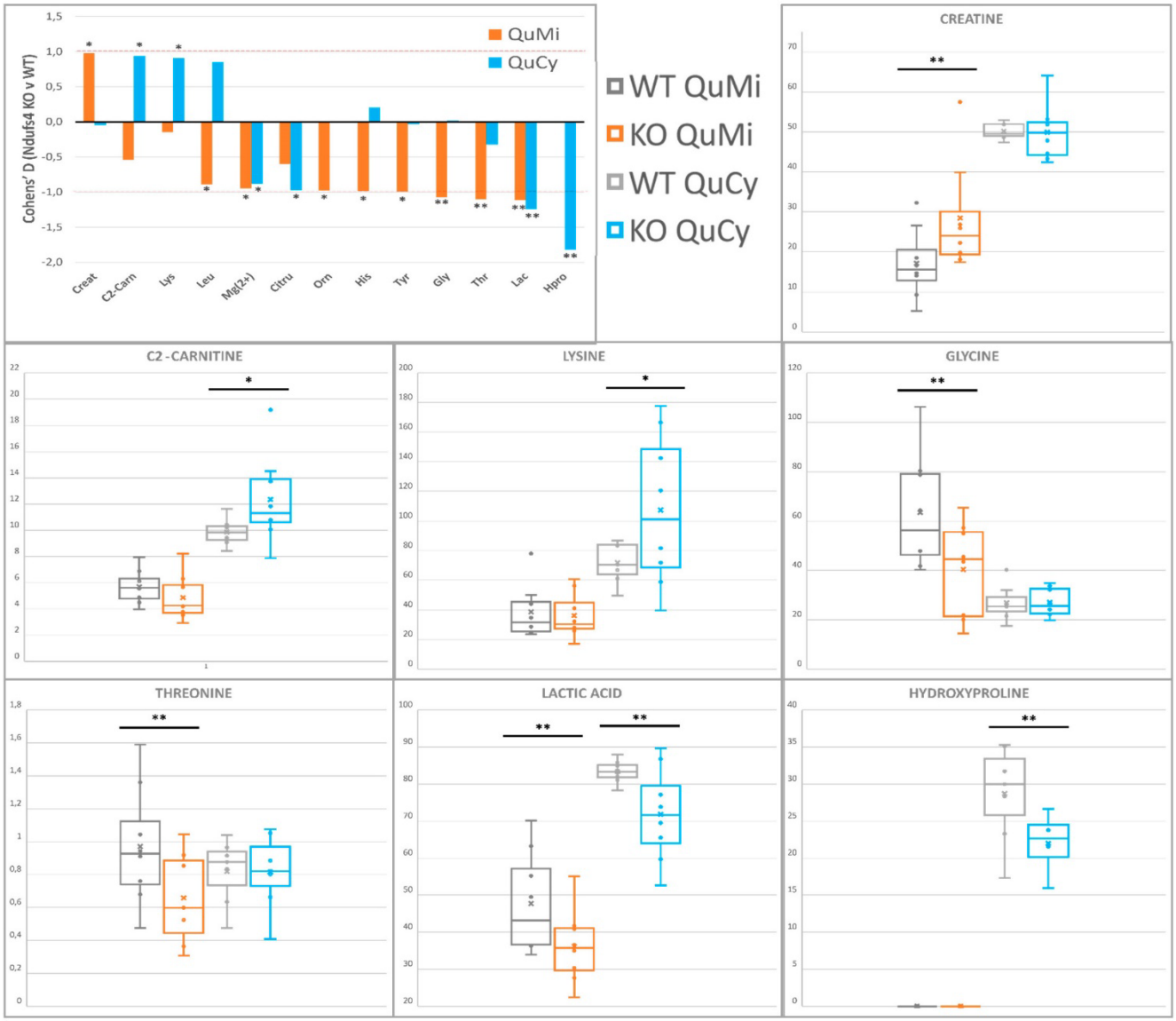


Figure 5. Compartment−specific metabolite alterations in Ndufs4 KO quadriceps muscle, identified by ^{1}H−NMR and LC-MS/MS. Histograms indicate mean differences with size and directionality, graphed as Cohen's D values, while boxplots summarize the sample value distributions for each compound across the two genotypes and cell compartments analyzed. Statistical significance via Student's *t*-test is indicated as (*) for $p < 0.1$ or (**) for $p < 0.05$. Abbreviations: C2-carn: acetyl-carnitine, Citru: citrulline, Creat: creatine, Gly: glycine, His: histidine, Hpro: 4-hydroxyproline, Lac: lactic acid, Leu: leucine, Lys: lysine, Mg(2+): Mg(II)-EDTA, Orn: ornithine, Src: sarcosine, Thr: threonine, Tyr: tyrosine.

2.6. First Report of Tissue- and Compartment-Specific Bivalent Cation Measuremnt in Ndufs4 Mice Highlights Role of Metal Homeostasis in Integrated Stress Responses

During ^{1}H-NMR analyses, we exploited a recently developed procedure for quantifying bivalent metal cations through their chelation with ethylenediaminetetraacetic acid (EDTA) [77,78]. As the sub-cellular samples contain a molar excess of EDTA as part of the isolation buffer environment [47,79], chelated calcium (Ca-EDTA) and magnesium (Mg-EDTA) concentrations are representative of the relative amounts of the cations present. Here, we report the first direct measurement (to our knowledge) of altered compartment-specific metallostasis in affected LS model tissues, as indicated in Figure 6.

A significant increase in brain mitochondrial Ca^{2+} levels was observed, with virtually no difference in its cytoplasmic concentrations due to Ndufs4 KO. This is in line with mitochondria–endoplasmic reticulum (ER) coupling and subsequent mitochondrial Ca^{2+} influx during ER stress responses to RC insult [1,25,80]. This buffering mechanism serves to upregulate multiple Ca^{2+}-dependent metabolic enzymes, independently of cytosolic calcium pools. The skeletal muscle Mg^{2+} levels were significantly lower over both cell compartments. Although no present direct explanation suffices, lowered Mg^{2+} levels are also involved in bioenergetic feedback signaling during the mitochondrial stress responses [81,82]. This may also reflect alterations in protein turnover as described in the preceding section, as Mg^{2+} readily serves as a co-factor in multiple enzyme complexes, most notably in ATP-consuming proteins; however, whole-body Mg^{2+} decreases are often associated with decreased intestinal absorption and renal reabsorption due to energy deficiency [83].

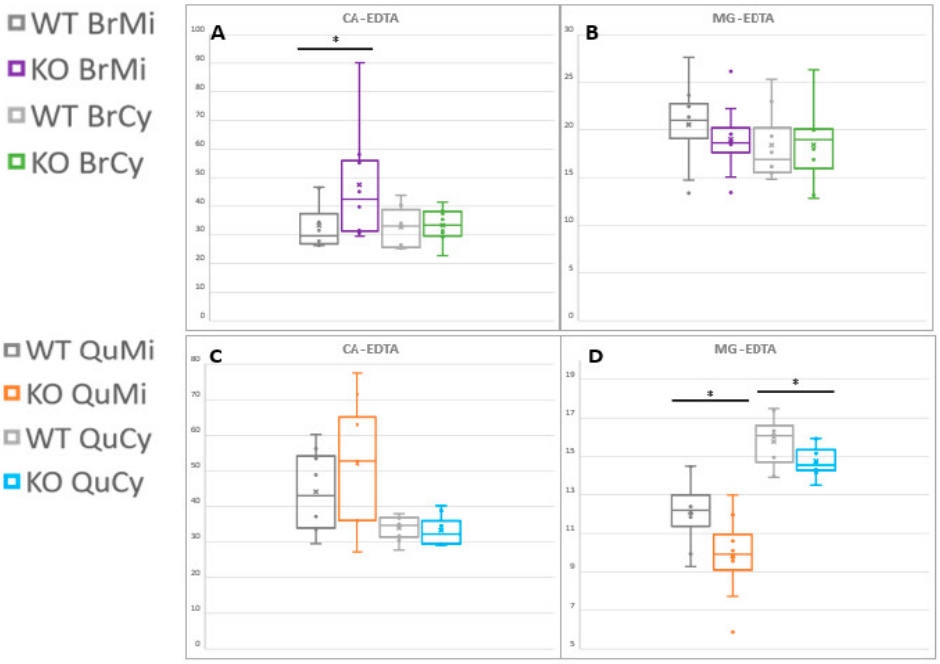


Figure 6. (**A**–**D**) Compartment–specific magnesium and calcium levels, detected as EDTA chelates by ^{1}H–NMR. Statistical significance via Student's *t*-test is indicated as (*) for $p < 0.1$. Ca-EDTA: Ca(II)-ethylenediaminetetraacetate, Mg-EDTA: Mg(II)-ethylenediaminetetraacetate.

3. Discussion

3.1. Contribution towards In Vivo Ndufs4 Model and In Vitro CID Knowledge Base

The reported mitochondrial and cytosolic metabolites from these LS model tissues highlight current metabolomic hypotheses underlying in vivo pathogenic and adaptive responses to Ndufs4 KO [15,21]. Central to the problem addressed by this study are detected metabolite alterations at the mitochondrial level in neural and glycolytic muscles that their correlated whole-cell and cytosolic samples do not reveal [23,24,26,84]. The whole-brain VIPs support the reported role of multiple bioenergetic and anabolic pathways at the core of the LS phenotype. In the related glycolytic muscle, differential patterns of metabolic change were observed across both compartments; however, all of them related to the presumed depletion of similar pathways to those upregulated in whole-brain tissues.

Both tissues clearly reverberate redox perturbations and the upregulation of pathways that attempt to restore reductant pools [59]. BCAA, Pro [56,72], Lac and Cr perturbations support this, with a greater visible effect in the mitochondrial samples. Most notably, the reported results indicate the roles of lesser-described mitochondrial mLDH and mCK isoforms, emphasizing the value of organelle-level resolution in these core classic bioenergetic pathways [67,71,85]. As mitochondrial NADH pools are presumably affected to a greater extent than the accompanying cytosolic pool [41,86], the greater observed perturbation of redox-related pathways at the sub-cellular level was expected. These results also further implicate core biosynthetic and anaplerotic pathways, as dysregulated anabolic signaling is a core feature and therapeutic target for CID [22,28]. Presumably, this shift attempts to replenish proteins that mediate cellular responses to energetic stress via mito-nuclear signaling and the ISR [4]. Specifically, altered levels of Leu, Pro, Gly and other 1C substrates underlie this statement [63,65,66], although the tight correlation between amino acid availability and protein synthesis may insinuate a direct correlation of all the reported amino acids with dysregulated protein turnover [76]. In contrast, increased liberation of free amino acids towards energy metabolism and concurrent RC/TCA congestion may also viably underlie the overall amino acid accumulation described here [26,62]. Regardless, mitochondrial proteostasis is regulated both separately and in unison with whole-cell levels [32]; therefore, the study of mitochondria-specific amino acid perturbations may well serve to deconvolute their differential metabolic fates under various conditions.

Very few studies to date have provided sub-cellular metabolomics data on RC distress; however, similar pathway perturbations and compartment-specific adaptations have been reported for in vitro CID models [39,44,45]. Ac-CoA and Lys accumulation, Glu/Gln disturbances and Pro and urea cycle upregulation have been reported in human and murine cells after CI inhibition by rotenone, but with cell type-specific patterns [44,45]. Our application of sub-cellular methods to a living mouse model thus also capitulates the value of extending these techniques to in vivo studies, by factoring in tissue-specific effects and considering systemic metabolic contributions. Whole-brain VIPs overall presented amphibolic pathway substrates that may drive the catabolic/anabolic shifts at the core of the phenotype [23]. In accordance, increased mitochondrial Ca^{2+} levels without a concomitant cytosolic increase indicate ER–mitochondrial contact—a key feature of ISR induction [80,87]. In vivo neural metabolomics, however, presents unique challenges regarding specialized, intercellular metabolic shuttles. For instance, astrocytic Leu serves as a key carbon source for neuronal TCA anaplerosis when this axis is depleted [88], while lactate and fatty acid shuttling between microglia and neurons is a key neuroinflammatory feature in late-stage LS [29,30]. Furthermore, the role of aromatic amino acids and Gly in neurotransmitter metabolism must be considered [23,89]. Glutamatergic neurons, however, are of predominant focus in LS models—implicating perturbed Gln/Glu/a-KG metabolism within their mitochondria [15,23,88].

The most striking contrast seen in the quadriceps tissue remains a global depletion of intermediates relating to the same pathways deemed increased in the Ndufs4 brain. Urea, Cr and Lac metabolic derangements were also unique to the muscle samples, in agreement with the current metabolic knowledge on mitochondria-related myopathies [26,33,90]. Lac and Leu depletions also implicate the muscle–liver Cahill cycle alongside the intracellular pathways described [55,73]. Of note, magnesium, and not calcium, was determined as the perturbed cation in this tissue. As a key co-factor for ATP-utilizing enzymes and an indicator of healthy protein turnover [81,82], this is a significant effect deserving of further study. Non-muscle metabolic contributions should, again, also be considered, as the Mg^{2+} depletion may also be related to reduced renal reabsorption or intestinal reabsorption due to energy deficits in these tissues under Ndufs4 KO [27,83].

In conclusion, rudimentary sub-cellular, mitochondria-targeted metabolomics captures known alterations in in vivo LS model mice while granting the ability to further elucidate minor tissue-specific and major mitochondrial responses to *Ndufs4* KO at a sub-

cellular level. Herein lies the value of sub-cellular metabolomics for mitochondria-related research, as these effects were not detectable in whole-cell studies of the same tissues.

3.2. Limitations and Future Directions

Without the direct interrogation of several of the intermediates related to all the pathways discussed here, no mechanistic conclusions as to the full underlying significance of these effects can be established. In the face of many practical issues regarding technical variation in metabolomics studies using isolated mitochondria [34], the statistical selection criteria were set very strictly comparative to the statistical power-lacking small sample groups employed here. The purpose of this was to exclude the possibility of type I errors (false positives) while accepting the loss in information from an increased chance of type II error (falsely excluding positive correlations) [53,54] and thus focus on only the most prominent and abundant intergroup variation in this study.

Metabolic intermediates of significant interest but higher subjectivity to technical variance were thus not able to be quantified, while they are indirectly implicated in many of the implicated pathways. Concurrently, accurate analysis of compartmentalized Glu, Gln, Ser and Asp would deliver excellent insights on the LS pathology as these amino acids are critical intermediates to TCA anaplerosis, transamination reactions, urea cycling, 1C metabolism, biosynthetic pathways, cellular senescence and neurotransmitter metabolism. The quantification of 1C-related transsulfuration and methylation intermediates (Cys, cystathionine, methionine, etc.) would also serve to complement or rule out many of the hypothesized metabolic shifts described here. The methodological advancements published in the late course of this study allow even more targeted mitochondrial immunopurification techniques that promise interrogation of highly specified mitochondrial sub-populations from tissue matrices [46,91], while novel proteomics-based mitochondrial content assays may enable more accurate quantitative studies [92]. Regardless, the outcomes of this study accentuate the ability of sub-cellular metabolomics to further clarify the compartmentalized nature of pathways currently implicated in LS and other RC-related disease. Mitochondrial neuromyopathy research and clinical interventions thus stand to gain much from further targeted in vivo study of compartmentalized metabolic intermediate concentrations and fluxes for these anabolic and bioenergetic pathways.

4. Materials and Methods

4.1. Animals and Sampling

Male mice harboring a homozygous Ndufs4 truncation (KO) were used for this study, along with age- and sex-matched healthy controls (WT). Only males were included in this study to minimize known differences in sex-related metabolic variation which might occlude interpretation of the results [93,94]. KO mice were born from heterozygous crosses (Ndufs4$^{-/+}$; B6.129S4-Ndufs4$^{tm1.1Rpa/J}$) obtained from Jackson Laboratory (JAX stock #027058). Ndufs4 genotypes were confirmed by polymerase chain reaction using tail snips. The animals were bred and housed at the specific pathogen-free unit of the Vivarium (SAVC reg. no. FR15/13458) of the Pre-Clinical Drug Development Platform (PCDDP; NWU, RSA). This study was ethically approved (NWU-00568-19-A5) and governed by the Animal Research Ethics Committee of the NWU. Animals were housed under controlled conditions—temperature (22 ± 1 °C), humidity (55 ± 10%) and light (12:12 h light/dark cycle), with standard laboratory chow (Rodent Breeder, #RM1845, LabChef, Nutritionhub) and water provided ad libitum.

Based on survival curves and phenotypic analyses described in Miller et al. [95], mice of post-natal age of 45–50 days (P45–50) were selected for the study, as they phenotypically resemble the late stage of LS in patients. Mice were euthanized between P45 and 50 via cervical dislocation at the same time of day. Whole-brain and quadriceps femoris tissues were removed and rinsed with ice-cold saline solution (SABAX PBS; 0.9% NaCl (*w*/*v*),

#7634, Adcock Ingram) to remove the surrounding blood and hair. These tissues were immediately processed for mitochondrial isolation.

4.2. Mitochondrial Isolation and Cytosol Preparation

To produce mitochondrial and cytosolic fractions of sufficient purity for metabolomics analysis, fractionated magnetic mitochondrial separation (FMSS) and cytosolic reverse filtration were performed according to a recently established kit-based method [47]. The process was performed at 4 °C using the MACS Mitochondria Extraction Kit for mouse tissue (Miltenyi Biotec) with slight variations from the manufacturer's instructions [79]. Brains (100 mg) and quadriceps muscles (150 mg) were finely cut and homogenized in MACS lysis buffer to produce 10% and 15% (*w*/*v*) homogenates for the brains and muscles, respectively. Brief centrifugation at 1300× *g* (2 min) followed, before the post-nuclear supernatant was diluted 10× (*v*/*v*) in 1× separation buffer (SB).

For magnetic enrichment, mitochondria were labeled with anti-TOM22 microbeads (1.5 and 0.5 µL/mg tissue for brain and muscle samples, respectively) for 1 h at 4 °C. The suspension was loaded onto a magnetized LS column, in a MACS Separator at 4 °C to retain labeled mitochondria. Of the flow-through, regarded as a crude cytoplasm, 2.5 mL was subjected to centrifugal filtering to prepare the cytosolic fraction. Centrisart® 100 kDa centrifugal cut-off filters (#13269E, Sigma Aldrich, St. Louis, MI, USA), accelerated to 2000× *g* for 15 min at 4 °C, were employed for the centrifugal filtering. Labeled mitochondria were eluted from the LS column in 1× SB after removal from the magnet—this was repeated 3× for each sample. Before further analysis, the eluates were centrifuged at 13,000× *g* for 2 min (4 °C), and the mitochondrial pellets were resuspended in 120 µL chromatography-grade water (Burdick & Jackson, Muskegon, MI, USA) containing the selected internal standard (IS) compounds described in Section 4.3.1. The mitochondria isolation procedure took approximately 90 min from tissue homogenization to mitochondrial elution.

4.3. Metabolomics Group Structure and Preparation for Multiplatform Studies

Established untargeted proton nuclear magnetic resonance (^{1}H-NMR) and semi-targeted liquid chromatography-tandem mass spectrometry (LC-MS/MS) metabolomics methodologies [26,49] were applied to each mitochondrial and cytosolic sample produced from the quadriceps and whole-brain homogenates of each Ndufs4 KO (n = 8) or WT (n = 8) animal. To maximize the information gained from the small sample volumes available, samples were first analyzed with ^{1}H-NMR, which requires minimal sample preparation, before preparing and analyzing the recollected samples on LC-MS/MS. All cytosolic samples were analyzed together as a batch on each platform, while the mitochondria were analyzed as their own separate batch on each platform.

4.3.1. Internal Standards and Quality Control Samples

The IS compounds N,N-dimethyl-L-phenylalanine (DMPA; Sigma-Aldrich) and 3-phenylbutyric acid (3-PBA; Sigma-Aldrich) were added during the resuspension of the mitochondrial fractions as described above, while a small volume of the mixed stock solution thereof was added to each cytosolic fraction prior to metabolomics sample preparations to obtain similar concentrations of each IS across all samples. For each batch analyzed, a quality control (QC) sample (consisting of pooled aliquots from each sample therein) was periodically re-analyzed to monitor technical variation, while a single sample composed of pure chemical reference standards for each targeted LC-MS/MS feature was also analyzed at the end of each LC batch to aid metabolite identification. Unless otherwise stated, all solvents used were of chromatography grade or equivalent purity.

4.3.2. Untargeted ^{1}H-NMR Spectroscopy

Mitochondrial and cytosolic samples were prepared according to the recently established miniaturized ^{1}H-NMR protocol [49], as follows: Samples were centrifugally filtered using Centrifree 3 kDa cut-off filters (Merck/Millipore) at 12,000× *g* and room temperature to remove proteins and other macromolecules, before 54 µL filtrate was transferred to a 2 mm NMR tube using the eVol® NMR digital syringe (Sigma-Aldrich). The programmed pipetting sequence added the selected chemical shift standard for ^{1}H-NMR (3-(trimethylsylil)-propionic acid (TSP; Merck/MagniSolv™) in deuterated water (D_2O)), such that a 10:90% ratio of D_2O/H_2O was maintained as per the standard protocol. The 2 mm NMR tube was inserted into the gripper adaptor of the Bruker MATCH system, before each NMR MATCH assembly was loaded onto a SampleXpress autosampler for NMR analysis.

Analysis proceeded at 500 MHz on a Bruker Avance III HD NMR system, equipped with a 5 mm TXI probe head optimized for ^{1}H observation. Briefly, ^{1}H spectra were acquired as 128 transients in 32 K data points with a spectral width of 6000 Hz (12.0 ppm). The H_2O resonance at 4.70 ppm was suppressed using the pulse sequence program NOESY-presat. With the number of dummy scans = 4 and the number of scans = 128, this yielded a run time of 15.75 min per sample. Each sample was automatically shimmed on the deuterium signal, locked, probe tuned and matched and pulse calibrated using Bruker Topspin (V3.5), before further processing was conducted using Bruker AMIX (V3.9.14).

NMR samples were recollected post-analyses for LC-MS/MS preparation, as the employed NMR methodology employed is innately non-destructive. Of the recollected samples, 41 µL of each was transferred to separate microcentrifuge tubes for LC-MS analyses, while the approximately 19 µL remainder was pooled for each tissue matrix (brain and quad cyto, brain and quad mito) to perform additional 2D correlation spectroscopy (COSY) and 2D J-resolved spectroscopy (JRES) to confirm metabolite identification [96].

4.3.3. LC-MS/MS Amino Acid and Acylcarnitine Profiling

LC-MS/MS amino acid and acylcarnitine profiling was performed according to the methodology previously described in [26] for murine model tissue samples—with minor modifications to better suit the post-MACS mitochondrial and cytosolic sample matrices.

To each post-NMR extract (41 µL), an internal standard mixture consisting of several deuterium-labeled versions of selected target compounds (2.5 ppm per compound) was added before LC-MS/MS sample preparation (valine_d8, isoleucine_d10, phenylalanine_d5, lysine_d4, acetylcarnitine_d3, octanoylcarnitine_d3, octadecanoylcarnitine_d3; all from Cambridge Isotope Laboratories). Metabolites were extracted in a molar excess (~300 µL) of acetonitrile at 4 °C (10 min) before 10 min centrifugation (20,000× *g* at 4 °C). The metabolite-containing supernatant was thereafter evaporated under nitrogen gas stream. Metabolites were butylated via a reaction with 4:1 (*v*/*v*) 1-butanol (Sigma-Aldrich)/acetyl chloride (Fluka Analytical) and heatblock incubation at 50 °C for 1 h. Samples were again evaporated under nitrogen stream, before being reconstituted in a final volume of 100 µL water/acetonitrile (50:50, *v*/*v*; Burdick & Jackson) and transferred to 250 µL pulled point glass vial inserts.

The LC-MS/MS system consisted of an Agilent© 2021 series HPLC front end, coupled to an Agilent© 2021 series triple quadrupole mass analyzer with an electrospray ionization (ESI) source, operated in the positive ionization mode. Analytes were separated on a C18 Zorbax SB-Aq reverse phase column (Agilent©, 2.1 mm × 150 mm × 3.5 µm) kept at 30 °C. A sample volume of 2.5 µL was separated using a mobile phase gradient. The chromatographic gradient started at 100% solvent A (water with 0.1% formic acid (Sigma-Aldrich)) and 0% solvent B (acetonitrile with 0.1% formic acid), with a flow of 0.3 mL/min, maintained for 1 min, before ramping to 5% solvent B over 1 min. Thereafter, solvent B was increased to 20% over a period of 2 min, where it was then kept constant for 3 min. Thereafter, it was increased linearly to 100% solvent B over 7 min. Over this period, the flow was linearly increased to 0.35 mL/min (between 14 and 14.1 min). After maintaining

these conditions for 5 min, the gradient was decreased to 5% solvent B at 19.5 min and kept constant for 1.5 min. A post-run of 8 min was allowed to ensure equilibration of the column between samples, capping the 29 min total run time. The ESI source gas (nitrogen) temperature was kept at 300 °C, with a flow rate of 7.5 L/min. Nebulizer pressure was kept at 30 psi, and the capillary voltage at 3500 V. The Agilent© MassHunter Workstation Software (v B09.00) was used for data acquisition and extraction.

4.3.4. Data Processing

Spectral data were extracted into matrices, where an extra NMR data matrix reporting only the untargeted spectral bin sums for each sample was also extracted for calculation of a total useful NMR signal (NMR-TUS) normalization factor, as none of the selected IS compounds could accurately represent the variance due to pre-metabolomics tissue sampling and MACS isolation procedures. All datasets were individually inspected for data quality, through correct peak picking, alignment and batch precision (Figure 2) as IS and QC coefficients of variance (CV%), and preprocessed (50% QC-CV% filtering, missing value imputation via randomized ¼ minimum area replacement and normalization).

Metabolites were normalized to tissue mass through normalization with NMR-TUS as the most applicable factor for the data reported here (Figures S2 and S3). For LC-MS/MS data, metabolites were normalized to their own isotope (where possible) or the isotope showing the strongest linear correlation thereto, based on the analyte peak area (Pearson's r correlation analyses) prior to the above-mentioned normalizations. No significant batch effects were evident; thus, no batch corrections were performed.

Finally, data pretreatment (glog transformation and Pareto scaling) and outlier detection (PCA Hotelling's T2 ellipses, loadings plot and biplots) were conducted. Data processing was conducted using Excel 2013 (Microsoft), SPSS Statistics (v.25.0; IBM) and MetaboAnalyst 5.0 [97]. The metabolomics data obtained in this study (file name: Gunter007dekok_20210916_012612) can be accessed at the Common Fund's National Metabolomics Data Repository (NMDR) website, the Metabolomics Workbench (https://www.metabolomicsworkbench.org (accessed on 18 September 2021), where it has been assigned the Data Track ID 2843

4.3.5. Statistical Analyses

Univariate analyses were used to determine significant discriminatory features between Ndufs4 KO and WT sub-cellular metabolic profiles. Comparisons were performed between genotypes (WT vs. KO) in each separate tissue compartment dataset only, with only the results of these tests being compared between compartments and tissues.

An independent, two-sample Student *t*-test was carried out on the unpretreated, NMR-TUS-normalized datasets to identify compounds with significantly altered intensities between diseased mice and controls (VIPs). In line with power calculations performed (G* Power 3; Universität Dusseldorf) at the inception of this study, a t-statistic with a *p*-value of <0.1 was considered statistically significant, while effect sizes (Cohen's D value; D) of ≥1.0 were considered practically significant and used complimentary to the *t*-test [48]. Principal component analysis (PCA) and partial least squares discriminant analyses (PLS-DA) were used to visually investigate the clustering, covariance and discriminatory power of the univariately selected VIPs. This was performed in MetaboAnalyst 5.0 [97] on a log-transformed and Pareto-scaled dataset comprising only the important metabolites identified on each platform.

Dataset features were identified via spectral and retention time matching using the analyzed pure chemical reference standards, and commercial and in-house spectral libraries together with public databases and metabolite identities were assigned to spectral features, all with the highest (Level 1) confidence [39,40].

Supplementary Materials: The following are available online at www.mdpi.com/article/10.3390/metabo11100658/s1: Table S1: Positively detected features and measurement stability;

Figures S1 and S2: Comparison of selected data normalization factors for LC-MS/MS and NMR batches, respectively; Figure S3: PLS-DA group separation based on selected VIPs; Figures S4 and S5: Additional VIP feature boxplots for brain and quadriceps groups, respectively.

Author Contributions: Conceptualization, R.L. and G.v.d.W.; methodology, R.L., G.v.d.W., S.M. and J.Z.L.; software, G.v.d.W. and S.M.; formal analysis and investigation, G.v.d.W., S.M. and R.L.; data curation, G.V, R.L., S.M. and J.Z.L.; writing—original draft preparation, G.v.d.W.; writing—review and editing, R.L., S.M., J.Z.L. and G.v.d.W.; supervision, R.L.; project administration and funding acquisition, R.L. All authors have read and agreed to the published version of the manuscript.

Funding: This research was funded by the South African Department of Science and Technology via two of its funding mechanisms, namely, the National Research Foundation of South Africa (NRF; grant numbers 92736 and 117424), and the Technological Innovation Agency (TIA; grant number Metabol.01). Opinions expressed and conclusions arrived at are those of the authors and are not necessarily to be attributed to the NRF or the TIA.

Institutional Review Board Statement: This study was conducted according to the appropriate South African guidelines for pre-clinical research on laboratory-bred animals and approved by the institutional animal research ethics committee (REC), AnimCare REC, of the North-West University (NWU-000568-19-S5, as approved on 23 July 2019).

Informed Consent Statement: Not applicable.

Data Availability Statement: The metabolomics data obtained in this study can be accessed at the Common Fund's National Metabolomics Data Repository (NMDR) website, the Metabolomics Workbench (https://www.metabolomicsworkbench.org (accessed on 18 September 2021), where it has been assigned the Data track ID: 2843, and the file name Gunter007dekok_20210916_012612.

Acknowledgments: The authors greatly thank the PCDDP Vivarium personnel on campus, as well as Francois van der Westhuizen and Marianne Pretorius for their assistance in sample collection during the initial waves of the pandemic, and Daneel Nel for her assistance in genotype confirmation and data processing. Many thanks to Peet Jansen van Rensburg for supplying the MassHunter software and critical technical assistance during LC-MS/MS analyses, as well as Luciano Willemse and Tiaan van Zyl for their assistance during ^{1}H-NMR sample preparation.

Conflicts of Interest: The authors declare no conflict of interest. The funders had no role in the design of the study; in the collection, analyses or interpretation of data; in the writing of the manuscript, or in the decision to publish the results.

References

1. Nunnari, J.; Suomalainen, A. Mitochondria: In sickness and in health. *Cell* **2012**, *148*, 1145–1159, doi:10.1016/j.cell.2012.02.035.
2. Shaughnessy, D.T.; McAllister, K.; Worth, L.; Haugen, A.C.; Meyer, J.N.; Domann, F.E.; Houten, B.V.; Mostoslavsky, R.; Bultman, S.J.; Baccarelli, A.A.; et al. Mitochondria, Energetics, Epigenetics, and Cellular Responses to Stress. *Environ. Health Perspect.* **2014**, *122*, 1271–1278, doi:doi:10.1289/ehp.1408418.
3. Aouacheria, A.; Baghdiguian, S.; Lamb, H.M.; Huska, J.D.; Pineda, F.J.; Hardwick, J.M. Connecting mitochondrial dynamics and life-or-death events via Bcl-2 family proteins. *Neurochem. Int.* **2017**, *109*, 141–161, https://doi.org/10.1016/j.neuint.2017.04.009.
4. Quirós, P.M.; Mottis, A.; Auwerx, J. Mitonuclear communication in homeostasis and stress. *Nat. Rev. Mol. Cell Biol.* **2016**, *17*, 213–226, doi:10.1038/nrm.2016.23.
5. Wasilewski, M.; Chojnacka, K.; Chacinska, A. Protein trafficking at the crossroads to mitochondria. *Biochim. Biophys. Acta Mol. Cell Res* **2017**, *1864*, 125–137, doi:10.1016/j.bbamcr.2016.10.019.
6. Eysert, F.; Kinoshita, P.F.; Mary, A.; Vaillant-Beuchot, L.; Checler, F.; Chami, M. Molecular Dysfunctions of Mitochondria-Associated Membranes (MAMs) in Alzheimer's Disease. *Int. J. Mol. Sci.* **2020**, *21*, 9521, doi:10.3390/ijms21249521.
7. Wallace, D.C. Mitochondria and cancer. *Nat. Rev. Cancer* **2012**, *12*, 685–698, doi:10.1038/nrc3365.
8. Saleh, J.; Peyssonnaux, C.; Singh, K.K.; Edeas, M. Mitochondria and microbiota dysfunction in COVID-19 pathogenesis. *Mitochondrion* **2020**, *54*, 1–7.
9. Stepien, K.M.; Heaton, R.; Rankin, S.; Murphy, A.; Bentley, J.; Sexton, D.; Hargreaves, I.P. Evidence of Oxidative Stress and Secondary Mitochondrial Dysfunction in Metabolic and Non-Metabolic Disorders. *J. Clin. Med.* **2017**, *6*, 71, doi:10.3390/jcm6070071.
10. Ylikallio, E.; Suomalainen, A. Mechanisms of mitochondrial diseases. *Ann. Med.* **2012**, *44*, 41–59, doi:10.3109/07853890.2011.598547.
11. Craven, L.; Alston, C.L.; Taylor, R.W.; Turnbull, D.M. Recent advances in mitochondrial disease. *Annu. Rev. Genom. Hum. Genet.* **2017**, *18*, 257–275.

12. Triepels, R.; Van Den Heuvel, L.; Trijbels, J.; Smeitink, J. Respiratory chain complex I deficiency. *Am. J. Med. Genet.* **2001**, *106*, 37–45.
13. Ghezzi, D.; Zeviani, M. Human diseases associated with defects in assembly of OXPHOS complexes. *Essays Biochem.* **2018**, *62*, 271–286.
14. Lake, N.J.; Bird, M.J.; Isohanni, P.; Paetau, A. Leigh syndrome: Neuropathology and pathogenesis. *J. Neuropathol. Exp. Neurol.* **2015**, *74*, 482–492, doi:10.1097/NEN.0000000000000195.
15. Quintana, A.; Kruse, S.E.; Kapur, R.P.; Sanz, E.; Palmiter, R.D. Complex I deficiency due to loss of Ndufs4 in the brain results in progressive encephalopathy resembling Leigh syndrome. *Proc. Natl. Acad. Sci. USA* **2010**, *107*, 10996–11001, doi:10.1073/pnas.1006214107.
16. Newgard, C.B. Metabolomics and Metabolic Diseases: Where Do We Stand? *Cell Metab.* **2017**, *25*, 43–56, doi:10.1016/j.cmet.2016.09.018.
17. Priori, R.; Scrivo, R.; Brandt, J.; Valerio, M.; Casadei, L.; Valesini, G.; Manetti, C. Metabolomics in rheumatic diseases: The potential of an emerging methodology for improved patient diagnosis, prognosis, and treatment efficacy. *Autoimmun. Rev.* **2013**, *12*, 1022–1030, doi:10.1016/j.autrev.2013.04.002.
18. Nagrath, D.; Caneba, C.; Karedath, T.; Bellance, N. Metabolomics for mitochondrial and cancer studies. *Biochim. Biophys. Acta* **2011**, *1807*, 650–663, doi:10.1016/j.bbabio.2011.03.006.
19. Kruse, S.E.; Watt, W.C.; Marcinek, D.J.; Kapur, R.P.; Schenkman, K.A.; Palmiter, R.D. Mice with mitochondrial complex I deficiency develop a fatal encephalomyopathy. *Cell Metab.* **2008**, *7*, 312–320, doi:10.1016/j.cmet.2008.02.004.
20. Leong, D.W.; Komen, J.C.; Hewitt, C.A.; Arnaud, E.; McKenzie, M.; Phipson, B.; Bahlo, M.; Laskowski, A.; Kinkel, S.A.; Davey, G.M.; et al. Proteomic and metabolomic analyses of mitochondrial complex I-deficient mouse model generated by spontaneous B2 short interspersed nuclear element (SINE) insertion into NADH dehydrogenase (ubiquinone) Fe-S protein 4 (Ndufs4) gene. *J. Biol. Chem.* **2012**, *287*, 20652–20663, doi:10.1074/jbc.M111.327601.
21. Esterhuizen, K.; van der Westhuizen, F.H.; Louw, R. Metabolomics of mitochondrial disease. *Mitochondrion* **2017**, *35*, 97–110, doi:10.1016/j.mito.2017.05.012.
22. Johnson, S.C.; Yanos, M.E.; Kayser, E.B.; Quintana, A.; Sangesland, M.; Castanza, A.; Uhde, L.; Hui, J.; Wall, V.Z.; Gagnidze, A.; et al. mTOR inhibition alleviates mitochondrial disease in a mouse model of Leigh syndrome. *Science* **2013**, *342*, 1524–1528, doi:10.1126/science.1244360.
23. Johnson, S.C.; Kayser, E.B.; Bornstein, R.; Stokes, J.; Bitto, A.; Park, K.Y.; Pan, A.; Sun, G.; Raftery, D.; Kaeberlein, M.; et al. Regional metabolic signatures in the Ndufs4(KO) mouse brain implicate defective glutamate/alpha-ketoglutarate metabolism in mitochondrial disease. *Mol. Genet. Metab.* **2020**, *130*, 118–132, doi:10.1016/j.ymgme.2020.03.007.
24. Terburgh, K.; Coetzer, J.; Lindeque, J.Z.; van der Westhuizen, F.H.; Louw, R. Aberrant BCAA and glutamate metabolism linked to regional neurodegeneration in a mouse model of Leigh syndrome. *Biochim. Biophys. Acta Mol. Basis Dis.* **2021**, *1867*, 166082, doi:10.1016/j.bbadis.2021.166082.
25. Emmerzaal, T.L.; Preston, G.; Geenen, B.; Verweij, V.; Wiesmann, M.; Vasileiou, E.; Gruter, F.; de Groot, C.; Schoorl, J.; de Veer, R.; et al. Impaired mitochondrial complex I function as a candidate driver in the biological stress response and a concomitant stress-induced brain metabolic reprogramming in male mice. *Transl. Psychiatry* **2020**, *10*, 176, doi:10.1038/s41398-020-0858-y.
26. Terburgh, K.; Lindeque, Z.; Mason, S.; van der Westhuizen, F.; Louw, R. Metabolomics of *Ndufs4*$^{-/-}$ skeletal muscle: Adaptive mechanisms converge at the ubiquinone-cycle. *Biochim. Biophys. Acta Mol. Basis Dis.* **2019**, *1865*, 98–106, doi:10.1016/j.bbadis.2018.10.034.
27. Finsterer, J. Leigh and Leigh-like syndrome in children and adults. *Pediatr. Neurol.* **2008**, *39*, 223–235, doi:10.1016/j.pediatrneurol.2008.07.013.
28. Khan, N.A.; Nikkanen, J.; Yatsuga, S.; Jackson, C.; Wang, L.; Pradhan, S.; Kivela, R.; Pessia, A.; Velagapudi, V.; Suomalainen, A. mTORC1 Regulates Mitochondrial Integrated Stress Response and Mitochondrial Myopathy Progression. *Cell Metab.* **2017**, *26*, 419–428 e415, doi:10.1016/j.cmet.2017.07.007.
29. Liu, L.; MacKenzie, K.R.; Putluri, N.; Maletić-Savatić, M.; Bellen, H.J. The Glia-Neuron Lactate Shuttle and Elevated ROS Promote Lipid Synthesis in Neurons and Lipid Droplet Accumulation in Glia via APOE/D. *Cell Metab.* **2017**, *26*, 719–737.e6, doi:10.1016/j.cmet.2017.08.024.
30. Mason, S. Lactate Shuttles in Neuroenergetics—Homeostasis, Allostasis and Beyond. *Front. Neurosci.* **2017**, *11*, 43, doi:10.3389/fnins.2017.00043.
31. Schiaffino, S.; Reggiani, C. Fiber types in mammalian skeletal muscles. *Physiol. Rev.* **2011**, *91*, 1447–1531, doi:10.1152/physrev.00031.2010.
32. Johnson, M.A.; Vidoni, S.; Durigon, R.; Pearce, S.F.; Rorbach, J.; He, J.; Brea-Calvo, G.; Minczuk, M.; Reyes, A.; Holt, I.J.; et al. Amino acid starvation has opposite effects on mitochondrial and cytosolic protein synthesis. *PLoS ONE* **2014**, *9*, e93597, doi:10.1371/journal.pone.0093597.
33. Tyynismaa, H.; Carroll, C.J.; Raimundo, N.; Ahola-Erkkila, S.; Wenz, T.; Ruhanen, H.; Guse, K.; Hemminki, A.; Peltola-Mjosund, K.E.; Tulkki, V.; et al. Mitochondrial myopathy induces a starvation-like response. *Hum. Mol. Genet.* **2010**, *19*, 3948–3958, doi:10.1093/hmg/ddq310.
34. Liu, X.; Xu, G. Recent advances in using mass spectrometry for mitochondrial metabolomics and lipidomics—A review. *Anal. Chim. Acta* **2018**, *1037*, 3–12, doi:10.1016/j.aca.2017.11.080.
35. Palmieri, F. The mitochondrial transporter family SLC25: Identification, properties and physiopathology. *Mol. Asp. Med.* **2013**, *34*, 465–484, doi:10.1016/j.mam.2012.05.005.

36. Hewton, K.G.; Johal, A.S.; Parker, S.J. Transporters at the Interface between Cytosolic and Mitochondrial Amino Acid Metabolism. *Metabolites* **2021**, *11*, 112, doi:10.3390/metabo11020112.
37. Kaasik, A.; Safiulina, D.; Zharkovsky, A.; Veksler, V. Regulation of mitochondrial matrix volume. *Am. J. Physiol. Cell Physiol.* **2007**, *292*, C157–C163, doi:10.1152/ajpcell.00272.2006.
38. Wiechert, W. 13C metabolic flux analysis. *Metab. Eng.* **2001**, *3*, 195–206, doi:10.1006/mben.2001.0187.
39. Gravel, S.P.; Andrzejewski, S.; Avizonis, D.; St-Pierre, J. Stable isotope tracer analysis in isolated mitochondria from mammalian systems. *Metabolites* **2014**, *4*, 166–183, doi:10.3390/metabo4020166.
40. Roede, J.R.; Park, Y.; Li, S.; Strobel, F.H.; Jones, D.P. Detailed mitochondrial phenotyping by high resolution metabolomics. *PLoS ONE* **2012**, *7*, e33020, doi:10.1371/journal.pone.0033020.
41. Goodman, R.P.; Calvo, S.E.; Mootha, V.K. Spatiotemporal compartmentalization of hepatic NADH and NADPH metabolism. *J. Biol. Chem.* **2018**, *293*, 7508–7516, doi:10.1074/jbc.TM117.000258.
42. Go, Y.M.; Roede, J.R.; Orr, M.; Liang, Y.; Jones, D.P. Integrated redox proteomics and metabolomics of mitochondria to identify mechanisms of cd toxicity. *Toxicol. Sci.* **2014**, *139*, 59–73, doi:10.1093/toxsci/kfu018.
43. Kiebish, M.A.; Han, X.; Cheng, H.; Seyfried, T.N. In vitro growth environment produces lipidomic and electron transport chain abnormalities in mitochondria from non-tumorigenic astrocytes and brain tumours. *ASN Neuro* **2009**, *1*, AN20090011, doi:10.1042/AN20090011.
44. Chen, W.W.; Freinkman, E.; Wang, T.; Birsoy, K.; Sabatini, D.M. Absolute Quantification of Matrix Metabolites Reveals the Dynamics of Mitochondrial Metabolism. *Cell* **2016**, *166*, 1324–1337.e11, doi:10.1016/j.cell.2016.07.040.
45. Pan, D.; Lindau, C.; Lagies, S.; Wiedemann, N.; Kammerer, B. Metabolic profiling of isolated mitochondria and cytoplasm reveals compartment-specific metabolic responses. *Metabolomics* **2018**, *14*, 59, doi:10.1007/s11306-018-1352-x.
46. Bayraktar, E.C.; Baudrier, L.; Ozerdem, C.; Lewis, C.A.; Chan, S.H.; Kunchok, T.; Abu-Remaileh, M.; Cangelosi, A.L.; Sabatini, D.M.; Birsoy, K.; et al. MITO-Tag Mice enable rapid isolation and multimodal profiling of mitochondria from specific cell types in vivo. *Proc. Natl. Acad. Sci. USA* **2019**, *116*, 303–312, doi:10.1073/pnas.1816656115.
47. van der Walt, G.; Louw, R. Novel mitochondrial and cytosolic purification pipeline for compartment-specific metabolomics in mammalian disease model tissues. *Metabolomics* **2020**, *16*, 78, doi:10.1007/s11306-020-01697-9.
48. Faul, F.; Erdfelder, E.; Lang, A.-G.; Buchner, A. G* Power 3: A flexible statistical power analysis program for the social, behavioral, and biomedical sciences. *Behav. Res. Methods* **2007**, *39*, 175–191.
49. Mason, S.; Terburgh, K.; Louw, R. Miniaturized ^{1}H-NMR method for analyzing limited-quantity samples applied to a mouse model of Leigh disease. *Metabolomics* **2018**, *14*, 74, doi:10.1007/s11306-018-1372-6.
50. Mels, C.; Jansen van Rensburg, P.; van der Westhuizen, F.H.; Pretorius, P.J.; Erasmus, E. Increased excretion of C4-carnitine species after a therapeutic acetylsalicylic acid dose: Evidence for an inhibitory effect on short-chain fatty acid metabolism. *Int. Sch. Res. Not.* **2011**, *2011*, 851870.
51. Dunn, W.B.; Wilson, I.D.; Nicholls, A.W.; Broadhurst, D. The importance of experimental design and QC samples in large-scale and MS-driven untargeted metabolomic studies of humans. *Bioanalysis* **2012**, *4*, 2249–2264.
52. US FDA. *Guidance for Industry: Bioanalytical Method Validation*; US Department of Health and Human Services, Food and Drug Administration, Center for Drug Evaluation and Research (CDER), Center for Veterinary Medicine (CV): Rockville, MD, USA, 2001.
53. Vinaixa, M.; Samino, S.; Saez, I.; Duran, J.; Guinovart, J.J.; Yanes, O. A Guideline to Univariate Statistical Analysis for LC/MS-Based Untargeted Metabolomics-Derived Data. *Metabolites* **2012**, *2*, 775–795, doi:10.3390/metabo2040775.
54. Akobeng, A.K. Understanding type I and type II errors, statistical power and sample size. *Acta Paediatr.* **2016**, *105*, 605–609, doi:10.1111/apa.13384.
55. Bifari, F.; Nisoli, E. Branched-chain amino acids differently modulate catabolic and anabolic states in mammals: A pharmacological point of view. *Br. J. Pharmacol.* **2017**, *174*, 1366–1377, doi:10.1111/bph.13624.
56. Arany, Z.; Neinast, M. Branched Chain Amino Acids in Metabolic Disease. *Curr. Diabetes Rep.* **2018**, *18*, 76, doi:10.1007/s11892-018-1048-7.
57. Oka, K.; Ohya-Shimada, W.; Mizuno, S.; Nakamura, T. Up-regulation of cyclin-E1 via proline-mTOR pathway is responsible for HGF-mediated G1/S progression in the primary culture of rat hepatocytes. *Biochem. Biophys. Res. Commun.* **2013**, *435*, 120–125, https://doi.org/10.1016/j.bbrc.2013.04.052.
58. Krishnan, N.; Dickman, M.B.; Becker, D.F. Proline modulates the intracellular redox environment and protects mammalian cells against oxidative stress. *Free Radic. Biol. Med.* **2008**, *44*, 671–681, https://doi.org/10.1016/j.freeradbiomed.2007.10.054.
59. McDonald, A.E.; Pichaud, N.; Darveau, C.A. "Alternative" fuels contributing to mitochondrial electron transport: Importance of non-classical pathways in the diversity of animal metabolism. *Comp. Biochem. Physiol. B Biochem. Mol. Biol.* **2018**, *224*, 185–194, doi:10.1016/j.cbpb.2017.11.006.
60. Razak, M.A.; Begum, P.S.; Viswanath, B.; Rajagopal, S. Multifarious Beneficial Effect of Nonessential Amino Acid, Glycine: A Review. *Oxidative Med. Cell. Longev.* **2017**, *2017*, 1716701, doi:10.1155/2017/1716701.
61. Wang, W.; Wu, Z.; Dai, Z.; Yang, Y.; Wang, J.; Wu, G. Glycine metabolism in animals and humans: Implications for nutrition and health. *Amino Acids* **2013**, *45*, 463–477.
62. Yang, L.; Garcia Canaveras, J.C.; Chen, Z.; Wang, L.; Liang, L.; Jang, C.; Mayr, J.A.; Zhang, Z.; Ghergurovich, J.M.; Zhan, L.; et al. Serine Catabolism Feeds NADH when Respiration Is Impaired. *Cell Metab.* **2020**, *31*, 809–821.e6, doi:10.1016/j.cmet.2020.02.017.

63. Ducker, G.S.; Rabinowitz, J.D. One-Carbon Metabolism in Health and Disease. *Cell Metab.* **2017**, *25*, 27–42, doi:10.1016/j.cmet.2016.08.009.
64. Chen, Q.; Kirk, K.; Shurubor, Y.I.; Zhao, D.; Arreguin, A.J.; Shahi, I.; Valsecchi, F.; Primiano, G.; Calder, E.L.; Carelli, V. Rewiring of glutamine metabolism is a bioenergetic adaptation of human cells with mitochondrial DNA mutations. *Cell Metab.* **2018**, *27*, 1007–1025.e5.
65. Son, S.M.; Park, S.J.; Stamatakou, E.; Vicinanza, M.; Menzies, F.M.; Rubinsztein, D.C. Leucine regulates autophagy via acetylation of the mTORC1 component raptor. *Nat. Commun.* **2020**, *11*, 3148, doi:10.1038/s41467-020-16886-2.
66. Phang, J.M. Proline Metabolism in Cell Regulation and Cancer Biology: Recent Advances and Hypotheses. *Antioxid. Redox Signal.* **2019**, *30*, 635–649, doi:10.1089/ars.2017.7350.
67. Brooks, G.A. Lactate as a fulcrum of metabolism. *Redox Biol.* **2020**, *35*, 101454, doi:10.1016/j.redox.2020.101454.
68. Passarella, S.; de Bari, L.; Valenti, D.; Pizzuto, R.; Paventi, G.; Atlante, A. Mitochondria and L-lactate metabolism. *FEBS Lett.* **2008**, *582*, 3569–3576, doi:10.1016/j.febslet.2008.09.042.
69. Young, A.; Oldford, C.; Mailloux, R.J. Lactate dehydrogenase supports lactate oxidation in mitochondria isolated from different mouse tissues. *Redox Biol.* **2020**, *28*, 101339.
70. Karamanlidis, G.; Lee, C.F.; Garcia-Menendez, L.; Kolwicz, S.C., Jr.; Suthammarak, W.; Gong, G.; Sedensky, M.M.; Morgan, P.G.; Wang, W.; Tian, R. Mitochondrial complex I deficiency increases protein acetylation and accelerates heart failure. *Cell Metab.* **2013**, *18*, 239–250, doi:10.1016/j.cmet.2013.07.002.
71. Schlattner, U.; Tokarska-Schlattner, M.; Wallimann, T. Mitochondrial creatine kinase in human health and disease. *Biochim. Biophys. Acta* **2006**, *1762*, 164–180, doi:10.1016/j.bbadis.2005.09.004.
72. Schwörer, S.; Berisa, M.; Violante, S.; Qin, W.; Zhu, J.; Hendrickson, R.C.; Cross, J.R.; Thompson, C.B. Proline biosynthesis is a vent for TGFβ-induced mitochondrial redox stress. *EMBO J.* **2020**, *39*, e103334, doi:10.15252/embj.2019103334.
73. Sarabhai, T.; Roden, M. Hungry for your alanine: When liver depends on muscle proteolysis. *J. Clin. Investig.* **2019**, *129*, 4563–4566, doi:10.1172/JCI131931.
74. Holeček, M. Histidine in Health and Disease: Metabolism, Physiological Importance, and Use as a Supplement. *Nutrients* **2020**, *12*, 848, doi:10.3390/nu12030848.
75. Cui, P.; Shao, W.; Huang, C.; Wu, C.-J.; Jiang, B.; Lin, D. Metabolic derangements of skeletal muscle from a murine model of glioma cachexia. *Skelet. Muscle* **2019**, *9*, 3, doi:10.1186/s13395-018-0188-4.
76. Ross-Inta, C.; Tsai, C.Y.; Giulivi, C. The mitochondrial pool of free amino acids reflects the composition of mitochondrial DNA-encoded proteins: Indication of a post- translational quality control for protein synthesis. *Biosci. Rep.* **2008**, *28*, 239–249, doi:10.1042/BSR20080090.
77. Mathuthu, E.; Janse van Rensburg, A.; Du Plessis, D.; Mason, S. EDTA as a chelating agent in quantitative 1H-NMR of biologically important ions. *Biochem. Cell Biol.* **2021**, *99*, 465-475, doi:10.1139/bcb-2020-0543.
78. Hafer, E.; Holzgrabe, U.; Kraus, K.; Adams, K.; Hook, J.M.; Diehl, B. Qualitative and quantitative ^{1}H NMR spectroscopy for determination of divalent metal cation concentration in model salt solutions, food supplements, and pharmaceutical products by using EDTA as chelating agent. *Magn. Reson. Chem.* **2020**, *58*, 653–665, doi:10.1002/mrc.5009.
79. Hornig-Do, H.T.; Gunther, G.; Bust, M.; Lehnartz, P.; Bosio, A.; Wiesner, R.J. Isolation of functional pure mitochondria by superparamagnetic microbeads. *Anal. Biochem.* **2009**, *389*, 1–5, doi:10.1016/j.ab.2009.02.040.
80. Koshenov, Z.; Oflaz, F.E.; Hirtl, M.; Pilic, J.; Bachkoenig, O.A.; Gottschalk, B.; Madreiter-Sokolowski, C.T.; Rost, R.; Malli, R.; Graier, W.F. Sigma-1 Receptor Promotes Mitochondrial Bioenergetics by Orchestrating ER Ca^{2+} Leak during Early ER Stress. *Metabolites* **2021**, *11*, 422, doi:10.3390/metabo11070422.
81. Barbagallo, M.; Veronese, N.; Dominguez, L.J. Magnesium in Aging, Health and Diseases. *Nutrients* **2021**, *13*, 463, doi:10.3390/nu13020463.
82. Huskisson, E.; Maggini, S.; Ruf, M. The role of vitamins and minerals in energy metabolism and well-being. *J. Int. Med. Res.* **2007**, *35*, 277–289.
83. Heidari, R.; Ahmadi, A.; Mohammadi, H.; Ommati, M.M.; Azarpira, N.; Niknahad, H. Mitochondrial dysfunction and oxidative stress are involved in the mechanism of methotrexate-induced renal injury and electrolytes imbalance. *Biomed. Pharmacother.* **2018**, *107*, 834–840.
84. Alam, M.T.; Manjeri, G.R.; Rodenburg, R.J.; Smeitink, J.A.; Notebaart, R.A.; Huynen, M.; Willems, P.H.; Koopman, W.J. Skeletal muscle mitochondria of NDUFS4$^{-/-}$ mice display normal maximal pyruvate oxidation and ATP production. *Biochim. Biophys. Acta* **2015**, *1847*, 526–533, doi:10.1016/j.bbabio.2015.02.006.
85. Bonilla, D.A.; Kreider, R.B.; Stout, J.R.; Forero, D.A.; Kerksick, C.M.; Roberts, M.D.; Rawson, E.S. Metabolic Basis of Creatine in Health and Disease: A Bioinformatics-Assisted Review. *Nutrients* **2021**, *13*, 1238, doi:10.3390/nu13041238.
86. Lewis, C.A.; Parker, S.J.; Fiske, B.P.; McCloskey, D.; Gui, D.Y.; Green, C.R.; Vokes, N.I.; Feist, A.M.; Vander Heiden, M.G.; Metallo, C.M. Tracing compartmentalized NADPH metabolism in the cytosol and mitochondria of mammalian cells. *Mol. Cell* **2014**, *55*, 253–263, doi:10.1016/j.molcel.2014.05.008.
87. Szibor, M.; Gizatullina, Z.; Gainutdinov, T.; Endres, T.; Debska-Vielhaber, G.; Kunz, M.; Karavasili, N.; Hallmann, K.; Schreiber, F.; Bamberger, A.; et al. Cytosolic, but not matrix, calcium is essential for adjustment of mitochondrial pyruvate supply. *J. Biol. Chem.* **2020**, *295*, 4383–4397, doi:10.1074/jbc.RA119.011902.
88. Yudkoff, M. Interactions in the Metabolism of Glutamate and the Branched-Chain Amino Acids and Ketoacids in the CNS. *Neurochem. Res.* **2017**, *42*, 10–18, doi:10.1007/s11064-016-2057-z.

89. Neurauter, G.; Schrocksnadel, K.; Scholl-Burgi, S.; Sperner-Unterweger, B.; Schubert, C.; Ledochowski, M.; Fuchs, D. Chronic immune stimulation correlates with reduced phenylalanine turnover. *Curr. Drug Metab.* **2008**, *9*, 622–627, doi:10.2174/138920008785821738.
90. Nikkanen, J.; Forsstrom, S.; Euro, L.; Paetau, I.; Kohnz, R.A.; Wang, L.; Chilov, D.; Viinamaki, J.; Roivainen, A.; Marjamaki, P.; et al. Mitochondrial DNA Replication Defects Disturb Cellular dNTP Pools and Remodel One-Carbon Metabolism. *Cell Metab.* **2016**, *23*, 635–648, doi:10.1016/j.cmet.2016.01.019.
91. Hubbard, W.B.; Harwood, C.L.; Prajapati, P.; Springer, J.E.; Saatman, K.E.; Sullivan, P.G. Fractionated mitochondrial magnetic separation for isolation of synaptic mitochondria from brain tissue. *Sci. Rep.* **2019**, *9*, 9656, doi:10.1038/s41598-019-45568-3.
92. McLaughlin, K.L.; Hagen, J.T.; Coalson, H.S.; Nelson, M.A.M.; Kew, K.A.; Wooten, A.R.; Fisher-Wellman, K.H. Novel approach to quantify mitochondrial content and intrinsic bioenergetic efficiency across organs. *Sci. Rep.* **2020**, *10*, 17599, doi:10.1038/s41598-020-74718-1.
93. Ruoppolo, M.; Caterino, M.; Albano, L.; Pecce, R.; Di Girolamo, M.G.; Crisci, D.; Costanzo, M.; Milella, L.; Franconi, F.; Campesi, I. Targeted metabolomic profiling in rat tissues reveals sex differences. *Sci. Rep.* **2018**, *8*, 1–12.
94. Wells, A.; Barrington, W.; Threadgill, D.; Dearth, S.; Campagna, S.; Saxton, A.; Voy, B. Gene, Sex and Diet Interact to Control the Tissue Metabolome. *FASEB J.* **2016**, *30*, 127.2-127.2.
95. Miller, H.C.; Louw, R.; Mereis, M.; Venter, G.; Boshoff, J.-D.; Mienie, L.; Van Reenen, M.; Venter, M.; Lindeque, J.Z.; Domínguez-Martínez, A. Metallothionein 1 overexpression does not protect against mitochondrial disease pathology in *Ndufs4* knockout mice. *Mol. Neurobiol.* **2021**, *58*, 243–262.
96. Dona, A.C.; Kyriakides, M.; Scott, F.; Shephard, E.A.; Varshavi, D.; Veselkov, K.; Everett, J.R. A guide to the identification of metabolites in NMR-based metabonomics/metabolomics experiments. *Comput. Struct. Biotechnol. J.* **2016**, *14*, 135–153.
97. Pang, Z.; Chong, J.; Zhou, G.; de Lima Morais, D.A.; Chang, L.; Barrette, M.; Gauthier, C.; Jacques, P.-É.; Li, S.; Xia, J. MetaboAnalyst 5.0: Narrowing the gap between raw spectra and functional insights. *Nucleic Acids Res.* **2021**, *49*, W388–W396, doi:10.1093/nar/gkab382.

REFERENCES

Acin-Perez, R. & Enriquez, J.A. 2014. The function of the respiratory supercomplexes: the plasticity model. *Biochimica et Biophysica Acta (BBA) - Bioenergetics*, 1837(4):444-450. doi:10.1016/j.bbabio.2013.12.009

Adjobo-Hermans, M.J.W., de Haas, R., Willems, P., Wojtala, A., van Emst-de Vries, S.E., Wagenaars, J.A., van den Brand, M., Rodenburg, R.J., Smeitink, J.A.M., Nijtmans, L.G., Sazanov, L.A., Wieckowski, M.R. & Koopman, W.J.H. 2020. NDUFS4 deletion triggers loss of NDUFA12 in Ndufs4(-/-) mice and Leigh syndrome patients: A stabilizing role for NDUFAF2. *Biochimica et Biophysica Acta (BBA) - Bioenergetics*, 1861(8):148213. doi:10.1016/j.bbabio.2020.148213

Afanasyeva, M.A., Ustiugova, A.S., Golyshev, S.A., Kopylov, A.T., Bogolyubova, A.V., Demin, D.E., Belousov, P.V. & Schwartz, A.M. 2018. Isolation of Large Amounts of Highly Pure Mitochondria for "Omics" Studies. *Biochemistry (Moscow)*, 83(1):76-85. doi:10.1134/S0006297918010108

Akobeng, A.K. 2016. Understanding type I and type II errors, statistical power and sample size. *Acta Paediatrica*, 105(6):605-609. doi:10.1111/apa.13384

Alam, M.T., Manjeri, G.R., Rodenburg, R.J., Smeitink, J.A., Notebaart, R.A., Huynen, M., Willems, P.H. & Koopman, W.J. 2015. Skeletal muscle mitochondria of NDUFS4-/- mice display normal maximal pyruvate oxidation and ATP production. *Biochimica et Biophysica Acta (BBA) - Bioenergetics*, 1847(6-7):526-533. doi:10.1016/j.bbabio.2015.02.006

Alston, C.L., Rocha, M.C., Lax, N.Z., Turnbull, D.M. & Taylor, R.W. 2017. The genetics and pathology of mitochondrial disease. *The Journal of Pathology*, 241(2):236-250. doi:10.1002/path.4809

Alves, C., Teixeira, S.R., Martin-Saavedra, J.S., Guimaraes Goncalves, F., Lo Russo, F., Muraresku, C., McCormick, E.M., Falk, M.J., Zolkipli-Cunningham, Z., Ganetzky, R., Vossough, A., Goldstein, A. & Zuccoli, G. 2020. Pediatric Leigh syndrome: neuroimaging features and genetic correlations. *Annals of Neurology*, 88(2):218-232. doi:10.1002/ana.25789

Aouacheria, A., Baghdiguian, S., Lamb, H.M., Huska, J.D., Pineda, F.J. & Hardwick, J.M. 2017. Connecting mitochondrial dynamics and life-or-death events via Bcl-2 family proteins. *Neurochemistry International*, 109:141-161. doi:10.1016/j.neuint.2017.04.009

Arany, Z. & Neinast, M. 2018. Branched Chain Amino Acids in Metabolic Disease. *Current Diabetes Reports*, 18(10):76. doi:10.1007/s11892-018-1048-7

Aucamp, J., Bronkhorst, A.J., Peters, D.L., Van Dyk, H.C., Van der Westhuizen, F.H. & Pretorius, P.J. 2017. Kinetic analysis, size profiling, and bioenergetic association of DNA released by selected cell lines in vitro. *Cellular and Molecular Life Sciences*, 74(14):2689-2707. doi:10.1007/s00018-017-2495-z

Barbagallo, M., Veronese, N. & Dominguez, L.J. 2021. Magnesium in Aging, Health and Diseases. *Nutrients*, 13(2):832-839. doi:10.3390/nu13020463

Barrientos, A. & Ugalde, C. 2013. I function, therefore I am: overcoming skepticism about mitochondrial supercomplexes. *Cell Metabolism*, 18(2):147-149. doi:10.1016/j.cmet.2013.07.010

Bayraktar, E.C., Baudrier, L., Ozerdem, C., Lewis, C.A., Chan, S.H., Kunchok, T., Abu-Remaileh, M., Cangelosi, A.L., Sabatini, D.M., Birsoy, K. & Chen, W.W. 2019. MITO-Tag Mice enable rapid isolation and multimodal profiling of mitochondria from specific cell types in vivo. *Proceedings of the National Academy of Sciences*, 116(1):303-312. doi:10.1073/pnas.1816656115

Becker, T. & Wagner, R. 2018. Mitochondrial Outer Membrane Channels: Emerging Diversity in Transport Processes. *Bioessays*, 40(7):e1800013. doi:10.1002/bies.201800013

Beckonert, O., Keun, H.C., Ebbels, T.M., Bundy, J., Holmes, E., Lindon, J.C. & Nicholson, J.K. 2007. Metabolic profiling, metabolomic and metabonomic procedures for NMR spectroscopy of urine, plasma, serum and tissue extracts. *Nature Protocols*, 2(11):2692-2703. doi:10.1038/nprot.2007.376

Berry, B.J., Trewin, A.J., Amitrano, A.M., Kim, M. & Wojtovich, A.P. 2018. Use the protonmotive force: mitochondrial uncoupling and reactive oxygen species. *Journal of Molecular Biology*, 430(21):3873-3891. doi:10.1016/j.jmb.2018.03.025

Bhaskaran, S., Pharaoh, G., Ranjit, R., Murphy, A., Matsuzaki, S., Nair, B.C., Forbes, B., Gispert, S., Auburger, G., Humphries, K.M., Kinter, M., Griffin, T.M. & Deepa, S.S. 2018. Loss of mitochondrial protease ClpP protects mice from diet-induced obesity and insulin resistance. *EMBO Reports*, 19(3):e45009. doi:10.15252/embr.201745009

Bifari, F. & Nisoli, E. 2017. Branched-chain amino acids differently modulate catabolic and anabolic states in mammals: a pharmacological point of view. *British Journal of Pharmacology*, 174(11):1366-1377. doi:10.1111/bph.13624

Birsoy, K., Wang, T., Chen, W.W., Freinkman, E., Abu-Remaileh, M. & Sabatini, D.M. 2015. An essential role of the mitochondrial electron transport chain in cell proliferation is to enable aspartate synthesis. *Cell*, 162(3):540-551. doi:10.1016/j.cell.2015.07.016

Bissantz, C., Kuhn, B. & Stahl, M. 2010. A medicinal chemist's guide to molecular interactions. *Journal of Medicinal Chemistry*, 53(14):5061-5084. doi:10.1021/jm100112j

Bonilla, D.A., Kreider, R.B., Stout, J.R., Forero, D.A., Kerksick, C.M., Roberts, M.D. & Rawson, E.S. 2021. Metabolic basis of creatine in health and disease: a bioinformatics-assisted review. *Nutrients*, 13(4):1238. doi:10.3390/nu13041238

Brand, M.D. & Nicholls, D.G. 2011. Assessing mitochondrial dysfunction in cells. *Biochemical Journal*, 435(2):297-312. doi:10.1042/BJ20110162

Breuer, M.E., Koopman, W.J., Koene, S., Nooteboom, M., Rodenburg, R.J., Willems, P.H. & Smeitink, J.A. 2013. The role of mitochondrial OXPHOS dysfunction in the development of neurologic diseases. *Neurobiology of Disease*, 51:27-34. doi:10.1016/j.nbd.2012.03.007

Broadhurst, D., Goodacre, R., Reinke, S.N., Kuligowski, J., Wilson, I.D., Lewis, M.R. & Dunn, W.B. 2018. Guidelines and considerations for the use of system suitability and quality control samples in mass spectrometry assays applied in untargeted clinical metabolomic studies. *Metabolomics*, 14(6):1-17. doi:10.1007/s11306-018-1367-3

Broër, S. & Palacin, M. 2011. The role of amino acid transporters in inherited and acquired diseases. *Biochemical Journal*, 436(2):193-211. doi:10.1042/BJ20101912

Brooks, G.A. 2020. Lactate as a fulcrum of metabolism. *Redox Biology*, 35:101454. doi:10.1016/j.redox.2020.101454

Calvaruso, M.A., Willems, P., van den Brand, M., Valsecchi, F., Kruse, S., Palmiter, R., Smeitink, J. & Nijtmans, L. 2012. Mitochondrial complex III stabilizes complex I in the absence of NDUFS4 to provide partial activity. *Human Molecular Genetics*, 21(1):115-120. doi:10.1093/hmg/ddr446

Calvo, S.E., Clauser, K.R. & Mootha, V.K. 2016. MitoCarta2.0: an updated inventory of mammalian mitochondrial proteins. *Nucleic Acids Research*, 44(D1):D1251-1257. doi:10.1093/nar/gkv1003

Canto, C., Menzies, K.J. & Auwerx, J. 2015. NAD^+ metabolism and the control of energy homeostasis: a balancing act between mitochondria and the nucleus. *Cell Metabolism*, 22(1):31-53. doi:10.1016/j.cmet.2015.05.023

Carling, P.J., Cree, L.M. & Chinnery, P.F. 2011. The implications of mitochondrial DNA copy number regulation during embryogenesis. *Mitochondrion*, 11(5):686-692. doi:10.1016/j.mito.2011.05.004

Chan, C.C., Lee, Y., Lam, H. & Zhang, X.-M. 2004. *Analytical method validation and instrument performance verification*. Hoboken, NJ: John Wiley & Sons.

Chance, B. & Williams, G. 1955. Respiratory enzymes in oxidative phosphorylation I. Kinetics of oxygen utilization. *Journal of Biological Chemistry*, 217(1):383-394.

Chen, H. & Chan, D.C. 2009. Mitochondrial dynamics–fusion, fission, movement, and mitophagy–in neurodegenerative diseases. *Human Molecular Genetics*, 18(R2):R169-R176.

Chen, Q., Kirk, K., Shurubor, Y.I., Zhao, D., Arreguin, A.J., Shahi, I., Valsecchi, F., Primiano, G., Calder, E.L., Carelli, V., Denton, T.T., Beal, M.F., Gross, S.S., Manfredi, G. & D'Aurelio, M. 2018. Rewiring of Glutamine Metabolism Is a Bioenergetic Adaptation of Human Cells with Mitochondrial DNA Mutations. *Cell Metabolism*, 27(5):1007-1025. doi:10.1016/j.cmet.2018.03.002

Chen, W.W., Freinkman, E., Wang, T., Birsoy, K. & Sabatini, D.M. 2016. Absolute quantification of matrix metabolites reveals the dynamics of mitochondrial metabolism. *Cell*, 166(5):1324-1337. doi:10.1016/j.cell.2016.07.040

Cheng, M.Y., Hartl, F.-U., Martin, J., Pollock, R.A., Kalousek, F., Neuper, W., Hallberg, E.M., Hallberg, R.L. & Horwich, A.L. 1989. Mitochondrial heat-shock protein hsp60 is essential for assembly of proteins imported into yeast mitochondria. *Nature Communications*, 337(6208):620-625.

Chinnery, P.F. & Hudson, G. 2013. Mitochondrial genetics. *British Medical Bulletin*, 106(1):135-159. doi:10.1093/bmb/ldt017

Chong, J., Soufan, O., Li, C., Caraus, I., Li, S., Bourque, G., Wishart, D.S. & Xia, J. 2018. MetaboAnalyst 4.0: towards more transparent and integrative metabolomics analysis. *Nucleic Acids Research*, 46(W1):W486-W494. doi:10.1093/nar/gky310

Cobley, J.N., Fiorello, M.L. & Bailey, D.M. 2018. 13 Reasons why the brain is susceptible to oxidative stress. *Redox Biology*, 15:490-503. doi:10.1016/j.redox.2018.01.008

Colombini, M. 2004. VDAC: the channel at the interface between mitochondria and the cytosol. *Molecular and Cellular Biochemistry*, 256-257(1-2):107-115. doi:10.1023/b:mcbi.0000009862.17396.8d

Corcelli, A., Saponetti, M.S., Zaccagnino, P., Lopalco, P., Mastrodonato, M., Liquori, G.E. & Lorusso, M. 2010. Mitochondria isolated in nearly isotonic KCl buffer: focus on cardiolipin and organelle morphology. *Biochimica et Biophysica Acta (BBA) - Biomembranes*, 1798(3):681-687. doi:10.1016/j.bbamem.2010.01.005

Craven, L., Alston, C.L., Taylor, R.W. & Turnbull, D.M. 2017. Recent Advances in Mitochondrial Disease. *Annual Review of Genomics and Human Genetics*, 18:257-275. doi:10.1146/annurev-genom-091416-035426

Cui, P., Shao, W., Huang, C., Wu, C.-J., Jiang, B. & Lin, D. 2019. Metabolic derangements of skeletal muscle from a murine model of glioma cachexia. *Skeletal Muscle*, 9(1):1-3. doi:10.1186/s13395-018-0188-4

D'Imprima, E., Mills, D.J., Parey, K., Brandt, U., Kuhlbrandt, W., Zickermann, V. & Vonck, J. 2016. Cryo-EM structure of respiratory complex I reveals a link to mitochondrial sulfur metabolism. *Biochimica et Biophysica Acta (BBA) - Bioenergetics*, 1857(12):1935-1942. doi:10.1016/j.bbabio.2016.09.014

de Bari, L. & Atlante, A. 2018. Including the mitochondrial metabolism of L-lactate in cancer metabolic reprogramming. *Cellular and Molecular Life Sciences*, 75(15):2763-2776. doi:10.1007/s00018-018-2831-y

Deprez, S., Sweatman, B.C., Connor, S.C., Haselden, J.N. & Waterfield, C.J. 2002. Optimisation of collection, storage and preparation of rat plasma for ^{1}H-NMR spectroscopic analysis in toxicology studies to determine inherent variation in biochemical profiles. *Journal of Pharmaceutical and Biomedical Analysis*, 30(4):1297-1310. doi:10.1016/s0731-7085(02)00455-7

Dona, A.C., Kyriakides, M., Scott, F., Shephard, E.A., Varshavi, D., Veselkov, K. & Everett, J.R. 2016. A guide to the identification of metabolites in NMR-based metabonomics/metabolomics experiments. *Computational and structural biotechnology journal*, 14:135-153.

Dona, A.C., Jimenez, B., Schafer, H., Humpfer, E., Spraul, M., Lewis, M.R., Pearce, J.T., Holmes, E., Lindon, J.C. & Nicholson, J.K. 2014. Precision high-throughput proton NMR spectroscopy of human urine, serum, and plasma for large-scale metabolic phenotyping. *Analytical Chemistry*, 86(19):9887-9894. doi:10.1021/ac5025039

Du Plessis, C. 2019. Evaluating the effect of a mitochondrial isolation (MACS) buffer on a GC-TOF-MS metabolomics assay. Potchefstroom: North-West University. (Mini-dissertation - BSc Hons.).

Ducker, G.S. & Rabinowitz, J.D. 2017. One-carbon metabolism in health and disease. *Cell Metabolism*, 25(1):27-42. doi:10.1016/j.cmet.2016.08.009

Ducker, G.S., Chen, L., Morscher, R.J., Ghergurovich, J.M., Esposito, M., Teng, X., Kang, Y. & Rabinowitz, J.D. 2016. Reversal of cytosolic one-carbon flux compensates for loss of the mitochondrial folate pathway. *Cell Metabolism*, 23(6):1140-1153. doi:10.1016/j.cmet.2016.04.016

Dunn, W.B., Wilson, I.D., Nicholls, A.W. & Broadhurst, D. 2012. The importance of experimental design and QC samples in large-scale and MS-driven untargeted metabolomic studies of humans. *Bioanalysis*, 4(18):2249-2264.

Dunn, W.B., Broadhurst, D.I., Atherton, H.J., Goodacre, R. & Griffin, J.L. 2011. Systems level studies of mammalian metabolomes: the roles of mass spectrometry and nuclear magnetic resonance spectroscopy. *Chemical Society Reviews*, 40(1):387-426. doi:10.1039/b906712b

Dunn, W.B., Erban, A., Weber, R.J., Creek, D.J., Brown, M., Breitling, R., Hankemeier, T., Goodacre, R., Neumann, S. & Kopka, J. 2013. Mass appeal: metabolite identification in mass spectrometry-focused untargeted metabolomics. *Metabolomics*, 9(1):44-66.

Emmerzaal, T.L., Preston, G., Geenen, B., Verweij, V., Wiesmann, M., Vasileiou, E., Gruter, F., de Groot, C., Schoorl, J., de Veer, R., Roelofs, M., Arts, M., Hendriksen, Y., Klimars, E., Donti, T.R., Graham, B.H., Morava, E., Rodenburg, R.J. & Kozicz, T. 2020. Impaired mitochondrial complex I function as a candidate driver in the biological stress response and a concomitant stress-induced brain metabolic reprogramming in male mice. *Translational Psychiatry*, 10(1):1-13. doi:10.1038/s41398-020-0858-y

Erban, A., Schauer, N., Fernie, A.R. & Kopka, J. 2007. Nonsupervised Construction and Application of Mass Spectral and Retention Time Index Libraries From Time-of-Flight Gas Chromatography-Mass Spectrometry Metabolite Profiles. In: Weckwerth, W., ed. *Metabolomics: Methods and Protocols*. Totowa, NJ: Humana Press. pp. 19-38.

Esterhuizen, K., van der Westhuizen, F.H. & Louw, R. 2017. Metabolomics of mitochondrial disease. *Mitochondrion*, 35:97-110. doi:10.1016/j.mito.2017.05.012

Eysert, F., Kinoshita, P.F., Mary, A., Vaillant-Beuchot, L., Checler, F. & Chami, M. 2020. Molecular Dysfunctions of Mitochondria-Associated Membranes (MAMs) in Alzheimer's Disease. *International Journal of Molecular Sciences*, 21(24):9521. doi:10.3390/ijms21249521

Fang, H., Ye, X., Xie, J., Li, Y., Li, H., Bao, X., Yang, Y., Lin, Z., Jia, M., Han, Q., Zhu, J., Li, X., Zhao, Q., Yang, Y. & Lyu, J. 2021. A membrane arm of mitochondrial complex I sufficient to promote respirasome formation. *Cell Reports*, 35(2):108963. doi:10.1016/j.celrep.2021.108963

Faul, F., Erdfelder, E., Lang, A.G. & Buchner, A. 2007. G*Power 3: a flexible statistical power analysis program for the social, behavioral, and biomedical sciences. *Behaviour Research Methods*, 39(2):175-191. doi:10.3758/bf03193146

FDA (Food and Drug Administration). 2001. *Guidance for industry: bioanalytical method validation.* https://www.fda.gov/downloads/Drugs/GuidanceComplianceRegulatoryInformation/Guidances/ucm070107.pdf, Date of access: 23 September 2021.

Fex, M., Nicholas, L.M., Vishnu, N., Medina, A., Sharoyko, V.V., Nicholls, D.G., Spegel, P. & Mulder, H. 2018. The pathogenetic role of beta-cell mitochondria in type 2 diabetes. *Journal of Endocrinology*, 236(3):R145-R159. doi:10.1530/JOE-17-0367

Fiedorczuk, K. & Sazanov, L.A. 2018. Mammalian mitochondrial complex I structure and disease-causing mutations. *Trends in Cell Biology*, 28(10):835-867. doi:10.1016/j.tcb.2018.06.006

Fiehn, O. 2002. Metabolomics - the link between genotypes and phenotypes. In: Town, C., ed. *Functional Genomics*. Dordrecht: Springer Netherlands. pp. 155-171.

Finsterer, J. 2008. Leigh and Leigh-like syndrome in children and adults. *Pediatric Neurology*, 39(4):223-235. doi:10.1016/j.pediatrneurol.2008.07.013

Foriel, S., Beyrath, J., Eidhof, I., Rodenburg, R.J., Schenck, A. & Smeitink, J.A.M. 2018. Feeding difficulties, a key feature of the Drosophila NDUFS4 mitochondrial disease model. *Disease Models and Mechanisms*, 11(3):dmm032482. doi:10.1242/dmm.032482

Franko, A., Baris, O.R., Bergschneider, E., von Toerne, C., Hauck, S.M., Aichler, M., Walch, A.K., Wurst, W., Wiesner, R.J., Johnston, I.C. & de Angelis, M.H. 2013. Efficient isolation of pure and functional mitochondria from mouse tissues using automated tissue disruption and enrichment with anti-TOM22 magnetic beads. *Plos One*, 8(12):e82392. doi:10.1371/journal.pone.0082392

Fratila, R.M. & Velders, A.H. 2011. Small-volume nuclear magnetic resonance spectroscopy. *Annual Review of Analytical Chemistry*, 4:227-249. doi:10.1146/annurev-anchem-061010-114024

Frezza, C. 2017. Mitochondrial metabolites: undercover signalling molecules. *Interface Focus*, 7(2):20160100. doi:10.1098/rsfs.2016.0100

García-Sevillano, M., García-Barrera, T., Navarro, F., Montero-Lobato, Z. & Gómez-Ariza, J. 2015. Shotgun metabolomic approach based on mass spectrometry for hepatic mitochondria of mice under arsenic exposure. *Biometals*, 28(2):341-351.

Garrido-Perez, N., Vela-Sebastian, A., Lopez-Gallardo, E., Emperador, S., Iglesias, E., Meade, P., Jimenez-Mallebrera, C., Montoya, J., Bayona-Bafaluy, M.P. & Ruiz-Pesini, E. 2020. Oxidative phosphorylation dysfunction modifies the cell secretome. *International Journal of Molecular Sciences*, 21(9):3374. doi:10.3390/ijms21093374

Genova, M.L. & Lenaz, G. 2014. Functional role of mitochondrial respiratory supercomplexes. *Biochimica et Biophysica Acta (BBA) - Bioenergetics*, 1837(4):427-443. doi:10.1016/j.bbabio.2013.11.002

Gerencser, A.A., Neilson, A., Choi, S.W., Edman, U., Yadava, N., Oh, R.J., Ferrick, D.A., Nicholls, D.G. & Brand, M.D. 2009. Quantitative microplate-based respirometry with correction for oxygen diffusion. *Analytical Chemistry*, 81(16):6868-6878. doi:10.1021/ac900881z

Ghezzi, D. & Zeviani, M. 2018. Human diseases associated with defects in assembly of OXPHOS complexes. *Essays in Biochemistry*, 62(3):271-286. doi:10.1042/EBC20170099

Gielisch, I. & Meierhofer, D. 2015. Metabolome and proteome profiling of complex I deficiency induced by rotenone. *J Proteome Res*, 14(1):224-235. doi:10.1021/pr500894v

Glaves, J., Li, M., Mercier, P., Fahlman, R. & Sykes, B. 2014. High-throughput, multi-platform metabolomics on very small volumes: 1 H NMR metabolite identification in an unadulterated tube-in-tube system. *Metabolomics*, 10(6):1145-1151. doi:10.1007/s11306-014-0678-2

Go, Y.M. & Jones, D.P. 2013. Thiol/disulfide redox states in signaling and sensing. *Critical Reviews in Biochemistry and Molecular Biology*, 48(2):173-181. doi:10.3109/10409238.2013.764840

Go, Y.M., Roede, J.R., Orr, M., Liang, Y. & Jones, D.P. 2014a. Integrated redox proteomics and metabolomics of mitochondria to identify mechanisms of cd toxicity. *Toxicological Sciences*, 139(1):59-73. doi:10.1093/toxsci/kfu018

Go, Y.M., Uppal, K., Walker, D.I., Tran, V.L., Dury, L., Strobel, F.H., Baubichon-Cortay, H., Pennell, K.D., Roede, J.R. & Jones, D.P. 2014b. Mitochondrial metabolomics using high-resolution Fourier-transform mass spectrometry. In: Raftery, D., ed. *Methods in Molecular Biology (Methods and Protocols)*. 1198. New York, NY: Humana Press. pp. 43-73.

Goodman, R.P., Calvo, S.E. & Mootha, V.K. 2018. Spatiotemporal compartmentalization of hepatic NADH and NADPH metabolism. *Journal of Biological Chemistry*, 293(20):7508-7516. doi:10.1074/jbc.TM117.000258

Gorman, G.S., Chinnery, P.F., DiMauro, S., Hirano, M., Koga, Y., McFarland, R., Suomalainen, A., Thorburn, D.R., Zeviani, M. & Turnbull, D.M. 2016. Mitochondrial diseases. *Nature Reviews Disease Primers*, 2(1):1-22. doi:10.1038/nrdp.2016.80

Gorman, G.S., Schaefer, A.M., Ng, Y., Gomez, N., Blakely, E.L., Alston, C.L., Feeney, C., Horvath, R., Yu-Wai-Man, P., Chinnery, P.F., Taylor, R.W., Turnbull, D.M. & McFarland, R. 2015. Prevalence of nuclear and mitochondrial DNA mutations related to adult mitochondrial disease. *Annals of Neurology*, 77(5):753-759. doi:10.1002/ana.24362

Gravel, S.P., Andrzejewski, S., Avizonis, D. & St-Pierre, J. 2014. Stable isotope tracer analysis in isolated mitochondria from mammalian systems. *Metabolites*, 4(2):166-183. doi:10.3390/metabo4020166

Gross, V.S., Greenberg, H.K., Baranov, S.V., Carlson, G.M., Stavrovskaya, I.G., Lazarev, A.V. & Kristal, B.S. 2011. Isolation of functional mitochondria from rat kidney and skeletal muscle without manual homogenization. *Analytical Biochemistry*, 418(2):213-223. doi:10.1016/j.ab.2011.07.017

Gucek, M. & Sack, M.N. 2021. Proteomic and metabolomic advances uncover biomarkers of mitochondrial disease pathophysiology and severity. *Journal of Clinical Investigation*, 131(2):e145158. doi:10.1172/JCI145158

Guerrero-Castillo, S., Baertling, F., Kownatzki, D., Wessels, H.J., Arnold, S., Brandt, U. & Nijtmans, L. 2017. The assembly pathway of mitochondrial respiratory chain complex I. *Cell Metabolism*, 25(1):128-139. doi:10.1016/j.cmet.2016.09.002

Gullberg, J., Jonsson, P., Nordstrom, A., Sjostrom, M. & Moritz, T. 2004. Design of experiments: an efficient strategy to identify factors influencing extraction and derivatization of Arabidopsis thaliana samples in metabolomic studies with gas chromatography/mass spectrometry. *Analytical Biochemistry*, 331(2):283-295. doi:10.1016/j.ab.2004.04.037

Gustafsson, C.M., Falkenberg, M. & Larsson, N.G. 2016. Maintenance and expression of mammalian mitochondrial DNA. *Annual Review of Biochemistry*, 85:133-160. doi:10.1146/annurev-biochem-060815-014402

Hafer, E., Holzgrabe, U., Kraus, K., Adams, K., Hook, J.M. & Diehl, B. 2020. Qualitative and quantitative ^{1}H-NMR spectroscopy for determination of divalent metal cation concentration in model salt solutions, food supplements, and pharmaceutical products by using EDTA as chelating agent. *Magnetic Resonance in Chemistry*, 58(7):653-665. doi:10.1002/mrc.5009

Hall, A.M. & Roberson, E.D. 2012. Mouse models of Alzheimer's disease. *Brain Research Bulletin*, 88(1):3-12. doi:10.1016/j.brainresbull.2011.11.017

Harris, J.J., Jolivet, R. & Attwell, D. 2012. Synaptic energy use and supply. *Neuron*, 75(5):762-777. doi:10.1016/j.neuron.2012.08.019

Heidari, R., Ahmadi, A., Mohammadi, H., Ommati, M.M., Azarpira, N. & Niknahad, H. 2018. Mitochondrial dysfunction and oxidative stress are involved in the mechanism of methotrexate-induced renal injury and electrolytes imbalance. *Biomedicine & Pharmacotherapy*, 107:834-840.

Hewton, K.G., Johal, A.S. & Parker, S.J. 2021. Transporters at the interface between cytosolic and mitochondrial amino acid metabolism. *Metabolites*, 11(2):112. doi:10.3390/metabo11020112

Hirst, J. & Roessler, M.M. 2016. Energy conversion, redox catalysis and generation of reactive oxygen species by respiratory complex I. *Biochimica et Biophysica Acta (BBA) - Bioenergetics*, 1857(7):872-883. doi:10.1016/j.bbabio.2015.12.009

Hoefs, S.J., Rodenburg, R.J., Smeitink, J.A. & van den Heuvel, L.P. 2012. Molecular base of biochemical complex I deficiency. *Mitochondrion*, 12(5):520-532. doi:10.1016/j.mito.2012.07.106

Hohmann, M., Felbinger, C., Christoph, N., Wachter, H., Wiest, J. & Holzgrabe, U. 2014. Quantification of taurine in energy drinks using ^{1}H-NMR. *Journal of Pharmaceutical and Biomedical Analysis*, 93:156-160. doi:10.1016/j.jpba.2013.08.046

Holeček, M. 2020. Histidine in health and disease: metabolism, physiological importance, and use as a supplement. *Nutrients*, 12(3):848. doi:10.3390/nu12030848

Hornig-Do, H.T., Gunther, G., Bust, M., Lehnartz, P., Bosio, A. & Wiesner, R.J. 2009. Isolation of functional pure mitochondria by superparamagnetic microbeads. *Analytical Biochemistry*, 389(1):1-5. doi:10.1016/j.ab.2009.02.040

Hubbard, W.B., Harwood, C.L., Prajapati, P., Springer, J.E., Saatman, K.E. & Sullivan, P.G. 2019. Fractionated mitochondrial magnetic separation for isolation of synaptic mitochondria from brain tissue. *Scientific Reports*, 9(1):1-13. doi:10.1038/s41598-019-45568-3

Huskisson, E., Maggini, S. & Ruf, M. 2007. The role of vitamins and minerals in energy metabolism and well-being. *Journal of International Medical Research*, 35(3):277-289. doi:10.1177/147323000703500301

Hüttemann, M., Lee, I., Pecinova, A., Pecina, P., Przyklenk, K. & Doan, J.W. 2008. Regulation of oxidative phosphorylation, the mitochondrial membrane potential, and their role in human disease. *Journal of Bioenergetics and Biomembranes*, 40(5):445. doi:10.1007/s10863-008-9169-3

Ingraham, C.A., Burwell, L.S., Skalska, J., Brookes, P.S., Howell, R.L., Sheu, S.S. & Pinkert, C.A. 2009. NDUFS4: creation of a mouse model mimicking a complex I disorder. *Mitochondrion*, 9(3):204-210. doi:10.1016/j.mito.2009.02.001

Iommarini, L., Peralta, S., Torraco, A. & Diaz, F. 2015. Mitochondrial diseases part II: mouse models of OXPHOS deficiencies caused by defects in regulatory factors and other components required for mitochondrial function. *Mitochondrion*, 22:96-118. doi:10.1016/j.mito.2015.01.008

Jain, I.H., Zazzeron, L., Goldberger, O., Marutani, E., Wojtkiewicz, G.R., Ast, T., Wang, H., Schleifer, G., Stepanova, A. & Brepoels, K. 2019. Leigh syndrome mouse model can be rescued by interventions that normalize brain hyperoxia, but not HIF activation. *Cell Metabolism*, 30(4):824-832. doi:10.1016/j.cmet.2019.07.006

Jin, F., Wu, Q., Lu, Y.F., Gong, Q.H. & Shi, J.S. 2008. Neuroprotective effect of resveratrol on 6-OHDA-induced Parkinson's disease in rats. *European Journal of Pharmacology*, 600(1-3):78-82. doi:10.1016/j.ejphar.2008.10.005

Jin, Z., Wei, W., Yang, M., Du, Y. & Wan, Y. 2014. Mitochondrial complex I activity suppresses inflammation and enhances bone resorption by shifting macrophage-osteoclast polarization. *Cell Metabolism*, 20(3):483-498. doi:10.1016/j.cmet.2014.07.011

Johnson, M.A., Vidoni, S., Durigon, R., Pearce, S.F., Rorbach, J., He, J., Brea-Calvo, G., Minczuk, M., Reyes, A., Holt, I.J. & Spinazzola, A. 2014. Amino acid starvation has opposite effects on mitochondrial and cytosolic protein synthesis. *Plos One*, 9(4):e93597. doi:10.1371/journal.pone.0093597

Johnson, S.C., Kayser, E.B., Bornstein, R., Stokes, J., Bitto, A., Park, K.Y., Pan, A., Sun, G., Raftery, D., Kaeberlein, M., Sedensky, M.M. & Morgan, P.G. 2020. Regional metabolic signatures in the Ndufs4(KO)

mouse brain implicate defective glutamate/alpha-ketoglutarate metabolism in mitochondrial disease. *Molecular Genetics & Metabolism*, 130(2):118-132. doi:10.1016/j.ymgme.2020.03.007

Johnson, S.C., Yanos, M.E., Kayser, E.B., Quintana, A., Sangesland, M., Castanza, A., Uhde, L., Hui, J., Wall, V.Z., Gagnidze, A., Oh, K., Wasko, B.M., Ramos, F.J., Palmiter, R.D., Rabinovitch, P.S., Morgan, P.G., Sedensky, M.M. & Kaeberlein, M. 2013. mTOR inhibition alleviates mitochondrial disease in a mouse model of Leigh syndrome. *Science*, 342(6165):1524-1528. doi:10.1126/science.1244360

Junghans, L., Teleki, A., Wijaya, A.W., Becker, M., Schweikert, M. & Takors, R. 2019. From nutritional wealth to autophagy: in vivo metabolic dynamics in the cytosol, mitochondrion and shuttles of IgG producing CHO cells. *Metabolic Engineering*, 54:145-159. doi:10.1016/j.ymben.2019.02.005

Kaasik, A., Safiulina, D., Zharkovsky, A. & Veksler, V. 2007. Regulation of mitochondrial matrix volume. *American Journal of Physyiology - Cell Physiology*, 292(1):C157-163. doi:10.1152/ajpcell.00272.2006

Kahlhofer, F., Kmita, K., Wittig, I., Zwicker, K. & Zickermann, V. 2017. Accessory subunit NUYM (NDUFS4) is required for stability of the electron input module and activity of mitochondrial complex I. *Biochimica et Biophysica Acta (BBA) - Bioenergetics*, 1858(2):175-181. doi:10.1016/j.bbabio.2016.11.010

Kappler, L. & Lehmann, R. 2019. Mass-spectrometric multi-omics linked to function – State-of-the-art investigations of mitochondria in systems medicine. *TrAC: Trends in Analytical Chemistry*, 119:115635. doi:10.1016/j.trac.2019.115635

Kappler, L., Li, J., Häring, H.-U., Weigert, C., Lehmann, R., Xu, G. & Hoene, M. 2016. Purity matters: a workflow for the valid high-resolution lipid profiling of mitochondria from cell culture samples. *Scientific Reports*, 6:21107. doi:10.1038/srep21107

Karamanlidis, G., Lee, C.F., Garcia-Menendez, L., Kolwicz, S.C., Jr., Suthammarak, W., Gong, G., Sedensky, M.M., Morgan, P.G., Wang, W. & Tian, R. 2013. Mitochondrial complex I deficiency increases protein acetylation and accelerates heart failure. *Cell Metabolism*, 18(2):239-250. doi:10.1016/j.cmet.2013.07.002

Karlberg, O., Canback, B., Kurland, C.G. & Andersson, S.G. 2000. The dual origin of the yeast mitochondrial proteome. *Yeast*, 17(3):170-187. doi:10.1002/1097-0061(20000930)17:3<170::AID-YEA25>3.0.CO;2-V

Kayser, E.B., Sedensky, M.M. & Morgan, P.G. 2016. Region-specific defects of respiratory capacities in the Ndufs4(KO) mouse brain. *Plos One*, 11(1):e0148219. doi:10.1371/journal.pone.0148219

Kazak, L. & Cohen, P. 2020. Creatine metabolism: energy homeostasis, immunity and cancer biology. *Nature Reviews Endocrinology*, 16(8):421-436. doi:10.1038/s41574-020-0365-5

Khan, N.A., Nikkanen, J., Yatsuga, S., Jackson, C., Wang, L., Pradhan, S., Kivela, R., Pessia, A., Velagapudi, V. & Suomalainen, A. 2017. mTORC1 regulates mitochondrial integrated stress response and mitochondrial myopathy progression. *Cell Metabolism*, 26(2):419-428. doi:10.1016/j.cmet.2017.07.007

Khattar, N.K., Yablonska, S., Baranov, S.V., Baranova, O.V., Kretz, E.S., Larkin, T.M., Carlisle, D.L., Richardson, R.M. & Friedlander, R.M. 2016. Isolation of functionally active and highly purified neuronal mitochondria from human cortex. *Journal of Neuroscience Methods*, 263:1-6. doi:10.1016/j.jneumeth.2016.01.017

Kiebish, M.A., Han, X., Cheng, H. & Seyfried, T.N. 2009. In vitro growth environment produces lipidomic and electron transport chain abnormalities in mitochondria from non-tumorigenic astrocytes and brain tumours. *ASN Neuro*, 1(3), doi:10.1042/AN20090011

Kiebish, M.A., Han, X., Cheng, H., Chuang, J.H. & Seyfried, T.N. 2008a. Cardiolipin and electron transport chain abnormalities in mouse brain tumor mitochondria: lipidomic evidence supporting the Warburg theory of cancer. *Journal of Lipid Research*, 49(12):2545-2556. doi:10.1194/jlr.M800319-JLR200

Kiebish, M.A., Han, X., Cheng, H., Lunceford, A., Clarke, C.F., Moon, H., Chuang, J.H. & Seyfried, T.N. 2008b. Lipidomic analysis and electron transport chain activities in C57BL/6J mouse brain mitochondria. *Journal of Neurochemistry*, 106(1):299-312. doi:10.1111/j.1471-4159.2008.05383.x

Kiebish, M.A., Yang, K., Liu, X., Mancuso, D.J., Guan, S., Zhao, Z., Sims, H.F., Cerqua, R., Cade, W.T., Han, X. & Gross, R.W. 2013. Dysfunctional cardiac mitochondrial bioenergetic, lipidomic, and signaling in a murine model of Barth syndrome. *Journal of Lipid Research*, 54(5):1312-1325. doi:10.1194/jlr.M034728

Kory, N., Wyant, G.A., Prakash, G., Uit de Bos, J., Bottanelli, F., Pacold, M.E., Chan, S.H., Lewis, C.A., Wang, T., Keys, H.R., Guo, Y.E. & Sabatini, D.M. 2018. SFXN1 is a mitochondrial serine transporter required for one-carbon metabolism. *Science*, 362(6416), doi:10.1126/science.aat9528

Koshenov, Z., Oflaz, F.E., Hirtl, M., Pilic, J., Bachkoenig, O.A., Gottschalk, B., Madreiter-Sokolowski, C.T., Rost, R., Malli, R. & Graier, W.F. 2021. Sigma-1 receptor promotes mitochondrial bioenergetics by orchestrating ER Ca^{2+} leak during early ER stress. *Metabolites*, 11(7):422. doi:10.3390/metabo11070422

Krishnan, N., Dickman, M.B. & Becker, D.F. 2008. Proline modulates the intracellular redox environment and protects mammalian cells against oxidative stress. *Free Radical Biology and Medicine*, 44(4):671-681. doi:10.1016/j.freeradbiomed.2007.10.054

Kruse, S.E., Watt, W.C., Marcinek, D.J., Kapur, R.P., Schenkman, K.A. & Palmiter, R.D. 2008. Mice with mitochondrial complex I deficiency develop a fatal encephalomyopathy. *Cell Metabolism*, 7(4):312-320. doi:10.1016/j.cmet.2008.02.004

Kulawiak, B., Hopker, J., Gebert, M., Guiard, B., Wiedemann, N. & Gebert, N. 2013. The mitochondrial protein import machinery has multiple connections to the respiratory chain. *Biochimica et Biophysica Acta (BBA) - Bioenergetics*, 1827(5):612-626. doi:10.1016/j.bbabio.2012.12.004

Laemmli, U.K. 1970. Cleavage of Structural Proteins during the Assembly of the Head of Bacteriophage T4. *Nature*, 227(5259):680-685. doi:10.1038/227680a0

Lake, N.J., Bird, M.J., Isohanni, P. & Paetau, A. 2015. Leigh syndrome: neuropathology and pathogenesis. *Journal of Neuropathology & Experimental Neurology*, 74(6):482-492. doi:10.1097/NEN.0000000000000195

Leary, S.L., Underwood, W., Anthony, R., Cartner, S., Corey, D., Grandin, T., Greenacre, C., Gwaltney-Brant, S., McCrackin, M. & Meyer, R. 2013. AVMA guidelines for the euthanasia of animals: 2013 edition. In.: American Veterinary Medical Association Schaumburg, IL.

Lee, J. & Wolfgang, M.J. 2012. Metabolomic profiling reveals a role for CPT1c in neuronal oxidative metabolism. *BMC Biochemistry*, 13(1):23. doi:10.1186/1471-2091-13-23

Lee, W.D., Mukha, D., Aizenshtein, E. & Shlomi, T. 2019. Spatial-fluxomics provides a subcellular-compartmentalized view of reductive glutamine metabolism in cancer cells. *Nature Communications*, 10(1):1351. doi:10.1038/s41467-019-09352-1

Legros, F., Malka, F., Frachon, P., Lombes, A. & Rojo, M. 2004. Organization and dynamics of human mitochondrial DNA. *Journal of Cell Science*, 117(Pt 13):2653-2662. doi:10.1242/jcs.01134

Lehtonen, J.M., Auranen, M., Darin, N., Sofou, K., Bindoff, L., Hikmat, O., Uusimaa, J., Vieira, P., Tulinius, M., Lonnqvist, T., de Coo, I.F., Suomalainen, A. & Isohanni, P. 2021. Diagnostic value of serum biomarkers FGF21 and GDF15 compared to muscle sample in mitochondrial disease. *Journal of Inherited Metabolic Disease*, 44(2):469-480. doi:10.1002/jimd.12307

Lenaz, G., Tioli, G., Falasca, A.I. & Genova, M.L. 2016. Complex I function in mitochondrial supercomplexes. *Biochimica et Biophysica Acta (BBA) - Bioenergetics*, 1857(7):991-1000. doi:10.1016/j.bbabio.2016.01.013

Leong, D.W., Komen, J.C., Hewitt, C.A., Arnaud, E., McKenzie, M., Phipson, B., Bahlo, M., Laskowski, A., Kinkel, S.A., Davey, G.M., Heath, W.R., Voss, A.K., Zahedi, R.P., Pitt, J.J., Chrast, R., Sickmann, A.,

Ryan, M.T., Smyth, G.K., Thorburn, D.R. & Scott, H.S. 2012. Proteomic and metabolomic analyses of mitochondrial complex I-deficient mouse model generated by spontaneous B2 short interspersed nuclear element (SINE) insertion into NADH dehydrogenase (ubiquinone) Fe-S protein 4 (Ndufs4) gene. *Journal of Biological Chemistry*, 287(24):20652-20663. doi:10.1074/jbc.M111.327601

Lewis, C.A., Parker, S.J., Fiske, B.P., McCloskey, D., Gui, D.Y., Green, C.R., Vokes, N.I., Feist, A.M., Vander Heiden, M.G. & Metallo, C.M. 2014. Tracing compartmentalized NADPH metabolism in the cytosol and mitochondria of mammalian cells. *Molecular Cell*, 55(2):253-263. doi:10.1016/j.molcel.2014.05.008

Li, B., Tang, J., Yang, Q., Cui, X., Li, S., Chen, S., Cao, Q., Xue, W., Chen, N. & Zhu, F. 2016. Performance evaluation and online realization of data-driven normalization methods used in LC/MS based untargeted metabolomics analysis. *Scientific Reports*, 6(1):1-13. doi:10.1038/srep38881

Li, H., Uittenbogaard, M., Hao, L. & Chiaramello, A. 2021. Clinical insights into mitochondrial neurodevelopmental and neurodegenerative disorders: their biosignatures from mass spectrometry-based metabolomics. *Metabolites*, 11(4):233. doi:10.3390/metabo11040233

Lindeque, J.Z., Hidalgo, J., Louw, R. & van der Westhuizen, F.H. 2013. Systemic and organ specific metabolic variation in metallothionein knockout mice challenged with swimming exercise. *Metabolomics*, 9(2):418-432. doi:10.1007/s11306-012-0459-8

Lindon, J.C., Nicholson, J.K. & Everett, J.R. 1999. NMR spectroscopy of biofluids. In. *Annual Reports on NMR Spectroscopy*. 38: Elsevier. pp. 1-88.

Liu, L., MacKenzie, K.R., Putluri, N., Maletić-Savatić, M. & Bellen, H.J. 2017. The glia-neuron lactate shuttle and elevated ROS promote lipid synthesis in neurons and lipid droplet accumulation in glia via APOE/D. *Cell Metabolism*, 26(5):719-737. doi:10.1016/j.cmet.2017.08.024

Liu, X. & Xu, G. 2018. Recent advances in using mass spectrometry for mitochondrial metabolomics and lipidomics - A review. *Analytica Chimica Acta*, 1037:3-12. doi:10.1016/j.aca.2017.11.080

Logan, A., Pell, V.R., Shaffer, K.J., Evans, C., Stanley, N.J., Robb, E.L., Prime, T.A., Chouchani, E.T., Cocheme, H.M. & Fearnley, I.M. 2016. Assessing the mitochondrial membrane potential in cells and in vivo using targeted click chemistry and mass spectrometry. *Cell Metabolism*, 23(2):379-385. doi:10.1016/j.cmet.2015.11.014

Luo, R., David, L., Hung, H., Devaney, J. & Gilson, M.K. 1999. Strength of solvent-exposed salt-bridges. *The Journal of Physical Chemistry B*, 103(4):727-736.

Mamer, O., Gravel, S.-P., Choinière, L., Chénard, V., St-Pierre, J. & Avizonis, D. 2013. The complete targeted profile of the organic acid intermediates of the citric acid cycle using a single stable isotope dilution analysis, sodium borodeuteride reduction and selected ion monitoring GC/MS. *Metabolomics*, 9(5):1019-1030. doi:10.1007/s11306-013-0521-1

Mannella, C.A. 2006. Structure and dynamics of the mitochondrial inner membrane cristae. *Biochimica et Biophysica Acta (BBA) - Molecular Cell Research*, 1763(5-6):542-548. doi:10.1016/j.bbamcr.2006.04.006

Martinez-Reyes, I. & Chandel, N.S. 2020. Mitochondrial TCA cycle metabolites control physiology and disease. *Nature Communications*, 11(1):1-11. doi:10.1038/s41467-019-13668-3

Mason, S. 2017. Lactate Shuttles in Neuroenergetics—Homeostasis, Allostasis and Beyond. *Frontiers in Neuroscience*, 11:43. doi:10.3389/fnins.2017.00043

Mason, S., Terburgh, K. & Louw, R. 2018. Miniaturized 1H-NMR method for analyzing limited-quantity samples applied to a mouse model of Leigh disease. *Metabolomics*, 14(6):74. doi:10.1007/s11306-018-1372-6

Mathuthu, E., Janse van Rensburg, A., Du Plessis, D. & Mason, S. 2021. EDTA as a chelating agent in quantitative ^{1}H-NMR of biologically important ions. *Biochemistry and Cell Biology*, 99(4):465-475. doi:10.1139/bcb-2020-0543

Matic, S., Muders, V. & Meisinger, C. 2018. Tuning the mitochondrial protein import machinery by reversible phosphorylation: from metabolic switches to cell cycle regulation. *Current Opinion in Physiology*, 3:49-56. doi:10.1016/j.cophys.2018.02.011

Matuszczyk, J.C., Teleki, A., Pfizenmaier, J. & Takors, R. 2015. Compartment-specific metabolomics for CHO reveals that ATP pools in mitochondria are much lower than in cytosol. *Biotechnology Journal*, 10(10):1639-1650. doi:10.1002/biot.201500060

McDonald, A.E., Pichaud, N. & Darveau, C.A. 2018. "Alternative" fuels contributing to mitochondrial electron transport: Importance of non-classical pathways in the diversity of animal metabolism. *Comparative Biochemistry and Physiology Part B: Biochemistry and Molecular Biology*, 224:185-194. doi:10.1016/j.cbpb.2017.11.006

McLaughlin, K.L., Hagen, J.T., Coalson, H.S., Nelson, M.A.M., Kew, K.A., Wooten, A.R. & Fisher-Wellman, K.H. 2020. Novel approach to quantify mitochondrial content and intrinsic bioenergetic efficiency across organs. *Scientific Reports*, 10(1):17599-17599. doi:10.1038/s41598-020-74718-1

Meissner-Roloff, M. 2009. The occurrence of mitochondrial DNA polymerase gamma gene mutations in mitochondrial deficiencies, in a selection of South African paediatric patients. Potchefstroom: NWU. (Dissertation - MSc). https://repository.nwu.ac.za/handle/10394/5095

Mels, C.M., Jansen van Rensburg, P., van der Westhuizen, F.H., Pretorius, P.J. & Erasmus, E. 2011. Increased excretion of c4-carnitine species after a therapeutic acetylsalicylic Acid dose: evidence for an inhibitory effect on short-chain Fatty Acid metabolism. *International Scholarly Research Notices - Pharmacology*, 2011:851870. doi:10.5402/2011/851870

Mereis, M. 2017. Evaluating the involvement of metallothionein I in complex I deficiency: an in vitro study. Potchefstroom: North-West University. (Dissertation - MSc). http://hdl.handle.net/10394/31274

Milenkovic, D., Blaza, J.N., Larsson, N.G. & Hirst, J. 2017. The enigma of the respiratory chain supercomplex. *Cell metabolism*, 25(4):765-776. doi:10.1016/j.cmet.2017.03.009

Miller, H.C., Louw, R., Mereis, M., Venter, G., Boshoff, J.-D., Mienie, L., Van Reenen, M., Venter, M., Lindeque, J.Z. & Domínguez-Martínez, A. 2021. Metallothionein 1 overexpression does not protect against mitochondrial disease pathology in Ndufs4 knockout mice. *Molecular Neurobiology*, 58(1):243-262. doi:10.1007/s12035-020-02121-y

Miltenyi, S., Muller, W., Weichel, W. & Radbruch, A. 1990. High gradient magnetic cell separation with MACS. *Cytometry Part A: Journal of Quantitative Cell Science*, 11(2):231-238. doi:10.1002/cyto.990110203

Moffett, J.R., Ross, B., Arun, P., Madhavarao, C.N. & Namboodiri, A.M. 2007. *Progress in Neurobiology*, 81(2):89-131. doi:10.1016/j.pneurobio.2006.12.003

Mráček, T., Drahota, Z. & Houštěk, J. 2013. The function and the role of the mitochondrial glycerol-3-phosphate dehydrogenase in mammalian tissues. *Biochimica et Biophysica Acta (BBA)-Bioenergetics*, 1827(3):401-410. doi:10.1016/j.bbabio.2012.11.014

Nagrath, D., Caneba, C., Karedath, T. & Bellance, N. 2011. Metabolomics for mitochondrial and cancer studies. *Biochimica et Biophysica Acta (BBA) - Bioenergetics*, 1807(6):650-663. doi:10.1016/j.bbabio.2011.03.006

Neagu, M., Constantin, C., Popescu, I.D., Zipeto, D., Tzanakakis, G., Nikitovic, D., Fenga, C., Stratakis, C.A., Spandidos, D.A. & Tsatsakis, A.M. 2019. Inflammation and metabolism in cancer cell-mitochondria key player. *Frontiers in Oncology*, 9:348. doi:10.3389/fonc.2019.00348

Neurauter, G., Schrocksnadel, K., Scholl-Burgi, S., Sperner-Unterweger, B., Schubert, C., Ledochowski, M. & Fuchs, D. 2008. Chronic immune stimulation correlates with reduced phenylalanine turnover. *Current Drug Metabolism*, 9(7):622-627. doi:10.2174/138920008785821738

Newgard, C.B. 2017. Metabolomics and metabolic diseases: where do we stand? *Cell Metabolism*, 25(1):43-56. doi:10.1016/j.cmet.2016.09.018

Nikkanen, J., Forsstrom, S., Euro, L., Paetau, I., Kohnz, R.A., Wang, L., Chilov, D., Viinamaki, J., Roivainen, A., Marjamaki, P., Liljenback, H., Ahola, S., Buzkova, J., Terzioglu, M., Khan, N.A., Pirnes-Karhu, S., Paetau, A., Lonnqvist, T., Sajantila, A., Isohanni, P., Tyynismaa, H., Nomura, D.K., Battersby, B.J., Velagapudi, V., Carroll, C.J. & Suomalainen, A. 2016. Mitochondrial DNA replication defects disturb cellular dNTP pools and remodel one-carbon metabolism. *Cell Metabolism*, 23(4):635-648. doi:10.1016/j.cmet.2016.01.019

Nunnari, J. & Suomalainen, A. 2012. Mitochondria: in sickness and in health. *Cell*, 148(6):1145-1159. doi:10.1016/j.cell.2012.02.035

Oka, K., Ohya-Shimada, W., Mizuno, S. & Nakamura, T. 2013. Up-regulation of cyclin-E_1 via proline-mTOR pathway is responsible for HGF-mediated G_1/S progression in the primary culture of rat hepatocytes. *Biochemical and Biophysical Research Communications*, 435(1):120-125. doi:10.1016/j.bbrc.2013.04.052

Ortigoza-Escobar, J.D., Oyarzabal, A., Montero, R., Artuch, R., Jou, C., Jimenez, C., Gort, L., Briones, P., Muchart, J., Lopez-Gallardo, E., Emperador, S., Pesini, E.R., Montoya, J., Perez, B., Rodriguez-Pombo, P. & Perez-Duenas, B. 2016. Ndufs4 related Leigh syndrome: a case report and review of the literature. *Mitochondrion*, 28:73-78. doi:10.1016/j.mito.2016.04.001

Pagnamenta, A.T., Wei, W., Rahman, S. & Chinnery, P.F. 2021. Biparental inheritance of mitochondrial DNA revisited. *Nature Reviews Genetics*, 22(8):477-478. doi:10.1038/s41576-021-00380-6

Palmieri, F. 2013. The mitochondrial transporter family SLC25: identification, properties and physiopathology. *Molecular Aspects of Medicine*, 34(3):465-484. doi:10.1016/j.mam.2012.05.005

Palmieri, F. & Pierri, C.L. 2010. Structure and function of mitochondrial carriers - role of the transmembrane helix P and G residues in the gating and transport mechanism. *FEBS Letters*, 584(9):1931-1939. doi:10.1016/j.febslet.2009.10.063

Palmieri, F. & Monne, M. 2016. Discoveries, metabolic roles and diseases of mitochondrial carriers: A review. *Biochimica et Biophysica Acta (BBA) - Molecular Cell Research*, 1863(10):2362-2378. doi:10.1016/j.bbamcr.2016.03.007

Palmieri, L., Papaleo, V., Porcelli, V., Scarcia, P., Gaita, L., Sacco, R., Hager, J., Rousseau, F., Curatolo, P., Manzi, B., Militerni, R., Bravaccio, C., Trillo, S., Schneider, C., Melmed, R., Elia, M., Lenti, C., Saccani, M., Pascucci, T., Puglisi-Allegra, S., Reichelt, K.L. & Persico, A.M. 2010. Altered calcium homeostasis in autism-spectrum disorders: evidence from biochemical and genetic studies of the mitochondrial aspartate/glutamate carrier AGC1. *Molecular Psychiatry*, 15(1):38-52. doi:10.1038/mp.2008.63

Pan, D., Lindau, C., Lagies, S., Wiedemann, N. & Kammerer, B. 2018. Metabolic profiling of isolated mitochondria and cytoplasm reveals compartment-specific metabolic responses. *Metabolomics*, 14(5):59. doi:10.1007/s11306-018-1352-x

Pang, Z., Chong, J., Zhou, G., de Lima Morais, D.A., Chang, L., Barrette, M., Gauthier, C., Jacques, P.-É., Li, S. & Xia, J. 2021. MetaboAnalyst 5.0: narrowing the gap between raw spectra and functional insights. *Nucleic Acids Research*, doi:10.1093/nar/gkab382

Papa, S. 2002. The NDUFS4 nuclear gene of complex I of mitochondria and the cAMP cascade. *Biochimica et Biophysica Acta (BBA) - Bioenergetics*, 1555(1-3):147-153. doi:10.1016/s0005-2728(02)00270-0

Papa, S., Scacco, S., De Rasmo, D., Signorile, A., Papa, F., Panelli, D., Nicastro, A., Scaringi, R., Santeramo, A., Roca, E., Trentadue, R. & Larizza, M. 2010. cAMP-dependent protein kinase regulates post-translational processing and expression of complex I subunits in mammalian cells. *Biochimica et Biophysica Acta (BBA) - Bioenergetics*, 1797(6-7):649-658. doi:10.1016/j.bbabio.2010.03.013

Passarella, S. & Schurr, A. 2018. L-lactate transport and metabolism in mitochondria of hep G2 cells—the Cori cycle revisited. *Frontiers in Oncology*, 8(120), doi:10.3389/fonc.2018.00120

Passarella, S., de Bari, L., Valenti, D., Pizzuto, R., Paventi, G. & Atlante, A. 2008. Mitochondria and L-lactate metabolism. *FEBS Letters*, 582(25-26):3569-3576. doi:10.1016/j.febslet.2008.09.042

Pastorino, J.G. & Hoek, J.B. 2008. Regulation of hexokinase binding to VDAC. *Journal of Bioenergetics and Biomembranes*, 40(3):171-182. doi:10.1007/s10863-008-9148-8

Patti, M.-E. & Corvera, S. 2010. The role of mitochondria in the pathogenesis of type 2 diabetes. *Endocrine Reviews*, 31(3):364-395. doi:10.1210/er.2009-0027

Paul, M.H. & Sperling, E. 1952. Cyclophorase system. XXIII. Correlation of cyclophorase activity and mitochondrial density in striated muscle. *Proceedings of the Society for Experimental Biology and Medicine*, 79(3):352-354. doi:10.3181/00379727-79-19375

Pfeffer, G. & Chinnery, P.F. 2013. Diagnosis and treatment of mitochondrial myopathies. *Annals of Medicine*, 45(1):4-16. doi:10.3109/07853890.2011.605389

Phang, J.M. 2019. Proline metabolism in cell regulation and cancer biology: recent advances and hypotheses. *Antioxidants and Redox Signaling*, 30(4):635-649. doi:10.1089/ars.2017.7350

Picard, M., White, K. & Turnbull, D.M. 2013. Mitochondrial morphology, topology, and membrane interactions in skeletal muscle: a quantitative three-dimensional electron microscopy study. *Journal of Applied Physiology*, 114(2):161-171. doi:10.1152/japplphysiol.01096.2012

Picard, M., Wallace, D.C. & Burelle, Y. 2016. The rise of mitochondria in medicine. *Mitochondrion*, 30:105-116. doi:10.1016/j.mito.2016.07.003

Priori, R., Scrivo, R., Brandt, J., Valerio, M., Casadei, L., Valesini, G. & Manetti, C. 2013. Metabolomics in rheumatic diseases: the potential of an emerging methodology for improved patient diagnosis, prognosis, and treatment efficacy. *Autoimmunity Reviews*, 12(10):1022-1030. doi:10.1016/j.autrev.2013.04.002

Pronicka, E. 2017. Hypocapnic hypothesis of Leigh disease. *Medical Hypotheses*, 101:23-27. doi:10.1016/j.mehy.2017.01.016

Pustylnikov, S., Costabile, F., Beghi, S. & Facciabene, A. 2018. Targeting mitochondria in cancer: current concepts and immunotherapy approaches. *Translational Research*, 202:35-51. doi:10.1016/j.trsl.2018.07.013

Quintana, A., Kruse, S.E., Kapur, R.P., Sanz, E. & Palmiter, R.D. 2010. Complex I deficiency due to loss of Ndufs4 in the brain results in progressive encephalopathy resembling Leigh syndrome. *Proceedings of the National Academy of Sciences*, 107(24):10996-11001. doi:10.1073/pnas.1006214107

Quintana, A., Morgan, P.G., Kruse, S.E., Palmiter, R.D. & Sedensky, M.M. 2012. Altered anesthetic sensitivity of mice lacking NDUFS4, a subunit of mitochondrial complex I. *Plos One*, 7(8):e42904. doi:10.1371/journal.pone.0042904

Quirós, P.M., Mottis, A. & Auwerx, J. 2016. Mitonuclear communication in homeostasis and stress. *Nature Reviews Molecular Cell Biology*, 17(4):213-226. doi:10.1038/nrm.2016.23

Rahman, J., Noronha, A., Thiele, I. & Rahman, S. 2017. Leigh map: a novel computational diagnostic resource for mitochondrial disease. *Annals of Neurology*, 81(1):9-16. doi:10.1002/ana.24835

Razak, M.A., Begum, P.S., Viswanath, B. & Rajagopal, S. 2017. Multifarious beneficial effect of nonessential amino acid, glycine: a review. *Oxidative Medicine and Cellular Longevity*, 2017:1716701. doi:10.1155/2017/1716701

Reyes, A., He, J., Mao, C.C., Bailey, L.J., Di Re, M., Sembongi, H., Kazak, L., Dzionek, K., Holmes, J.B., Cluett, T.J., Harbour, M.E., Fearnley, I.M., Crouch, R.J., Conti, M.A., Adelstein, R.S., Walker, J.E. & Holt, I.J. 2011. Actin and myosin contribute to mammalian mitochondrial DNA maintenance. *Nucleic Acids Research*, 39(12):5098-5108. doi:10.1093/nar/gkr052

Riley, J.S., Quarato, G., Cloix, C., Lopez, J., O'Prey, J., Pearson, M., Chapman, J., Sesaki, H., Carlin, L.M., Passos, J.F., Wheeler, A.P., Oberst, A., Ryan, K.M. & Tait, S.W. 2018. Mitochondrial inner membrane permeabilisation enables mtDNA release during apoptosis. *The EMBO Journal*, 37(17):e99238. doi:10.15252/embj.201899238

Rodenburg, R.J. 2016. Mitochondrial complex I-linked disease. *Biochimica et Biophysica Acta (BBA) - Bioenergetics*, 1857(7):938-945. doi:10.1016/j.bbabio.2016.02.012

Roede, J.R., Park, Y., Li, S., Strobel, F.H. & Jones, D.P. 2012. Detailed mitochondrial phenotyping by high resolution metabolomics. *Plos One*, 7(3):e33020. doi:10.1371/journal.pone.0033020

Rogers, G.W., Brand, M.D., Petrosyan, S., Ashok, D., Elorza, A.A., Ferrick, D.A. & Murphy, A.N. 2011. High throughput microplate respiratory measurements using minimal quantities of isolated mitochondria. *Plos One*, 6(7):e21746. doi:10.1371/journal.pone.0021746

Ross-Inta, C., Tsai, C.Y. & Giulivi, C. 2008. The mitochondrial pool of free amino acids reflects the composition of mitochondrial DNA-encoded proteins: indication of a post- translational quality control for protein synthesis. *Bioscience Reports*, 28(5):239-249. doi:10.1042/BSR20080090

Ruggeri, B.A., Camp, F. & Miknyoczki, S. 2014. Animal models of disease: pre-clinical animal models of cancer and their applications and utility in drug discovery. *Biochemical Pharmacology*, 87(1):150-161. doi:10.1016/j.bcp.2013.06.020

Ruoppolo, M., Caterino, M., Albano, L., Pecce, R., Di Girolamo, M.G., Crisci, D., Costanzo, M., Milella, L., Franconi, F. & Campesi, I. 2018. Targeted metabolomic profiling in rat tissues reveals sex differences. *Scientific reports*, 8(1):1-12. doi:10.1038/s41598-018-22869-7

Russell, O.M., Gorman, G.S., Lightowlers, R.N. & Turnbull, D.M. 2020. Mitochondrial diseases: hope for the future. *Cell*, 181(1):168-188. doi:10.1016/j.cell.2020.02.051

Sahebekhtiari, N., Thomsen, M.M., Sloth, J.J., Stenbroen, V., Zeviani, M., Gregersen, N., Viscomi, C. & Palmfeldt, J. 2016. Quantitative proteomics suggests metabolic reprogramming during ETHE1 deficiency. *Proteomics*, 16(7):1166-1176. doi:10.1002/pmic.201500336

Saleh, J., Peyssonnaux, C., Singh, K.K. & Edeas, M. 2020. Mitochondria and microbiota dysfunction in COVID-19 pathogenesis. *Mitochondrion*, 54:1-7. doi:10.1016/j.mito.2020.06.008

Samluk, L., Chroscicki, P. & Chacinska, A. 2018. Mitochondrial protein import stress and signaling. *Current Opinion in Physiology*, 3:41-48. doi:10.1016/j.cophys.2018.02.010

Sarabhai, T. & Roden, M. 2019. Hungry for your alanine: when liver depends on muscle proteolysis. *The Journal of Clinical Investigation*, 129(11):4563-4566. doi:10.1172/JCI131931

Sazanov, L.A. 2015. A giant molecular proton pump: structure and mechanism of respiratory complex I. *Nature Reviews Molecular Cell Biology*, 16(6):375-388. doi:10.1038/nrm3997

Scacco, S., Petruzzella, V., Budde, S., Vergari, R., Tamborra, R., Panelli, D., van den Heuvel, L.P., Smeitink, J.A. & Papa, S. 2003. Pathological mutations of the human *Ndufs4* gene of the 18-kDa (AQDQ) subunit of complex I affect the expression of the protein and the assembly and function of the complex. *Journal of Biological Chemistry*, 278(45):44161-44167. doi:10.1074/jbc.M307615200

Schiaffino, S. & Reggiani, C. 2011. Fiber types in mammalian skeletal muscles. *Physiological Reviews*, 91(4):1447-1531. doi:10.1152/physrev.00031.2010

Schieber, M. & Chandel, N.S. 2014. ROS function in redox signaling and oxidative stress. *Current Biology*, 24(10):R453-462. doi:10.1016/j.cub.2014.03.034

Schiff, M., Benit, P., Coulibaly, A., Loublier, S., El-Khoury, R. & Rustin, P. 2011. Mitochondrial response to controlled nutrition in health and disease. *Nutrition Reviews*, 69(2):65-75. doi:10.1111/j.1753-4887.2010.00363.x

Schlattner, U., Tokarska-Schlattner, M. & Wallimann, T. 2006. Mitochondrial creatine kinase in human health and disease. *Biochimica et Biophysica Acta (BBA) - Molecular Basis of Disease*, 1762(2):164-180. doi:10.1016/j.bbadis.2005.09.004

Schmitt, S., Saathoff, F., Meissner, L., Schropp, E.M., Lichtmannegger, J., Schulz, S., Eberhagen, C., Borchard, S., Aichler, M., Adamski, J., Plesnila, N., Rothenfusser, S., Kroemer, G. & Zischka, H. 2013. A semi-automated method for isolating functionally intact mitochondria from cultured cells and tissue biopsies. *Analytical Biochemistry*, 443(1):66-74. doi:10.1016/j.ab.2013.08.007

Schwörer, S., Berisa, M., Violante, S., Qin, W., Zhu, J., Hendrickson, R.C., Cross, J.R. & Thompson, C.B. 2020. Proline biosynthesis is a vent for TGFβ-induced mitochondrial redox stress. *The EMBO Journal*, 39(8):e103334. doi:10.15252/embj.2019103334

Schymanski, E.L., Jeon, J., Gulde, R., Fenner, K., Ruff, M., Singer, H.P. & Hollender, J. 2014. Identifying small molecules via high resolution mass spectrometry: communicating confidence. *Environmental Science and Technology*, 48(4):2097-2098. doi:10.1021/es5002105

Sharma, R., Reinstadler, B., Engelstad, K., Skinner, O.S., Stackowitz, E., Haller, R.G., Clish, C.B., Pierce, K., Walker, M.A., Fryer, R., Oglesbee, D., Mao, X., Shungu, D.C., Khatri, A., Hirano, M., De Vivo, D.C. & Mootha, V.K. 2021. Circulating markers of NADH-reductive stress correlate with mitochondrial disease severity. *Journal of Clinical Investigation*, 131(2):e136055. doi:10.1172/JCI136055

Shaughnessy, D.T., McAllister, K., Worth, L., Haugen, A.C., Meyer, J.N., Domann, F.E., Van Houten, B., Mostoslavsky, R., Bultman, S.J., Baccarelli, A.A., Begley, T.J., Sobol, R.W., Hirschey, M.D., Ideker, T., Santos, J.H., Copeland, W.C., Tice, R.R., Balshaw, D.M. & Tyson, F.L. 2014. Mitochondria, energetics, epigenetics, and cellular responses to stress. *Environmental Health Perspectives*, 122(12):1271-1278. doi:10.1289/ehp.1408418

Shepherd, D. & Garland, P.B. 1969. The kinetic properties of citrate synthase from rat liver mitochondria. *Biochemical Journal*, 114(3):597-610. doi:10.1042/bj1140597

Shibata, T., Yamashita, S., Hirusaki, K., Katoh, K. & Ohta, Y. 2015. Isolation of mitochondria by gentle cell membrane disruption, and their subsequent characterization. *Biochemical and Biophysical Research Communications*, 463(4):563-568. doi:10.1016/j.bbrc.2015.05.095

Sies, H. & Jones, D.P. 2020. Reactive oxygen species (ROS) as pleiotropic physiological signalling agents. *Nature reviews Molecular cell biology*, 21(7):363-383. doi:10.1038/s41580-020-0230-3

Sivanand, S., Viney, I. & Wellen, K.E. 2018. Spatiotemporal control of acetyl-CoA metabolism in chromatin regulation. *Trends in Biochemical Sciences*, 43(1):61-74. doi:10.1016/j.tibs.2017.11.004

Smith, P.K., Krohn, R.I., Hermanson, G.T., Mallia, A.K., Gartner, F.H., Provenzano, M.D., Fujimoto, E.K., Goeke, N.M., Olson, B.J. & Klenk, D.C. 1985. Measurement of protein using bicinchoninic acid. *Analytical Biochemistry*, 150(1):76-85. doi:10.1016/0003-2697(85)90442-7

Son, S.M., Park, S.J., Stamatakou, E., Vicinanza, M., Menzies, F.M. & Rubinsztein, D.C. 2020. Leucine regulates autophagy via acetylation of the mTORC1 component raptor. *Nature Communications*, 11(1):3148. doi:10.1038/s41467-020-16886-2

Steinhauser, M.L. & Lechene, C.P. 2013. Quantitative imaging of subcellular metabolism with stable isotopes and multi-isotope imaging mass spectrometry. *Seminars in Cell & Developmental Biology*, 24(8-9):661-667. doi:10.1016/j.semcdb.2013.05.001

Stepien, K.M., Heaton, R., Rankin, S., Murphy, A., Bentley, J., Sexton, D. & Hargreaves, I.P. 2017. Evidence of oxidative stress and secondary mitochondrial dysfunction in metabolic and non-metabolic disorders. *Journal of Clinical Medicine*, 6(7):71. doi:10.3390/jcm6070071

Steyn, H.S. & Ellis, S.M. 2003. Practical significance (effect sizes) versus or in combination with statistical significance (p-values): research note. *Management Dynamics*, 12(4):51-53.

Stroud, D.A., Surgenor, E.E., Formosa, L.E., Reljic, B., Frazier, A.E., Dibley, M.G., Osellame, L.D., Stait, T., Beilharz, T.H., Thorburn, D.R., Salim, A. & Ryan, M.T. 2016. Accessory subunits are integral for assembly and function of human mitochondrial complex I. *Nature*, 538(7623):123-126. doi:10.1038/nature19754

Sullivan, G.M. & Feinn, R. 2012. Using effect size - or why the P value is not enough. *Journal of Graduate Medical Education*, 4(3):279-282. doi:10.4300/JGME-D-12-00156.1

Szibor, M., Gizatullina, Z., Gainutdinov, T., Endres, T., Debska-Vielhaber, G., Kunz, M., Karavasili, N., Hallmann, K., Schreiber, F., Bamberger, A., Schwarzer, M., Doenst, T., Heinze, H.J., Lessmann, V., Vielhaber, S., Kunz, W.S. & Gellerich, F.N. 2020. Cytosolic, but not matrix, calcium is essential for adjustment of mitochondrial pyruvate supply. *Journal of Biological Chemistry*, 295(14):4383-4397. doi:10.1074/jbc.RA119.011902

Tahrir, F.G., Shanmughapriya, S., Ahooyi, T.M., Knezevic, T., Gupta, M.K., Kontos, C.D., McClung, J.M., Madesh, M., Gordon, J., Feldman, A.M., Cheung, J.Y. & Khalili, K. 2018. Dysregulation of mitochondrial bioenergetics and quality control by HIV-1 Tat in cardiomyocytes. *Journal of Cell Physiology*, 233(2):748-758. doi:10.1002/jcp.26002

Takahashi, Y., Kioka, H., Shintani, Y., Ohki, A., Takashima, S., Sakata, Y., Higuchi, T. & Saito, S. 2019. Detection of increased intracerebral lactate in a mouse model of Leigh syndrome using proton MR spectroscopy. *Magnetic Resonance Imaging*, 58:38-43. doi:10.1016/j.mri.2019.01.010

Terburgh, K., Lindeque, Z., Mason, S., van der Westhuizen, F. & Louw, R. 2019. Metabolomics of Ndufs4$^{-/-}$ skeletal muscle: adaptive mechanisms converge at the ubiquinone-cycle. *Biochimica et Biophysica Acta (BBA) - Molecular Basis of Disease*, 1865(1):98-106. doi:10.1016/j.bbadis.2018.10.034

Terburgh, K., Coetzer, J., Lindeque, J.Z., van der Westhuizen, F.H. & Louw, R. 2021. Aberrant BCAA and glutamate metabolism linked to regional neurodegeneration in a mouse model of Leigh syndrome. *Biochimica et Biophysica Acta (BBA) - Molecular Basis of Disease*, 1867(5):166082. doi:10.1016/j.bbadis.2021.166082

Thompson, K., Collier, J.J., Glasgow, R.I.C., Robertson, F.M., Pyle, A., Blakely, E.L., Alston, C.L., Olahova, M., McFarland, R. & Taylor, R.W. 2020. Recent advances in understanding the molecular genetic basis of mitochondrial disease. *Journal of Inherited Metabolic Disease*, 43(1):36-50. doi:10.1002/jimd.12104

Tiku, V., Tan, M.-W. & Dikic, I. 2020. Mitochondrial functions in infection and immunity. *Trends in Cell Biology*, 30(4):263-275. doi:10.1016/j.tcb.2020.01.006

Torraco, A., Peralta, S., Iommarini, L. & Diaz, F. 2015. Mitochondrial diseases part I: mouse models of OXPHOS deficiencies caused by defects in respiratory complex subunits or assembly factors. *Mitochondrion*, 21:76-91. doi:10.1016/j.mito.2015.01.009

Triepels, R., Van Den Heuvel, L., Trijbels, J. & Smeitink, J. 2001. Respiratory chain complex I deficiency. *American Journal of Medical Genetics*, 106(1):37-45. doi:10.1002/ajmg.1397

Tsai, C. 1967. Spontaneous decarboxylation of oxalacetic acid. *Canadian Journal of Chemistry*, 45(8):873-880.

Tsai, G. & Coyle, J.T. 1995. N-acetylaspartate in neuropsychiatric disorders. *Progress in Neurobiology*, 46(5):531-540. doi:10.1016/0301-0082(95)00014-M

Tyynismaa, H., Carroll, C.J., Raimundo, N., Ahola-Erkkila, S., Wenz, T., Ruhanen, H., Guse, K., Hemminki, A., Peltola-Mjosund, K.E., Tulkki, V., Oresic, M., Moraes, C.T., Pietilainen, K., Hovatta, I. & Suomalainen, A. 2010. Mitochondrial myopathy induces a starvation-like response. *Human Molecular Genetics*, 19(20):3948-3958. doi:10.1093/hmg/ddq310

Tzelepis, F., Blagih, J., Khan, N., Gillard, J., Mendonca, L., Roy, D.G., Ma, E.H., Joubert, P., Jones, R.G. & Divangahi, M. 2018. Mitochondrial cyclophilin D regulates T cell metabolic responses and disease tolerance to tuberculosis. *Science Immunology*, 3(23), doi:10.1126/sciimmunol.aar4135

Ugalde, C., Janssen, R.J., van den Heuvel, L.P., Smeitink, J.A. & Nijtmans, L.G. 2004. Differences in assembly or stability of complex I and other mitochondrial OXPHOS complexes in inherited complex I deficiency. *Human Molecular Genetics*, 13(6):659-667. doi:10.1093/hmg/ddh071

Valsecchi, F., Monge, C., Forkink, M., de Groof, A.J., Benard, G., Rossignol, R., Swarts, H.G., van Emst-de Vries, S.E., Rodenburg, R.J., Calvaruso, M.A., Nijtmans, L.G., Heeman, B., Roestenberg, P., Wieringa, B., Smeitink, J.A., Koopman, W.J. & Willems, P.H. 2012. Metabolic consequences of NDUFS4 gene deletion in immortalized mouse embryonic fibroblasts. *Biochimica et Biophysica Acta (BBA) - Bioenergetics*, 1817(10):1925-1936. doi:10.1016/j.bbabio.2012.03.006

Van Aardt, W.J., Le Roux, J.M., Lindeque, J.Z., Mason, S. & Louw, R. 2016. The effect of temperature on the respiration and metabolism of the African burrowing scorpion (Opistophthalmus latimanus). *Comparative biochemistry and physiology part D: genomics and proteomics*, 20:50-56. doi:10.1016/j.cbd.2016.07.003

van den Berg, R.A., Hoefsloot, H.C., Westerhuis, J.A., Smilde, A.K. & van der Werf, M.J. 2006. Centering, scaling, and transformations: improving the biological information content of metabolomics data. *BMC Genomics*, 7(1):142. doi:10.1186/1471-2164-7-142

Van der Walt, G. 2018. Development of a compartment metabolomics approach for studying mitochondrial complex I deficiency in mouse skeletal muscle. Potchefstroom: North-West University. (Mini-dissertation - BSc Hons.).

Van der Walt, G. & Louw, R. 2020. Novel mitochondrial and cytosolic purification pipeline for compartment-specific metabolomics in mammalian disease model tissues. *Metabolomics*, 16(7):78. doi:10.1007/s11306-020-01697-9

Van der Walt, G., Lindeque, J.Z., Mason, S. & Louw, R. 2021. Sub-cellular metabolomics contributes mitochondria-specific metabolic insights to a mouse model of Leigh syndrome. *Metabolites*, 11(10):658. doi:10.3390/metabo11100658

Van Vranken, J.G. & Rutter, J. 2015. You down with ETC? Yeah, you know D! *Cell*, 162(3):471-473. doi:10.1016/j.cell.2015.07.027

Van Vranken, J.G. & Rutter, J. 2016. The whole (cell) is less than the sum of its parts. *Cell*, 166(5):1078-1079. doi:10.1016/j.cell.2016.08.011

Vendelin, M., Béraud, N., Guerrero, K., Andrienko, T., Kuznetsov, A.V., Olivares, J., Kay, L. & Saks, V.A. 2005. Mitochondrial regular arrangement in muscle cells: a “crystal-like” pattern. *American Journal of Physiology-Cell Physiology*, 288(3):C757-C767. doi:10.1152/ajpcell.00281.2004

Villa-Cuesta, E. & Rand, D.M. 2015. Preparation of mitochondrial enriched fractions for metabolic analysis in drosophila. *Journal of Visualized Experiments*, (103):53149. doi:10.3791/53149

Vinaixa, M., Samino, S., Saez, I., Duran, J., Guinovart, J.J. & Yanes, O. 2012. A guideline to univariate statistical analysis for LC/MS-based untargeted metabolomics-derived data. *Metabolites*, 2(4):775-795. doi:10.3390/metabo2040775

Vinogradov, A.D. & Grivennikova, V.G. 2016. Oxidation of NADH and ROS production by respiratory complex I. *Biochimica et Biophysica Acta (BBA) - Bioenergetics*, 1857(7):863-871. doi:10.1016/j.bbabio.2015.11.004

Wallace, D.C. 2012. Mitochondria and cancer. *Nature Reviews Cancer*, 12(10):685-698. doi:10.1038/nrc3365

Walter, L. & Hajnóczky, G. 2005. Mitochondria and endoplasmic reticulum: the lethal interorganelle cross-talk. *Journal of Bioenergetics and Biomembranes*, 37(3):191-206. doi:10.1007/s10863-005-6600-x

Walzel, B., Speer, O., Zanolla, E., Eriksson, O., Bernardi, P. & Wallimann, T. 2002. Novel mitochondrial creatine transport activity: implications for intracellular creatine compartments and bioenergetics. *Journal of Biological Chemistry*, 277(40):37503-37511. doi:10.1074/jbc.M201168200

Wang, A.C. & Bax, A. 1993. Minimizing the effects of radio-frequency heating in multidimensional NMR experiments. *Journal of biomolecular NMR*, 3(6):715-720. doi:10.1007/BF00198374

Wang, H., Liang, X., Luo, G., Ding, M. & Liang, Q. 2016. Protection effect of nicotinamide on cardiomyoblast hypoxia/re-oxygenation injury: study of cellular mitochondrial metabolism. *Molecular Biosystems*, 12(7):2257-2264. doi:10.1039/c6mb00108d

Wang, W., Wu, Z., Dai, Z., Yang, Y., Wang, J. & Wu, G. 2013. Glycine metabolism in animals and humans: implications for nutrition and health. *Amino Acids*, 45(3):463-477. doi:10.1007/s00726-013-1493-1

Wasilewski, M., Chojnacka, K. & Chacinska, A. 2017. Protein trafficking at the crossroads to mitochondria. *Biochimica et Biophysica Acta (BBA) - Molecular Cell Research*, 1864(1):125-137. doi:10.1016/j.bbamcr.2016.10.019

Wells, A., Barrington, W., Threadgill, D., Dearth, S., Campagna, S., Saxton, A. & Voy, B. 2016. Gene, sex and diet interact to control the tissue metabolome. *The FASEB Journal*, 30:127.122. doi:10.1096/fasebj.30.1_supplement.127.2

Wiechert, W. 2001. ^{13}C metabolic flux analysis. *Metabolic Engineering*, 3(3):195-206. doi:10.1006/mben.2001.0187

Willemse, L. 2019. Establishment of a sub-cellular approach for efficient mitochondria isolation from skeletal muscle and analysis via ^{1}H-NMR. Potchefstroom: North-West University. (Mini-dissertation - BSc Hons.).

Wirth, C., Brandt, U., Hunte, C. & Zickermann, V. 2016. Structure and function of mitochondrial complex I. *Biochimica et Biophysica Acta (BBA) - Bioenergetics*, 1857(7):902-914. doi:10.1016/j.bbabio.2016.02.013

Wu, H., Southam, A.D., Hines, A. & Viant, M.R. 2008. High-throughput tissue extraction protocol for NMR-and MS-based metabolomics. *Analytical Biochemistry*, 372(2):204-212. doi:10.1016/j.ab.2007.10.002

Wu, M., Gu, J., Guo, R., Huang, Y. & Yang, M. 2016. Structure of mammalian respiratory supercomplex $I_1III_2IV_1$. *Cell*, 167(6):1598-1609 doi:10.1016/j.cell.2016.11.012

Wu, M., Neilson, A., Swift, A.L., Moran, R., Tamagnine, J., Parslow, D., Armistead, S., Lemire, K., Orrell, J., Teich, J., Chomicz, S. & Ferrick, D.A. 2007. Multiparameter metabolic analysis reveals a close link between attenuated mitochondrial bioenergetic function and enhanced glycolysis dependency in human tumor cells. *American Journal of Physiology-Cell Physiology*, 292(1):C125-136. doi:10.1152/ajpcell.00247.2006

Xie, X., Venit, T., Drou, N. & Percipalle, P. 2018. In mitochondria b-actin regulates mtDNA transcription and is required for mitochondrial quality control. *iScience*, 3:226-237. doi:10.1016/j.isci.2018.04.021

Yang, L., Garcia Canaveras, J.C., Chen, Z., Wang, L., Liang, L., Jang, C., Mayr, J.A., Zhang, Z., Ghergurovich, J.M., Zhan, L., Joshi, S., Hu, Z., McReynolds, M.R., Su, X., White, E., Morscher, R.J. & Rabinowitz, J.D. 2020. Serine catabolism feeds NADH when respiration is impaired. *Cell Metabolism*, 31(4):809-821. doi:10.1016/j.cmet.2020.02.017

Yang, Y. & Sauve, A.A. 2016. NAD^+ metabolism: bioenergetics, signaling and manipulation for therapy. *Biochimica et Biophysica Acta (BBA) - Proteins and Proteomics*, 1864(12):1787-1800. doi:10.1016/j.bbapap.2016.06.014

Yao, J., Irwin, R.W., Zhao, L., Nilsen, J., Hamilton, R.T. & Brinton, R.D. 2009. Mitochondrial bioenergetic deficit precedes Alzheimer's pathology in female mouse model of Alzheimer's disease. *Proceedings of the National Academy of Sciences*, 106(34):14670-14675. doi:10.1073/pnas.0903563106

Ylikallio, E. & Suomalainen, A. 2012. Mechanisms of mitochondrial diseases. *Annals of Medicine*, 44(1):41-59. doi:10.3109/07853890.2011.598547

Yoshida, G.J. 2021. The harmonious interplay of amino acid and monocarboxylate transporters induces the robustness of cancer cells. *Metabolites*, 11(1):27. doi:10.3390/metabo11010027

Young, A., Oldford, C. & Mailloux, R.J. 2020. Lactate dehydrogenase supports lactate oxidation in mitochondria isolated from different mouse tissues. *Redox Biology*, 28:101339. doi:10.1016/j.redox.2019.101339

Yudkoff, M. 2017. Interactions in the metabolism of glutamate and the branched-chain amino acids and ketoacids in the CNS. *Neurochemical Research*, 42(1):10-18. doi:10.1007/s11064-016-2057-z

Zhang, L., Zhou, Y., Wu, W., Hou, L., Chen, H., Zuo, B., Xiong, Y. & Yang, J. 2017. Skeletal muscle-specific overexpression of PGC-1alpha induces fiber-type conversion through enhanced mitochondrial respiration and fatty acid oxidation in mice and pigs. *International Journal of Biological Sciences*, 13(9):1152-1162. doi:10.7150/ijbs.20132

Zhou, Z., Austin, G.L., Young, L.E.A., Johnson, L.A. & Sun, R. 2018. Mitochondrial metabolism in major neurological diseases. *Cells*, 7(12):E229. doi:10.3390/cells7120229

Zhu, J., Vinothkumar, K.R. & Hirst, J. 2016. Structure of mammalian respiratory complex I. *Nature*, 536(7616):354-358. doi:10.1038/nature19095

Zickermann, V., Wirth, C., Nasiri, H., Siegmund, K., Schwalbe, H., Hunte, C. & Brandt, U. 2015. Structural biology: mechanistic insight from the crystal structure of mitochondrial complex I. *Science*, 347(6217):44-49. doi:10.1126/science.1259859

Zorova, L.D., Popkov, V.A., Plotnikov, E.Y., Silachev, D.N., Pevzner, I.B., Jankauskas, S.S., Babenko, V.A., Zorov, S.D., Balakireva, A.V., Juhaszova, M., Sollott, S.J. & Zorov, D.B. 2018. Mitochondrial membrane potential. *Analytical Biochemistry*, 552:50-59. doi:10.1016/j.ab.2017.07.009